A model of material failure for reinforced concrete via continuum strong discontinuity approach and mixing theory

D.L. Linero
J. Oliver
A. Huespe

Monograph CIMNE Nº-106, November 2007

A model of material failure for reinforced concrete via continuum strong discontinuity approach and mixing theory

D.L. Linero
J. Oliver
A. Huespe

Monograph CIMNE Nº-106, November 2007

Centro Internacional de Métodos Numéricos en Ingeniería
Gran Capitán s/n, 08034 Barcelona, España

CENTRO INTERNACIONAL DE MÉTODOS NUMÉRICOS EN INGENIERÍA
Edificio C1, Campus Norte UPC
Gran Capitán s/n
08034 Barcelona, Spain

Primera edición: November 2007

A MODEL OF MATERIAL FAILURE FOR REINFORCED CONCRETE VIA CONTINUUM STRONG DISCONTINUITY APPROACH AND MIXING THEORY
Monograph CIMNE M106

ISBN: 978-84-96736-34-4

Abstract

In this work a two-dimensional formulation describing the fracture process in reinforced concrete is developed, implemented and validated. The cracks in the material are captured by means of *continuum strong discontinuity approach (CSDA)* (Oliver 1996) and the constitutive model of composite material is defined through *mixing theory* (Truesdell & Toupin 1960).

The composite material consists of one or two groups of long fibers or steel bars embedded within a concrete matrix. Likewise, each component is characterized by a constitutive model. The concrete is described by a damage model with degradation in tension and compression (Oliver, Cervera et al. 1990). A uniaxial plasticity model (Simó & Hughes 1998) is used for the steel. Also, phenomena as *bond-slip* and *dowel action* (Park & Paulay 1975) are included and represented by additional models of interaction between concrete and steel.

The initiation and propagation of cracks are understood as a strain localization process described by means of CSDA. A bifurcation analysis of composite material is proposed to establish the bifurcation time and direction of the crack.

The model has been implemented in a two-dimensional analysis program using the finite element method (FEM), where it is assumed material non-linearity and infinitesimal strains. An implicit-explicit integration scheme for the constitutive equation (Oliver, Huespe et al. 2004; Oliver, Huespe et al. 2006) ensures a positive defined stiffness matrix of the problem and increases the robustness and stability of the solution. On the other hand, a strategy to tracking discontinuity paths (Samaniego 2002; Oliver & Huespe 2004), allows that the discontinuity paths correspond among the elements.

According to the proposed formulation, on each point of solid, the strain and stress fields of the reinforced concrete are described as a composite material. This has the following advantages: first, the model facilitates the implementation on the finite element method, since many ingredients of standard numerical process remain, and secondly, the macroscopic

scale of analysis avoids the discretization of each component material and the interaction effects, and consequently the computational cost is reduced.

The model can reproduce two different stages of cracking in the reinforced concrete. Initially, the steel capacity and the adherence in the interface produce a stable stage of distributed cracking, where appear many cracks with constant spacing and opening. Afterward, a localization cracking stage is characterized by few cracks while the structural response decreases.

Reinforced concrete members subjected to tension, bending and shear are simulated. The numerical results, mainly the structural response and the crack pattern, are compared with experimental test (Leonhardt 1965; Collins, Vecchio et al. 1985; Ouyang & Shah 1994; Ruiz, Elices et al. 1998). The correlation between numerical results using the proposed formulation and actual results is quantitative and qualitatively satisfactory.

Contents

List of main symbols

$\left[\mathbf{B}^{(e)}\right],\left[\mathbf{G}^{(e)}\right]$	strain - displacement matrices.
$\left[\mathbb{C}_{tg}^{dr}\right]$	tangent constitutive matrix of the fibers in **r** given by the slipping fiber model (Voigt notation).
$\left[\mathbb{C}_{tg}^{ds}\right]$	tangent constitutive matrix of the fibers in **s** given by the slipping fiber model (Voigt notation).
$\left[\mathbb{C}_{tg}^{f\tau}\right]$	tangent constitutive matrix of the dowel action model (Voigt notation).
$\left[\mathbb{C}_{tg}^{m}\right]$	tangent constitutive matrix of the concrete matrix model (Voigt notation).
$\left[\mathbb{C}_{tg}\right]$	tangent constitutive matrix of the composite material (Voigt notation).
$\left\{\dot{\boldsymbol{\varepsilon}}\right\}$	strain rate vector of the composite material (Voigt notation).
$[\![\dot{\boldsymbol{\varepsilon}}]\!]$	difference between the strain rate inside and outside the discontinuity surface.
$\left\{\dot{F}_{ext}^{(e)}\right\}$	external forces rate vector in the finite element.
$\left[\mathbf{K}^{(e)}\right]$	stiffness matrix of the finite element.
$\left[\mathbf{Q}_{tg}^{dr}\right]$	localization matrix of the fibers in **r** given by the slipping fiber model.
$\left[\mathbf{Q}_{tg}^{ds}\right]$	localization matrix of the fibers in **s** given by the slipping fiber model.
$\left[\mathbf{Q}_{tg}^{f\tau}\right]$	localization matrix of the dowel action model.

$[\mathbf{Q}_{tg}^{m}]$	localization matrix of the concrete matrix material model.
$[\mathbf{Q}_{tg}]$	localization matrix of the composite material.
$\{\dot{r}^{(e)}\}$	residual forces rate vector associated to the degrees of freedom of the displacement jump in the finite element.
$\{\dot{R}^{(e)}\}$	residual forces rate vector associated to the degrees of freedom of the compatible displacement in the finite element.
$\{\dot{\boldsymbol{\sigma}}\}$	stress rate vector of the composite material (Voigt notation).
$\{\dot{\boldsymbol{\sigma}}^{f\tau}\}$	stress rate vector of the dowel action model (Voigt notation).
$\{\dot{\boldsymbol{\sigma}}^{fr}\}$	stress rate vector of the fibers in **r** (Voigt notation).
$\{\dot{\boldsymbol{\sigma}}^{fs}\}$	stress rate vector of the fibers in **s** (Voigt notation).
$\{\dot{\boldsymbol{\sigma}}^{m}\}$	stress rate vector of the concrete matrix (Voigt notation).
$[\![\dot{\mathbf{u}}]\!]$	displacement rate jump in a point of composite material.
$\alpha^{f\tau}$	strain-like internal variable of the dowel action model.
α^{fr}	strain-like internal variable of the fibers in **r** given by the deformable fiber model.
$\bar{\alpha}^{f\tau}$	discrete internal variable of the dowel action model.
$\bar{\alpha}^{fr}$	discrete internal variable of the fibers in **r**.
$\bar{\alpha}^{fs}$	discrete internal variable of the fibers in **s**.
$\bar{\alpha}^{m}$	discrete internal variable of the concrete matrix.
$\boldsymbol{\beta}^{(e)}$	displacement jump vector of a finite element.
δ^{τ}	relative displacement between the faces of a crack, perpendicular to the axis of the fiber due to the dowel action.
δ^{i}	slipping in the end of a bar in a pull-out test.
δ_{S}^{k}	Dirac's delta regularized function.
δ_{S}	Dirac's delta function in discontinuity surface.
$\boldsymbol{\varepsilon}$	strain tensor of the composite material.
$\boldsymbol{\varepsilon}_{\Omega\backslash S}$	strain tensor of the composite material in $\Omega\backslash S$.
ε_{rr}^{dr}	normal strain of the fibers in **r** given by the slipping fiber model.
ε_{ss}^{ds}	normal strain of the fibers in **s** given by the slipping fiber model.

ε_p^{fr}	plastic mechanical strain of the fibers in **r**.
ε_{rr}^{fr}	normal mechanical strain the fibers in **r**.
ε_p^{ir}	plastic strain of the fibers in **r** given by the bond-slip model.
ε_{rr}^{ir}	bond-slip strain in interface between the concrete matrix and the fibers in **r**.
ε_{ss}^{is}	bond-slip strain in interface between the fibers in **s** and the concrete matrix.
$\boldsymbol{\varepsilon}^m$	strain tensor of the concrete matrix.
$\varepsilon_{rr}^m, \varepsilon_{ss}^m, \gamma_{rs}^m$	components of strain tensor for the concrete matrix in *rs*-plane.
ε_{ss}^{fs}	normal mechanical strain the fibers in **s**.
$\varepsilon_{rr}, \varepsilon_{ss}, \gamma_{rs}$	components of strain tensor for the composite material in *rs*-plane.
$\boldsymbol{\varepsilon}_S$	strain rate tensor of the composite material in *S*.
ϕ	amplification parameter of the strain norm of the damage model with degradation in tension and compression.
$\boldsymbol{\gamma}$	admissible strain field.
γ_p^f	plastic strain in the dowel action model.
γ_{rs}^f	shear strain of the fibers in *rs*-plane.
φ	arbitrary continuous function.
φ_{fr}	angle formed between vector **r** and *x*-axis.
φ_{fs}	angle formed between vector **r** and *x*-axis.
$\lambda^{f\tau}$	plastic multiplier of the dowel action model.
λ^{fr}	plastic multiplier of the fibers in **r** given by deformable fiber model.
λ^{fs}	plastic multiplier of the deformable fiber model for fibers in **s**.
λ^{ir}	plastic multiplier of the bond-slip model for fibers in **r**.
λ^m	damage multiplier of concrete matrix model.
Γ_σ	boundary of the solid where the traction rate is prescribed.
ν^f	Poisson's ratio of the reinforcement steel.
ν^m	Poisson's ratio of the concrete matrix.
$\boldsymbol{\eta}'$	discontinuous displacements.
$\bar{\boldsymbol{\eta}}$	admissible regular displacements.
θ_{loc}	angle formed between the *1*-direction of principal strain and vector $\mathbf{n}_{loc}$, called localization angle.

θ_n	angle formed between the *1*-direction of principal strain and vector **n.**
$\boldsymbol{\sigma}$	stress tensor of the composite material.
$\boldsymbol{\sigma}_{\Omega\backslash S}$	stress tensor of the composite material in $\Omega\backslash S$.
σ_{rr}^{dr}	stress of the fibers in **r** given by the slipping fiber model.
σ_{adh}^{ir}	stress of total loss of adherence between the concrete matrix and the fibers in **r**.
σ_{rr}^{fr}	normal stress of fibers in **r**.
$\sigma_{rr(\Omega\backslash S)}^{f}$	normal stress of fibers parallel to **r** in $\Omega\backslash S$.
σ_{y}^{fr}	yielding stress of fibers in **r**.
$\sigma_{ss(\Omega\backslash S)}^{fs}$	normal stress of fibers parallel to **s** in $\Omega\backslash S$.
$\sigma_{ss(S)}^{fs}$	normal stress of fibers parallel to **s** on *S*.
σ_{y}^{f}	yielding stress of reinforcement steel.
σ_{rr}^{ir}	stress in the interface between the concrete matrix and the fibers in **r**, given by the bond-slip model.
σ_{ss}^{is}	stress in the interface between the concrete matrix and the fibers in **s**, given by the bond-slip model.
$\boldsymbol{\sigma}^{m}$	stress tensor of the concrete matrix.
$\boldsymbol{\sigma}_{\Omega\backslash S}^{m}$	stress tensor of the concrete matrix in $\Omega\backslash S$.
σ_{u}^{m}	tensile strength of the concrete matrix.
$\sigma_{u(c)}^{m}$	compressive strength of the concrete matrix.
σ_{ss}^{ds}	stress of the fiber in **s** given by slipping fiber model.
$\boldsymbol{\sigma}_{(S)}^{m}$	stress tensor of the concrete matrix on *S*.
$\boldsymbol{\sigma}_{S}$	stress tensor of the composite material on *S*.
$\sigma_{rr}, \sigma_{ss}, \sigma_{rs}$	components of stress tensor for the composite material in *rs*-plane.
$\bar{\boldsymbol{\sigma}}^{m}$	effective stress tensor of the concrete matrix.
$\bar{\sigma}_{i}^{m}$	effective stress of the concrete matrix in *i*-principal direction.
$\bar{\sigma}_{r}^{m}$	distance between the origin and the point that represents the tensional state in Mohr's circle.
$\bar{\sigma}_{xx}^{m}, \bar{\sigma}_{yy}^{m}, \bar{\sigma}_{xy}^{m}$	components of effective stress tensor for the concrete matrix in *xy*-plane.
$\tau_{\varepsilon(tc)}$	strain norm of the damage model with degradation to tension and compression.
τ_{rs}^{f}	shear stress of the fibers in *rs*-plane.

$\tau^{f}_{rs(\Omega\backslash S)}$	shear stress of the fibers in *rs*-plane, in $\Omega\backslash S$.
τ^{f}_{y}	yielding equivalent shear stress of the fiber associated to the dowel action.
$\tau^{f}_{rs(S)}$	shear stress of the fiber on *S*.
Ω	domain of the composite material.
Ω^{+},Ω^{-}	sub-domains of the composite material limited by the solid boundary and discontinuity surface.
ψ	free energy in the damage model of the concrete matrix.
$\mathbf{v}_{t}$	unit vector normal to solid boundary.
$\mathbf{1}$	second-order identity tensor.
$\mathbf{A}$	second-order tensor defined as $\mathbf{A} = \mathbb{C}^{m} : \partial_{\boldsymbol{\sigma}}\phi$
A^{f}	cross section area of a circular bar of diameter *d*.
$\mathbf{b}$	body forces vector in the solid.
$\mathbb{C}^{m}$	elastic constitutive tensor in the concrete matrix.
$\mathbb{C}^{m}_{tg}$	tangent constitutive tensor in the composite material.
$\mathbb{C}_{tg}$	tangent constitutive tensor in the concrete matrix.
d	diameter of a reinforcement bar.
$\mathbf{d}_{i}$	compatible displacement vector in node *i* of a finite element in two-dimensional space.
E^{dr}_{tg}	tangent constitutive operator of the fibers in **r** given by the slipping fiber model.
E^{ds}_{tg}	tangent constitutive operator of the fibers in **s** given by the slipping fiber model.
E^{f}	módulo de Young del acero de refuerzo.
E^{fr}	Young's modulus of the fibers in **r**.
E^{fr}_{tg}	tangent constitutive operator of the fibers in **r** given by the deformable fiber model.
E^{fs}	Young's modulus of the fibers in **s**.
E^{fs}_{tg}	tangent constitutive operator of the fibers in **s** given by the deformable fiber model.
E^{ir}	elastic modulus in the interface between the concrete matrix and the fibers in **r**, given by the bond-slip model.
E^{ir}_{tg}	tangent constitutive operator in the interface between the concrete matrix and the fibers in **r**, given by the bond-slip model.

E^{is}	elastic modulus in the interface between the concrete matrix and the fibers in **s**, given by the bond-slip model.
E^{is}_{tg}	tangent constitutive operator in the interface between the concrete matrix and the fibers in **s**, given by the bond-slip model.
E^{m}	Young's modulus of the concrete matrix.
$f^{f\tau}$	yielding function in the dowel action model.
f^{fr}	yielding function of the fibers in **r** given by the deformable fiber model.
f^{ir}	yielding function in the interface between the concrete matrix and the fibers in **r**, given by the bond-slip model.
f^{m}	damage function of the concrete matrix.
G^{f}	fracture energy of the concrete matrix.
$G^{f\tau}$	equivalent shear modulus of the fiber associated to dowel action.
$G^{f\tau}_{tg}$	tangent constitutive model operator of the dowel action model.
$H^{f\tau}$	softening parameter of the dowel action model.
H^{fr}	softening parameter of the fibers in **r** given deformable fiber model.
H^{fs}	softening parameter of the fibers in **s** given deformable fiber model.
H^{m}	softening parameter of the concrete matrix.
$\mathcal{H}_S$	Heaviside's function on the discontinuity surface *S*.
$\overline{H}^{f\tau}$	discrete softening parameter in the dowel action model.
$\overline{H}^{fr}$	discrete softening parameter of the fibers in **r** given deformable fiber model.
$\overline{H}^{fs}$	discrete softening parameter of the fibers in **s** given deformable fiber model.
$\overline{H}^{m}$	discrete softening parameter of the concrete matrix.
I^{f}	moment of inertia of a bar or fiber.
k^{fr}	volumetric participation factor of the fibers in **r**.
k^{fs}	volumetric participation factor of the fibers in **s**.
k^{m}	volumetric participation factor of the concrete matrix.

l^{τ}	opening of a crack parallel to the longitudinal axis of the fiber, which represents the free span of a bar fixed at both ends subjected to bending (dowel action).
L^{i}	length of a steel bar embedded in the concrete for the pull-out test.
M	maximum bending moment in a bar produced by the dowel action.
$\mathcal{M}_{S}$	unit jump function in continuum medium.
M_{y}	plastic bending moment in a bar produced by the dowel action.
$\mathbf{n}$	unit vector **n** normal to discontinuity surface.
n_{σ}	relation between compression strength $\sigma^{m}_{u(c)}$ and tensile strength σ^{m}_{u} of the concrete matrix.
N_{i}	shape function of a linear triangular finite element.
$\mathbf{n}_{loc}$	unit vector **n** normal to discontinuity surface at bifurcation time.
P^{i}	force applied in the end of a bar, for the pull-out test.
P^{i}_{max}	maximum load of a bar in the pull-out test.
$q^{f\tau}$	stress-like internal variable of the dowel action model.
$q^{f\tau}_{s}$	stress-like internal variable of the dowel action model, defined on the discontinuity surface *S*.
$q^{f\tau}_{s(SD)}$	stress-like internal variable of the dowel action model, defined on the surface *S*, at strong discontinuity time.
q^{fr}	stress-like internal variable of the fibers in **r** given by deformable fiber model.
q^{fr}_{s}	stress-like internal variable of the fibers in **r** given by deformable fiber model, defined on the surface *S*.
$q^{fr}_{s(SD)}$	stress-like internal variable of the fibers in **r** given by deformable fiber model, defined on the surface *S*, at strong discontinuity time.
q^{fs}_{s}	stress-like internal variable of the fibers in **s** given by deformable fiber model, defined on the surface *S*.
$q^{fs}_{s(SD)}$	stress-like internal variable of the fibers in **s** given by deformable fiber model, defined on the surface *S*, at strong discontinuity time.

q^m	stress-like internal variable of the concrete matrix.
$\mathbf{Q}^m$	elastic localization tensor or acoustic tensor of the concrete matrix.
q_s^m	stress-like internal variable of the concrete matrix on *S*.
$q_{s(SD)}^m$	stress-like internal variable of the concrete matrix on *S*, for strong discontinuity time.
$\mathbf{Q}_{tg}^m$	localization tensor of the concrete matrix.
$\mathbf{Q}_{tg}$	localization tensor of the composite material.
$\mathbf{r}$	unit vector parallel to longitudinal axis of the first fiber package.
r^m	strain-like internal variable of the concrete matrix.
r_S^m	strain-like internal variable of the concrete matrix on *S*.
r_x, r_y	vector components of **r** in *xy*-plane.
$\mathbf{s}$	unit vector parallel to longitudinal axis of the second fiber package (vector **s** is considered perpendicular to vector **r**).
S	discontinuity surface inside of the solid.
s_x, s_y	vector components of **s** in *xy*-plane.

$\mathbf{t}^*$	prescribed traction vector in the solid.
$\mathbf{t}_{\Omega\backslash S}$	traction vector of the composite material in $\Omega\backslash S$.
t_B	material bifurcation time.
$\mathbf{t}_S$	traction vector of the composite material on *S*.
$\mathbf{u}$	displacement vector in a composite material point.
$\dot{\mathbf{u}}$	displacement rate vector (or velocity vector) in a composite material point.
$\dot{\bar{\mathbf{u}}}$	continuous part of the displacement rate vector in a composite material point.
V	shear force in a bar due to the dowel action.
V^{fr}	fibers volume parallel to vector **r**.
V^{fs}	fibers volume parallel to vector **s**.
V^m	concrete matrix volume.
$\bar{V}$	total volume of the composite material.
V_y	yielding shear force in a bar due to the dowel action.

Chapter 1
Introduction

1.1. Motivation

The reinforced concrete is used commonly as construction material; therefore, its behavior is permanently studied as much in the experimental field as in the numerical simulation.

The integration between a quasi-fragile material as the concrete and a ductile material as the steel offers a complex structural response during the fracture process mainly. The stiffness, the loading capacity and the formation of cracks depend on the mechanical properties of the materials and on the effects of interaction between the concrete and the steel bars.

In order to represent the behavior of the reinforced concrete during the fracture process, it is necessary a technique able to capture the formation and propagation of cracks in all the points of the solid, from the particular properties of the simple concrete and the steel. Different approaches allow reaching this goal.

In some cases, the structure can be modeled to a sufficiently small scale or mesoscopic scale, in such a way that each material point of the analyzed domain responds only to one of the component materials. The drawback of this technique is the high computational cost.

The formulation proposed in this work expects to reduce such a cost by using a homogenized macroscopic model, in which a material point can represent the behavior of the reinforced concrete treated as a composite material, through a model that contains the constitutive law of each component material and its effects of interaction.

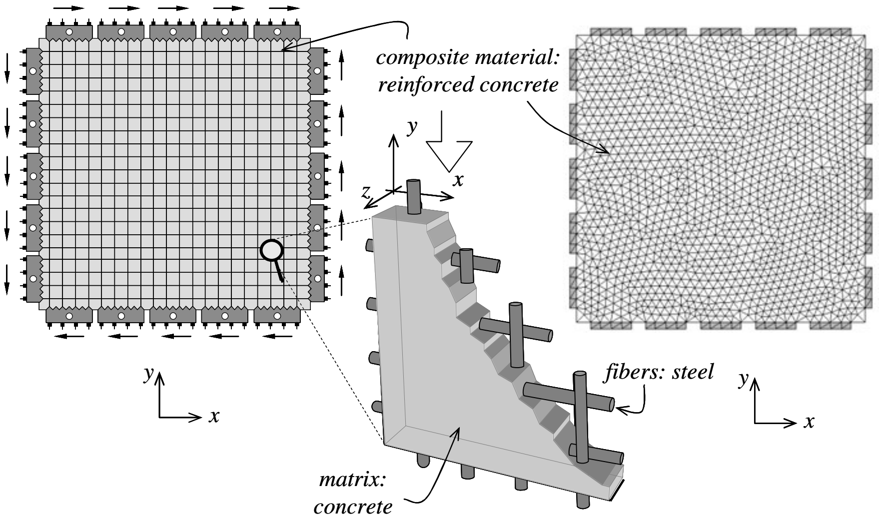

Figure 1.1. Numerical modeling of reinforced concrete walls subjected to shear.

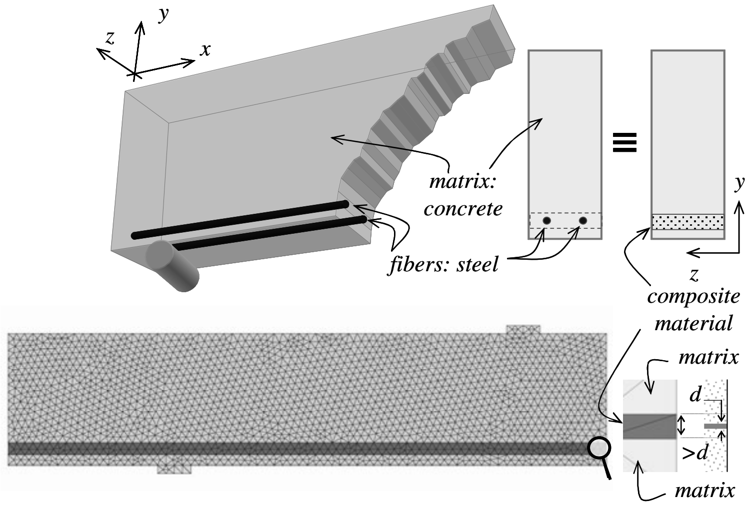

Figure 1.2. Numerical modeling of reinforced concrete beams.

In continuum mechanics, the phenomenon of strain localization caused by the appearance of a crack can be represented by means of enriched kinematics describing a jump in the strain field.

If the constitutive model of the composite material considers a common strain field among the materials that form it, then the kinematics equipped to capture discontinuities in simple materials can be applied in an equal way in the composite material, this constitutes an important advantage which is used by the formulation presented here.

The implementation of the formulation in the finite elements method will allow the two-dimensional numerical simulation of reinforced concrete structures in general.

1.1.1. Application of the numerical model

The proposed model describes the fracture process in the reinforced concrete represented as a composite material. The structural response and the formation and propagation of the cracks are some of the results obtained.

In high beams and walls or panels subjected to shear, it is common that the reinforcement steel is distributed in the whole structure as shown in Figure 1.1. The formulation allows simulating these problems regarded as a homogenous medium of composite material, where each point contains a concrete percentage and another of steel.

In the case of structures reinforced in specific zones such as the beam shown in Figure 1.2, the finite elements in dark gray represent the reinforced concrete through a constitutive model of composite material, while the rest of the beam corresponds to simple concrete model.

1.1.2. One-dimensional model of composite material

As part of the problem motivation, the constitutive model of a composite material appears next, assuming an exclusively axial behavior of the matrix and fibers, and admitting a perfect adherence condition between both components.

A point of composite material consists of a volumetric participation of matrix k^m and of fiber k^f and it is subjected to tension as indicated in Figure 1.3(a). It was established that the strain is equal to $\varepsilon = \varepsilon^m = \varepsilon^f$ and the stress corresponds to $\sigma = k^m \sigma^m + k^f \sigma^f$, from the compatibility conditions and equilibrium equations in the composite material, where ε^m is matrix strain, ε^f is fiber strain, σ^m is matrix stress and σ^f is fiber stress. Likewise, the strain rate and the stress rate in the composite material are:

$$\dot{\varepsilon} = \dot{\varepsilon}^m = \dot{\varepsilon}^f \tag{1.1}$$

$$\dot{\sigma} = k^m \dot{\sigma}^m + k^f \dot{\sigma}^f \tag{1.2}$$

The earlier equations represent the special case of *mixing theory* (Truesdell & Toupin 1960) applied in one-dimensional space.

The behavior of the matrix can be represented with a one-dimensional damage model (Figure 1.3(b)), whose ingredients are summarized in the following table (Oliver, Huespe et al. 2002), where E^m is Young's modulus, $\bar{\sigma}^m$ is the effective stress, H^m is the softening parameter, r^m and q^m are strain-like and stress-like internal variables.

$$\psi(\varepsilon^m, r^m) = \frac{q^m}{2r^m} E^m (\varepsilon^m)^2 \quad \text{(free energy)} \tag{1.3}$$

$$\sigma^m = \frac{\partial \psi}{\partial \boldsymbol{\varepsilon}^m} = \frac{q^m}{r^m} E^m \varepsilon^m = \frac{q^m}{r^m} \bar{\sigma}^m \quad \text{(constitutive equation)} \tag{1.4}$$

$$\dot{r}^m = \lambda^m, \quad r^m \geq r^m_{t=0} = \sigma^m_u \quad \text{(evolution law)} \tag{1.5}$$

$$f^m(\sigma^m, q^m) = \left|\sigma^m\right| - q^m \quad \text{(damage criterion)} \tag{1.6}$$

$$\left.\begin{array}{r} f^m \leq 0, \quad \lambda^m \geq 0, \quad \lambda^m f^m = 0 \\ \lambda^m \dot{f}^m = 0 \ \ (f^m = 0) \end{array}\right\} \quad \begin{array}{l}\text{(loading-unloading and} \\ \text{persistency conditions)}\end{array} \tag{1.7}$$

$$\left.\begin{array}{r} \dot{q}^m = H^m(r)\dot{r}^m, \quad H^m = \dfrac{dq^m}{dr^m} \leq 0 \\ 0 \leq q^m \leq r^m_{t=0}, \quad q^m_{t=0} = r^m_{t=0} \end{array}\right\} \quad \text{(softening rule)} \tag{1.8}$$

Table 1.1. Ingredients of a scalar isotropic damage model in a one-dimensional space.

From the earlier expressions the tangent constitutive equation of the matrix can be established as:

$$\dot{\sigma}^m = E^m_{tg} \dot{\varepsilon}^m \ \text{ where } \ E^m_{tg} = \begin{cases} E^m & \text{elastic /unloading regime} \\ E^m H^m & \text{inelastic loading regime} \end{cases} \tag{1.9}$$

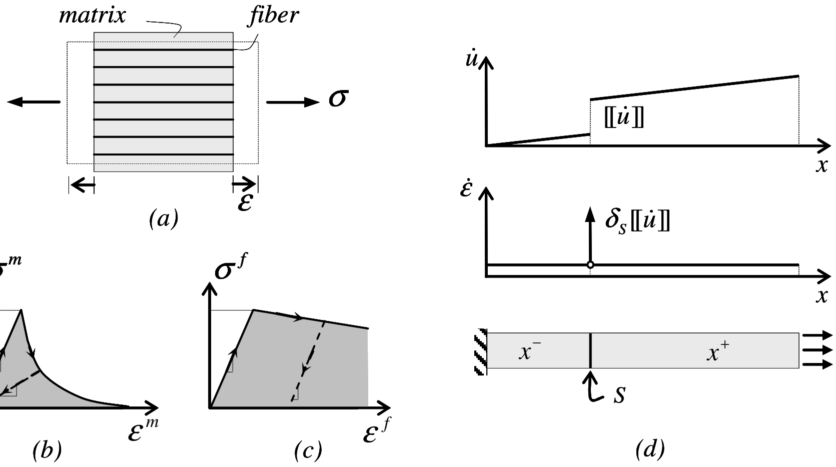

Figure 1.3. One-dimensional model of composite material: (a) representation of a material point, (b) stress *vs* strain curves of the matrix, (c) stress *vs* strain curves of the fibers, (d) distribution of the displacement rates and strain rate in a bar subjected to tension.

On the other hand, the behavior of fibers is represented by a one-dimensional plasticity model (Figure 1.3(c)), defined by the following expressions (Simó & Hughes 1998):

$\sigma^f = E^f(\varepsilon^f - \varepsilon_p^f)$	(constitutive equation)	(1.10)
$\dot{\varepsilon}_p^f = \lambda^f \operatorname{sign}(\sigma^f)$	(flow rule)	(1.11)
$\dot{\alpha}^f = \lambda^f$	(evolution law)	(1.12)
$f^f(\sigma^f, \alpha^f) = \lvert\sigma^f\rvert - (q^f + \sigma_y^f)$	(plastic yield criterion)	(1.13)
$\dot{q}^f = H^f \dot{\alpha}^f$	(softening rule)	(1.14)
$\left.\begin{array}{r} f^f \le 0\,;\ \lambda^f \ge 0\,;\ \lambda^f f^f = 0 \\ \lambda^f \dot{f}^f = 0\ (f^f = 0) \end{array}\right\}$	(loading-unloading and persistency conditions)	(1.15)

Table 1.2. Ingredients of a one-dimensional plasticity model describing the mechanical axial behavior of the fiber.

In the fiber, E^f is Young's modulus, ε_p^f corresponds to the plastic strain, H^f is softening parameter, q^f and α^f are stress-like and strain-like internal variables. The tangent constitutive equation obtained from the earlier expressions is equal to:

$$\dot{\sigma}^f = E_{tg}^f \dot{\varepsilon}^f \ \text{ where } \ E_{tg}^f = \begin{cases} E^f & \text{elastic/unloading regime} \\ \dfrac{E^f H^f}{E^f + H^f} & \text{inelastic loading regime} \end{cases} \tag{1.16}$$

Substituting Equations (1.9) and (1.16) into Equation (1.2), and replacing the strain of each component according to Equation (1.1), the constitutive equation of the composite is obtained thus,

$$\dot{\sigma} = E_{tg} \dot{\varepsilon} \tag{1.17}$$

whose tangent constitutive operator is equal to:

$$E_{tg} = k^m E_{tg}^m + k^f E_{tg}^f \tag{1.18}$$

The common strain between the components indicated in Equation (1.1) allows establishing the kinematics of the problem in macroscopic form without discriminating between matrix and fiber.

In accord with continuum strong discontinuity approach (Oliver 1996a), a discontinuity S dividing the continuum into the domains x^+ and x^- (Figure 1.3(d)) is described as a jump of the displacements rate $[[\dot{u}]] = \dot{u}\big|_{x_s^+} - \dot{u}\big|_{x_s^-}$ and consequently it arise a singularity in the strain rate. This latter can be divided into a regular part (bounded) $\dot{\bar{\varepsilon}}$ and a singular part (unbounded) $\delta_S [[\dot{u}]]$, as:

$$\dot{\varepsilon} = \dot{\bar{\varepsilon}} + \delta_S [[\dot{u}]] \tag{1.19}$$

where δ_S is Dirac's delta function on the discontinuity surface *S*.

In addition, a one-dimensional condition of internal traction compatibility is established of the form $[[\dot{\sigma}]] = \dot{\sigma}\big|_{x_s^+} - \dot{\sigma}\big|_{x_s^-} = 0$. Replacing Equations (1.18) and (1.19) into the previous expression, it is obtained that:

$$E_{tg} [[\dot{u}]] = 0 \tag{1.20}$$

Therefore, if $[[\dot{u}]] \neq 0$, it must be fulfilled that $E_{tg} = 0$ in a specific stage of inelastic loading. It can be demonstrated that negative values of E_{tg} produce material bifurcation considering inelastic loading regime in the discontinuity and elastic unloading outside it (Runesson, Ottosen et al. 1991). According to the mentioned earlier, the necessary condition which generates material bifurcation from the formation of a discontinuity in the strain field is:

$$E_{tg} \leq 0 \tag{1.21}$$

It is observed that the parameters of each component material and its volumetric participation determine the appearance of discontinuities on the composite material in a macroscopic scale.

The bifurcation condition of the composite material for the different behaviors of the matrix and the fiber is following:

- During the elastic regime of the matrix and the fiber, the bifurcation condition establishes that $k^m E^m + k^f E^f \leq 0$, which cannot occur due to the positive character of the elastic modulus and the volumetric participation factors.

- When the damage state in the matrix begins and the fiber is still in elastic regime, the bifurcation condition $k^m E^m H^m + k^f E^f \leq 0$ depends on the softening parameter of the matrix H^m; however, it is common that the steel ratio maintains the character positive of E_{tg}.

- In a damage state in the matrix and a plasticity state in the steel, the strain localization takes place when $k^m E^m H^m + (k^f E^f H^f / (E^f + H^f)) \leq 0$. Such a condition is fulfilled easily, still more if there is perfect plasticity in the steel.

1.2. Mechanical behavior of reinforced concrete

1.2.1. Structural response and cracking of the reinforced concrete

The fracture process in the reinforced concrete reveals different stages related directly to the formation of cracks. Next the typical tendencies in the tests of lightly reinforced beams (Ruiz, Elices et al. 1998) and panels subjected to tension (Ouyang, Wollrab et al. 1997) are collected. In the former, the reinforcement is located near to the maximum tension zone parallel to the axis of the beam, however, in the latter, the bars are distributed in the whole cross section of the member.

In lightly reinforced beams, the curve that relates the applied load and the displacement in mid-span indicated in Figure 1.4(a) shows the following tendency (Ruiz & Planas 1994; Ruiz, Elices et al. 1998):

- *Stage without cracking*. This stage describes the elastic behavior of the concrete developed in the portion OL of the curve.

- *Stage of crack initiation.* After the elastic regime of both materials, the cracking of the cover begins while it increases the load until reaching the maximum value M.

- *Stage of crack propagation in the concrete*. From the earlier pseudo-time the curve decays due to the propagation of a single crack in mid-span of the beam. The load reaches minimum value N which depends on the reinforcement ratio and on the adherence level between the concrete and the steel bars.

- *Elastic stage of the reinforcement.* The contribution of the reinforcement to the structural response of the beam is more obvious at the same time as the stress in the concrete tends to zero. The elastic capacity of the bars increases the stiffness of the beam until the yielding stress of the steel at step P.

- *Plastic stage of the reinforcement.* The initiation of the plastic branch of the steel depends on the reinforcement ratio, whereas its decreasing tendency is given by softening of the cracked concrete. This portion of the curve tends to a horizontal asymptote reached when the crack is completely open (assuming that there is not strain hardening in the steel).

In reinforced concrete panel subjected to tension where the reinforcement is uniformly distributed (Beeby & Narayanan 1995; Ouyang, Wollrab et al. 1997), the relationship between load and displacement in the end of the member (Figure 1.4(b)) describes the following stages:

- *Stage without cracking.* During the first increases of load, when the concrete has not yet been cracked, the behavior of both materials is elastic and therefore the load *vs* displacement curve is linear.

- *Stage of cracks formation.* The first crack forms when the strength in the notched cross section is reached, producing a local redistribution of the stress. The stiffness of the panel decays gradually with the appearance of each additional crack. During this stage, the reinforced concrete stiffness is less than the stiffness of the steel bars, even; it could be negative as it occurs in members with very little reinforcement.

- *Stage of homogenous cracking.* The formation of new cracks is limited by the transference capacity of stress between reinforcement and concrete. When the member arrives at the saturated crack condition, the increase in the load produces greater opening of the existing cracks without the appearance of additional cracks. For greater displacements, the contribution of the cracked concrete is minimum compared with the contribution given by the reinforcement, for this reason the structural response of the reinforced concrete tends to the elastic steel curve.

This test considers that the reinforcement remains in elastic regime, therefore, the structural behavior after reached the yielding limit of the steel is not observed.

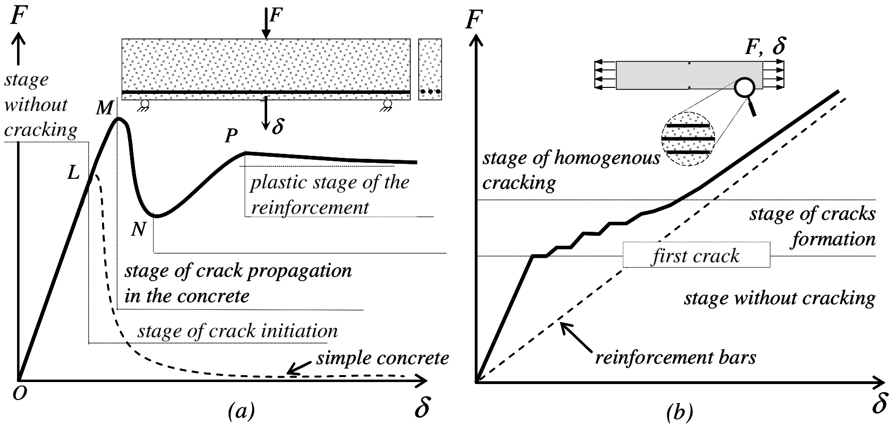

Figure 1.4. Sketch of the typical structural response in members of reinforced concrete: (a) in lightly reinforced beams (Ruiz, Elices et al. 1998), (b) In panel subjected to tension where the reinforcement is uniformly distributed (Beeby & Narayanan 1995; Ouyang, Wollrab et al. 1997).

1.2.2. Adherence loss between concrete and steel

The adherence between concrete and steel is mainly determined by the friction between both materials, which depends on the geometric characteristics of the surface of the reinforcement bars, for example, the corrugated bars provides a high capacity of adherence due to the interlocking between the rib of the reinforcement and the surrounding concrete. For low load levels, the chemical adhesion between concrete and steel also contributes to the adherence (Park & Paulay 1975).

The adherence loss is related to different mechanisms such as the concrete crushing in front of each rib, the appearance of horizontal cracks in the ends, and the presence of transverse secondary cracks. Of the three mechanisms inducing the adherence loss, the most important is the formation of secondary cracks, which are located in the neighborhood of a *primary crack* (Figure 1.5(a)), and they propagate radially from each of the ribs of the bar. Figure 1.5(b) shows the primary and the secondary crack path obtained experimentally by Goto and Otsuka (1979).

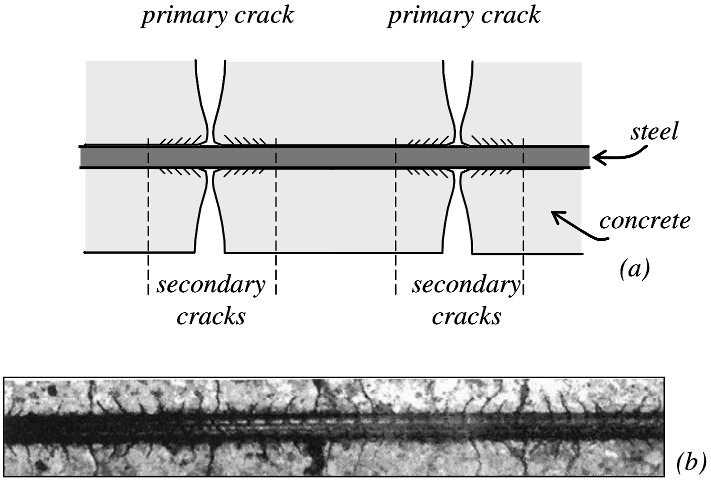

Figure 1.5. Primary and secondary crack path: (a) sketch, (b) experimental result (Goto & Otsuka 1979).

This phenomenon has been studied through different types of tests (Eligehausen, Popov et al. 1983; Gambarova, Rosati et al. 1989; Malvar 1992), obtaining a relationship characteristic between the average stress of adherence and the slipping between the concrete and the steel. Similarly, some pull-out tests (Naaman, Namur et al. 1991; Ruiz, Elices et al. 1998) provide a relationship between the applied load and the slipping in the end of a bar embedded in the concrete.

1.2.3. Dowel action

In a reinforced concrete member where the cracks are mainly opened in mode II of fracture due to shear failure, part of the shear force is taken by the internal interlocking between aggregate particles of the concrete. However, the steel bars crossing the faces of a crack provide the most important contribution to the shear capacity (Park & Paulay 1975). This phenomenon called *dowel action* is produced by bending of the bars in the free span given by the crack opening or by direct shear in the cross section of the reinforcement steel crossing a crack (Figure 1.6).

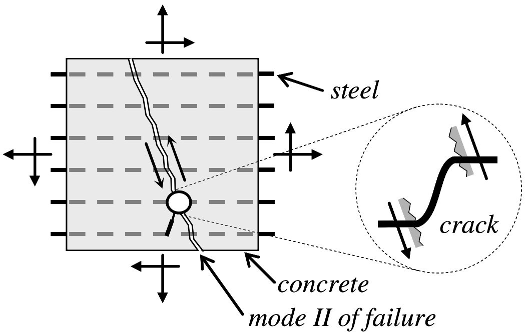

Figure 1.6. Sketch of the dowel action on a cracked member of reinforced concrete in mode II of fracture.

Some authors (Kollegger & Mehlhorn 1990; Belletti, Cerioni et al. 2001; Pietruszczak & Winnicki 2003) have included the dowel action in its numerical models as an additional contribution of the bars to the global behavior of the reinforced concrete.

1.3. Some approaches to the fracture mechanics for homogenous materials

The fracture process in a homogenous material as the concrete can be described by means of a *cohesive crack model*, in which all the cracking zone is concentrated in a surface characterized by a traction *vs* displacement jump law, or by a *smeared crack model*, where the strain inelastic in the fracture zone is spread on a band of defined width (Bazant & Planas 1998). Other models as *strong discontinuity approach* establish a link between the continuous and discrete formulations. Next these models are indicated briefly.

1.3.1. Cohesive crack models

The *cohesive crack model* initially formulated by Dugdale (1960) and Barenblatt (1962), describes the fracture process introducing cohesive forces between the faces of a preexisting crack, considering the energy dissipation associated to the phenomenon of crack propagation. Based on this model, Hillerborg and collaborators (Hillerborg, Modeer et al. 1976; Hillerborg 1985) developed the called *fictitious crack model*, in which, the cohesive crack can be formed and propagated in any place, without the earlier existence of a crack.

In this type of approaches, a discontinuity line controlled by a relationship traction *vs* opening prevails after fulfilling the failure criterion, describing the cohesive nature of the crack.

There are different ways to implement the cohesive crack model into the finite elements method. A way considers the crack faces like part of the contour of the finite elements mesh and it obtains the cohesive forces by means of non-linear mixed boundary conditions or through interface elements that connect the nodes to both sides of the crack (Carol, Prat et al. 1992; Carol & Prat 1997; Carol, López et al. 2001). In this case it is required a remeshing process except in the problems where its crack path is previously known (Ortiz & Quigley 1991). Another way establishes that the discontinuity crosses the element, as indicated in some earlier works (Ortiz, Leroy et al. 1987; Dvorking, Cuitino et al. 1990) and in other more recent works (Belytschko, Moes et al. 2001; Sancho, Planas et al. 2006).

1.3.2. Smeared crack models

The *smeared crack models* represent the fracture process smeared in a region. Rashid (1968) considers an infinite amount of parallel cracks with infinitely small opening smeared in the domain of the finite element. This can be properly modeled by reducing the stiffness and the strength in the normal direction of the crack after being reached the maximum stress of the material. The evolution of the fracture process implies inelastic strains by softening, that is, reduction of the post-maximum stress while increases the strain.

The smeared crack models showed initially certain difficulties, as the instability by localization and sensitivity to the size and direction of the finite elements.

The problem of material instability caused by the strain localization by softening in an arbitrarily small zone has been solved through the *band crack model* proposed by Bazant (1976) and widely developed in some references (Bazant & Cedolin 1983; Bazant & Oh 1983). This model provides a constitutive relationship with softening associated to a specific width of the crack band, which is treated as a material property.

According to the evolution of the smeared crack direction adopted in the calculation algorithm, two different approaches have been developed. The *fixed crack models* assumes that the crack remains fixed in the direction given by the initial cracking state during the evolution of the strain (Cervenka 1985). In return, the *rotating crack models* allows that the crack direction evolves in accord with the change in the direction of the maximum principal direction, conserving also, the same principal direction between the stress states and strain states during the load process (Gupta & Akbar 1984). This approach is more appropriate in problems where the formation of a new crack family of different direction is expected (Vecchio 2000; Pietruszczak & Winnicki 2003).

1.3.3. Strong discontinuity approach

Strong discontinuity is understood as the jump in the displacement field developed on a material surface of the solid. In return, the *weak discontinuity* is defined as the jump in the strain field preserving the continuity of the displacements field on a zone or band of the solid. Therefore, the cohesive crack models exhibit a strong discontinuity, whereas the smeared crack models present a weak discontinuity (Figure 1.7).

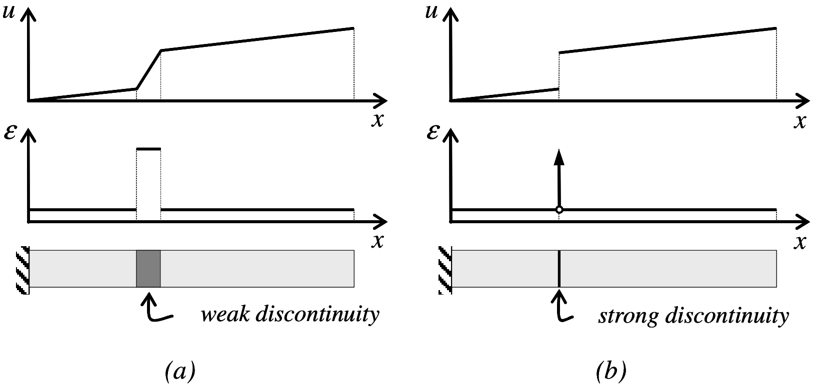

Figure 1.7. Distribution of the axial displacement and the axial strain in a bar subjected to tension: (a) cohesive crack model, (b) band crack model.

In the numerical simulation of the strong discontinuities, the forces of interaction between the faces of a crack can be classified as discrete and continuous. The *discrete methodologies* suppose a relationship between the traction vector and the displacement jump that characterizes the cohesive behavior in the discontinuity, while in the continuous part of the body, a standard constitutive equation stress *vs* strain (generally elastic) is used. In return, the *continuous methodologies* consider the whole solid in the context of the continuum mechanics, in such a way that, the strain concept is defined in the continuous part of the body and also is defined in the discontinuity surface, allowing to apply conventional constitutive equations in any point of the solid (Oliver 1996a).

This methodology is called *continuum strong discontinuity approach (CSDA)* (Oliver 1996a), which establishes the existence of a jump in the displacements field through the failure surface, producing unbounded values (in distributional sense) in the strain field.

In the numerical model, finite elements that can capture these jumps adding *enriched modes of strain* (Simó & Rifai 1990) are used, which are controlled by additional degrees of freedom. These special elements equipped in their interior with displacement discontinuities are called *finite elements with embedded discontinuities* (Ortiz 1987; Larsson, Runnesson et al. 1993; Simó, Oliver et al. 1993; de Borst 2001). Additionally, each finite element has *elemental support* of the discontinuity or *elemental enrichment*, allowing the condensation at level of the element of the degrees of freedom related to the jump.

The concept of *strong discontinuity analysis* (Simó, Oliver et al. 1993) is used as link between the continuous and discrete approaches. Its objective is to identify, in an independent context to the numerical simulation method, the essential qualitative characteristics that remain the consistency of the conventional constitutive equation in appearance of the strong discontinuity. Particularly, this analysis provides a discrete constitutive equation, that is, a relationship stress *vs* displacement jump between the faces of the discontinuity, which is consistent with the selected continuous constitutive equation.

During the fracture process, three successive stages can be distinguished in a material point (Figure 1.8). Likewise, it can observe each stage in different material points at a load step *t* (Figure 1.9). The first stage, called *diffuse failure zone* exhibits a concentration of the strain without showing an obvious discontinuity. Then, the *weak discontinuity zone* shows a continuous displacements field and a discontinuous strain field bounded into a defined band. Finally, the *strong discontinuity zone* presents a considerable displacement jump and therefore, a strain field unbounded into a band of width equal to zero (Manzoli 1998; Oliver, Cervera et al. 1999; Oliver & Huespe 2004a).

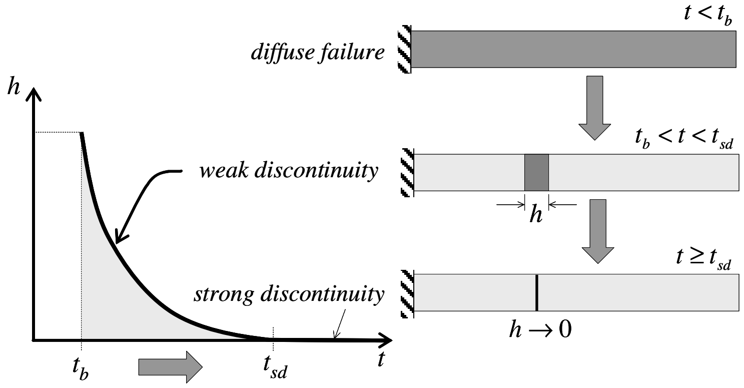

Figure 1.8. Evolution of the crack band in the strong discontinuity approach.

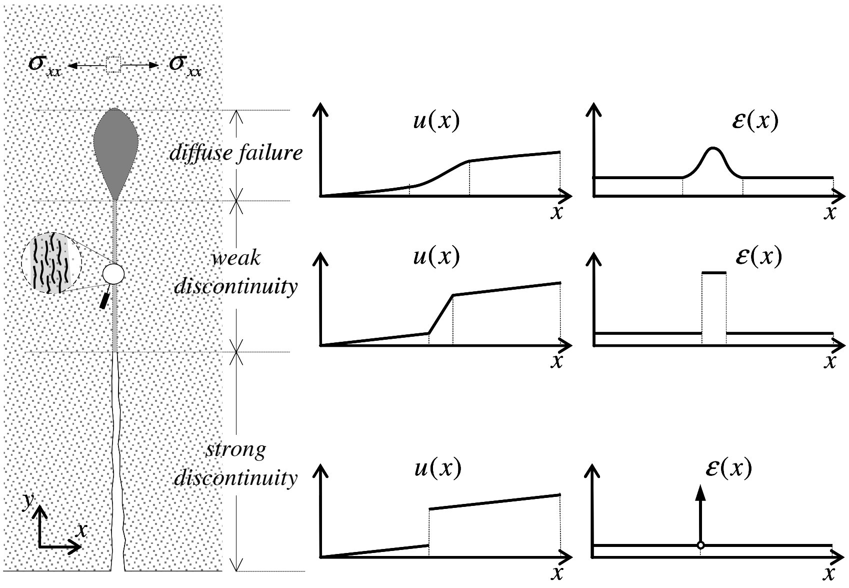

Figure 1.9. Fracture process zones

1.4. Modeling of the material failure of the reinforced concrete

Some authors have developed different methodologies that allow predicting the behavior of the reinforced concrete considering the contribution of the concrete, the steel and the effects of interaction between them.

The simulation of tests of adherence loss between the steel and the surrounding concrete is of great interest since it is a more important mechanism of material failure.

In some approaches, analytical models applicable to particular cases appear, for example: lightly reinforced beams or panels subjected to pure shear. For more general problems, formulations considering non-linear behavior due to the constitutive models of each material are used.

1.4.1. Analysis scale of the reinforced concrete

The reinforced concrete can be modeled numerically in one of the three analysis scales indicated as follows (Cox & Hermann 1998):

- In the *rib-scale* (Figure 1.10(a)), each rib of the bars is meshed by finite elements. The size of these elements can be much smaller than the *representative volume element (RVE)* [1] of the concrete and consequently it can not assumed that the simple concrete is a homogenous material.

- In a intermediate scale called *bar-scale* or *meso-scale*[2] (Figure 1.10(b)), the mechanical interaction of the ribs is homogenized, describing the adherence phenomenon with a layer of finite elements adjacent to the bar.

- In the *member-scale* or *macro-scale* (Figure 1.10(c)), each material point is a structural unit composed by concrete, steel and interface. In this scale is typical that the reinforcement has one-dimensional behavior and that the adherence model is characterized by a pull-out test.

---

[1] The representative volume element (RVE) corresponds to minimum zone where a material can be defined as homogenous.

[2] In the context of the micromechanics exist different interpretations from the terms meso-scale and macro-scale. In this work such terms have been used to distinguish between the simulation in the bar-scale and member-scale.

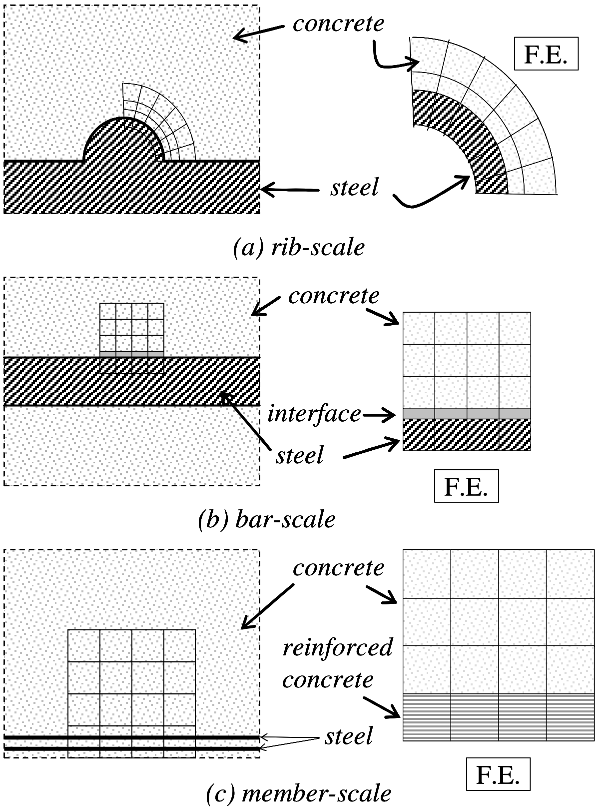

Figure 1.10. Analysis scales of the reinforced concrete (Cox & Hermann 1998): (a) rib-scale, (b) bar-scale and (c) member-scale.

1.4.2. Analytical models of the reinforced concrete

By means of analytical models the behavior of lightly reinforced beams can be studied, where the path of the unique crack is known *a priori*. Two examples of it are observed in some references (Ruiz 2001; Carpinteri, Ferro et al. 2003).

Ruiz (2001) analyzes the propagation of cohesive cracks in lightly reinforced beams subjected to bending, where the structural behavior is controlled mainly by a crack in the midspan. The reinforcement is represented by a *free slipping bar* anchored to both faces of the crack. The spacing between the lips of a crack called *slipping effective length* is obtained supposing that the *free slipping bar* is mechanically equivalent to the true bonded reinforcement. This model reproduces approximately the experimental results (Ruiz, Elices et al. 1998) considering the influence of the size, the reinforcement ratio and the variations in the adherence.

In the works of Carpinteri and collaborators (Carpinteri, Ferro et al. 2003) an adimensional formulation with the cohesive crack models (Bazant & Planas 1998) and the bridged crack models is developed, with the aim of reproducing the bending behavior of reinforced concrete elements. The non-linear modeling of the concrete matrix considers the contribution of forces near the faces of the crack which increase the strength to the fracture of the cross section. The particularity of these models consists of the imposition of the equilibrium conditions and compatibility conditions in the cracked element.

Some works of Vecchio and collaborators (Vecchio & Collins 1986) present an analytical model that predicts the structural response in reinforced concrete panels subjected to shear and normal stress in its plane. The constitutive equations, the equilibrium conditions and compatibility conditions are defined in terms of average stress and average strain; nevertheless, an additional condition between the local stresses on the crack is considered. The model supposes total adherence between the concrete and the steel and uniform distribution of the reinforcement bars on the whole member. The behavior of the concrete is represented by means of a smeared crack model, considering rotation of crack direction and despising the loading history. The direction of the cracks is orthogonal to the maximum principal strain and the spacing among them is established *a priori* by means of empirical expressions.

In some works of Ouyang and collaborators (Ouyang, Wollrab et al. 1997), the load *vs* displacement curve of reinforced concrete panels subjected to tension is obtained. In this case, an analytical model based on the fracture energy of the cracking concrete which includes the slipping effects between concrete and steel are used. The behavior during the cracking process is predicted through the balance among the strain energy, the debounded energy and slipping energy in the interface.

1.4.3. Models of adherence loss between concrete and steel

The slipping effect between the steel bars and the surrounding concrete has been modeled numerically, as much in the rib-scale, as in the bar-scale. Next, some of these works are indicated.

In the works of Ingraffea and others (Ingraffea, Gerstle et al. 1984), the slipping phenomenon of a steel bar embedded in a concrete matrix is numerically modeled, considering that the mechanism of adherence loss is based on the radial propagation of secondary cracks. This approach establishes a law stress *vs* slipping in the interface elements by means of the simulation of a pull-out test. In addition, a *fictitious crack model* (Hillerborg, Modeer et al. 1976) predefining the crack pattern is used. During the remeshing process associated to the change in the crack path, interface elements within the same are inserted to model the slipping steel-concrete.

Reinhardt and others (1984) model a concrete layer around the corrugated surface of the reinforcement bar, using a plasticity model with tension softening and the failure criterion of Mohr-Coulomb. Outside this layer, behavior elastic of the concrete is considered.

In the works of Cox and Hermann (Cox & Hermann 1998; Cox & Herrmann 1999), a non-associated plasticity model which describes the adherence between the corrugated bars and the adjacent concrete have been developed and validated. In this model a characteristic length associate to the form of the ribs is defined which helps to quantify the interaction steel-concrete. The calibrated model satisfactorily reproduces the experimental results (Eligehausen, Popov et al. 1983).

1.4.4. Numerical modeling of the reinforced concrete material

The reinforced concrete structures can be simulated in the meso-scale (bar-scale) treating separately each material or in the macro-scale (member-scale) considering a constitutive model of the composite material. In the following sections, some formulations developed in the last years are summarized.

1.4.4.1. Modeling in the meso-scale (bar-scale)

The meso-scale analysis can accurately describe the topology of the problem since each reinforcement bars and its interface with the concrete is meshed in an independent form. This type of analysis usually has high computational cost, mainly in problems with materials reinforced by many fiber packages oriented in several directions.

A classic way but still current to approach the problem consists in meshing the concrete with two-dimensional or three-dimensional finite elements, meshing the steel with lattice elements and meshing the interface with special elements which keep the displacements compatibility in the common nodes between the elements of concrete and steel. Some approaches utilize a smeared crack model in order to represent the fracture process (Kwak & Filippou 1997; Chen & Baker 2003; Chong, Gilbert et al. 2004), while others use discrete cohesive crack models (Yu & Ruiz 2004; Yu & Ruiz 2005).

In the matrix analysis of framed structures, some models consider an element finite type beam, composes by a steel and concrete filament group arranged to long of the element (Buckle & Jackson 1981; Lin 1997; Marí 2000). This allows accurately defining the geometry and the location of the reinforcement in the cross section of the element. The stiffness by bending around the reference axis is obtained from the sum of the axial contribution of each filament of steel and concrete.

1.4.4.2. Modeling in the macro-scale (member-scale)

In the macro-scale, finite elements can be used whose constitutive model altogether describes the behavior of the composite material formed by concrete and a specific steel ratio, considering also the possible slipping between both materials.

The works of Vecchio and others (Vecchio 2000; Vecchio 2001; Vecchio, Lai et al. 2001) show the implementation in the finite elements method of the constitutive model described in (Vecchio & Collins 1986), providing a suitable treatment of the shear stress in the crack surface and allowing the reorientation of the strain and the maximum principal stress.

Another formulation (Belletti, Cerioni et al. 2001; Belletti, Bernardi et al. 2003) considers an isotropic linear elastic behavior of the reinforced concrete before the cracking and a behavior orthotropic non-linear behavior after it. There the cracks have a fixed direction and they are distributed uniformly with an constant spacing which are evaluated by methods based on the transference length of interface forces (CEB-FIB 2000). The kinematics of the problem is defined by the normal and tangential relative displacement between the lips of the crack, and the concrete strain in the orthogonal direction to the crack. The equilibrium conditions include some phenomena as: the dowel action, the interlocking of aggregates and the softening of the concrete by compression.

Feenstra and de Borst (1995) consider that the total stress of the reinforced concrete is the sum of the individual contributions of the simple concrete, the reinforcement steel and the effects of interaction between both materials. The simple concrete behavior is defined by a smeared crack model controlled by the fracture energy. This model supposes that in the presence of the reinforcement, the fracture energy is distributed in a tributary area given by the average spacing among cracks according to CEB-FIB modelcode (CEB-FIB 1990).

The constitutive model presented by Pietruszczak and Xu (2003) describes the behavior of the concrete and two orthogonal fiber packages, during the homogenous and localized cracking mode. This latter mode is determined by means of an approach similar to the *embedded discontinuities model* presented by the same authors (Pietruszczak & Xu 1995), which uses a traction *vs* jump law characteristic for each component material. The formulation considers that the average stress and the average strain of the reinforced concrete is defined by integration on a representative volume, as indicated by the *mean field method* (Hill 1963). Also, the beginning and direction of the strain localization are regulated by the tensile fracture criterion and by the orthogonal direction of the maximum principal stress in the matrix, respectively.

Oller and collaborators (Car 2000; Oller 2003) present a general constitutive model of composite material, considering large strain and the slipping effects between the fibers and the matrix. A composite material type in which applies this model is the reinforced concrete. Similarly, in other works (Luccioni, Lopez et al. 2005), a model of composite material constituted by a concrete matrix and a steel long fiber package based on *mixing theory* (Truesdell & Toupin 1960) is proposed. There, the effect of adherence loss between fiber and matrix appears as an additional inelastic strain in the fiber constitutive model, determined according to the concrete – steel interface model proposed by Cox and Hermann (1998).

The models indicated in this section suitably describe the behavior of the reinforced concrete; however, they show the following limitations:

- They do not use an algorithm describing the crack paths in an independent way to the direction of the finite elements mesh.

- When the fracture process begins, they lose the context of the continuum mechanics, requiring, consequently, additional relations *ad hoc* that define the mechanical behavior between the faces of a crack.

- Unlike the material bifurcation analysis, the criteria used to establish the formation of a crack are explicitly independent of the condition of existence of the displacement jump.

- In some cases (Feenstra & de Borst 1995; Vecchio 2000; Belletti, Cerioni et al. 2001; Vecchio 2001; Vecchio, Lai et al. 2001; Belletti, Bernardi et al. 2003), a distributed cracking state is considered from inelastic regime of the concrete, in which the cracks maintain a constant spacing evaluated in an analytical form. Consequently, the formation of a macro-crack located in the composite material cannot be captured.

- One of the previous models (Pietruszczak & Winnicki 2003) completely describes the fracture process of the reinforced concrete by means of a discrete model, assuming an enriched kinematics that considers the presence of discontinuities in continuum medium. Unlike the continuous models, this model explicitly requires relationships traction *vs* jump, as much of the matrix, as of fibers. Also, the beginning and the direction of the cracks is exclusively established from the properties of the matrix, neglecting the influence of the capacity, amount and direction of the reinforcement.

1.5. The reinforced concrete described as a composite material

Many materials used in the industry and the construction, as well as, most of the materials observed in nature, consist of a group of component materials, this characteristic defines them as composite materials. This section briefly describes one of the methodologies that represents the reinforced concrete by means of a constitutive model of composite material.

1.5.1. Definition of composite material

In general, the material constituted by two or more different component in the analysis scale is called *composite material*. Each of these components has a particular material direction and mechanical properties. Likewise, a component could be a composite material in a smaller scale.

The composite materials can be classified in different ways, one of them according to the type and forms of its components, as follows (Vasiliev & Morozov 2001):

- *Filled materials*. These materials are formed by a matrix whose mechanical properties are improved with the inclusion of a percentage of particles (Figure 1.11(a)). They can be treated as a homogenous and isotropic material, whose properties are mainly governed by the matrix, in spite of the modifications given by the particles.

- *Reinforced materials*. This materials are constituted by short or long fibers uniformly distributed in the matrix and oriented in a specific or random way (Figure 1.11(b)-(c)). Generally, the stiffness and strength given by fibers are greater than the contribution of the matrix. The long fibers reach the contour of the composite material in continuous way and they are oriented in specific directions. However, the short fibers are small segments totally embedded in the matrix, distributed commonly in random way inside the composite material.

The reinforced concrete is a composite material formed by one or several embedded long steel fiber packages in a simple concrete matrix (Figure 1.11(c)), which consists of gravels and mortar.

Generally, and as in this work is made, the simple concrete can be considered a homogenous material, however, some micro-mechanical models describe their behavior by means of a *representative volume element* consisted of a mortar matrix and aggregate particles inside it (Carol, López et al. 2001).

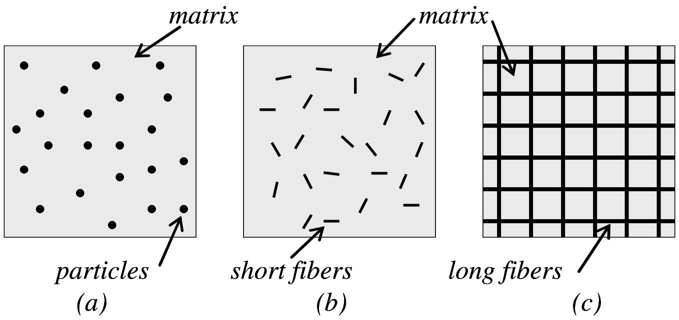

Figure 1.11. Classification of the composite materials: (a) filled material, (b) material reinforced with short fibers and (c) material with long fibers.

1.5.2. Analysis of the composite material as a problem in several scales

In many cases, the behavior of the composite material in each point is described from the mechanical response of its components, which requires two different analysis scales. A scale describes the action of all the components inside a material point and obtains as a result the fields of stress and strain of the composite material. The other scale represents the mechanical response in the domain of the solid, according to the boundary conditions and the constitutive model of the material established in the earlier scale.

In the *material point scale*, the composite material can be studied in different ways. In a *global or macroscopic* form, the volumetric participation of fibers or particles including in the matrix is considered and its geometry is neglected. In return, a *local or microscopic* form represents a typical portion of composite material called *representative volume element*, which describes its internal structure given by the geometry of the component materials (Sanchez-Palencia & Zaoui 1987). In the *material point scale*, the solution methodologies can be analytical as *mean field method* or *mixing theory*, in which case a *global* analysis way is used, or also they can be numerical procedures where a representative volume element is solved in a *local way* through the finite elements method.

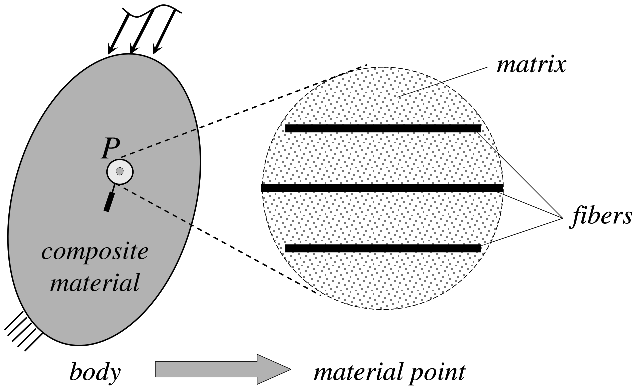

Figure 1.12. Analysis scales of the composite material.

1.5.3. Mixing theory

The behavior in a point of composite material can be represented from the constitutive models of its component materials by means of *mixing theory or rule of mixtures* (Truesdell & Toupin 1960), which is based on the following hypotheses:

- In each infinitesimal volume of composite material, all the participated component materials.
- Each component contributes to the behavior of the composite material in proportion to its volumetric participation.
- The volume occupied by each component is less than the total volume of the composite material.
- All the component materials have the same strain (compatibility equation).

In accord with the two first hypotheses, there is a homogenous distribution of all the components in each point of the composite material, which is determined by volumetric participation factor:

$$k^c = \frac{dV^c}{d\bar{V}} \tag{1.22}$$

where $d\bar{V}$ and dV^c correspond to the infinitesimal volume of the composite material and of the component *c*, respectively.

The last hypothesis establishes that the strain compatibility equation is of the form:

$$\boldsymbol{\varepsilon} = \boldsymbol{\varepsilon}^{(1)} = \boldsymbol{\varepsilon}^{(2)} = \ldots = \boldsymbol{\varepsilon}^{c} = \ldots = \boldsymbol{\varepsilon}^{cn} \tag{1.23}$$

where $\boldsymbol{\varepsilon}$ and $\boldsymbol{\varepsilon}^c$ are strains in the composite material and in the component *c*.

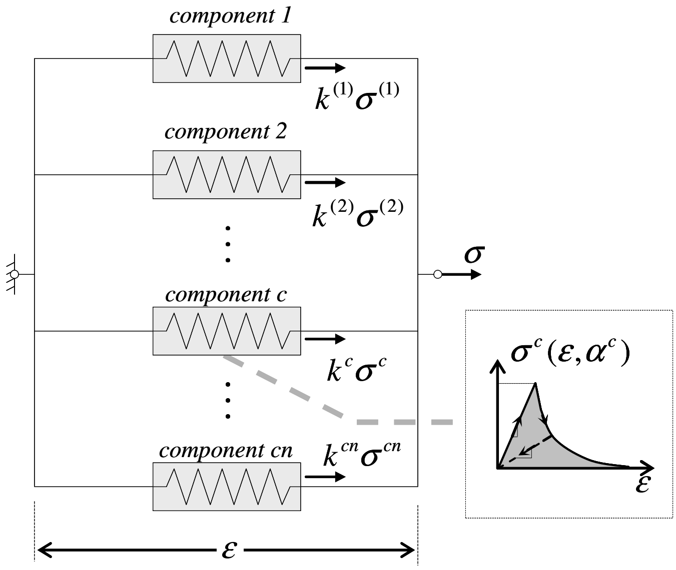

Figure 1.13. Mixing theory represented as a reologic model in parallel

This theory considers that the free energy of a composite material is given by the sum of the free energies of each of the component materials, weighted according to its volume of participation in the composite material. Applying Coleman's method to Clausius-Duhem's inequality (Lubliner 1990), as shown in some references (Oller, Oñate et al. 1996; Car 2000; Luccioni & Lopez 2002; Oller 2003) and in Appendix B, the stress tensor of the composite material is obtained of the form:

$$\boldsymbol{\sigma} = \sum_{c=1}^{cn} k^{c} \boldsymbol{\sigma}^{c}(\boldsymbol{\varepsilon},\alpha^{c}) \tag{1.24}$$

where $\boldsymbol{\sigma}^{c}(\boldsymbol{\varepsilon},\alpha^{c})$ is the stress tensor computed from the constitutive equation of the component *c*, which is expressed in terms of the common strain $\boldsymbol{\varepsilon}$ and internal variables α^{c}.

It is observed that each component can have a particular behavior law expressed in terms of its internal variables and of the composite material strain. For example, in the reinforced concrete, the simple concrete matrix can be represented with an isotropic damage model and the fibers through a plasticity model.

In the one-dimensional space, mixing theory can be represented as a reologic model of *cn* components in parallel contributing stress to the composite material according to its volumetric participation (Figure 1.13).

1.5.4. Vanishing fiber diameter model

Dvorak and collaborators (Dvorak & Bahei-el-Din 1982) have developed a constitutive model for materials reinforced with cylindrical long fibers, whose diameter is neglected, although its volume represents a finite portion of the composite material. This approach is known as *vanishing fiber diameter model.* This model establishes that the strain of both materials is common in the axial direction of the fiber and the stress of the composite material corresponds to the weighted sum of the stresses of the matrix and fibers. However, in the other tensor components, the composite material strain is equal to the weighted sum of the strain of the materials, whereas the stresses of matrix and fiber are the same. In summary, first, the fiber does not interact with the strain components of the matrix whit the exception of its axial strain and secondly, the load in the longitudinal direction of the fiber is carried between both materials.

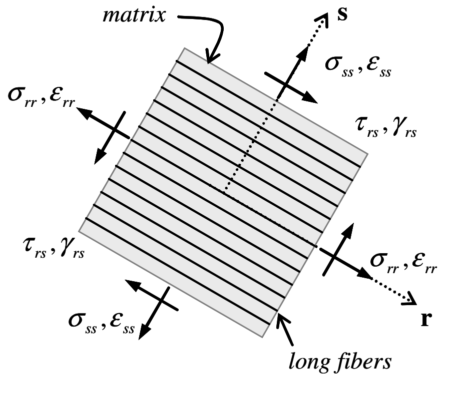

Figure 1.14. Vanishing fiber diameter model. Tensorial state in an element differential of composite material.

Consequently, in *rs*-plane (Figure 1.14), the model establishes that the conditions of equilibrium and compatibility between the matrix and a fiber package oriented in **r** correspond to:

$$\dot{\varepsilon}_{rr}=\dot{\varepsilon}_{rr}^{m}=\dot{\varepsilon}_{rr}^{f}\quad;\quad\dot{\sigma}_{rr}=k^{m}\dot{\sigma}_{rr}^{m}+k^{f}\dot{\sigma}_{rr}^{f}\tag{1.25}$$

$$\begin{cases}\dot{\varepsilon}_{ss}=k^{m}\dot{\varepsilon}_{ss}^{m}+k^{f}\dot{\varepsilon}_{ss}^{f}\\ \dot{\gamma}_{rs}=k^{m}\dot{\gamma}_{rs}^{m}+k^{f}\dot{\gamma}_{rs}^{f}\end{cases}\quad;\quad\begin{cases}\dot{\sigma}_{ss}=\dot{\sigma}_{ss}^{m}=\dot{\sigma}_{ss}^{f}\\ \dot{\tau}_{rs}=\dot{\tau}_{rs}^{m}=\dot{\tau}_{rs}^{f}\end{cases}\tag{1.26}$$

1.5.5. Mean field methods

This method allows to obtain the fields of stress and strain in the macroscopic scale, through the mean values of these fields in the microscopic scale (Hill 1967). Given a representative volume *V*, the macroscopic values of the stress and the strain are equal to:

$$\boldsymbol{\sigma} = \frac{1}{V}\int \hat{\boldsymbol{\sigma}}\, dV \quad ; \quad \boldsymbol{\varepsilon} = \frac{1}{V}\int \hat{\boldsymbol{\varepsilon}}\, dV \tag{1.27}$$

where $\hat{\boldsymbol{\sigma}}$ and $\hat{\boldsymbol{\varepsilon}}$ correspond to the microscopic value of the stress and the strain, respectively.

Considering that the matrix and the fibers maintain constant stresses and strains in the representative volume of a reinforced material, the composite material stress $\boldsymbol{\sigma}$ is equal to the weighted sum of the stresses of each component. Likewise, the mean strain $\boldsymbol{\varepsilon}$ corresponds to the weighted sum of the matrix strain and the reinforcement strain. This entails to the following conditions (Hill 1963):

$$\boldsymbol{\sigma} = k^m \boldsymbol{\sigma}^m + k^f \boldsymbol{\sigma}^f \quad ; \quad \boldsymbol{\varepsilon} = k^m \boldsymbol{\varepsilon}^m + k^f \boldsymbol{\varepsilon}^f \tag{1.28}$$

where the volumetric participation factors k^m, k^f, the stress tensors $\boldsymbol{\sigma}^m, \boldsymbol{\sigma}^f$ and strain tensors $\boldsymbol{\varepsilon}^m, \boldsymbol{\varepsilon}^f$ are associated to the matrix and reinforcement, respectively.

Equation (1.28) indicates in a general way the stress and the strain in the composite material. The conditions given in the *vanishing fiber diameter model* or in *mixing theory* can be obtained by applying some additional restrictions of equilibrium or compatibility.

1.5.6. Slipping fiber – matrix

Classical mixing theory where there is a common strain of the components is limited to composite material models whose components is perfectly adhered. A strategy that allows to maintain a common strain including the slipping between fiber and matrix, in materials reinforced with long fibers consists in modifying the constitutive model of the fiber (Car 2000; Oller 2003). The debonding of the fiber produces a difference between the matrix strain and the fibers strain that corresponds to a strain by slipping in the interface called *bond-slip strain*. In other works (Luccioni & Lopez 2002), this strain is included in the constitutive equation of fibers and it is described by means of the specific elasto-plastic model for reinforced concrete (Cox & Hermann 1998).

1.6. Objectives of this work

The main objective of this work is: to develop, to implement and validate a numerical model based on continuum strong discontinuity approach and mixing theory, which describes the fracture process of the reinforced concrete, treated as a composite material.

The specific objectives derived from the main objective are the following:

- To review the state of the art about the numerical simulation methodologies of the material failure in reinforced concrete structures.

- To develop a constitutive model of composite material according to *mixing theory* that represents the behavior of the reinforced concrete from particular constitutive laws for the concrete, the steel and the effects of interaction between both materials.

- To incorporate the composite material model the ingredients of *continuum strong discontinuity approach* which allow capturing the formation and propagation of cracks during the fracture process.

- To implement such a formulation in the context of the finite elements method for two-dimensional static problems.

- To validate the propose formulation by means of the numerical simulation and the comparison of results with some experimental tests.

1.7. Developed model

The model developed in this work describes the fracture process in reinforced concrete structures during its elastic and inelastic behavior and for distributed and localized cracking states. Some references (Oliver, Huespe et al. 2004b; Linero, Oliver et al. 2005; Oliver, Huespe et al. 2005b; Oliver, Huespe et al. 2005c; Oliver, Huespe et al. 2005d; Linero, Oliver et al. 2006), include the preliminary works that have led to this formulation.

The general features of the material failure model are the following:

- The reinforced concrete is represented as a composite material defined by *mixing theory* (Truesdell & Toupin 1960), which consists of a concrete matrix and two long steel fiber packages perpendicular to each other.

- *Mixing theory* allows that each component material and the interaction effects have their own constitutive model. The formulation considers a two-dimensional behavior of the concrete and a one-dimensional behavior of the fibers, as well as, the bond-slip effect and the dowel action (Park & Paulay 1975).

- The simple concrete is represented by an isotropic scalar damage model, whose damage criterion is determined by a strain norm and it is limited by the tensile and compressive strength (Oliver, Cervera et al. 1990).

- The axial behavior of the steel is described through a particular model of one-dimensional plasticity (Simó & Hughes 1998) for each package of parallel bars.

- The adherence loss effect is represented by a constitutive relationship between the axial stress of the fiber and a fictitious strain due to the relative displacement between concrete and steel, which, added to the fiber strain corresponds to the common strain (shared with the matrix). The properties of this model are characterized by means of some results of pull-out tests.
- The dowel action is defined by means of constitutive relationship between shear stress and shear strain, which is determined by the stiffness and the bending or shear capacity of the steel bars between the faces of a crack.
- The appearance and propagation of cracks, understood as a strain localization process of the composite material is captured by means of a embedded discontinuities model, specifically continuum strong discontinuity approach (Oliver 1996b; Oliver 1996a; Oliver 2000; Oliver, Huespe et al. 2003; Oliver & Huespe 2004a; Huespe, Oliver et al. 2006; Oliver, Huespe et al. 2006).
- The outset of the material instability and the direction of crack propagation are determined by a bifurcation analysis of the composite material.
- The *implicit-explicit integration scheme (IMPLEX)* (Oliver, Huespe et al. 2004a; Oliver, Huespe et al. 2006) is used in the constitutive models of damage and plasticity of the component materials.
- The problem is modeled in the macro-scale by means of a two-dimensional non-linear analysis considering infinitesimal strain and static loads. The non-linearity is provided by the constitutive models of the component materials.

1.8. Outline of this work

In Chapter 2, the formulation of the composite material model and its implementation in the finite elements method is described. Particularly, the constitutive models of each component and of the composite material that represents to the reinforced concrete are defined. Next, continuum strong discontinuity approach and the bifurcation analysis are applied to composite materials. At the end of this chapter, the matrices characteristical of the finite element and the calculation algorithm are defined and presented.

Chapter 3 shows the obtained response of the numerical simulation of some reinforced concrete panels subjected to tension, bending and shear, and the comparison with the respective experimental results obtained in different works.

Finally in Chapter 4, the conclusions and contributions of the work are indicated, as well as the future works derived from the same.

The Appendix A to F indicate the ingredients necessary for the development of the proposed formulation as: the basic concepts of the damage and plasticity models, continuum strong discontinuity approach, mixing theory in the composite materials, the implicit-explicit integration scheme of the constitutive model and the tracking strategy of discontinuity paths.

Chapter 2
Formulation of the model

In this chapter the essential issues of the presented formulation are described. Initially, the adopted basic considerations are indicated, as well as, the constitutive models of the composite material, of each component material and its interaction effects. Then, the kinematics of the composite material is established by means of *continuum strong discontinuity approach* (CSDA) and the phenomenon of material bifurcation is analyzed. Finally the most important ingredients of the implementation of the numerical model with the finite elements method are presented.

2.1. Basic considerations

The basic considerations established as departure point of the formulation presented here, can be summarized according to the following items:

- *Mixing theory* (Truesdell & Toupin 1960) is used in order to establish the constitutive model of the composite material and *continuum strong discontinuity approach* (Oliver 1996b; Oliver 1996a; Samaniego 2002; Oliver, Huespe et al. 2005a) is utilized to capture the discontinuity surfaces in the reinforced concrete treated as a composite material.

- Each point of continuous medium obeys to the behavior of a composite material conformed by a concrete matrix and two packages of steel long fiber, perpendiculars to each other, oriented in directions **r** and **s**, respectively (Figure 2.1). The displacement field and consequently the strain field are defined in the scale of the composite material as well.

- Although many equations indicated in the following sections are generalized for a three-dimensional space, the model was implemented for plane stress state or plane strain. Therefore, the external actions and the displacements, as well as, the matrix and the fibers are contained within the analysis plane, showing the same behavior in the thickness of the structural element.

- The formulation allows the non-linear analysis considered infinitesimal strain in quasi-static two-dimensional problems. The external actions are progressively applied in intervals denominated load steps or pseudo-time instants t.

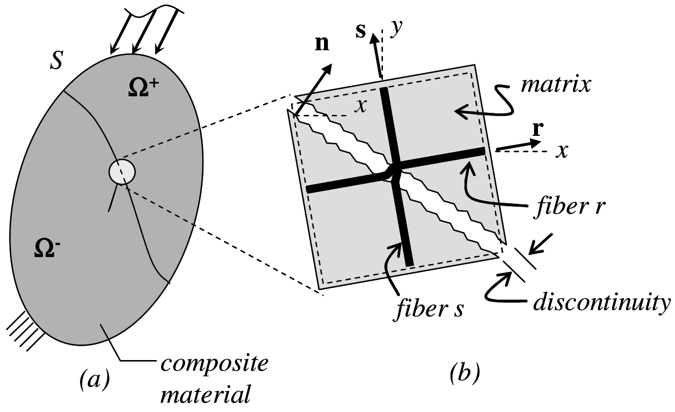

Figure 2.1. Composite material with discontinuity: (a) solid with discontinuity surface S, (b) detail of a material point of composite material.

2.2. Constitutive models of the component materials

2.2.1. Behavior of the concrete matrix

The damage models have been used to describe the behavior of the concrete and other quasi-fragile materials. The difference between the compressive and tensile strength of the concrete can be represented by means of the damage model proposed by Oliver, Cervera et al. (1990), developed from the work of Simó & Ju (1987). The presented formulation uses a damage model for two-dimensional problems, described by the following equations:

$$\psi(\boldsymbol{\varepsilon}^m, r^m) = \frac{q^m}{r^m}\left(\frac{1}{2}\boldsymbol{\varepsilon}^m : \mathbb{C}^m : \boldsymbol{\varepsilon}^m\right) \quad \text{(free energy)} \tag{2.1}$$

$$\boldsymbol{\sigma}^m = \frac{\partial \psi}{\partial \boldsymbol{\varepsilon}^m} = \frac{q^m}{r^m}\mathbb{C}^m : \boldsymbol{\varepsilon}^m = \frac{q^m}{r^m}\bar{\boldsymbol{\sigma}}^m \quad \text{(constitutive equation)} \tag{2.2}$$

$$\dot{r}^m = \lambda^m, \quad r^m \ge r^m_{t=0} = \sigma^m_u \big/ \sqrt{E^m} \quad \text{(evolution law)} \tag{2.3}$$

$$\left.\begin{aligned} \dot{q}^m = H^m(r)\,\dot{r}^m, \quad H^m = \frac{dq^m}{dr^m} \le 0 \\ 0 \le q^m \le r^m_{t=0}, \quad q^m_{t=0} = r^m_{t=0} \end{aligned}\right\} \quad \text{(Softening rule)} \tag{2.4}$$

Table 2.1. Ingredients of a isotropic scalar damage model.

Superscript m is used in the own variables of the matrix. The dot upon a variable indicates its material derivative, i.e. $\dot{\wp} = d\wp/dt$

In the matrix, the stress and strain tensors are indicated as $\boldsymbol{\sigma}^m$ and $\boldsymbol{\varepsilon}^m$. The effective stress is equal to $\bar{\boldsymbol{\sigma}}^m = \mathbb{C}^m : \boldsymbol{\varepsilon}^m$, where $\mathbb{C}^m$ is the elastic constitutive tensor of the matrix expressed in the Appendix A.1. σ^m_u is the tensile strength of the matrix, H^m is the softening parameter, λ^m is the damage multiplier, r^m and q^m are strain-like and stress-like internal variable, respectively. The damage criterion in the strain field and the loading-unloading conditions can be written as:

$$f^m(\boldsymbol{\varepsilon}^m, r^m) = \tau_{\varepsilon(tc)} - r^m \tag{2.5}$$

$$f^m \le 0, \quad \lambda^m \ge 0, \quad \lambda^m f^m = 0, \quad \lambda^m \dot{f}^m = 0 \ \ (f^m = 0) \tag{2.6}$$

where $\tau_{\varepsilon(tc)}$ is the strain norm that for the tensile-compressive damage model is equal to:

$$\tau_{\varepsilon(tc)} = \phi\sqrt{\bar{\boldsymbol{\sigma}}^m : (\mathbb{C}^m)^{-1} : \bar{\boldsymbol{\sigma}}^m} \tag{2.7}$$

and,

$$\phi = \frac{\sum_{i=1}^{3}\left\langle \bar{\sigma}^m_i \right\rangle}{\sum_{i=1}^{3}\left| \bar{\sigma}^m_i \right|}\left(1 - \frac{1}{n_\sigma}\right) + \frac{1}{n_\sigma} \tag{2.8}$$

$\bar{\sigma}_1^m, \bar{\sigma}_2^m, \bar{\sigma}_3^m$ correspond respectively to the effective stress of the matrix in principal directions 1, 2 and 3. The factor n_σ is the relation between the compressive $\sigma_{u(c)}^m$ and tensile strength σ_u^m of the matrix, i.e. $n_\sigma = \sigma_{u(c)}^m / \sigma_u^m$. The Mac-Auley's parenthesis corresponds to $\langle \wp \rangle = 0.5(\wp + |\wp|)$.

For a two-dimensional stress state where $(\bar{\sigma}_1^m < 0, \bar{\sigma}_2^m < 0)$, the elastic domain is n_σ times greater than the domain defined in the case $(\bar{\sigma}_1^m > 0, \bar{\sigma}_2^m > 0)$, as shown in Figure 2.2(a). When $\bar{\sigma}_1^m$ is positive and $\bar{\sigma}_2^m$ is negative or vice versa, an approximate transition defined by the factor ϕ of Equation (2.8) appears.

Unlike the plasticity models, in the used damage model it is not necessary that the elastic domain be convex in order to conserve uniqueness in the solution, therefore, the slope changes of the damage surface are permissible for this constitutive model (Figure 2.2(a)).

When expressing the relation between the rate of strain and stress in the matrix, a tangent constitutive equation is obtained as:

$$\dot{\boldsymbol{\sigma}}^m = \mathbb{C}_{tg}^m : \dot{\boldsymbol{\varepsilon}}^m \tag{2.9}$$

In this case the tangent constitutive tensor in elastic loading or unloading regime is equal to:

$$\mathbb{C}_{tg}^m = \frac{q^m}{r^m} \mathbb{C}^m \tag{2.10}$$

and for inelastic loading regime corresponds to:

$$\mathbb{C}_{tg}^m = \frac{q^m}{r^m} \mathbb{C}^m - \left(\frac{q^m - H^m r^m}{(r^m)^3} \right) \cdot \left[\frac{(r^m)^2}{\phi} \left(\bar{\boldsymbol{\sigma}}^m \otimes \mathbf{A} \right) + \phi^2 \left(\bar{\boldsymbol{\sigma}}^m \otimes \bar{\boldsymbol{\sigma}}^m \right) \right] \tag{2.11}$$

The second-order tensor $\mathbf{A} = \mathbb{C}^m : \partial_{\bar{\boldsymbol{\sigma}}} \phi$ is defined in Appendix A.1.

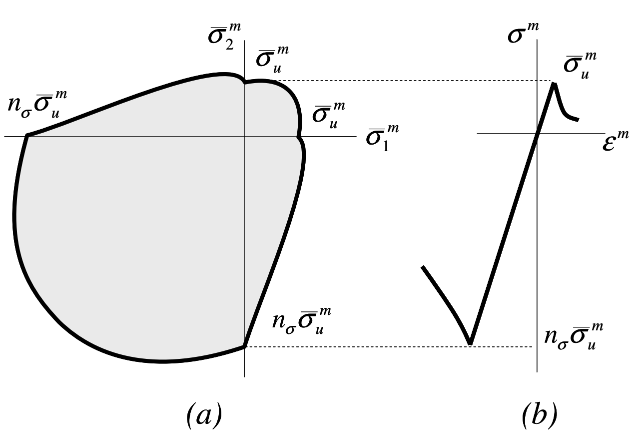

Figure 2.2. Damage model with degradation in tension and compression: (a) damage surface, (b) stress vs strain uniaxial curve.

2.2.2. Mechanical behavior of fibers or steel bars: deformable fiber model

The mechanical behavior of fibers is represented in a one-dimensional space by means of a plasticity model with isotropic linear hardening/softening (Simó & Hughes 1998), denominated *deformable fiber model.* For a package of parallel fibers to vector **r**, the ingredients of the constitutive model are indicated in Table 2.2, where, ε_{rr}^{fr} is the mechanical strain, ε_{p}^{fr} is the plastic strain, λ^{fr} is the plastic multiplier, E^{fr} is Young's modulus, σ_{rr}^{fr} is axial stress in **r** and σ_{y}^{fr} is the yielding stress. The softening is determined by the modulus $H^{fr} < 0$, the strain-like internal variable corresponds to α^{fr} and the stress-like internal variable is q^{fr}. The variables associated to the deformable fiber model in **r** direction are indicated with the superscript *fr*.

The relationship between the rates of stress and strain for the loading or unloading regime given by the tangent constitutive equation can be written as:

$$\dot{\sigma}_{rr}^{fr} = E_{tg}^{fr}\dot{\varepsilon}_{rr}^{fr} \tag{2.12}$$

where the tangent constitutive operator of the fiber is equal to:

$$E_{tg}^{fr} = \begin{cases} E^{fr} & if \quad \lambda^{fr} = 0 \\ \dfrac{E^{fr}H^{fr}}{E^{fr} + H^{fr}} & if \quad \lambda^{fr} > 0 \end{cases} \tag{2.13}$$

$\sigma_{rr}^{fr} = E^{fr}(\varepsilon_{rr}^{fr} - \varepsilon_{p}^{fr})$	(constitutive equation)	(2.14)
$\dot{\varepsilon}_{p}^{fr} = \lambda^{fr}\,\mathrm{sign}(\sigma_{rr}^{fr})$	(flow rule)	(2.15)
$\dot{\alpha}^{fr} = \lambda^{fr}$	(evolution law)	(2.16)
$f^{fr}(\sigma_{rr}^{fr}, \alpha^{fr}) = \left\|\sigma_{rr}^{fr}\right\| - (q^{fr} + \sigma_{y}^{fr})$	(plastic yield criterion)	(2.17)
$\dot{q}^{fr} = H^{fr}\dot{\alpha}^{fr}$	(softening rule)	(2.18)
$\left.\begin{array}{r} f^{fr} \le 0\,;\, \lambda^{fr} \ge 0\,;\, \lambda^{fr} f^{fr} = 0 \\ \lambda^{fr}\dot{f}^{fr} = 0\;(f^{fr} = 0) \end{array}\right\}$	(loading-unloading and persistency conditions)	(2.19)

Table 2.2. Ingredients of a one-dimensional plasticity model describing the mechanical behavior of a deformable fiber.

Figure 2.3(a) shows the one-dimensional relationship between stress and strain for a plasticity model describing the tensile/compressive behavior of the fiber.

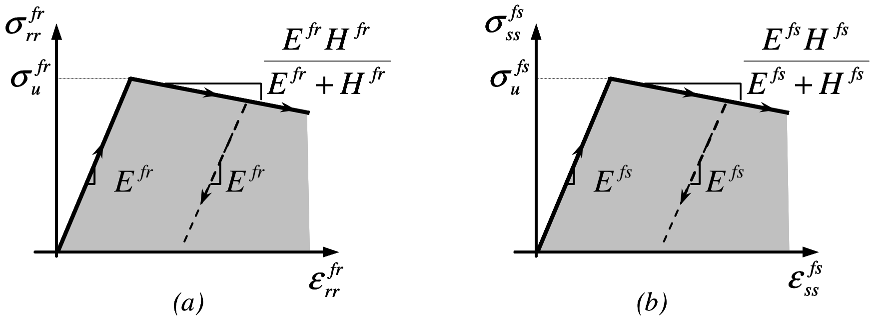

Figure 2.3. One-dimensional plasticity model: (a) fiber in **r** direction, (b) fiber in **s** direction.

The mechanical behavior of a fiber package oriented in **s** direction (Figure 2.3(b)), can be described in the same way than the fibers in **r** as indicated in Equations (2.12) and (2.13). Particularly, the constitutive equation of the mechanical behavior of the fibers in **s** is:

$$\dot{\sigma}_{ss}^{fs} = E_{tg}^{fs} \cdot \dot{\varepsilon}_{ss}^{fs} \quad , \quad E_{tg}^{fs} = \begin{cases} E^{fs} & if \quad \lambda^{fs} = 0 \\ \dfrac{E^{fs} H^{fs}}{E^{fs} + H^{fs}} & if \quad \lambda^{fs} > 0 \end{cases} \tag{2.20}$$

where $\dot{\sigma}_{ss}^{fs}$ is the stress rate, $\dot{\varepsilon}_{ss}^{fs}$ is the strain rate, H^{fs} is the softening modulus and λ^{fs} is the plastic multiplier. The elastic and tangent constitutive operator correspond to E^{fs} and E_{tg}^{fs}, respectively.

2.2.3. Bond-slip effect

The adherence loss between the steel bars and the surrounding concrete produces a slipping effect in the contact zone between both materials. This phenomenon will be represented by means of the *bond-slip model.*

2.2.3.1. Bond-slip model

This model presents a *bond-slip strain* ε_{rr}^{ir} due to the relative displacement between the steel fibers in **r** direction and the concrete matrix, which is equal to the subtraction between the strains of both materials.

In an infinitesimal element *dx* of composite material subjected to an axial stress σ, the concrete matrix slides *ds* with respect to the steel fibers as indicated in Figure 2.4(a). The compatibility equation that associates the matrix strain ε_{rr}^{m} and fiber strain ε_{rr}^{fr} including the slipping effects can be expressed of the form:

$$\varepsilon_{rr}^{fr} dx - \varepsilon_{rr}^{m} dx = -ds \tag{2.21}$$

Therefore, the variation of the slipping *ds* with respect to *x* is defined as the *bond-slip strain* in the interface:

$$\varepsilon_{rr}^{ir} = \frac{ds}{dx} = \varepsilon_{rr}^{m} - \varepsilon_{rr}^{fr} \tag{2.22}$$

Remark 2.1 *When there is perfect adherence in the interface, the strain* ε_{rr}^{ir} *disappears maintaining the matrix strain equal to the fiber strain.*

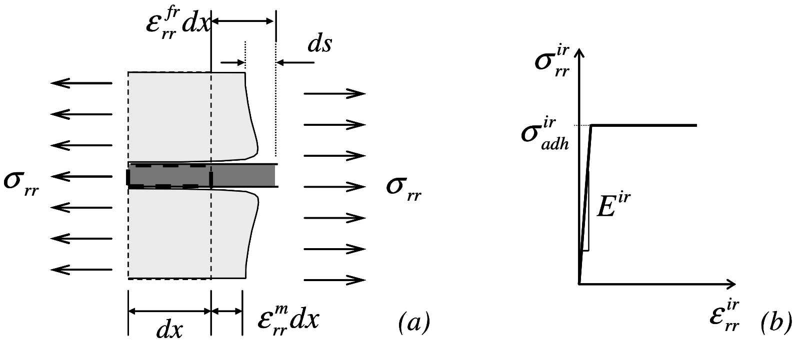

Figure 2.4. Bond-slip effect: (a) slipping in an infinitesimal reinforced concrete element, (b) stress in the interface vs bond-slip strain curve.

A one-dimensional perfect elasto-plastic model is used to describe the slipping between the concrete matrix and the steel fibers in **r** direction. Figure 2.4(b) shows the relationship between the stress in the interface σ_{rr}^{ir} and the bond-slip strain ε_{rr}^{ir}. The slope of the elastic branch is determined by the modulus E^{ir} and the maximum stress is defined as *stress of total loss of adherence* $\sigma_{adh}^{ir} \le \sigma_{y}^{fr}$. The basic ingredients of this model are the following:

$\sigma_{rr}^{ir} = E^{ir}(\varepsilon_{rr}^{ir} - \varepsilon_{p}^{ir})$	(constitutive equation)	(2.23)
$\dot{\varepsilon}_{p}^{ir} = \lambda^{ir}\,\mathrm{sign}(\sigma_{rr}^{ir})$	(flow rule)	(2.24)
$f^{ir}(\sigma_{rr}^{ir}) = \lvert\sigma_{rr}^{ir}\rvert - \sigma_{adh}^{ir}$	(plastic yield criterion)	(2.25)
$\left.\begin{array}{r} f^{ir} \le 0\,;\ \lambda^{ir} \ge 0\,;\ \lambda^{ir} f^{ir} = 0 \\ \lambda^{ir} \dot{f}^{ir} = 0\ (f^{ir} = 0) \end{array}\right\}$	(loading-unloading and persistency conditions)	(2.26)

Table 2.3. Ingredients of a one-dimensional plasticity model describing the bond-slip effect.

In the earlier equations, ε_{p}^{ir} is plastic strain and λ^{ir} is plastic multiplier in the bond-slip model. The tangent constitutive equation can be written as:

$$\dot{\sigma}_{rr}^{ir} = E_{tg}^{ir} \cdot \dot{\varepsilon}_{rr}^{ir} \quad \textit{where,}$$
$$E_{tg}^{ir} = \begin{cases} E^{ir} & \lambda^{ir} = 0 \\ 0 & \lambda^{ir} > 0 \end{cases} \tag{2.27}$$

In this case E_{tg}^{ir} is the tangent constitutive operator, $\dot{\sigma}_{rr}^{ir}$ is the stress rate in the interface and $\dot{\varepsilon}_{rr}^{ir}$ is the bond-slip strain rate in **r** direction.

> ***Remark 2.2*** *Since the values of the elastic modulus E^{ir} are usually quite great compared to Young's modulus of the fiber, this bond-slip model can be simplified considering that $E^{ir} \to \infty$, in which case, it is reduced to a rigid-plastic model characterized by the stress of total loss of adherence σ_{adh}^{ir}.*

The adherence loss between the concrete and steel fibers in **s** can be described in analogous form to the bond-slip model of the fiber in **r** shown in Equations (2.21) to (2.27). Particularly, the tangent constitutive equation of the bond-slip model in **s** corresponds to:

$$\dot{\sigma}_{ss}^{is} = E_{tg}^{is} \cdot \dot{\varepsilon}_{ss}^{is} \quad \textit{where,}$$
$$E_{tg}^{is} = \begin{cases} E^{is} & \lambda^{is} = 0 \\ 0 & \lambda^{is} > 0 \end{cases} \tag{2.28}$$

where E_{tg}^{is} is the tangent constitutive operator, whereas $\dot{\sigma}_{ss}^{is}$ and $\dot{\varepsilon}_{ss}^{is}$ corresponds to the stress rate in the interface and bond-slip strain rate, respectively.

2.2.3.2. Characterization of the bond-slip model

In the reinforced concrete the pull-out tests can provide the parameters of the bond-slip model. In some of these experiments, a bar of diameter *d* and area of cross-section $A^f = \pi d^2/4$ is embedded in the concrete at length L^i (Figure 2.5(a)).

Figure 2.5(b) shows the relationship between the force applied in the free end of the bar P^i and the produced slipping δ^i in a pull-out test. This curve can be used to characterize the relationship between the fiber stress and the bond-slip strain $(\sigma_{rr}^{ir} - \varepsilon_{rr}^{ir})$ (Figure 2.4(b)), considering the following suppositions:

- The stress of adherence loss is equal to $\sigma_{adh}^{ir} = P_{max}^i / A^f$, therefore it has been considered that the elastic regime of the bond-slip model corresponds to the first branch of the experimental curve for $P^i = [0, P_{max}^i]$. Whereas the perfect plasticity state in the model is obtained after reaching the load P_{max}^i in the test.

- In the elastic regime of the bond-slip model where $\sigma_{rr}^{ir} = E^{ir} \varepsilon_{rr}^{ir}$, it is regarded that $\sigma_{rr}^{i} = P^i / A^f$ and $\varepsilon_{rr}^{ir} = \delta^i / L^i$.

According to the aforementioned, the elastic modulus of the bond-slip model and the stress of adherence loss can be characterized as:

$$E^{ir} = \left(\frac{P^i}{\delta^i}\right) \cdot \left(\frac{L^i}{A^f}\right) \quad , \quad \sigma^{ir}_{adh} = \frac{P^i_{max}}{A^f} \tag{2.29}$$

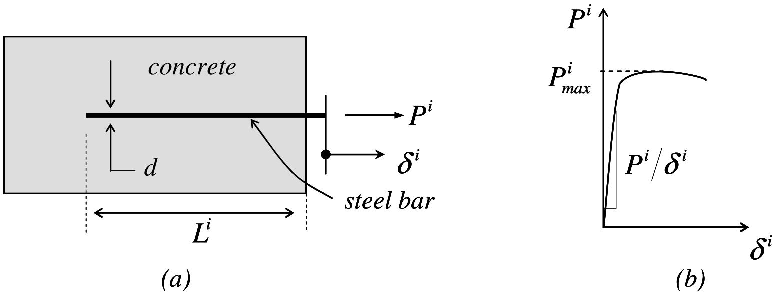

Figure 2.5. Bond-slip effect. Pull-out test: (a) descriptive sketch, (b) experimental curve of the applied load *vs* produced slipping.

2.2.4. Slipping fiber model

The *slipping fiber model* groups the effects of the mechanical strain of the fiber and their slipping with respect to the matrix using the *deformable fiber model* shown in Section 2.2.2 and *bond-slip model* presented in Section 2.2.3.

According to Equation (2.22) for parallel fibers to **r**, the matrix strain corresponds to $\varepsilon^m_{rr} = \varepsilon^{fr}_{rr} + \varepsilon^{ir}_{rr}$. Considering that the strain of the slipping fiber model is equal to the matrix strain, i.e. $\varepsilon^{dr}_{rr} = \varepsilon^m_{rr}$, then:

$$\varepsilon^{dr}_{rr} = \varepsilon^{fr}_{rr} + \varepsilon^{ir}_{rr} \tag{2.30}$$

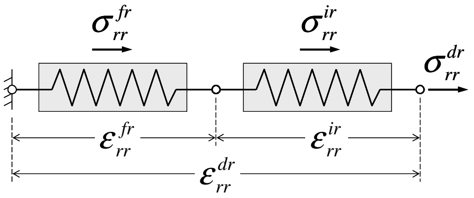

Figure 2.6. Slipping fiber model defined as a serial system consists of the capacity of the deformable fiber *fr* and the slipping action in the interface *ir*.

The action of the deformable fiber and the effects of adherence loss make up a serial system of fiber and interface (Figure 2.6), whose strain is the sum of the mechanical strain of the fiber ε^{fr}_{rr} (described in the Section 2.2.2), plus the bond-slip strain of the interface ε^{ir}_{rr} (described in the Section 2.2.3). The stress of this serial system σ_{rr}^{dr} is equal to the fiber stress σ_{rr}^{fr} and the interface stress σ_{rr}^{ir}, as indicated in the following equation:

$$\sigma_{rr}^{dr} = \sigma_{rr}^{fr} = \sigma_{rr}^{ir} \tag{2.31}$$

The *slipping fiber model* is defined by Equations (2.30) and (2.31), which indicate the strain and stress of the fiber including the slipping effects in the interface. This serial system is described in an incremental form as:

$$\dot{\varepsilon}_{rr}^{dr} = \dot{\varepsilon}_{rr}^{fr} + \dot{\varepsilon}_{rr}^{ir} \tag{2.32}$$

$$\dot{\sigma}_{rr}^{dr} = \dot{\sigma}_{rr}^{fr} = \dot{\sigma}_{rr}^{ir} \tag{2.33}$$

The strain rates $\dot{\varepsilon}_{rr}^{fr} = \dot{\sigma}_{rr}^{fr} / E_{tg}^{fr}$ and $\dot{\varepsilon}_{rr}^{ir} = \dot{\sigma}_{rr}^{ir} / E_{tg}^{ir}$ due to Equations (2.12) and (2.27) are replaced in Equation (2.32). Using Equation (2.33) and finding the stress rate, the constitutive equation of the sliding fiber model in **r** is obtained as:

$$\dot{\sigma}_{rr}^{dr} = E_{tg}^{dr} \cdot \dot{\varepsilon}_{rr}^{dr} \quad where, \quad E_{tg}^{dr} = \frac{1}{1/E_{tg}^{fr} + 1/E_{tg}^{ir}} = \frac{E_{tg}^{fr} E_{tg}^{ir}}{E_{tg}^{fr} + E_{tg}^{ir}} \tag{2.34}$$

In this case E_{tg}^{dr} is the tangent constitutive operator, whereas $\dot{\sigma}_{rr}^{dr}$ and $\dot{\varepsilon}_{rr}^{dr}$ are the stress and strain rates of the slipping fiber in **r**. As in Equation (2.27), E_{tg}^{ir} is defined by the bond-slip model and E_{tg}^{fr} is defined by the deformable fiber model in the Equation (2.13).

Remark 2.3 *<u>perfect adherence condition</u>. If the bond-slip modulus E_{tg}^{ir} tends to infinite ($E_{tg}^{ir} \to \infty \Rightarrow E_{tg}^{dr} = E_{tg}^{fr}$) and the adherence loss stress σ_{adh}^{fr} is equal to the yielding stress σ_{y}^{fr}, then slipping fiber model preserves a deformable fiber behavior, and consequently, the perfect adherence condition is obtained (Figure 2.7(a)).*

Remark 2.4 *<u>Rigid-plastic bond-slip model</u>. When a rigid-plastic model describes the bond-slip effect, that is, when $E_{tg}^{ir} \to \infty$ and $\sigma_{adh}^{fr} < \sigma_{y}^{fr}$, the stress vs strain curve of the slipping fiber model shows two branches: an elastic regime limited by σ_{adh}^{fr} and a perfect plasticity regime (Figure 2.7(b)).*

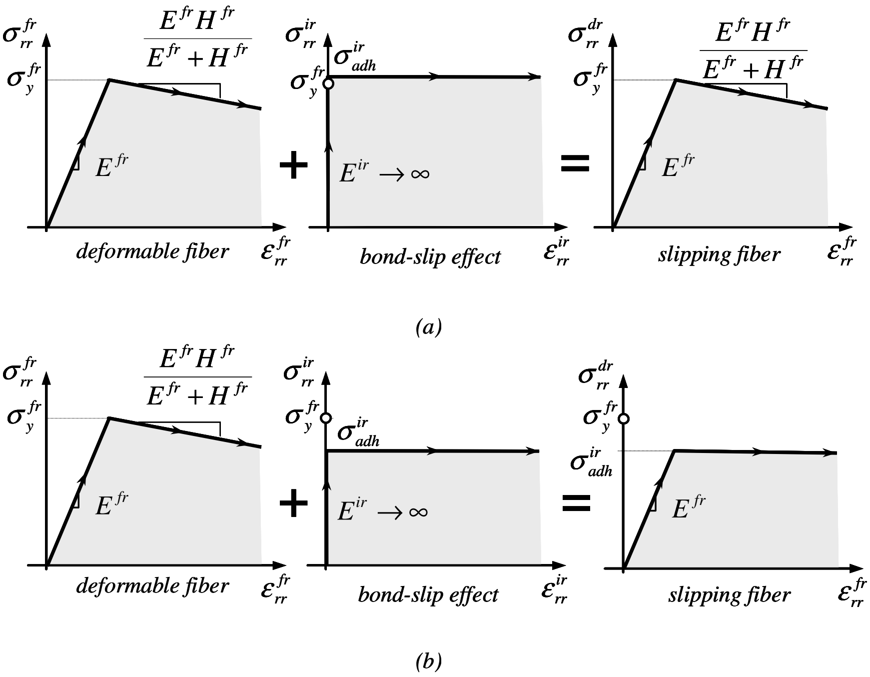

Figure 2.7. Stress vs strain curve that results of the slipping fiber model, for two special cases: (a) perfect adherence condition ($E_{tg}^{ir} \to \infty$; $\sigma_{adh}^{ir} = \sigma_{y}^{fr}$), (b) rigid-plastic bond-slip model ($E_{tg}^{ir} \to \infty$; $\sigma_{adh}^{ir} < \sigma_{y}^{fr}$).

Likewise, for the package of fibers parallel to **s**, Equations (2.32) and (2.33) can be rewritten:

$$\dot{\varepsilon}_{ss}^{ds} = \dot{\varepsilon}_{ss}^{fs} + \dot{\varepsilon}_{ss}^{is} \quad , \quad \dot{\sigma}_{ss}^{ds} = \dot{\sigma}_{ss}^{fs} = \dot{\sigma}_{ss}^{is} \tag{2.35}$$

where $\dot{\sigma}_{ss}^{ds}$ is the stress rate, $\dot{\varepsilon}_{ss}^{ds}$ is the strain rate of the slipping fiber in **s** and E_{tg}^{ds} is the tangent constitutive operator. The constitutive equation of the slipping fiber model in **s** corresponds to:

$$\dot{\sigma}_{ss}^{ds} = \dot{\sigma}_{ss}^{fs} = E_{tg}^{ds} \cdot \dot{\varepsilon}_{ss}^{ds} \quad , \quad E_{tg}^{ds} = \frac{E_{tg}^{fs} E_{tg}^{is}}{E_{tg}^{fs} + E_{tg}^{is}} \tag{2.36}$$

2.2.5. Dowel action

The structural elements as the bars have a dimension far greater than the other two, behaving mainly to normal tension or compression to its longitudinal axis. However, the crack opening in the concrete also depends on the stiffness to bending and shear of the steel bars, as described next.

In a reinforced concrete member where the cracks open in mode II of fracture, the shear force is carried by the internal interlocking of the aggregate particles of concrete and the shear capacity of the steel bars in the faces of a crack. The latter effect called *dowel action* is produced by some of the mentioned earlier mechanisms in Sections 2.2.5.1 and 2.2.5.2 (Park & Paulay 1975). Also, this phenomenon is represented by means of the constitutive model described in Section 2.2.5.3.

2.2.5.1. Mechanisms that produce the dowel action: bending of the bars between the faces of a crack

The bending behavior of the bars between the faces of a crack is due to a displacement relative δ^{τ} perpendicular to its axis, when the free span between the faces of a crack l^{τ} is far greater than his diameter *d* (Figure 2.8(a)). In this case, it is assumed that the parallel displacement to the crack plane is carried to a beam fixed at both ends with a span equal to the crack opening.

According to Timoshenko's theory for beams (Timoshenko & Young 1965), in the elastic regime the displacement δ^{τ} generates a shear force in the bar equal to:

$$V = \frac{12E^f I^f}{(l^{\tau})^3}\delta^{\tau} \tag{2.37}$$

where the area and the moment of inertia of a circular cross section of diameter *d* are equal to $A^f = \pi d^2/4$ and $I^f = \pi d^4/64$, respectively. E^f and σ_y^f corresponds to Young's modulus and the steel yielding stress.

The elastic behavior of the beam takes place whenever the maximum bending moment $M = Vl/2$ be least than the plastic moment $M_y = \left(d^3/6\right)\sigma_y^f$. Therefore, the shear force in the elastic limit is equal to:

$$V_y = \frac{4}{3\pi}\cdot\frac{d}{l^{\tau}}\cdot A^f\sigma_y^f \tag{2.38}$$

The shear forces V and V_y can also be written in terms of a *equivalent shear modulus* $G^{f\tau}$ and a *equivalent yielding shear stress* τ_y^f, as follows:

$$V = \frac{G^{f\tau}A^f}{l^{\tau}}\delta^{\tau} \quad , \quad V_y = A^f\tau_y^f \tag{2.39}$$

Replacing Equations (2.37) and (2.38) in Equation (2.39), then:

$$G^{f\tau} = E^f\cdot\frac{3d^2}{4(l^{\tau})^2} \quad , \quad \tau_y^f = \frac{4}{3\pi}\cdot\frac{d}{l^{\tau}}\sigma_y^f \tag{2.40}$$

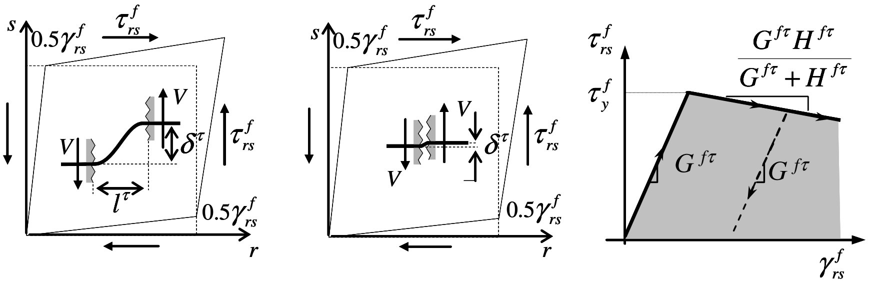

(a) (b) (c)

Figure 2.8. Dowel action: (a) bar subjected to bending between the faces of a crack, (b) direct shear in a bar crossing a crack, (c) relationship shear tension vs shear strain in the constitutive model.

2.2.5.2. Mechanisms that produce the dowel action: direct shear in bars crossing a crack

The direct shear in bars crossing a crack appears when the component in **r** direction of the crack opening is very small compared with its perpendicular component, in other words, when mode II of fracture dominates with respect to mode I (Figure 2.8(b)). In this case the shear force transmitted by the reinforcement is equal to:

$$V = \frac{G^{f\tau} A^f}{l^\tau} \delta^\tau \quad ; \quad G^{f\tau} = \frac{E^f}{2(1+\nu^f)} \tag{2.41}$$

In this mechanism, $G^{f\tau}$ corresponds to the elastic shear module and ν^f is the Poisson's ratio of the steel. Applying von Mises's yield criterion for a pure shear state, a shear force is obtained as:

$$V_y = \frac{\sigma_y^f}{\sqrt{3}} A^f \tag{2.42}$$

Replacing Equation (2.39) into the earlier equation, the *equivalent yielding shear stress* will be equal to:

$$\tau_y^f = \frac{\sigma_y^f}{\sqrt{3}} \tag{2.43}$$

2.2.5.3. Constitutive model of dowel action

Based on the earlier considerations, the dowel effect is represented by means of a equivalent one-dimensional elasto-plastic model, similar to the model mentioned in Section 2.2.2. This model relates the shear strain γ_{rs}^f with the shear stress of the fiber τ_{rs}^f in the *rs*-plane (Figure 2.8(c)), through of the following ingredients:

$\tau_{rs}^f = G^{f\tau}(\gamma_{rs}^f - \gamma_p^f)$	(constitutive equation)	(2.44)
$\dot{\gamma}_p^f = \lambda^{f\tau}\mathrm{sign}(\tau_{rs}^f)$	(flow rule)	(2.45)
$\dot{\alpha}^{f\tau} = \lambda^{f\tau}$	(evolution law)	(2.46)
$f^{f\tau}(\tau_{rs}^f,\alpha^{f\tau}) = \lvert\tau_{rs}^f\rvert - (\tau_y^f + q^{f\tau})$	(plastic yield criterion)	(2.47)
$\dot{q}^{f\tau} = H^{f\tau}\dot{\alpha}^{f\tau}$	(softening rule)	(2.48)
$f^{f\tau} \le 0,\quad \lambda^{f\tau} \ge 0,\quad \lambda^{f\tau} f^{f\tau} = 0,$ $\lambda^{f\tau}\dot{f}^{f\tau} = 0\ (f^{f\tau} = 0)$	(loading-unloading and persistency conditions)	(2.49)

Table 2.4. Ingredients of a one-dimensional plasticity model describing the dowel action.

In earlier equations, γ_p^f is the plastic shear strain, $G^{f\tau}$ is the equivalent shear modulus, τ_y^f is the equivalent yielding shear stress, $H^{f\tau}$ is the softening modulus, $\alpha^{f\tau}$ and $q^{f\tau}$ is the strain-like and stress-like internal variable. The tangent constitutive equation will be of the form:

$$\dot{\tau}_{rs}^f = G_{tg}^{f\tau}\dot{\gamma}_{rs}^f \tag{2.50}$$

where the tangent constitutive operator is equal to:

$$G_{tg}^{f\tau} = \begin{cases} G^{f\tau} & \lambda^{f\tau} = 0 \\ \dfrac{G^{f\tau}H^{f\tau}}{G^{f\tau} + H^{f\tau}} & \lambda^{f\tau} > 0 \end{cases} \tag{2.51}$$

The modulus $G^{f\tau}$ is calculated with Equation (2.40) or (2.41) depending on the dominant mechanism in the dowel action (Sections 2.2.5.1 and 2.2.5.2). Likewise, the stress τ_y^f is defined with Equation (2.40) or (2.43) according to case.

Remark 2.5 *It can be generally considered that the steel shear stress in the inelastic regime of the model remains constant, that is, the softening modulus* $H^{f\tau}$ *is equal to zero.*

Remark 2.6 *As Sections 2.2.4 and 2.2.5 describe it, the behavior of each package of reinforcement bars is defined by means of two uncouple constitutive models: one associated to the shear behavior* $\tau_{rs}^f(\gamma_{rs}^f)$ *and the other related to the axial behavior* $\sigma_{rr}^{fr}(\varepsilon_{rr}^{fr} + \varepsilon_{rr}^{ir})$ *. This latter called slipping fiber model is the result of a serial system that includes the mechanical capacity of a deformable fiber and the bond-slip effects in the interface fiber-matrix.*

2.3. Constitutive model of the composite material

According to the mentioned earlier, the reinforced concrete is treated as a composite material formed by a concrete matrix and two perpendicular long steel fiber packages. The behavior of the concrete is defined by a damage model with degradation in tension and compression, in return, the axial mechanical strain of the fiber is described through a one-dimensional elasto-plastic model.

In addition, two interaction effects between both materials have been considered: the *adherence loss* and the *dowel action*. The former is represented by the relationship between the fiber axial stress and a fictitious strain produced by the relative displacement between both materials which added to the fiber mechanical strain is equal to the strain of the *slipping fiber model*. In return, the latter is described by the constitutive relationship between shear stress and shear strain, determined by the stiffness and capacity to bending or shear of the steel bars between the faces of a crack.

The constitutive model of the composite material requires a link between its strain and the strain of the component materials, as well as, it needs a link between its stress and the stresses of the matrix and the fibers (Hill 1963). From *mixing theory or rule of mixtures* (Truesdell & Toupin 1960) on described in Section 1.5.3 and Appendix B, the necessary relationships between the composite material and the component materials are established.

The hypotheses considered in the model are:

- The matrix strain rate $\dot{\boldsymbol{\varepsilon}}^m$ is equal to common strain rate $\dot{\boldsymbol{\varepsilon}}$ defined on a two- or three-dimensional space.

- The strain rate of the fiber in **r** direction including the bond-slip effect (*slipping fiber model*), corresponds to the tensorial component *rr* of strain rate of the composite material $\dot{\varepsilon}_{rr}$.

- The strain rate of the fiber in **s** direction including the bond-slip effect (*slipping fiber model*), corresponds to the tensorial component *ss* of strain rate of the composite material $\dot{\varepsilon}_{ss}$.

- The shear capacity of the fibers is associated to the shear strain rate in *rs-plane* indicated as $\dot{\gamma}_{rs}$.

According to the mentioned earlier, the compatibility conditions of strains presented as the relationship between the strain rate of each component material and the composite material are:

$\dot{\boldsymbol{\varepsilon}}^m = \dot{\boldsymbol{\varepsilon}}$	(matrix strain)	(2.52)
$\dot{\varepsilon}^{dr}_{rr} = \dot{\varepsilon}_{rr} = \mathbf{r}\cdot\dot{\boldsymbol{\varepsilon}}\cdot\mathbf{r}$	(normal strain of the slipping fiber in **r**)	(2.53)
$\dot{\varepsilon}^{ds}_{ss} = \dot{\varepsilon}_{ss} = \mathbf{s}\cdot\dot{\boldsymbol{\varepsilon}}\cdot\mathbf{s}$	(normal strain of the slipping fiber in **s**)	(2.54)
$\dot{\gamma}^f_{rs} = \dot{\gamma}_{rs} = 2\,\mathbf{r}\cdot\dot{\boldsymbol{\varepsilon}}\cdot\mathbf{s}$	(shear strain of the fiber in *rs*-plane)	(2.55)

Table 2.5. Strain rate of each component in terms of the composite material strain rate.

Such as *mixing theory* indicates, the stress rate of the composite material is considered equal to the sum of the stress rates of matrix and fibers multiplied by its respective volumetric participation factor, which can be written as:

$$\dot{\boldsymbol{\sigma}} = k^m\dot{\boldsymbol{\sigma}}^m + k^{fr}(\mathbf{r}\otimes\mathbf{r})\dot{\sigma}^{fr}_{rr} + k^{fs}(\mathbf{s}\otimes\mathbf{s})\dot{\sigma}^{fs}_{ss} + 2(k^{fr}+k^{fs})(\mathbf{r}\otimes\mathbf{s})^S\,\dot{\tau}^f_{rs} \tag{2.56}$$

where the factors k^m, k^{fr}, k^{fs} correspond to the volume ratio of each component material, i.e.,

$$k^m = \frac{V^m}{\overline{V}} \quad , \quad k^{fr} = \frac{V^{fr}}{\overline{V}} \quad , \quad k^{fs} = \frac{V^{fs}}{\overline{V}} \quad , \quad k^m + k^{fr} + k^{fs} = 1 \tag{2.57}$$

In this case $\overline{V}$ is the total volume of composite material, V^m is the volume of matrix, V^{fr} and V^{fs} are the volumes of the fibers oriented in the directions **r** and **s** respectively.

In the model an axial behavior of the fibers is considered, neglecting its contributions to the stress of the composite material in the perpendicular direction of its longitudinal axis, that is, the normal stress in **s** direction of the fibers parallel to **r** $(\sigma^{fr}_{ss} = 0)$ and the normal stress in **r** of the fibers parallel to vector **s** $(\sigma^{fs}_{rr} = 0)$ are equal to zero.

Figure 2.9 indicates the stresses of each component material in its local coordinate system.

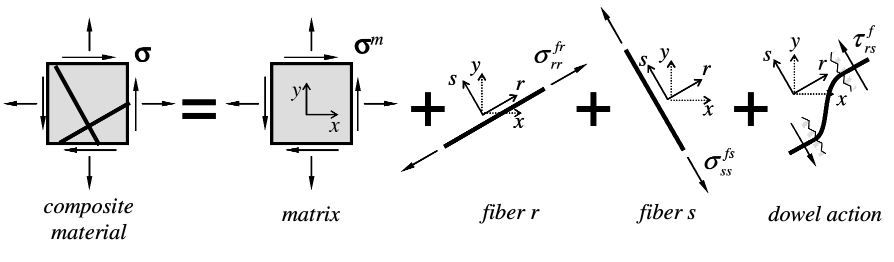

Figure 2.9. Constitutive model of the composite material. Stresses in the component materials.

Remark 2.7 *In rs-coordinate system, the tensor of stress rate of the composite material will have the following components:*

$$\begin{aligned}
\dot{\sigma}_{rr} &= k^{m}\dot{\sigma}^{m}_{rr} + k^{fr}\dot{\sigma}^{fr}_{rr}\\
\dot{\sigma}_{ss} &= k^{m}\dot{\sigma}^{m}_{ss} + k^{fs}\dot{\sigma}^{fs}_{ss}\\
\dot{\tau}_{rs} &= k^{m}\dot{\tau}^{m}_{rs} + (k^{fr} + k^{fs})\dot{\tau}^{f}_{rs}
\end{aligned} \tag{2.58}$$

Likewise, the components of the strain rate indicated in Equations (2.52) to (2.55) can be rewritten of the form:

$$\begin{aligned}
\dot{\varepsilon}^{m}_{rr} &= \dot{\varepsilon}^{dr}_{rr} = \dot{\varepsilon}_{rr}\\
\dot{\varepsilon}^{m}_{ss} &= \dot{\varepsilon}^{ds}_{ss} = \dot{\varepsilon}_{ss}\\
\dot{\gamma}^{m}_{rs} &= \dot{\gamma}^{f}_{rs} = \dot{\gamma}_{rs}
\end{aligned} \tag{2.59}$$

Equations (2.58) and (2.59) describe the application of mixing theory to three systems in parallel, as shown in Figure 2.10. The first is constituted by the component rr of the matrix and the sliding fiber in **r** *direction, the second is formed by the component ss of the matrix and the sliding fiber in* **s**, *the third is defined by the shear capacity of the matrix and fibers (dowel action) in rs-plane.*

Remark 2.8 *The mean field method described in Section 1.5.5 supposes that the stress and strain rates of the composite material correspond to:*

$$\dot{\boldsymbol{\sigma}} = k^{m}\dot{\boldsymbol{\sigma}}^{m} + k^{fr}\dot{\boldsymbol{\sigma}}^{fr} + k^{fs}\dot{\boldsymbol{\sigma}}^{fs} \quad \rightarrow \quad \begin{cases} \dot{\sigma}_{rr} = k^{m}\dot{\sigma}^{m}_{rr} + k^{fr}\dot{\sigma}^{fr}_{rr} + k^{fs}\dot{\sigma}^{fs}_{rr}\\ \dot{\sigma}_{ss} = k^{m}\dot{\sigma}^{m}_{ss} + k^{fr}\dot{\sigma}^{fr}_{ss} + k^{fs}\dot{\sigma}^{fs}_{ss}\\ \dot{\tau}_{rs} = k^{m}\dot{\tau}^{m}_{rs} + (k^{fr} + k^{fs})\dot{\tau}^{f}_{rs} \end{cases} \tag{2.60}$$

$$\dot{\boldsymbol{\varepsilon}} = k^{m}\dot{\boldsymbol{\varepsilon}}^{m} + k^{fr}\dot{\boldsymbol{\varepsilon}}^{dr} + k^{fs}\dot{\boldsymbol{\varepsilon}}^{ds} \quad \rightarrow \quad \begin{cases} \dot{\varepsilon}_{rr} = k^{m}\dot{\varepsilon}^{m}_{rr} + k^{fr}\dot{\varepsilon}^{dr}_{rr} + k^{fs}\dot{\varepsilon}^{ds}_{rr}\\ \dot{\varepsilon}_{ss} = k^{m}\dot{\varepsilon}^{m}_{ss} + k^{fr}\dot{\varepsilon}^{dr}_{ss} + k^{fs}\dot{\varepsilon}^{ds}_{ss}\\ \dot{\gamma}_{rs} = k^{m}\dot{\gamma}^{m}_{rs} + (k^{fr} + k^{fs})\dot{\gamma}^{f}_{rs} \end{cases} \tag{2.61}$$

where volumetric participation factor k^{m}, k^{fr}, k^{fs}*, the stress rates* $\dot{\boldsymbol{\sigma}}^{m}, \dot{\boldsymbol{\sigma}}^{fr}, \dot{\boldsymbol{\sigma}}^{fs}$ *and strain rates* $\dot{\boldsymbol{\varepsilon}}^{m}, \dot{\boldsymbol{\varepsilon}}^{dr}, \dot{\boldsymbol{\varepsilon}}^{ds}$*, are associated to the matrix, the slipping fiber in* **r** *and the slipping fiber in* **s**, *respectively. If there is a common strain such as the mixing theory establishes it (*$\dot{\boldsymbol{\varepsilon}}^{m} = \dot{\boldsymbol{\varepsilon}}^{dr} = \dot{\boldsymbol{\varepsilon}}^{ds} = \dot{\boldsymbol{\varepsilon}}$*), and the fibers capacity in direction perpendicular to its longitudinal axis is neglected (*$\sigma^{fr}_{ss} = 0, \sigma^{fs}_{rr} = 0$*), then Equations (2.60) and (2.61) become Equations (2.58) and (2.59), plus the additional expressions* $\dot{\varepsilon}^{m}_{rr} = \dot{\varepsilon}^{ds}_{rr} = \dot{\varepsilon}_{rr}$, $\dot{\varepsilon}^{m}_{ss} = \dot{\varepsilon}^{dr}_{ss} = \dot{\varepsilon}_{ss}$ *which do not take part in the evaluation of the composite material stress.*

The stress rates obtained from the constitutive equations of each component is summarized in the following table:

$\dot{\boldsymbol{\sigma}}^m = \mathbb{C}^m_{tg} : \dot{\boldsymbol{\varepsilon}}$	(matrix stress rate)	(2.62)
$\dot{\sigma}^{fr}_{rr} = E^{dr}_{tg}\,\dot{\varepsilon}_{rr}$	(normal stress rate in the fiber **r**)	(2.63)
$\dot{\sigma}^{fs}_{ss} = E^{ds}_{tg}\,\dot{\varepsilon}_{ss}$	(normal stress rate in the fiber **s**)	(2.64)
$\dot{\tau}^{f}_{rs} = G^{f\tau}_{tg}\,\dot{\gamma}_{rs}$	(shear stress rate in the fiber)	(2.65)

Table 2.6. Tangent constitutive equation for each component.

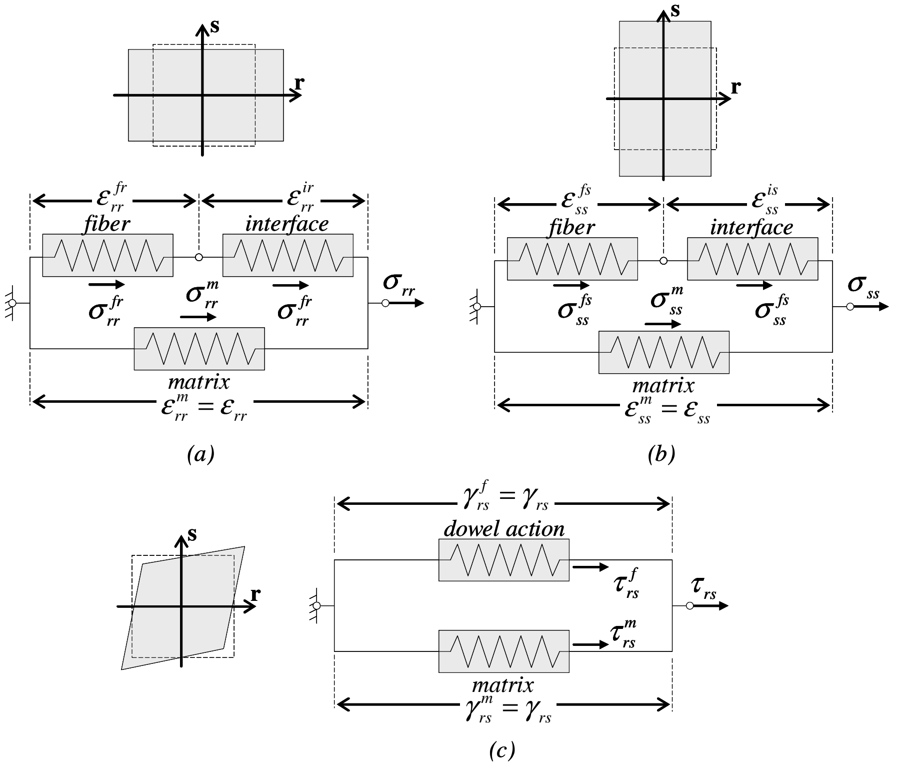

Figure 2.10. Constitutive model of the composite material. Considered reologic model for: (a) normal stress in **r**, (b) normal stress in **s**, (c) shear stress in *rs*-plane.

Given the strain compatibility among the components, the tangent constitutive equation of the composite material can be defined as:

$$\dot{\boldsymbol{\sigma}} = \mathbb{C}_{tg} : \dot{\boldsymbol{\varepsilon}} \tag{2.66}$$

The tangent constitutive tensor $\mathbb{C}_{tg}$ can be evaluated by replacing the constitutive equations of the components (2.62) to (2.65) in Equation (2.56) and replacing this result with Equation (2.66), is obtained:

$$\begin{aligned} \mathbb{C}_{tg} = {} & k^{m}\mathbb{C}_{tg}^{m} + k^{fr}(\mathbf{r}\otimes\mathbf{r})\otimes(\mathbf{r}\otimes\mathbf{r})E_{tg}^{dr} + \\ & + k^{fs}(\mathbf{s}\otimes\mathbf{s})\otimes(\mathbf{s}\otimes\mathbf{s})E_{tg}^{ds} + \\ & + \left(k^{fr} + k^{fs}\right)\left(4(\mathbf{r}\otimes\mathbf{s})^{s}\otimes(\mathbf{r}\otimes\mathbf{s})^{s}\right)G_{tg}^{f\tau} \end{aligned} \tag{2.67}$$

2.4. Application of continuum strong discontinuity approach to composite materials

In some tests of reinforced concrete members, after of the elastic regime of the concrete, a non-linear state is observed which begins with the *distributed micro-cracking* or *diffuse failure zone* and finishes with the cracks formation of significant opening (Vecchio, Lai et al. 2001). These phenomena can be represented by a reinforced concrete model treated as a composite material that captures the strain localization from the behavior of its components (matrix concrete and steel fibers).

The *continuum strong discontinuity approach (CSDA)* describes the mechanism of structural failure, showing the elastic behavior, the process of fracture and the general collapse, by means of enhanced kinematics within the *continuum mechanics* (Oliver 1996a). Appendix C summarizes the general characteristics of this formulation from the works produced by Oliver and collaborator (Oliver 1996a; Oliver 1996b; Oliver, Huespe et al. 2003; Oliver & Huespe 2004a; Oliver & Huespe 2004b). Next this methodology is applied to the composite material.

2.4.1. Strong discontinuity kinematics in the composite material

CSDA establishes a jump of the strain field on the failure surface which is able to generate unbounded values (in distributional sense) in the strain field.

> ***Hypothesis 2.1*** *The strain field is defined on the composite material as a common value for all the components, as indicated in Section 2.3. When the strains are obtained from the displacements field, it can be assumed that this is determined in the scale of the composite material. Therefore, the enhanced kinematics defined in the CSDA is applied to a composite material in the same way as it is used in a homogenous material.*

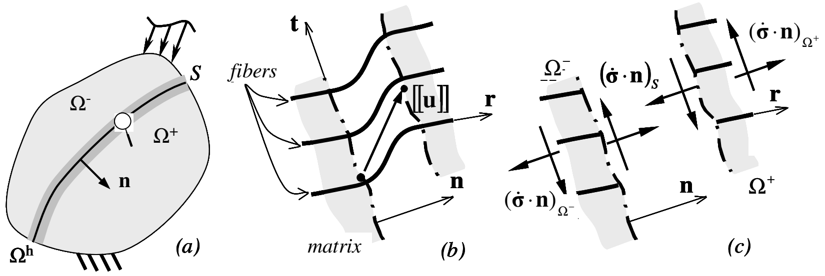

Figure 2.11. Application of CSDA to composite materials: (a) solid with discontinuity, (b) displacement jump in a material point and (c) continuity of tractions in a material point.

2.4.1.1. Strong discontinuity kinematics

Let Ω be a body of composite material exhibiting a strong discontinuity on surface S of normal $\mathbf{n}$, which splits the body into the domains Ω^+ and Ω^- as shown in Figure 2.11(a). The displacement rate (velocity) in a material point $\mathbf{x}$ and at a time t is defined as (Oliver, Huespe et al. 2003):

$$\dot{\mathbf{u}}(\mathbf{x},t)=\dot{\bar{\mathbf{u}}}(\mathbf{x},t)+\mathcal{M}_S(\mathbf{x})\cdot[\![\dot{\mathbf{u}}]\!](t) \tag{2.68}$$

where $\dot{\bar{\mathbf{u}}}$ and $[\![\dot{\mathbf{u}}]\!]$ corresponds to continuous part and jump of the velocity (Figure 2.11(b)), respectively. In the continuum, the unit jump function is defined as $\mathcal{M}_S(\mathbf{x})=\mathcal{H}_S(\mathbf{x})-\varphi(\mathbf{x})$, where $\mathcal{H}_S(\mathbf{x})$ is Heaviside's function and $\varphi(\mathbf{x})$ is an arbitrary continuous function limited by a small band Ω^h in S, as indicated in Figure 2.12.

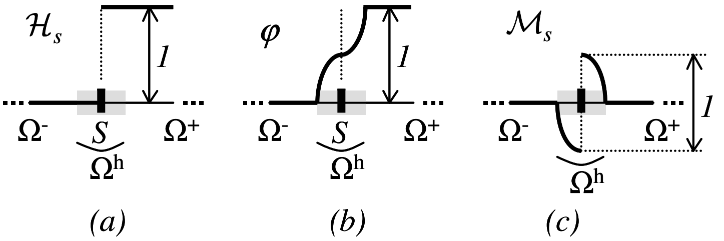

Figure 2.12. Application of CSDA to composite material: (a) Heaviside's function, (b) function φ and (c) unit jump function.

The following expression indicates the value of Heaviside's function and the continuous function $\varphi(\mathbf{x})$ outside the band Ω^h where its value is not arbitrary.

$$\mathcal{H}_S(\mathbf{x})=\begin{cases}0 & \forall\mathbf{x}\in\Omega^- \\ 1 & \forall\mathbf{x}\in\Omega^+\end{cases} \quad \text{and} \quad \varphi(\mathbf{x})=\begin{cases}0 & \forall\mathbf{x}\in\Omega^-/\Omega^h \\ 1 & \forall\mathbf{x}\in\Omega^+/\Omega^h\end{cases} \tag{2.69}$$

The strain rate field is evaluated by applying the symmetrical gradient operator on the velocity field, in such a way that the strain rate can split into a compatible part based on the velocity in the continuum and an enhanced part in terms of the jump velocity. Since the gradient (in a generalized sense), of Heaviside's function defines a singular function, the strain rate can be expressed as the sum of a bounded regular part plus a singular part (unbounded), thus:

$$\dot{\boldsymbol{\varepsilon}} = \nabla^s \dot{\mathbf{u}} = \underbrace{\overbrace{\nabla^s \dot{\bar{\mathbf{u}}}}^{compatible} \; \overbrace{-(\nabla\varphi \otimes [\![\dot{\mathbf{u}}]\!])^s}^{enhanced\ bounded}}_{regular\ \dot{\bar{\boldsymbol{\varepsilon}}}} + \underbrace{\overbrace{(\delta_s \mathbf{n} \otimes [\![\dot{\mathbf{u}}]\!])^s}^{enhanced\ unbounded}}_{sigular\ [\![\dot{\boldsymbol{\varepsilon}}]\!]} \tag{2.70}$$

where δ_S is Dirac's delta function acting on Ω. In general the jump of a field (●) is indicated as $[\![\bullet]\!] = \bullet\big|_{\Omega^+/S} - \bullet\big|_S$.

According to the earlier equation, the difference between the strain rate inside and outside of the discontinuity surface *S* is equal to:

$$[\![\dot{\boldsymbol{\varepsilon}}]\!] = \dot{\boldsymbol{\varepsilon}}_{\Omega^+/S} - \dot{\boldsymbol{\varepsilon}}_S = \delta_s (\mathbf{n} \otimes [\![\dot{\mathbf{u}}]\!])^s \tag{2.71}$$

2.4.1.2. Application to the composite material

Equations (2.72) to (2.75) indicate the regular and singular part of the tensor components of strain rate used by materials that make up the composite material, where the scalars $(\mathbf{r} \cdot [\![\dot{\mathbf{u}}]\!])$ and $(\mathbf{s} \cdot [\![\dot{\mathbf{u}}]\!])$ correspond to tensor components of the jump velocity in the directions **r** and **s**, respectively.

$\dot{\boldsymbol{\varepsilon}}^m = \dot{\bar{\boldsymbol{\varepsilon}}} + (\delta_s \mathbf{n} \otimes [\![\dot{\mathbf{u}}]\!])^s$	(strain rate in matrix)	(2.72)
$\dot{\varepsilon}^{dr}_{rr} = \mathbf{r} \cdot \dot{\bar{\boldsymbol{\varepsilon}}} \cdot \mathbf{r} + \delta_s\, (\mathbf{r} \cdot \mathbf{n})(\mathbf{r} \cdot [\![\dot{\mathbf{u}}]\!])$	(strain rate in fiber **r**)	(2.73)
$\dot{\varepsilon}^{ds}_{ss} = \mathbf{s} \cdot \dot{\bar{\boldsymbol{\varepsilon}}} \cdot \mathbf{s} + \delta_s\, (\mathbf{s} \cdot \mathbf{n})(\mathbf{s} \cdot [\![\dot{\mathbf{u}}]\!])$	(strain rate in fiber **s**)	(2.74)
$\dot{\gamma}^f_{rs} = 2\, \mathbf{r} \cdot \dot{\bar{\boldsymbol{\varepsilon}}} \cdot \mathbf{s} + \delta_s \left[(\mathbf{s} \cdot \mathbf{n})(\mathbf{r} \cdot [\![\dot{\mathbf{u}}]\!]) + (\mathbf{r} \cdot \mathbf{n})(\mathbf{s} \cdot [\![\dot{\mathbf{u}}]\!])\right]$	(shear strain in fiber)	(2.75)

Table 2.7. Tensor components of strain rate of the materials that make up the composite material.

Remark 2.9 *From Equation (2.73), it is deduced that the strain rate in fibers* **r** *on surface S corresponds to the regular part* $(\dot{\varepsilon}^{dr}_{rr} = \mathbf{r} \cdot \dot{\bar{\boldsymbol{\varepsilon}}} \cdot \mathbf{r})$*, when the discontinuity is parallel to fibers, i.e.* $(\mathbf{n} \perp \mathbf{r})$*. This result physically indicates that the opening of a parallel crack to a fiber does not generate any strain on it, as it is expected. In return, when* **n** *and* **r** *are parallel, the singular part of the strain rate take a maximum value* $\delta_s\,(\mathbf{r} \cdot [\![\dot{\mathbf{u}}]\!])$*. Let us notice that the tensor component of the jump velocity perpendicular to the axis of fibers does not produce axial strain on them. In an analogous way occurs with the fibers oriented in* **s***, as it can be observed in Equation (2.74).*

> ***Remark 2.10*** *In a point of composite material, the strain rate* $\dot{\boldsymbol{\varepsilon}}(\mathbf{x},t)$ *is given by the kinematics of CSDA indicated in Equation (2.70), whereas the stress rate* $\dot{\boldsymbol{\sigma}}(\mathbf{x},t)$ *is calculated by means of mixing theory with Equation (2.56).*

2.4.2. Equilibrium conditions in the composite material

> ***Hypothesis 2.2.*** *Since the stress field in a material point is defined in the scale of the composite material as indicated in Remark 2.10, the equilibrium equations and the traction continuity conditions used in CSDA on homogenous materials can be directly applied to composite materials.*

The equilibrium equations and the traction continuity conditions in the continuum of composite material are expressed in Table 2.8, where **b** is body force and $\mathbf{t}^*$ is the prescribed traction vector and $\mathbf{v}_t$ is a unit vector normal to boundary Γ_σ.

The subscript $\Omega^{(\bullet)}\backslash S$ indicates that the amount (•) is evaluated in a point belonging to $\Omega^{(\bullet)}$ but outside surface S. The discontinuity surface splits the domain Ω into two parts: Ω^+ and Ω^-, where vector **n** aims towards Ω^+ as indicated in Figure 2.11(a).

$$\nabla\cdot\dot{\boldsymbol{\sigma}}+\dot{\mathbf{b}}=0 \qquad \text{(internal equilibrium in } \Omega\backslash S) \tag{2.76}$$

$$\dot{\boldsymbol{\sigma}}\cdot\mathbf{v}_t=\dot{\mathbf{t}}^* \qquad \text{(external equilibrium on } \Gamma_\sigma) \tag{2.77}$$

$$[\![\dot{\boldsymbol{\sigma}}]\!]_{\Omega\backslash S}\cdot\mathbf{n}=\dot{\boldsymbol{\sigma}}_{\Omega^-\backslash S}\cdot\mathbf{n}-\dot{\boldsymbol{\sigma}}_{\Omega^+\backslash S}\cdot\mathbf{n}=0 \qquad \text{(outer traction continuity on } S) \tag{2.78}$$

$$[\![\dot{\boldsymbol{\sigma}}]\!]\cdot\mathbf{n}=\dot{\boldsymbol{\sigma}}_S\cdot\mathbf{n}-\dot{\boldsymbol{\sigma}}_{\Omega^+\backslash S}\cdot\mathbf{n}=0 \qquad \text{(inner traction continuity on } S) \tag{2.79}$$

Table 2.8. Equilibrium equations and traction continuity conditions in the composite material.

The inner traction continuity on S expressed in Equation (2.79) is fulfilled only if the stress values are bounded. By this reason, the continuum strong discontinuity approach allows to evaluate a bounded stress field with the same constitutive model of the continuum, as much in the discontinuity surface S, as outside it, in spite of the unbounded character of the strain on S.

2.4.3. Strong discontinuity analysis in the composite material

The strong discontinuity analysis establishes the conditions necessary to maintain the consistency between the stresses and strains when the displacement jump is different from zero $\left([\![\dot{\mathbf{u}}]\!]\neq 0\right)$. Under these circumstances the strain rate in the discontinuity is unbounded, however, the stress of the composite material and its components only have physical sense if they are bounded. This is obtained by means of the regularization of some parameters and internal variables of the constitutive model.

At the step of pseudo-time $t=t_{SD}$ from which a strong discontinuity appears, the strain $\boldsymbol{\varepsilon}_{\Omega\backslash S}$ and its rate $\dot{\boldsymbol{\varepsilon}}_{\Omega\backslash S}$, they maintain an bounded value defined by the regular part of the Equation (2.70). In the damage model used for the matrix, a bounded stress $\boldsymbol{\sigma}^m_{\Omega\backslash S}(\boldsymbol{\varepsilon}_{\Omega\backslash S},\alpha^m)$ is obtained from the strain $\boldsymbol{\varepsilon}_{\Omega\backslash S}$. In return, in the one-dimensional elasto-plastic models used in the other components of the composite material, a bounded stress in term of one of the tensor components of the strain can be found. The normal stress in fibers oriented in the directions **r** and **s**, $\sigma^{fr}_{rr(\Omega\backslash S)}(\mathbf{r}\cdot\boldsymbol{\varepsilon}_{\Omega\backslash S}\cdot\mathbf{r},\alpha^{fr})$ and $\sigma^{fs}_{ss(\Omega\backslash S)}(\mathbf{s}\cdot\boldsymbol{\varepsilon}_{\Omega\backslash S}\cdot\mathbf{s},\alpha^{fs})$ respectively, they are bounded, as well as tangential stress $\tau^{f}_{rs(\Omega\backslash S)}(2\mathbf{r}\cdot\boldsymbol{\varepsilon}_{\Omega\backslash S}\cdot\mathbf{s},\alpha^{f\tau})$ produced in the fiber by the dowel action. In addition, it can be indicated that the stress rates $\dot{\boldsymbol{\sigma}}^m_{(\Omega\backslash S)},\dot{\sigma}^{fr}_{rr(\Omega\backslash S)},\dot{\sigma}^{fs}_{ss(\Omega\backslash S)},\dot{\tau}^{f}_{rs(\Omega\backslash S)}$ are bounded values.

Since the sum between bounded values is equal to another bounded value, the stress rate in the composite material defined in Equation (2.80) will be a bounded value, as well as the traction rate $\dot{\mathbf{t}}_{\Omega\backslash S}=(\dot{\boldsymbol{\sigma}}_{\Omega\backslash S}\cdot\mathbf{n})$.

$$\begin{aligned}\dot{\boldsymbol{\sigma}}_{\Omega\backslash S} &= k^m\dot{\boldsymbol{\sigma}}^m_{\Omega\backslash S}+k^{fr}(\mathbf{r}\otimes\mathbf{r})\dot{\sigma}^{fr}_{rr(\Omega\backslash S)}+k^{fs}(\mathbf{s}\otimes\mathbf{s})\dot{\sigma}^{fs}_{ss(\Omega\backslash S)}+\\ &+2(k^{fr}+k^{fs})(\mathbf{r}\otimes\mathbf{s})^s\,\dot{\tau}^{f}_{rs(\Omega\backslash S)}\end{aligned} \tag{2.80}$$

In accord with the basic hypothesis that establishes internal continuity of the tractions rate in discontinuity *S*, described by Equation (2.79), the traction rate of the composite material in discontinuity *S*, $\dot{\mathbf{t}}_S=(\dot{\boldsymbol{\sigma}}_S\cdot\mathbf{n})$, it maintains a bounded value, like the stress rate $\dot{\boldsymbol{\sigma}}_S$. According to mixing theory this stress rate is defined as:

$$\begin{aligned}\dot{\boldsymbol{\sigma}}_S &= k^m\underbrace{\dot{\boldsymbol{\sigma}}^m_S}_{acotado}+k^{fr}(\mathbf{r}\otimes\mathbf{r})\underbrace{\dot{\sigma}^{fr}_{rr(S)}}_{acotado}+k^{fs}(\mathbf{s}\otimes\mathbf{s})\underbrace{\dot{\sigma}^{fs}_{ss(S)}}_{acotado}+\\ &+2(k^{fr}+k^{fs})(\mathbf{r}\otimes\mathbf{s})^S\underbrace{\dot{\tau}^{f}_{rs(S)}}_{acotado}\end{aligned} \tag{2.81}$$

where that k^m, k^{fr}, k^{fs}, **r** and **s** are bounded parameters.

Since a bounded value can be expressed as the sum of several bounded values, the stress rate of each one of the components in *S* is also a bounded value.

> ***Remark 2.11*** *An important conclusion of the strong discontinuity analysis establishes that the stress rate in S of the components and consequently, of the composite material are bounded values despite the strain rate* $\dot{\boldsymbol{\varepsilon}}_S$ *is not bounded.*

According to the mentioned earlier, in the continuous constitutive model of each component, a unbounded strain rate does not generate a bounded stress rate. This is obtained through the regularization of some parameters and internal variables as described next.

2.4.3.1. Regularization of the matrix constitutive model

The regularization of the matrix model is defined by the strong discontinuity analysis applied to damage models as shown in Appendix C.4. (Oliver 2000; Samaniego 2002; Oliver & Huespe 2004a).

A condition sufficient to regularize the model consists in the redefining of the parameter H^m of the constitutive model of the matrix as a parameter of discrete softening $\bar{H}^m$, of the form:

$$\frac{1}{H^m} = \delta_S \frac{1}{\bar{H}^m} \tag{2.82}$$

where δ_S is Dirac's delta function in the discontinuity surface (Appendix F). Likewise, the internal variable r_S^m in surface S is regularized through an bounded discrete variable $\bar{\alpha}^m$, thus:

$$\dot{r}_S^m = \delta_S \dot{\bar{\alpha}}^m \tag{2.83}$$

Replacing the earlier result in Equation (2.4), the discrete softening law is obtained as:

$$\dot{q}^m = \bar{H}^m \dot{\bar{\alpha}}^m \quad ; \quad q_s^m = q_{s(SD)}^m + \bar{H}^m \Delta\bar{\alpha}^m \tag{2.84}$$

where $\Delta\bar{\alpha}^m = \bar{\alpha}^m(t_{SD}) - \bar{\alpha}^m(t)$, and t_{SD} is strong discontinuity time.

2.4.3.2. Regularization of the constitutive models of the fibers

The regularization for the other components is obtained through strong discontinuity analysis applied to a one-dimensional elasto-plastic model as described in Appendix C.5 (Simó, Oliver et al. 1993). The indicated ingredients next are applicable to the dowel action and to the axial behavior of deformable fibers in the directions **r** and **s**.

In an similar way to the damage model, in the discrete elasto-plastic model of each phenomenon the internal variable, the regularization condition of the softening parameter and the softening rule are defined as:

$$\left.\begin{array}{l}\lambda^{fr}=\dot{\alpha}_S^{fr}=\delta_S\dot{\bar{\alpha}}^{fr} \quad ; \quad \dfrac{1}{H^{fr}}=\delta_S\dfrac{1}{\overline{H}^{fr}}\\ q_s^{fr}=q_{s(SD)}^{fr}+\overline{H}^{fr}\Delta\bar{\alpha}^{fr}\end{array}\right\} \quad \text{(deformable fiber in } \mathbf{r}\text{)} \tag{2.85}$$

$$\left.\begin{array}{l}\lambda^{fs}=\dot{\alpha}_S^{fs}=\delta_S\dot{\bar{\alpha}}^{fs} \quad ; \quad \dfrac{1}{H^{fs}}=\delta_S\dfrac{1}{\overline{H}^{fs}}\\ q_s^{fs}=q_{s(SD)}^{fs}+\overline{H}^{fs}\Delta\bar{\alpha}^{fs}\end{array}\right\} \quad \text{(deformable fiber in } \mathbf{s}\text{)} \tag{2.86}$$

$$\left.\begin{array}{l}\lambda^{f\tau}=\dot{\alpha}_S^{f\tau}=\delta_S\dot{\bar{\alpha}}^{f\tau} \quad ; \quad \dfrac{1}{H^{f\tau}}=\delta_S\dfrac{1}{\overline{H}^{f\tau}}\\ q_s^{f\tau}=q_{s(SD)}^{f\tau}+\overline{H}^{f\tau}\Delta\bar{\alpha}^{f\tau}\end{array}\right\} \quad \text{(dowel action in } rs\text{-plane)} \tag{2.87}$$

Table 2.9. Equations of regularization of the constitutive models of the fibers.

where the superscripts fr, fs and $f\tau$ correspond to the parameters associated to the deformable fiber model in **r**, deformable fiber model in **s** and dowel action in *rs*-plane, respectively.

2.5. Discontinuous bifurcation analysis in the composite material

In the tests where the reinforcement is distributed uniformly in the whole member, after the elastic regime of the concrete, two stages are distinguished. Initially in a *distributed cracking stage* many cracks of little opening and constant separation due to the steel capacity and to a good adherence between the concrete and the bars. In a *discontinuous or located failure stage*, it is observed that the opening of few cracks prevails on the others, whereas the structural capacity decays (Figure 2.13). In the context of the continuum mechanics, the discontinuous bifurcation analysis allows to determine the beginning and the direction of the cracks in the stage of located failure.

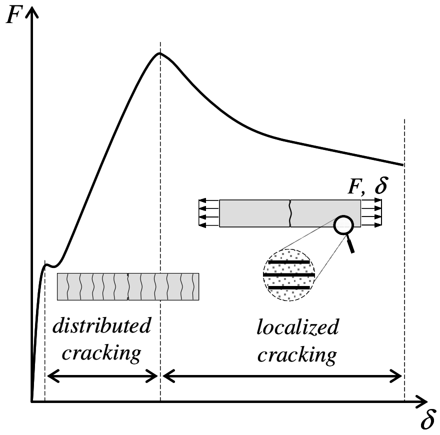

Figure 2.13. Scheme of the structural response of a member of reinforced concrete subjected to tension.

2.5.1. Bifurcation criterion

In composite materials where the fibers embedded in the matrix are distributed uniformly, the direction and the time of bifurcation will be determined by the mechanical properties of all the components.

> ***Hypothesis 2.3**. In a material point, the velocity field, the strain rate and the stress rate (obtained from the tangent constitutive relationship shown in Equation (2.66)), are defined in the scale of the composite. This allows to assume that the discontinuous bifurcation analysis used in homogenous materials (Rice 1976; Runesson, Ottosen et al. 1991) is applicable to composite materials as the reinforced concrete presented in this work.*

Considering that the tangent constitutive tensor of the composite material in the domains Ω+ and Ω- are equals, and replacing the constitutive equation of the composite material (Equation (2.66)), in the traction continuity condition (Equation (2.78)), it is obtained:

$$[[\dot{\boldsymbol{\sigma}} \cdot \mathbf{n}]] = \mathbf{n} \cdot \mathbb{C}_{tg} : [[\dot{\boldsymbol{\varepsilon}}]] = \mathbf{0} \tag{2.88}$$

replacing the equation of the jump strain rate (Equation (2.71)),

$$\left(\mathbf{n} \cdot \mathbb{C}_{tg} \cdot \mathbf{n}\right) \cdot [[\dot{\mathbf{u}}]] = \mathbf{0} \tag{2.89}$$

defining to the *localization tensor of the composite* material as:

$$\mathbf{Q}_{tg}(t,\mathbf{n}) = \mathbf{n}\cdot\mathbb{C}_{tg}\cdot\mathbf{n} \tag{2.90}$$

The classic criterion of bifurcation established by Hill (1962) is written in the form:

$$\mathbf{Q}_{tg}(t,\mathbf{n})\cdot[[\dot{\mathbf{u}}]] = \mathbf{0} \qquad \forall t \tag{2.91}$$

According to the aforementioned kinematics, a jump in the velocity field different from zero ($[[\dot{\mathbf{u}}]] \neq \mathbf{0}$) is a sufficient condition for the existence of a mode of strong discontinuity. Therefore fulfilling Equation (2.91), the localization tensor must be null at the time t_B and in the **n** direction, of such form that:

$$\mathbf{Q}_{tg}(t_B,\mathbf{n}) = 0 \quad \rightarrow \quad \det\lfloor\mathbf{Q}_{tg}(t_B,\mathbf{n})\rfloor = 0 \tag{2.92}$$

Replacing Equation (2.67) into Equation (2.90), the localization tensor of composite material is expressed as:

$$\begin{aligned}\mathbf{Q}_{tg} &= k^{m}\mathbf{Q}^{m}_{tg} + k^{fr}E^{dr}_{tg}(\mathbf{n}\cdot\mathbf{r})^{2}(\mathbf{r}\otimes\mathbf{r}) + \\ &+ k^{fs}E^{ds}_{tg}(\mathbf{n}\cdot\mathbf{s})^{2}(\mathbf{s}\otimes\mathbf{s}) + \\ &+ 4(k^{fr}+k^{fs})G^{f}_{tg}\left\lfloor\mathbf{n}\cdot(\mathbf{r}\otimes\mathbf{s})^{s}\otimes(\mathbf{r}\otimes\mathbf{s})^{s}\cdot\mathbf{n}\right\rfloor\end{aligned} \tag{2.93}$$

where $\mathbf{Q}^{m}_{tg} = \mathbf{n}\cdot\mathbb{C}^{m}_{tg}\cdot\mathbf{n}$ is localization tensor of the matrix for a isotropic damage model with degradation in tension and compression obtained from of Equation (2.11) as:

$$\mathbf{Q}^{m}_{tg} = \frac{q^{m}}{r^{m}}\mathbf{Q}^{m} - \left(\frac{q^{m}-H^{m}r}{(r^{m})^{3}}\right)\left(\frac{(r^{m})^{2}}{\phi}\left(\bar{\mathbf{t}}^{m}\otimes\bar{\mathbf{t}}^{A}\right) + \phi^{2}\left(\bar{\mathbf{t}}^{m}\otimes\bar{\mathbf{t}}^{m}\right)\right) \tag{2.94}$$

In earlier equation, $\bar{\mathbf{t}}^{m} = \mathbf{n}\cdot\bar{\boldsymbol{\sigma}}^{m}$, $\bar{\mathbf{t}}^{A} = \mathbf{n}\cdot\mathbf{A}$, the scalar value ϕ and the tensor **A** is defined by the damage model for two-dimensional problems described in Appendix A.1. The *elastic localization tensor or acoustic tensor of the matrix* defined as $\mathbf{Q}^{m} = \mathbf{n}\cdot\mathbb{C}^{m}\cdot\mathbf{n}$ (Hill 1962) is expressed of the form:

$$\mathbf{Q}^{m} = \frac{E^{m}}{1-(\nu^{m})^{2}}\left[\left(\frac{1+\nu^{m}}{2}\right)(\mathbf{n}\otimes\mathbf{n}) + \left(\frac{1-\nu^{m}}{2}\right)\mathbf{1}\right] \qquad \text{(plane stress)} \tag{2.95}$$

$$\mathbf{Q}^{m} = \frac{E^{m}}{(1+\nu^{m})(1-\nu^{m})}\left[\left(\frac{1}{2}\right)(\mathbf{n}\otimes\mathbf{n}) + \left(\frac{1-2\nu^{m}}{2}\right)\mathbf{1}\right] \qquad \text{(plane strain)} \tag{2.96}$$

2.5.2. Calculation strategy

The bifurcation time and the discontinuity direction are calculated by means of a process of search (at every step of pseudo-time), of the minimum values of the determinant of $[\mathbf{Q}_{tg}]$ with respect to **n**. This procedure can have a high computational cost in three-dimensional problems, however, in the two-dimensional case the cost is much smaller, first, because $[\mathbf{Q}_{tg}]$ is a two-order matrix and secondly, because vector **n** can be defined from a unique angle θ_n.

As convention θ_n is the angle formed between the *1*-direction of principal strain and vector **n**, this assures that the minimum values $\det(\mathbf{Q}_{tg}(t,\theta_n))$ appear between θ_n=-90° and θ_n=+90°, which is important in the numerical procedure.

> ***Remark 2.12*** *The anisotropy of the composite material produced by the direction of the fibers implies that the principal directions are different in strain and stress.*

For every pseudo-time t the minimum values of $\det(\mathbf{Q}_{tg}(t,\theta_n))$ are searched in terms of the angle θ_n. When $\det(\mathbf{Q}_{tg}(t_B,\theta_{loc}))=0$, the values of t and θ_n correspond to *bifurcation time* t_B and the *localization angle* θ_{loc}. From Figure 2.14 to Figure 2.17, this procedure is graphically represented through the curve between $(\det(\mathbf{Q}_{tg})/\det(\mathbf{Q}^m))$ and the angle θ_n, where $\mathbf{Q}^m$ is the elastic localization tensor of the matrix. Each relative minimum in this curve is called *bifurcation indicator* and is defined as:

$$\zeta_i = \min\left[\det(\mathbf{Q}_{tg}(t,\theta_i))/\det(\mathbf{Q}^m(t,\theta_i))\right] \quad i \in \{1,2\} \tag{2.97}$$

2.5.3. Examples of bifurcation on a material point

These examples study the state of a material point of reinforced concrete (composite material), when it is subjected to the load that produces bifurcation in the simple concrete (homogenous material).

A stress state where normal strain $\varepsilon_{xx} \neq 0$ and $\varepsilon_{yy} = \gamma_{xy} = 0$ is considered (except in Section 2.5.3.4). The mechanical properties of concrete and steel for all the examples are: E^m =20.0 GPa, ν^m =0.2, G^f =100.N/m and σ_u^m =2.00 MPa and E^{fr} =200.0 GPa. In return, the directions **r** and **s** of the fiber packages and its volumetric participation factor k^{fr} and k^{fs} are different according to the example.

In Sections 2.5.3.1 to 2.4.3.2, first the influence of the reinforcement ratio is studied, then the influence of the direction of the fiber and then the intervention of two perpendicular fiber packages to each other.

2.5.3.1. Influence of the reinforcement ratio in the strain localization of the composite material

In the discontinuous bifurcation analysis of the simple concrete represented by the dash line in Figure 2.14, the *bifurcation indicators* ζ_1^m, ζ_2^m are approximately equal to zero establishing the *bifurcation time* of the homogenous material t_B^m.

The composite materials is reinforced with fibers oriented in the direction of the tension ($\mathbf{r} = [1,0]^T$). For the load step given at the pseudo-time t_B^m, three different reinforcement ratio are compared. Figure 2.14(a) shows that the augment in the amount of reinforcement increases the bifurcation indicators ζ_1, ζ_2 and consequently, it delays the bifurcation time of the composite material t_B, nevertheless, the localization direction is conserved, as shown in Figure 2.14(b).

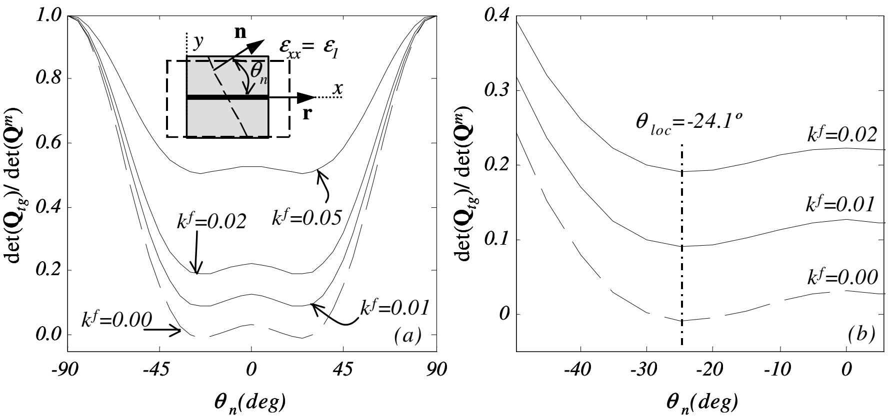

Figure 2.14. Discontinuous bifurcation analysis in composite material subjected to tension. Influence of the reinforcement ratio. Relationship between det[$\mathbf{Q}_{tg}$]/ det[$\mathbf{Q}^m$] and discontinuity angle θ_n. Properties of concrete: E^m= 20.0 GPa, ν = 0.2, G^f=100 N/m σ_u=2.00 MPa, $\sigma_{u(c)}$=20.00 MPa and of steel: E^f=200.0 GPa, φ_{fr} =0°. (a) whole graph, (b) close-up on one of the minimums of det[$\mathbf{Q}_{tg}$].

2.5.3.2. Influence of the direction of a fiber package in the localization of the composite material

This example study the bifurcation condition in a composite material with 2% reinforcement ratio and three different directions of the fibers. Figure 2.15(a) and Figure 2.15(b) show the bifurcation indicator and localization direction in terms of the fiber direction.

In Equation (2.93), it is observed that as much the angle between **r** and the direction of tension *x*, as the angle between **r** and the normal vector to discontinuity **n**, they modify in the localization tensor of the composite material.

In a material reinforced with inclined fibers 30° with respect to *x* (Figure 2.15(c)), the bifurcation indicators are different, which establishes a single direction of localization at the pseudo-time $t = t_B$.

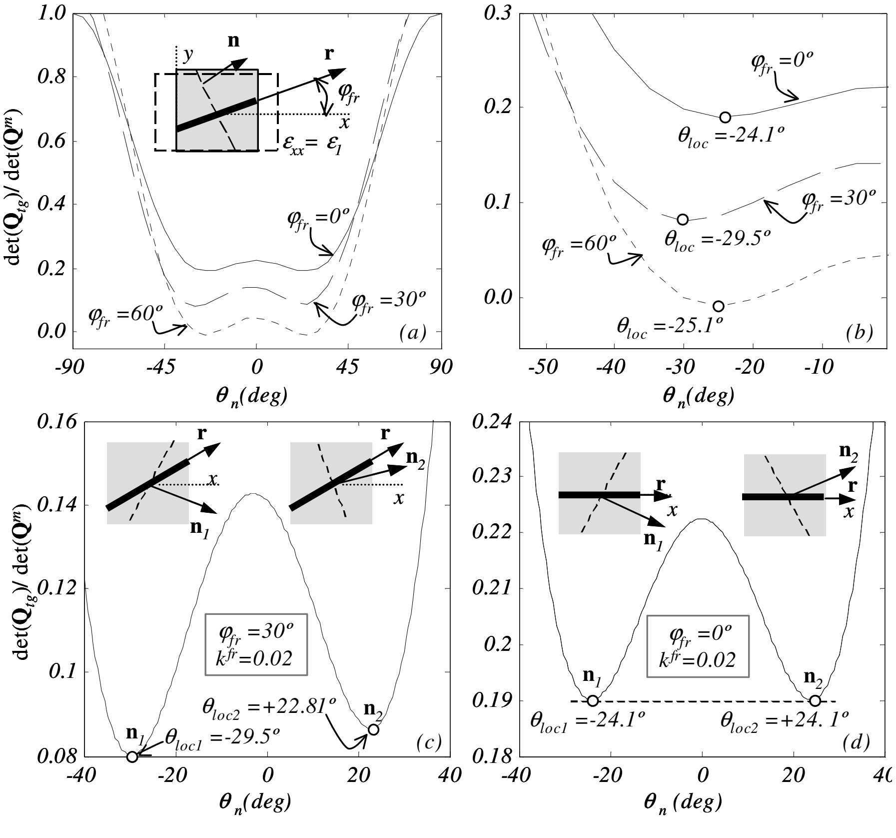

Figure 2.15. Discontinuous bifurcation analysis in composite material subjected to tension.. Influence of the direction of reinforcement. Relationship between det[$\mathbf{Q}_{tg}$]/ det[$\mathbf{Q}^m$] and discontinuity angle θ_n . Properties of concrete: E^m= 20.0 GPa, ν = 0.2, G^f=100 N/m σ_u=2.00 MPa, $\sigma_{u(c)}$=20.00 MPa and of steel: E^f=200.0 GPa, k^{fr}=0.02: (a) whole graph for differents fiber directions φ_{fr} , (b) close-up differents fiber directions φ_{fr} , (c) comparison between the bifurcation indicators for φ_{fr}=30°, (d) comparison between the bifurcation indicators for φ_{fr}=0°

In special cases in which the fiber direction and the applied loads maintain the symmetry of the problem, both bifurcation indicators are equals as in homogenous materials (Appendix C.3). An example is the composite material reinforced in the direction of the tension (**r** is parallel to principal direction 1), whose result is shown in Figure 2.15(d).

2.5.3.3. Influence of a second fiber package perpendicular to r.

A point of material reinforced in the directions x and y ($\mathbf{r}$=[1,0]^T and $\mathbf{s}$=[0,1]^T), with 2% of reinforcement ratio in x-direction is considered. This example compares the bifurcation conditions for three different reinforcement ratios in y direction.

The presence of a second fiber package in y direction delays the bifurcation time and changes the critical angle of localization (Figure 2.16), although the stress tensor only has component in x. The contribution of the second fiber to the localization tensor disappears when the normal to discontinuity **n** is perpendicular to **s**, as the third term of Equation (2.93) indicates it.

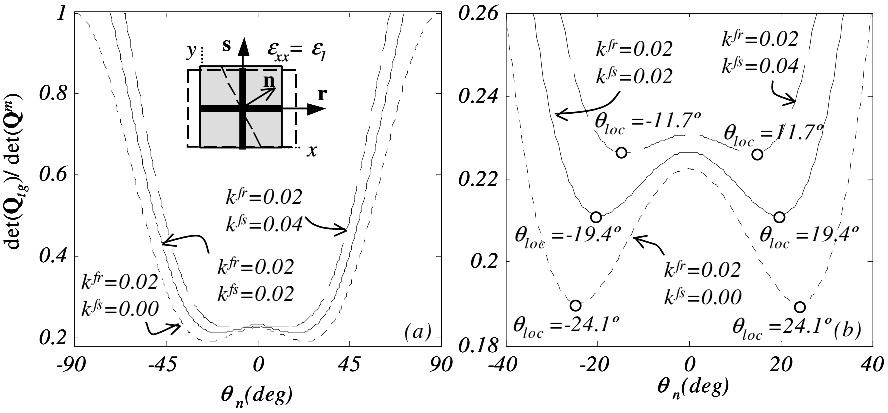

Figure 2.16. Discontinuous bifurcation analysis in composite material subjected to tension. Influence of the two fiber packages perpendicular to each other. Relationship between det[$\mathbf{Q}_{tg}$]/ det[$\mathbf{Q}^m$] and discontinuity angle θ_n. Comparison among different reinforcement ratios in **s** direction. Properties of concrete: E^m= 20.0 GPa, ν = 0.2, G^f=100 N/m σ_u=2.00 MPa, $\sigma_{u(c)}$=20.00 MPa and of steel: E^f=200.0 GPa, k^{fr}=0.02: (a) whole graph, (b) close-up.

Remark 2.13 *The bifurcation condition of the composite material depends on the stress state, the mechanical properties of the matrix and the amount, direction and mechanical properties of the fibers.*

2.5.3.4. Material point with fibers in two-way subjected to shear

A point of material reinforced with two fiber packages oriented 30º and 120º with respect to x is subjected to a displacement which only produces shear strain γ_{xy} , i.e. ε_{xx}=0 and ε_{yy}=0. The displacement increases indicating four pseudo-times or load steps (t_1, t_2, t_3, t_4) until obtaining the bifurcation time $t = t_B$.

The concrete matrix has Young's modulus E^m=20.0 GPa, Poisson's ratio ν^m=0.2, fracture energy G^f=100 N/m, tensile strength σ_u=2.0 Mpa and compressive strength $\sigma_{u(c)}$=20.0 MPa. The steel fibers have Young's modulus E^f=200.0 GPa, reinforcement ratio in the directions **r** and **s**, $k^{fr} = k^{fs} = 0.02$.

Figure 2.17 shows to the variation of $\det(\mathbf{Q}_{tg}(t,\theta_n))$ with respect to the angle θ_n. Here, different values of the bifurcation indicators are observed producing a unique angle θ_{loc} even for strain levels earlier to the bifurcation time.

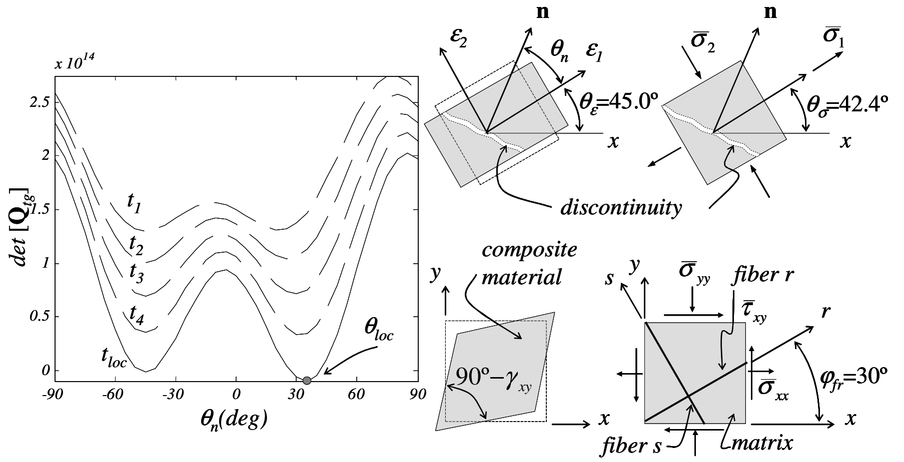

Figure 2.17. Discontinuous bifurcation analysis in composite material subjected to shear. Relationship between det[$\mathbf{Q}_{tg}$] and discontinuity angle θ_n. Comparison among different strain levels γ_{xy} (where ε_{xx}=0 y ε_{yy}=0). Properties of concrete: E^m= 20.0 GPa, ν = 0.2, G^f=100 N/m σ_u=2.00 MPa, $\sigma_{u(c)}$=20.00 MPa and of steel: E^f=200.0 GPa, φ_{fr} =30°, φ_{fs} =120°, k^{fr}=k^{fs}=0.02.

2.6. Finite element implementation of the formulated model by means of elements with embedded discontinuities

The formulation presented in the earlier sections has been implemented in a program of two-dimensional analysis with finite elements, considering infinitesimal strain and non-linear material (Cervera, Agelet et al. 2001). In general, a new constitutive model of the reinforced concrete treated as a composite material and equipped with CSDA (Oliver, Huespe et al. 2004a; Oliver, Huespe et al. 2005a; Blanco 2006) has been added. This model has the following characteristics:

- The numerical model uses finite elements that can capture the jumps adding enriched modes of strain, which are controlled by additional degrees of freedom. These special elements which are able to include the discontinuity of the displacement in their interior are called *finite elements with embedded discontinuities* (Figure 2.18) (Simó, Oliver et al. 1993). Each element has elemental support of the enrichment function, allowing the condensation to level of the element, of the degrees of freedom related to the jump.

- In the implementation of the model, *kinematically consistent symmetrical elements* have been used (Jirasek 2000), with the purpose of obtaining a symmetrical stiffness matrix of the problem. The kinematics of this type of elements capture the motion of rigid body of its parts splited by a discontinuity line; nevertheless, the traction continuity conditions as result from a variational formulation are approximate.

- The implicit integration algorithm allows obtaining good results with great time step in constitutive models equipped with softening strain. However, the stiffness matrix of the problem can be ill-conditioned, endangering the convergence of the solution. Therefore, the presented formulation uses the *implicit-explicit integration scheme (IMPLEX)* proposed by Oliver and collaborator (Oliver, Huespe et al. 2004a; Oliver, Huespe et al. 2005a), which guarantees the defined positive character of the algorithmic stiffness matrix of the problem, increasing substantially to the robustness and stability of the solution. Appendix E describes this form to integrate the constitutive model.

- From the material discontinuous bifurcation analysis, the direction of the discontinuity into a finite element is obtained, but its position within the element is unknown (Figure 2.19(a)). Then an algorithm establishing the geometric place of the discontinuity line inside each element is required, which assures the continuity among the segments that conform the discontinuity trajectory in the solid (Figure 2.19(b)). The global strategy of the *discontinuity tracking* described in some references (Samaniego 2002; Oliver & Huespe 2004a) and used in this work, it fulfills this objective (Appendix D). Other authors (Sancho, Planas et al. 2004; Sancho, Planas et al. 2005; Sancho, Planas et al. 2006) have developed local algorithms without needing establishing the interelemental continuity of the discontinuity line, considering a cohesive central-force model and a direction of propagation normal to maximum principal stress.

Remark 2.14. *In a kinematically consistent symmetrical element, the stiffness matrix loses its symmetry if the tangent constitutive operator is not symmetrical. This ocurrs when the tensor* $\mathbf{A}$ *of the constitutive model of the concrete matrix is different from zero (Equation (2.11)).*

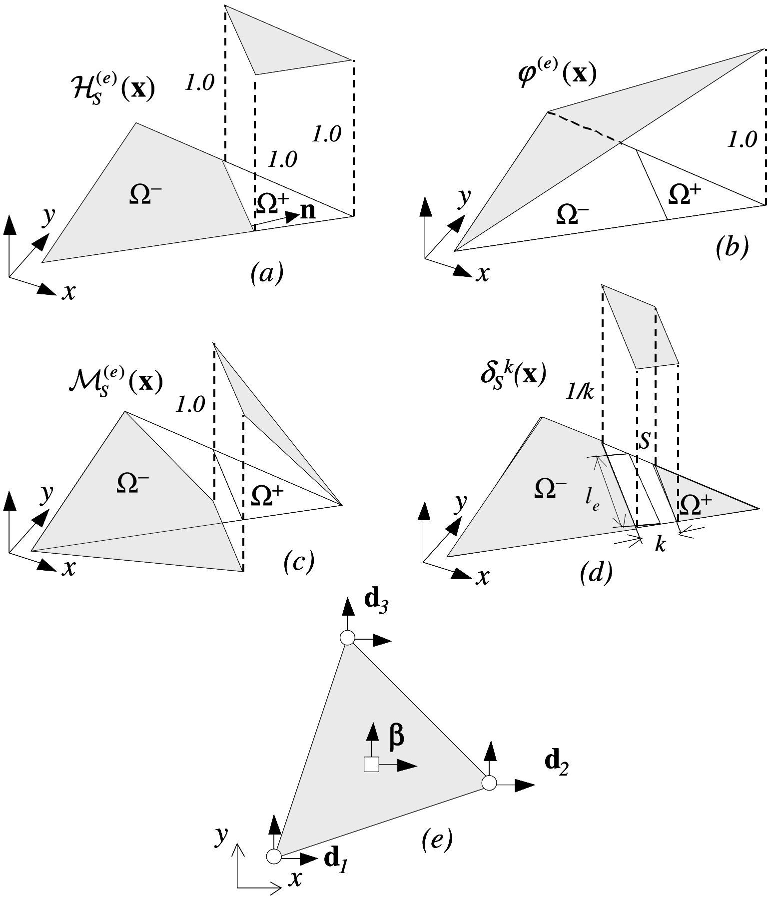

Figure 2.18. Implementation of the formulation in the FEM. Linear triangular element with embedded discontinuities: (a) Heaviside's function. (b) function φ.. (c) unit jump function, (d) Dirac's delta regularized function, (e) degrees of freedom (compatible displacements and jumps).

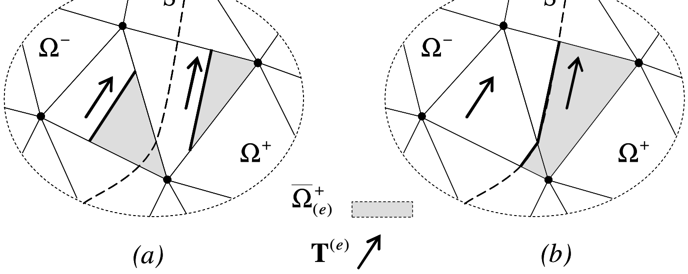

Figure 2.19. Implementation of the formulation in the FEM. Tracking of the discontinuity lines: (a) random position of the discontinuity line inside two finite elements, (b) alignment between the discontinuity trajectories of two finite elements.

2.6.1. Kinematics of the strain in the composite material

For a linear triangular element (Figure 2.18(e)), the displacements rate of a point x in its interior is obtained from the discretization of Equation (2.68), as:

$$\dot{\mathbf{u}}^{(e)}(\mathbf{x},t)=\sum_{i=1}^{3} N_i^{(e)}(\mathbf{x})\,\dot{\mathbf{d}}_i(t)+\mathcal{M}_S^{(e)}(\mathbf{x})\dot{\boldsymbol{\beta}}^{(e)}(t) \tag{2.98}$$

where $N_i^{(e)}(\mathbf{x})$ is the shape function of the element at node i, vector $\dot{\mathbf{d}}_i$ corresponds to the compatible displacement rate of node i, and vector $\dot{\boldsymbol{\beta}}^{(e)}$ represents the jump displacement rate. En two-dimensional space $\dot{\mathbf{d}}_i=\begin{bmatrix}\dot{u}_i & \dot{v}_i\end{bmatrix}^T$ and $\dot{\boldsymbol{\beta}}^{(e)}=\begin{bmatrix}\dot{\beta}_x & \dot{\beta}_y\end{bmatrix}^T$.

Since ς is the set of finite elements crossed by a discontinuity surface S, the unit jump discrete function for a linear triangular element $\mathcal{M}_S^{(e)}(\mathbf{x})$ (Figure 2.18) will be equal to:

$$\mathcal{M}_S^{(e)}(\mathbf{x})=\begin{cases}0 & \forall e\notin\varsigma\\ \mathcal{H}_S^{(e)}(\mathbf{x})-\varphi^{(e)}(\mathbf{x}) & \forall e\in\varsigma\end{cases} \tag{2.99}$$

where,

$$\mathcal{H}_S^{(e)}(\mathbf{x})=\begin{cases}0 & \forall\mathbf{x}\in\Omega^-\\ 1 & \forall\mathbf{x}\in\Omega^+\end{cases}\quad \text{y}\quad \varphi^{(e)}(\mathbf{x})=N_{i+}^{(e)}(\mathbf{x}) \tag{2.100}$$

In this case $N_{i+}^{(e)}(\mathbf{x})$ is shape function of node $i+$ belonging to the part Ω^+ of a finite element.

Differentiating Expression (2.98), the rate of the strain field in a point $\mathbf{x}$ within a finite element and at a pseudo-time t is obtained as:

$$\dot{\boldsymbol{\varepsilon}}^{(e)}(\mathbf{x},t)=\nabla^s\dot{\mathbf{u}}^{(e)}=\sum_{i=1}^{3}\left(\nabla N_i^{(e)}\otimes\dot{\mathbf{d}}_i\right)^s-(\nabla\varphi\otimes\dot{\boldsymbol{\beta}}^{(e)})^s+\delta_S^k(\mathbf{n}\otimes\dot{\boldsymbol{\beta}}^{(e)})^s \tag{2.101}$$

By computational purposes, it is necessary to regularize the Dirac's delta function δ_S^k in terms of parameter k as follows:

$$\delta_S^k(\mathbf{x})=\lim_{k\to 0}\left(\mu_S(\mathbf{x})\frac{1}{k}\right);\quad \mu_S(\mathbf{x})=\begin{cases}1 & \mathbf{x}\in S^k\\ 0 & \mathbf{x}\notin S^k\end{cases} \tag{2.102}$$

where S^k is a band of thickness k around S. Figure 2.18(d) shows this function for a linear triangular element.

> ***Remark 2.15*** *The second-order tensors as the stress and the strain are represented in two-dimensional notation of Voigt by means of a vector of the form* $\{\bullet\}=\left[(\bullet)_{xx},(\bullet)_{yy},(\bullet)_{xy}\right]^T$. *However, the localization tensor of Equation (2.93) is transformed into a square matrix.*

In matrix form and in the context of the finite elements method (Hughes 2000), the two-dimensional strain rate is expressed as:

$$\{\dot{\boldsymbol{\varepsilon}}\} = \left[\mathbf{B}^{(e)}\right]\left\{\dot{\mathbf{d}}^{(e)}\right\} + \left[\mathbf{G}^{(e)}\right]\left\{\dot{\boldsymbol{\beta}}^{(e)}\right\} \quad \text{o} \quad \{\dot{\boldsymbol{\varepsilon}}\} = \left[\mathbf{B}^{(e)}, \mathbf{G}^{(e)}\right] \cdot \begin{bmatrix} \dot{\mathbf{d}}^{(e)} \\ \dot{\boldsymbol{\beta}}^{(e)} \end{bmatrix} \text{ , where}$$
$$\dot{\mathbf{d}}^{(e)} = \left[\dot{\mathbf{d}}_1, \dot{\mathbf{d}}_2, \dot{\mathbf{d}}_3\right]^T \quad \dot{\mathbf{d}}_i = \left[\dot{u}_i, \dot{v}_i\right]^T \quad \dot{\boldsymbol{\beta}}^{(e)} = \left[\dot{\beta}_x, \dot{\beta}_y\right]^T \quad \{\dot{\boldsymbol{\varepsilon}}\} = \left[\dot{\varepsilon}_{xx}, \dot{\varepsilon}_{yy}, \dot{\gamma}_{xy}\right]^T \tag{2.103}$$

Comparing Equation (2.101) that defines the strain of tensorial form, with Equation (2.103), the elemental matrices $\mathbf{B}^{(e)}$ and $\mathbf{G}^{(e)}$ are obtained thus:

$$\left[\mathbf{B}_i\right] = \begin{bmatrix} \partial_x N_i^{(e)} & 0 \\ 0 & \partial_y N_i^{(e)} \\ \partial_y N_i^{(e)} & \partial_x N_i^{(e)} \end{bmatrix} \quad ; \quad \left[\mathbf{B}^{(e)}\right] = \left[\mathbf{B}_1, \mathbf{B}_2, \mathbf{B}_3\right] \tag{2.104}$$

$$\left[\mathbf{G}^{(e)}\right] = \begin{bmatrix} (\delta_S^k n_x - \partial_x \varphi^{(e)}) & 0 \\ 0 & (\delta_S^k n_y - \partial_x \varphi^{(e)}) \\ (\delta_S^k n_y - \partial_y \varphi^{(e)}) & (\delta_S^k n_x - \partial_x \varphi^{(e)}) \end{bmatrix} \tag{2.105}$$

2.6.2. Equilibrium conditions of the composite material

The equilibrium equations can be expressed in weak form by means of a variational formulation that assures symmetry of the stiffness matrix as indicated following (Samaniego 2002; Oliver, Huespe et al. 2003). Let $\boldsymbol{\gamma}$ be a strain field of admissible variations of the form:

$$\boldsymbol{\gamma} = \underbrace{\nabla^s \overline{\boldsymbol{\eta}}}_{compatible\ part} + \underbrace{\nabla^s \boldsymbol{\eta}'}_{enhanced\ part} \quad ; \quad \overline{\boldsymbol{\eta}} \in \mathcal{V}_u \quad ; \quad \boldsymbol{\eta}' \in \mathcal{V}_{u'} \tag{2.106}$$

where $\overline{\mathcal{V}}_u, \tilde{\mathcal{V}}_\varepsilon$ are the functional spaces for the admissible regular displacements $\overline{\boldsymbol{\eta}}$ and the discontinuous displacements $\boldsymbol{\eta}' = \mathcal{M}_S \tilde{\boldsymbol{\gamma}}$, respectively. It is fulfilled that:

$$\int_{\Omega / S} \dot{\boldsymbol{\sigma}} : \nabla^s \overline{\boldsymbol{\eta}}\, d\Omega - G_{ext}(\overline{\boldsymbol{\eta}}) = 0 \qquad \forall \overline{\boldsymbol{\eta}} \in \overline{\mathcal{V}}_u$$
$$G_{ext}(\overline{\boldsymbol{\eta}}) = \int_{\Omega} \dot{\mathbf{b}} \cdot \overline{\boldsymbol{\eta}}\, d\Omega + \int_{\Gamma_\sigma} \dot{\mathbf{t}}^* \cdot \overline{\boldsymbol{\eta}}\, d\Gamma \tag{2.107}$$

$$\int_{\Omega} \dot{\boldsymbol{\sigma}} : \nabla^s \boldsymbol{\eta}'\, d\Omega - G_{ext}(\boldsymbol{\eta}') = 0 \qquad \forall \boldsymbol{\eta}' \in \overline{\mathcal{V}}_{u'}$$
$$G_{ext}(\boldsymbol{\eta}') \approx 0 \tag{2.108}$$

It can be demonstrated that the variational format expressed in the earlier equations is equivalent to *statically consistent variational formulation* (Samaniego 2002). The gradient of the admissible displacement rate is equal to:

$$\left\{\nabla^s \boldsymbol{\eta}\right\} = \left[\mathbf{B}^{(e)}\right]\left\{\overline{\boldsymbol{\eta}}\right\} + \left[\mathbf{G}^{(e)}\right]\left\{\tilde{\boldsymbol{\gamma}}\right\} \tag{2.109}$$

Therefore, the incremental expression of residual forces in a finite element corresponds to:

$$\int_{\Omega^e} \left[\mathbf{B}^{(e)}\right]^T \{\dot{\boldsymbol{\sigma}}\}\, d\Omega - \left\{\dot{F}^{(e)}_{ext}\right\} = \left\{\dot{R}^{(e)}\right\} \tag{2.110}$$

$$\int_{\Omega} \left[\mathbf{G}^{(e)}\right]^T \{\dot{\boldsymbol{\sigma}}\}\, d\Omega = \left\{\dot{r}^{(e)}\right\} \tag{2.111}$$

The incremental vector of external forces in the element is $\left\{\dot{F}^{(e)}_{ext}\right\}$, and the vector of the two-dimensional stress rate of the composite material is:

$$\{\dot{\boldsymbol{\sigma}}\} = \left[\dot{\sigma}_{xx} \quad \dot{\sigma}_{yy} \quad \dot{\sigma}_{xy}\right]^T \tag{2.112}$$

2.6.3. Stiffness matrix of the finite element

The tangent constitutive equation of the composite material indicated in the Equation (2.66) can be written in matrix notation as:

$$\{\dot{\boldsymbol{\sigma}}\} = \left[\mathbb{C}_{tg}\right] \{\dot{\boldsymbol{\varepsilon}}\} \tag{2.113}$$

where $[\mathbb{C}_{tg}]$ is the tangent constitutive matrix of the composite material in Voigt notation for the two-dimensional case.

Replacing Equation (2.113) into Equations (2.110) and (2.111), the following matrix equation can be obtained,

$$\begin{bmatrix} K^{(e)}_{dd} & K^{(e)}_{d\beta} \\ K^{(e)}_{\beta d} & K^{(e)}_{\beta\beta} \end{bmatrix} \begin{Bmatrix} \dot{\mathbf{d}}^{(e)} \\ \dot{\boldsymbol{\beta}}^{(e)} \end{Bmatrix} - \begin{Bmatrix} \dot{F}^{(e)}_{ext} \\ 0 \end{Bmatrix} = \begin{Bmatrix} \dot{R}^{(e)} \\ \dot{r}^{(e)} \end{Bmatrix} \tag{2.114}$$

where the sub-matrices $K^{(e)}_{dd}, K^{(e)}_{d\beta}, K^{(e)}_{\beta d}, K^{(e)}_{\beta\beta}$ indicated following make up the *tangent stiffness matrix of a finite element of composite material* $[\mathbf{K}^{(e)}]$.

$$\begin{aligned} K^{(e)}_{dd} &= \int_{\Omega^e} \left[\mathbf{B}^{(e)}\right]^T \left[\mathbb{C}_{tg}\right] \left[\mathbf{B}^{(e)}\right] d\Omega \\ K^{(e)}_{d\beta} &= \int_{\Omega^e} \left[\mathbf{B}^{(e)}\right]^T \left[\mathbb{C}_{tg}\right] \left[\mathbf{G}^{(e)}\right] d\Omega \\ K^{(e)}_{\beta d} &= \int_{\Omega^e} \left[\mathbf{G}^{(e)}\right]^T \left[\mathbb{C}_{tg}\right] \left[\mathbf{B}^{(e)}\right] d\Omega \\ K^{(e)}_{\beta\beta} &= \int_{\Omega^e} \left[\mathbf{G}^{(e)}\right]^T \left[\mathbb{C}_{tg}\right] \left[\mathbf{G}^{(e)}\right] d\Omega \end{aligned} \tag{2.115}$$

> ***Remark 2.16*** *Of Equation (2.115), it concludes that the tangent stiffness matrix of the composite material* $[\mathbf{K}^{(e)}]$ *is a symmetrical matrix, whenever the tangent constitutive matrix* $[\mathbb{C}_{tg}]$ *be also it.*

The elemental enrichment allows including the degrees of freedom associated with the displacement jump in the matrix equation of equilibrium of the element, as shown in Equation (2.114). Likewise, the size of the stiffness matrix can be reduced by means of a process of condensation of additional degrees of freedom.

2.6.4. Stress rate vector of the composite material

The stress rate of the composite material written in tensorial notation in Equation (2.56) can be rewritten in Voigt notation as:

$$\{\dot{\boldsymbol{\sigma}}\} = k^m\{\dot{\boldsymbol{\sigma}}^m\} + k^{fr}\{\dot{\boldsymbol{\sigma}}^{fr}\} + k^{fs}\{\dot{\boldsymbol{\sigma}}^{fs}\} + (k^{fr} + k^{fs})\{\dot{\boldsymbol{\sigma}}^{f\tau}\} \tag{2.116}$$

For the earlier equation, the stress rate vectors of each component appear in Table 2.10.

$\{\dot{\boldsymbol{\sigma}}^m\} = [\dot{\sigma}^m_{xx} \quad \dot{\sigma}^m_{yy} \quad \dot{\sigma}^m_{xy}]^T$	(stress rate of the matrix)	(2.117)
$\{\dot{\boldsymbol{\sigma}}^{fr}\} = [r_x^2 \quad r_y^2 \quad r_x r_y]^T \dot{\sigma}^{fr}_{rr}$	(stress rate of slipping fiber in **r**)	(2.118)
$\{\dot{\boldsymbol{\sigma}}^{fs}\} = [s_x^2 \quad s_y^2 \quad s_x s_y]^T \dot{\sigma}^{fs}_{ss}$	(stress rate of slipping fiber in **s**)	(2.119)
$\{\dot{\boldsymbol{\sigma}}^{f\tau}\} = 2[r_x s_x \quad r_y s_y \quad \phi_{rs}]^T \dot{\tau}^f_{rs}$	(stress rate in fiber due to dowel action)	(2.120)
$\phi_{rs} = 0.5(r_x s_y + r_y s_x)$		

Table 2.10. Stress rate vector for each component material.

The stress rate of the matrix obtained from the damage model is the vector indicated in Equation (2.117). The tensor $(\mathbf{r} \otimes \mathbf{r})\dot{\sigma}^f_{rr}$ which indicates the stress rate of the fiber in **r** is represented by the vector $\{\dot{\boldsymbol{\sigma}}^{fr}\}$ of Equation (2.118). Likewise, the tensors $(\mathbf{s} \otimes \mathbf{s})\dot{\sigma}^f_{ss}$ and $2(\mathbf{r} \otimes \mathbf{s})^s \dot{\tau}^f_{rs}$ are represented with matrix format in Equations (2.119) and (2.120).

2.6.5. Tangent constitutive matrix of the composite material

The tangent constitutive matrix of the composite material indicated as a fourth-order tensor in Equation (2.66), is represented in Voigt notation as:

$$[\mathbb{C}_{tg}] = k^m[\mathbb{C}^m_{tg}] + k^{fr}[\mathbb{C}^{dr}_{tg}] + k^{fs}[\mathbb{C}^{ds}_{tg}] + (k^{fr} + k^{fs})[\mathbb{C}^{f\tau}_{tg}] \tag{2.121}$$

The tangent constitutive matrix of the concrete is determined directly by the damage model, whereas the tangent constitutive matrices of the other components in an *xy* coordinate system correspond to:

$$\left[\mathbb{C}_{tg}^{dr}\right] = E_{tg}^{dr}\begin{bmatrix} r_x^2 r_x^2 & r_x^2 r_y^2 & r_x^3 r_y \\ & r_y^2 r_y^2 & r_x r_y^3 \\ sim & & r_x^2 r_y^2 \end{bmatrix} \qquad \text{(slipping fiber in } \mathbf{r}\text{)} \qquad (2.122)$$

$$\left[\mathbb{C}_{tg}^{ds}\right] = E_{tg}^{ds}\begin{bmatrix} s_x^2 s_x^2 & s_x^2 s_y^2 & s_x^3 s_y \\ & s_y^2 s_y^2 & s_x s_y^3 \\ sim & & s_x^2 s_y^2 \end{bmatrix} \qquad \text{(slipping fiber in } \mathbf{s}\text{)} \qquad (2.123)$$

$$\left[\mathbb{C}_{tg}^{f\tau}\right] = 4G_{tg}^{f\tau}\begin{bmatrix} r_x^2 s_x^2 & r_x s_x r_y s_y & r_x s_x \phi_{rs} \\ & r_y^2 s_y^2 & r_y s_y \phi_{rs} \\ sim & & \phi_{rs}^2 \end{bmatrix} \qquad \text{(dowel action)} \qquad (2.124)$$

Table 2.11. Tangent constitutive matrix for each component.

2.6.6. Localization matrix of the composite material

Finally, the two-dimensional localization tensor of the composite material shown in Equation (2.93) is represented by a square matrix of order two, as the following equation indicates it. The minimum value of the determinant of this matrix in terms of **n** allows establishing the bifurcation condition.

$$\mathbf{Q}_{tg} \equiv \left[\mathbf{Q}_{tg}\right] = \begin{bmatrix} Q_{xx} & Q_{xy} \\ Q_{yx} & Q_{yy} \end{bmatrix} \tag{2.125}$$

The localization matrix of the composite material can be written as the weighted sum of the contributions of the components, thus:

$$\left[\mathbf{Q}_{tg}\right] = k^m\left[\mathbf{Q}_{tg}^m\right] + k^{fr}\left[\mathbf{Q}_{tg}^{dr}\right] + k^{fs}\left[\mathbf{Q}_{tg}^{ds}\right] + (k^{fr} + k^{fs})\left[\mathbf{Q}_{tg}^{f\tau}\right] \tag{2.126}$$

where,

$$\left[\mathbf{Q}_{tg}^{dr}\right] = E_{tg}^{dr}\phi_{rn}^2\begin{bmatrix} r_x^2 & r_x r_y \\ r_x r_y & r_y^2 \end{bmatrix} \tag{2.127}$$

$$\left[\mathbf{Q}_{tg}^{ds}\right] = E_{tg}^{ds}\phi_{sn}^2\begin{bmatrix} s_x^2 & s_x s_y \\ s_x s_y & s_y^2 \end{bmatrix} \tag{2.128}$$

$$\left[\mathbf{Q}_{tg}^{f\tau}\right] = G_{tg}^{f\tau}\begin{bmatrix} (\phi_{sn} r_x + \phi_{rn} s_x)^2 & (\phi_{sn} r_x + \phi_{rn} s_x)(\phi_{sn} r_y + \phi_{rn} s_y) \\ (\phi_{sn} r_x + \phi_{rn} s_x)(\phi_{sn} r_y + \phi_{rn} s_y) & (\phi_{sn} r_y + \phi_{rn} s_y)^2 \end{bmatrix} \tag{2.129}$$

$$\phi_{rn} = (r_x n_x + r_y n_y) \quad , \quad \phi_{sn} = (s_x n_x + s_y n_y)$$

2.6.7. Calculation procedure

The calculation procedure in the constitutive model of the composite material consists of:

- Evaluating the strain components in *rs* coordinate system as indicated in Equations (2.52) to (2.55).
- Calculating the stress and the tangent modulus of each constitutive model from the strain component and the particular internal variables.
- Evaluating the stress tensor of the composite material with the Equation (2.56) and the tangent constitutive tensor with the Equation (2.67).
- Through an discontinuous bifurcation analysis of the composite material, obtaining the bifurcation time and the discontinuity direction (Equations (2.92) and (2.93)).

The flow chart presented in Figure 2.20 indicates that the input parameters are the strain of the composite material and the internal variables of the components whereas the output parameters correspond to the stress, the tangent constitutive operator, the bifurcation time and the discontinuity direction.

The material failure model of the reinforced concrete presented in this work, it incorporates *continuum strong discontinuity approach* and *mixing theory* of composite materials, mainly at level of finite element, as shown Figure 2.21. However, the tracking of the discontinuity lines detailed in Appendix D, it is defined at global level.

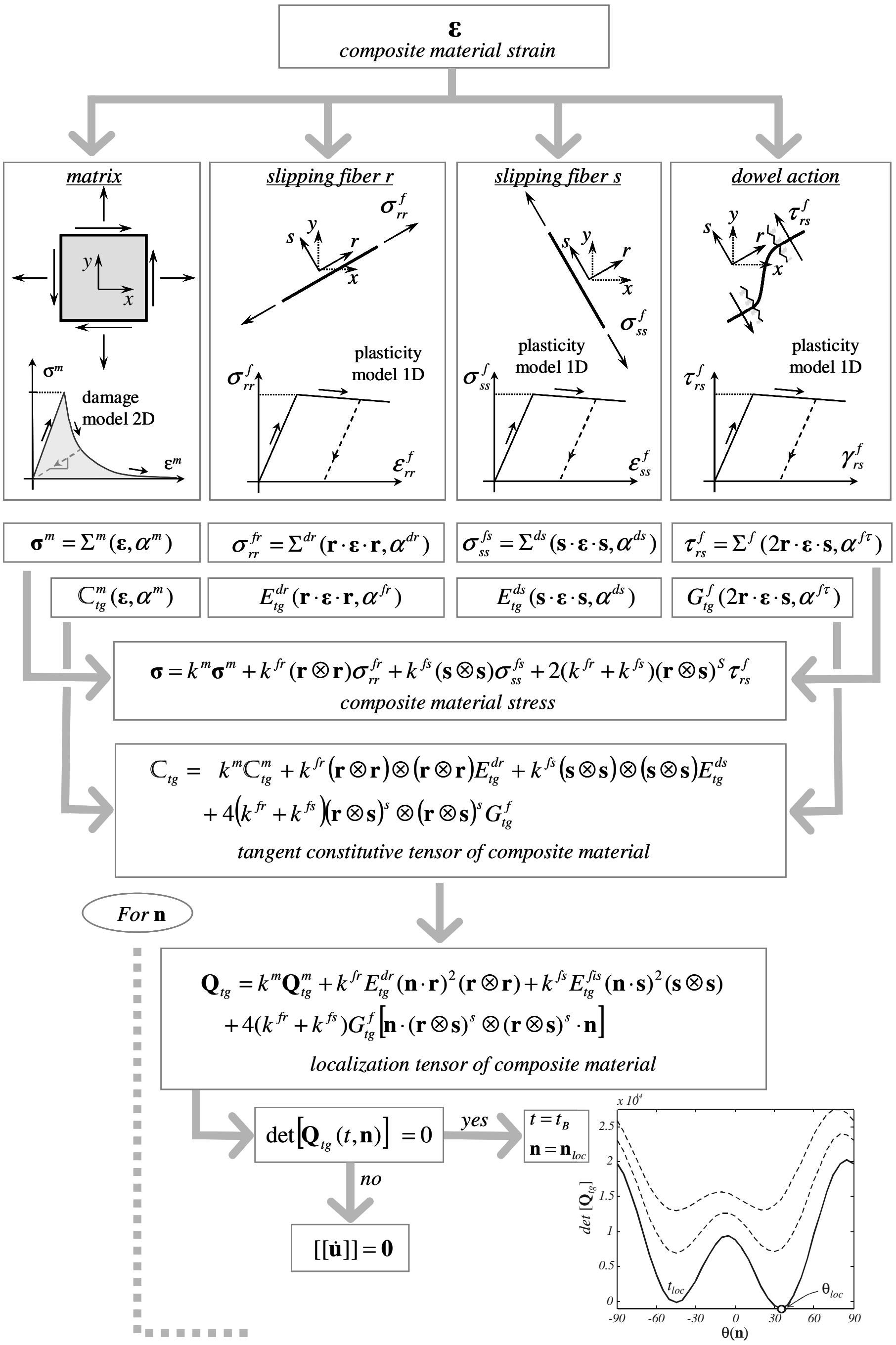

Figure 2.20. Constitutive model of composite material. Flow chart of the calculation of the stress tensor, the tangent constitutive tensor and the discontinuities bifurcation analysis.

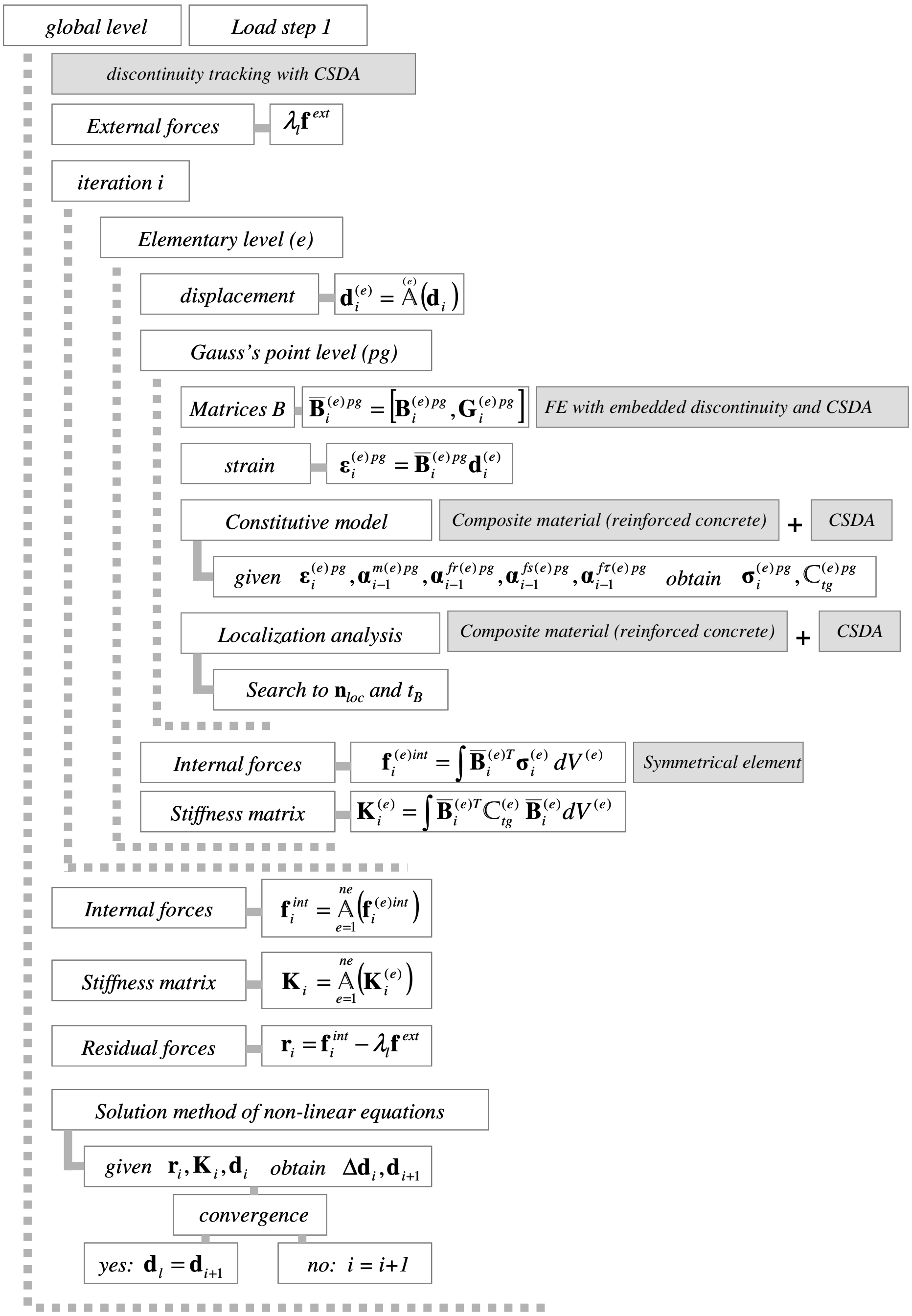

Figure 2.21. Flow chart of the finite element analysis.

2.7. Summary

Next the formulation of the model presented in the earlier sections is summarized and the most important issues of this chapter are described.

- The presented formulation represents the fracture process in reinforced concrete using two essencial ingredients: *continuum strong discontinuity approach* for describing the formation and propagation of discontinuity in the solid (Oliver 1996b; Oliver 1996a; Samaniego 2002; Oliver, Huespe et al. 2005a) and *mixing theory* for establishing the constitutive model of reinforced concrete treated as a composite material (Truesdell & Toupin 1960).

- Each point of continuum medium obeys to the behavior of a composite material make up by a concrete matrix and two long fiber packages of steel reinforcement, perpendiculars to each other, oriented in directions **r** and **s**, respectively.

- The behavior of the concrete matrix and the steel fibers, as well as, the dowel action and the adherence loss between concrete and steel, are described by means of particular constitutive models. The matrix is represented with a scalar damage model with degradation in tension and compression (Oliver, Cervera et al. 1990), and the other behaviors are described through one-dimensional elasto-plastic models (Simó & Hughes 1998).

- The strain field is defined in the composite material as a common value for the matrix and fibers, as shown in Equations (2.52) to (2.55). When obtaining the strain field from the displacements field, it is established that this latter is also defined in the scale of the composite material. Therefore, the enriched kinematics defined in CSDA is applied to a composite material of the same form as is used in a homogenous material (Equations (2.68) and (2.70)).

- The stress of the composite material computed in Equation (2.56) is the result of the weighted sum of the stresses of the components. Since the stress field of a material point is defined in the scale of the composite material, the equilibrium equations and the traction continuity conditions correspond to the expressions given for homogenous material (Equations (2.76) to (2.79)).

- The earlier feature allows supposing that the used discontinuous bifurcation analysis in homogenous materials is applicable to a composite material as the reinforced concrete, evaluating the localization tensor of composite material presented in Equation (2.93). In this way, the material instability and the discontinuity direction depend on the mechanical behavior and volumetric participation of the components of the composite material.

- In the discontinuous bifurcation analysis of the composite material, an algorithm search of the bifurcation indicator for two-dimensional problems is given. This indicator corresponds to the minimum value of the determinant of the localization tensor in terms of the discontinuity direction.

- In the implementation with the finite elements method, *embeded discontinuities elements* are used (Simó, Oliver et al. 1993), which have elemental support of the enrichment function, allowing the condensation to finite element level of the degrees of freedom related to the jump.

Chapter 3
Numerical examples

The proposed formulation is validated by means of the numerical simulation of different tests. In this chapter, the results of the modeling of reinforced concrete members subjected to tension, bending and shear are presented. Likewise, some results as the structural response and the distribution of cracks are compared with the experimental results found in specific references.

3.1. General considerations

The numerical simulation of reinforced concrete tests developed in this work presents the following characteristics:

- Infinitesimal strain, plane stress and non-linear material are considered in the simulation of the tests. Triangular finite elements with embedded discontinuities are used in the numerical analysis.

- The simulation was executed up to values of displacement greater than the anticipated values in the reference experiments. This is due to the interest in the structural response of the tests over the adherence limits, or, in some cases, of the yielding stress of the steel.

- The formation of a crack is due to the strain localization. The crack patterns have been represented by the zones where the spacing between contour lines of displacement is reduced.

- In some tests, the reinforcement steel is located in one or several thin strips and therefore it is not distributed in all the volume of the member; in these cases the mesh of finite elements has two types of materials. The reinforced zones use finite elements of composite material constituted by a matrix of concrete and one or two groups of steel fiber, in concordance with the formulation presented in Chapter 2. The rest of the member uses finite elements of a homogeneous material as the simple concrete which is represented by the damage model with degradation in tension and compression illustrated in the Section 2.2.1.

- Unlike the mesoscopic models where the problem in the fiber scale is described, the height of composite material zone can be greater than the diameter of the bars without loss of approach to the structural response.

- When the reinforcement steel is distributed uniformly by all the volume of the structural element, in other words, the amount and the disposition of the bars in the piece are constant; all the finite elements of the mesh are associated to the same composite material.

The behavior of a composite material as the reinforced concrete is characterized of the following way:

- The concrete matrix is represented by an isotropic damage model defined by Young´s modulus E^m, the Poisson´s ratio ν^m, fracture energy G^f, uniaxial strength to tension σ_u^m and compression $\sigma_{u(c)}^m$.

- The steel fibers bundle in **r** direction responds to a one-dimensional plasticity model described by: Young's modulus E^{fr}, yielding stress σ_y^{fr} and hardening parameter H^{fr}. The amount and orientation of the fibers on the composite material is determined by means of the participation volumetric factor k^{fr} and the angle between axis x and the vector **r**, respectively.

- In the same way previously indicated, the reinforcement bars orientated in **s** direction (orthogonal to **r**), are described by mechanical parameter E^{fs}, σ_y^{fs} y H^{fs} and participation volumetric factor k^{fs}.

- The slipping effect between the fiber in **r** and the matrix is characterized from the force-displacement curve obtained in some pull-out tests; wherein a bar of diameter d and length embedded on the concrete L^i, it is exacted. The stiffness (P^i/δ^i) and the maximum load P^i_{max} obtained in the test define the bond-slip modulus E^{ir} and the stress of adherence loss σ^{ir}_{adh} of a perfect plasticity one-dimensional model (Section 2.2.3). Alike, for fibers orientated in **s** the parameters E^{is} and σ^{is}_{adh} are used.

- In the tests in which prevails mode I of fracture, the effects produced by shear capacity of the bars in the faces of a crack are disregarded.

- In the simulation of shear panels, the dowel action is the result of direct shear in the bars crossing the crack. This phenomenon is characterized by means of a uniaxial elasto-plastic model which relates shear strain and equivalent shear stress in the fiber (Section 2.2.5). The mechanical properties of this model are: a yielding shear stress $\tau_y^f = \sigma_y^f / \sqrt{3}$ according to von Mises's criterion for pure shear and an elastic modulus $G^{f\tau} = E^f / 2(1+\nu^f)$ equal to shear modulus of steel. In this model, perfect plasticity is generally considered, i.e. $H^{f\tau} = 0$.

- The volumetric participation of the fibers is obtained as the ratio between volume of the bars and total volume of the composite material.

3.2. Crack spacing and bond-slip length

3.2.1. Definition of the bond-slip zone

The length of bond-slip zone around of a crack or simply *bond-slip length or slipping length* $2L_s$ is defined as the distance described by the relative displacement between concrete and steel (Bazant & Cedolin 1980).

In reinforced concrete panels subjected to tension appears an important crack or *primary crack*, which induces the formation of small cracks around it or *secondary cracks* (Goto & Otsuka 1979). The region defined by the secondary cracks to each side of a primary crack is considered the *bond-slip or slipping zone* (Figure 3.1(b)). Also, the distance between consecutive primary cracks is denominated *crack spacing* (Figure 3.1(a)).

Since the secondary cracks around two consecutive primary cracks propagate without superposing themselves, the spacing among them d_c must be greater or equal than the length of slipping zone to both sides of a crack $2L_s$, i.e. $d_c \geq 2L_s$ (Figure 3.1(a)).

The bond-slip phenomenon causes an additional shear stress in the interface surface, due to the friction between the bar and the surrounding concrete which is called *bond shear stress* τ^c (Figure 3.1(b)).

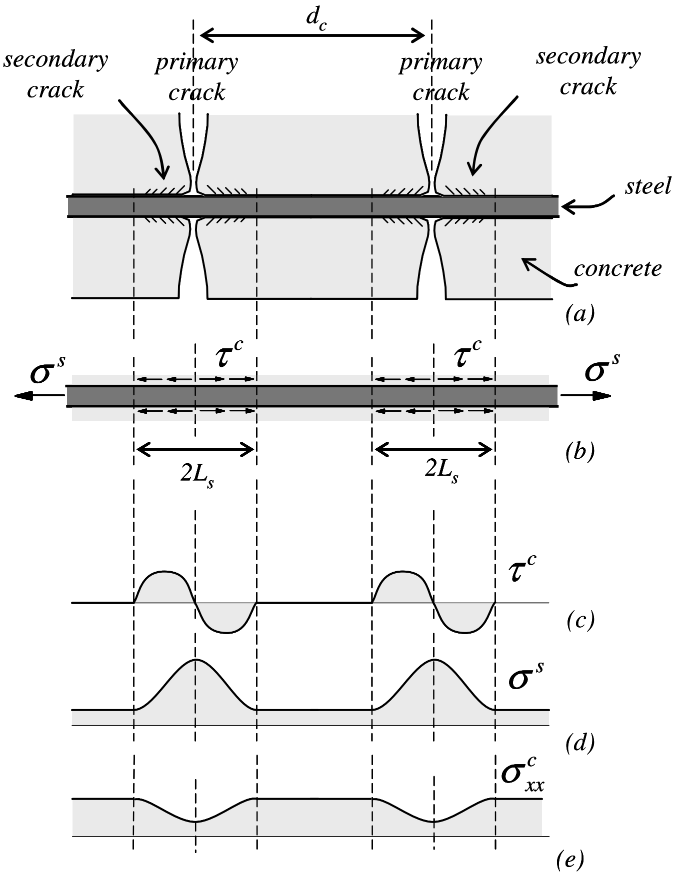

Figure 3.1. Bond-slip effect at neighbor of the primary cracks: (a) descriptive sketch, (b) stress on the bar, (c) shear stress on the concrete around of the bar, (d) axial stress in the steel, and (e) normal stress in the concrete.

By establishing the equilibrium of forces in an infinitesimal portion of reinforcement bar in which there are a slipping concrete-steel (Figure 3.2),

$$\tau = \frac{A^s}{p^s}\left(\frac{d\sigma^s}{dx}\right) = \frac{d}{4}\left(\frac{d\sigma^s}{dx}\right) \tag{3.1}$$

If the unique stress transferred to the bar is the friction due to slipping, in the earlier equation $\tau = \tau^c$ and τ will correspond to shear stress in the surrounding concrete to the reinforcement. In this case, the *bond shear stress* τ^c is proportional to the variation with respect to x of the axial stress in the steel σ^s. Figure 3.1(c) and (d) show the shear stress in the concrete near to the bar and the axial stress in the reinforcement steel. Around of every crack is observed that τ^c acts on the length $2L_s$ and $\tau^c = 0$ while σ^s remains constant in the perfect adherence zone between both materials.

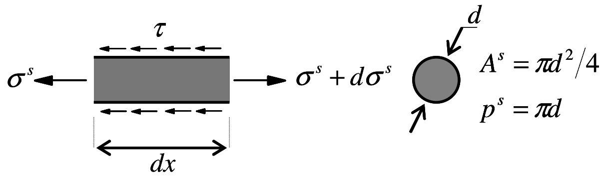

Figure 3.2. Free body diagram of an infinitesimal element of reinforcement bar.

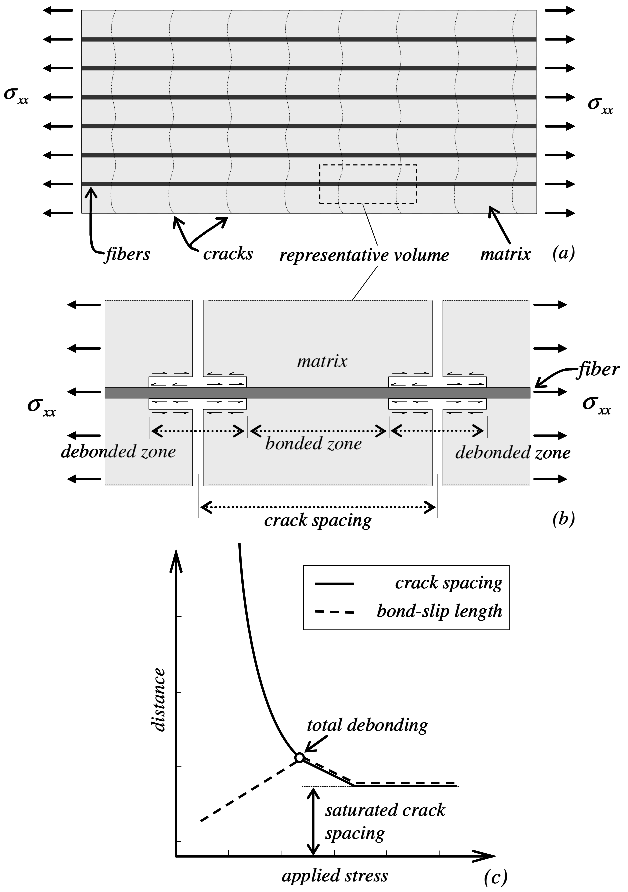

Figure 3.3. Composite material under tensile stress: (a) general sketch, (b) representative volume, (c)relationship between the bond-slip length, the crack spacing in the matrix and applied stress (Liao & Reifsnider 2000).

When a uniform horizontal displacement is applied in the end of a reinforced concrete panel (Figure 3.4(a)), the shear stress in the concrete is the result of the slipping effect of the reinforcement.

In some references (Hutchinson & Jensen 1990; Okabe, Komotori et al. 1999; Liao & Reifsnider 2000; Ogasawara, Ishikawa et al. 2001), appears the computation of the ultimate strength of a composite material reinforced with unidirectional fibers by means of a probabilistic model which represents the cracking in a representative volume (Figure 3.3(a) and (b)). Theses works study the crack spacing in the matrix and the slipping length while the load increases. Figure 3.3(c) shows that the load of total debonding is achieved when crack spacing is equal to the bond-slip length. For greater loads both lengths remain constant and equal to the *saturated crack spacing* (Liao & Reifsnider 2000), due to the impossibility of transference of stress between matrix and fibers.

3.2.2. Heterogeneous panel with elastic reinforcement in the center

This section describes the results of the numerical simulation of a reinforced concrete panel subjected to tension. The structural member has a length of L=500mm, a square cross section with height h=50mm and a steel bar located in his center with diameter d=10mm (Figure 3.4(a)). The displacement imposed in the free end δ is associated to the resultant forces F in the same end. The notch located on the right end of the panel has like purpose to induce the formation of the first crack, perturbing the initial homogeneous state of the strain field in a specific place. The following table shows the mechanical properties of concrete and steel.

Concrete	
Young's modulus:	$E^m =$ 27.35 Gpa
Poisson's ratio:	$\nu^m =$ 0.2
Fracture energy:	$G_f =$ 100 N/m
Tensile strength:	$\sigma_u^m =$ 3.19 Mpa
Steel	
Young's modulus:	$E^{fr} =$ 191.58 GPa

Table 3.1. Mechanical properties of the concrete and the steel.

The length of the panel and the level of applied load chosen for this example let observe the crack spacing and the slipping length.

The bond-slip zone around each crack is determined by the distribution of the bond shear stress in the interface concrete-steel. When a common displacement between the concrete and the steel is applied at the ends of the panel, the bond shear stress corresponds to the shear stress of the concrete surrounding the reinforcement bar.

In order to observe the major number of cracks that can be developed along panel, the elastic behavior of the steel and the perfect adherence fiber-matrix ($E_{tg}^{ir} \to \infty$) in composite material has been taken into account. On the other hand, in tension tests like this one, the stress state does not produce cracks in mode II of fracture, and therefore the dowel action disappears ($\gamma_{rs}^{f} = 0$).

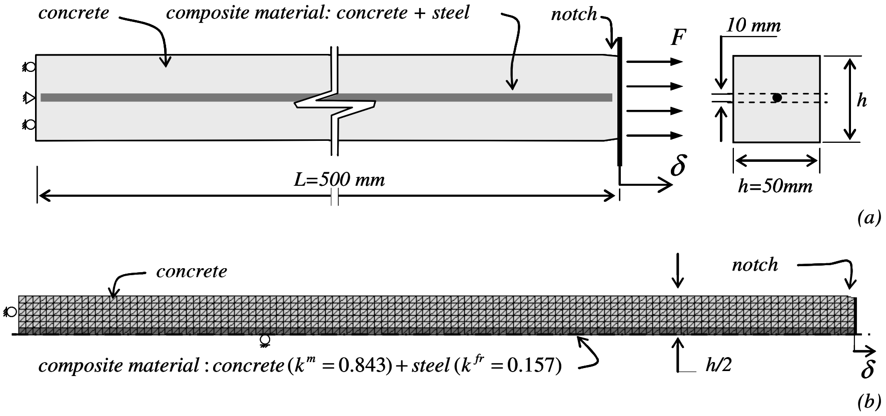

Figure 3.4. Numerical modeling of tension test with reinforcement in the center: (a) descriptive sketch, (b) finite elements mesh.

A reinforced concrete panel of 10mm x 50mm x 500mm is simulated in the *xy*-plane by means of a composite material model (Figure 3.4(a)); therefore, the stress field in the homogeneous material and the composite material are contained in the *xy*-plane, with which, a plane stress condition with a thickness equal to 50mm is considered.

Taking advantage of the symmetry of the problem, half panel was modeled with a structured mesh of 1000 linear triangular finite elements of 5mm side. In Figure 3.4(b), the bright gray corresponds to the simple concrete elements represented by a isotropic scalar damage model; on the other hand, the dark gray corresponds to the elements of composite material (concrete matrix and steel fibers), modeled according to the presented formulation.

The volumetric participation of the steel k^{fr} in a band of composite material of height $h_{mc} = d$ was obtained as the ratio between the volume of the reinforcement bar $V^{f} = L\pi d^{2}/4$ and the total volume of the band of composite material $V = L \cdot h \cdot h_{mc}$. Therefore, $k^{fr} = \pi d/4h = 0.157$.

The structural response of the panel (Figure 3.5(a)) is shown as the relationship between the average equivalent mean stress $\sigma = F/h^{2}$ divided by the tensile strength of the concrete σ_{u}^{m} and the displacement in the free end δ divided by the length of the panel *L*. In Figure 3.5(a), the next three stages are distinguished:

- *Stage I.* Elastic regime of both materials represented by the initial slope of the curve.

- *Stage II.* Degradation of the concrete without strain localization due to the presence of the steel.

- *Stage III.* Obvious strain localization in the zone of simple concrete of the panel; this stage is developed between the load step 1 to 7.

In the results of the numerical model, the crack spacing d_c is computed as the distance between two consecutive zones where the displacement contour lines have been concentrated, i.e., where strain localization has taken place. Figure 3.5(c) indicates the distances $d_{c(1)}$ and $d_{c(2)}$ as the spacing between cracks F1 and F2, and between the cracks F2 and F3, respectively. On the other hand, the slipping length can be measured by means of the distribution of the concrete shear stress in the interface (on the finite elements of composite material), to left and right of each crack: $2L_{s(1)}$ and $2L_{s(2)}$ (Figure 3.5(d)). The average value of this distance at a specific load step corresponds to summatory of slipping lengths $2L_{s(i)}$ divided by the amount of cracks.

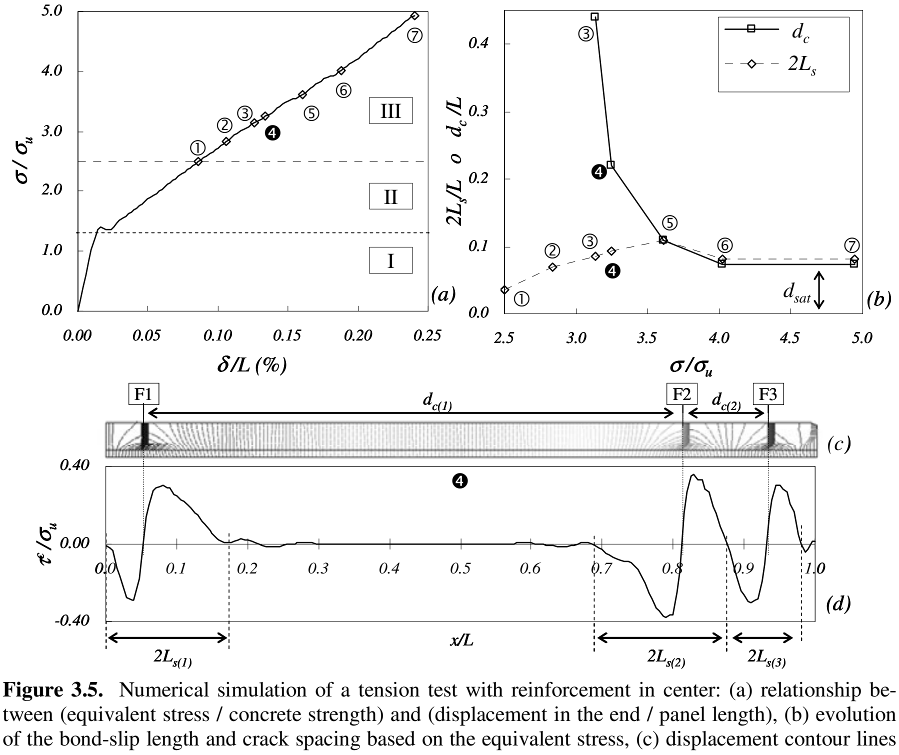

Figure 3.5. Numerical simulation of a tension test with reinforcement in center: (a) relationship between (equivalent stress / concrete strength) and (displacement in the end / panel length), (b) evolution of the bond-slip length and crack spacing based on the equivalent stress, (c) displacement contour lines and crack spacing for step 4, (d) shear stress along the panel in the composite material zone and bond-slip zone for step 4.

Figure 3.5(b) shows in 7 steps the evolution of the length of the slipping zone to both sides of a crack and the spacing among them, measured from the displacement contour lines (Figure 3.6) and the shear stress diagram of the neighboring concrete to the reinforcement (Figure 3.7). The distance d_c shown in Figure 3.5(b), is equal to the maximum value of the set of distances $d_{c(i)}$, where (i+1) is the amount cracks. The solid line indicates the variation of the average value of the slipping zone to both sides of a crack $2L_s$ and the dash line describes the evolution of the crack spacing d_c according to the equivalent stress $\sigma = F/h^2$. The distance d_c decreasing down to an inferior asymptote in the steps 6 and 7, called *saturated crack spacing* d_{sat} (Liao & Reifsnider 2000); this means in spite of the increase in the load level that a maximum amount of cracks is formed. On the other hand, the slipping zone grows progressively up to reach the same value of the crack spacing in load step 5. During steps 5 to 7, the two distances approximately remain equal until obtaining the condition of saturation of cracks; this corresponds with the behavior indicated in Figure 3.3(c).

> ***Remark 3.1*** *During the failure process of a tension panel reinforced in center, the amount of cracks and the slipping zone among them increase progressively. Nevertheless, after the total debonding between both materials has happened, the loss of stresses transference prevents the formation of new discontinuities in the concrete, maintaining constant spacing between the existing cracks. This stage denominates saturated crack condition.*

A single crack appears at steps 1 and 2, in which around a slipping zone is measured, although the distance between cracks does not exist yet (Figure 3.6(a)-(d)). From step 3 and during steps 4 and 5, more cracks are activated from the ends to center of panel (Figure 3.6(e)-(h) and Figure 3.7(a)-(b)). The distribution of the cracks remains constant from step 6, step in which the slipping zone of a crack limits with the slipping zone of neighboring crack such as the periodic behavior of the shear stress in Figure 3.7(c)-(f) indicates it.

The distances studied in this section qualitatively evolve in similar form as much in the numerical result shown in Figure 3.5(b) as in the model indicated in Figure 3.3 and presented in some references (Hutchinson & Jensen 1990; Okabe, Komotori et al. 1999; Liao & Reifsnider 2000; Ogasawara, Ishikawa et al. 2001).

> ***Remark 3.2*** *The localization process begins in the notched section as it is indicated at step 1; nevertheless, in other places of the panel quickly appear new cracks, relieving the concentration of the strain in the notch. This indicates that the spacing between cracks does not depend on the position of the disturbance.*

In the central strip of the panel the composite material does not show signs of strain localization, due to the presence of a part of reinforcement steel in elastic regime that delays the bifurcation time of the composite (Section 2.5).

For steps 5, 6 or 7, where $d_c \cong 2L_s$, the distribution of the concrete stress and steel stress in the strip of composite material is shown in Figure 3.8.

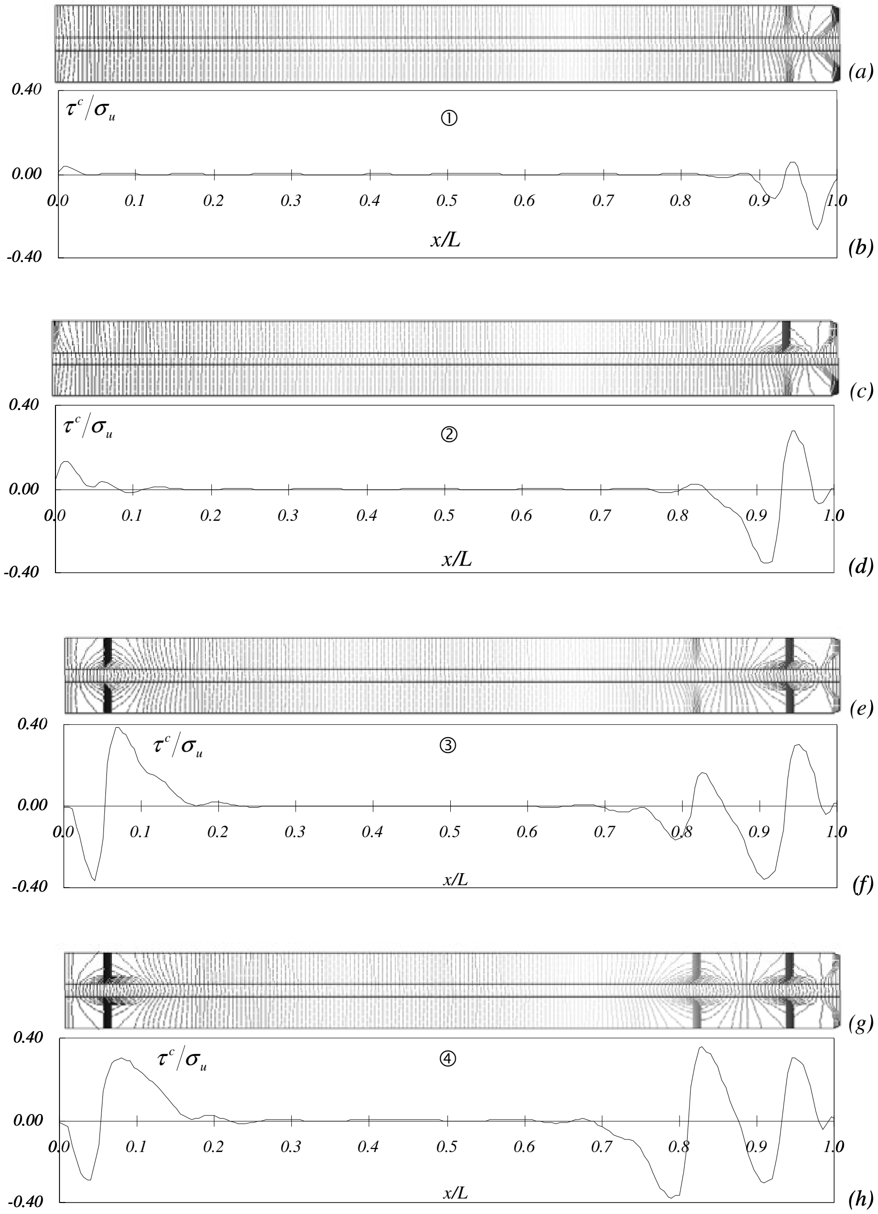

Figure 3.6. Numerical simulation of a tension test with reinforcement in center. Displacement contour lines and shear stress along the panel in the composite material zone: (a) and (b) for step 1, (c) and (d) for step 2, (e) and (f) for step 3, (g) and (h) for step 4.

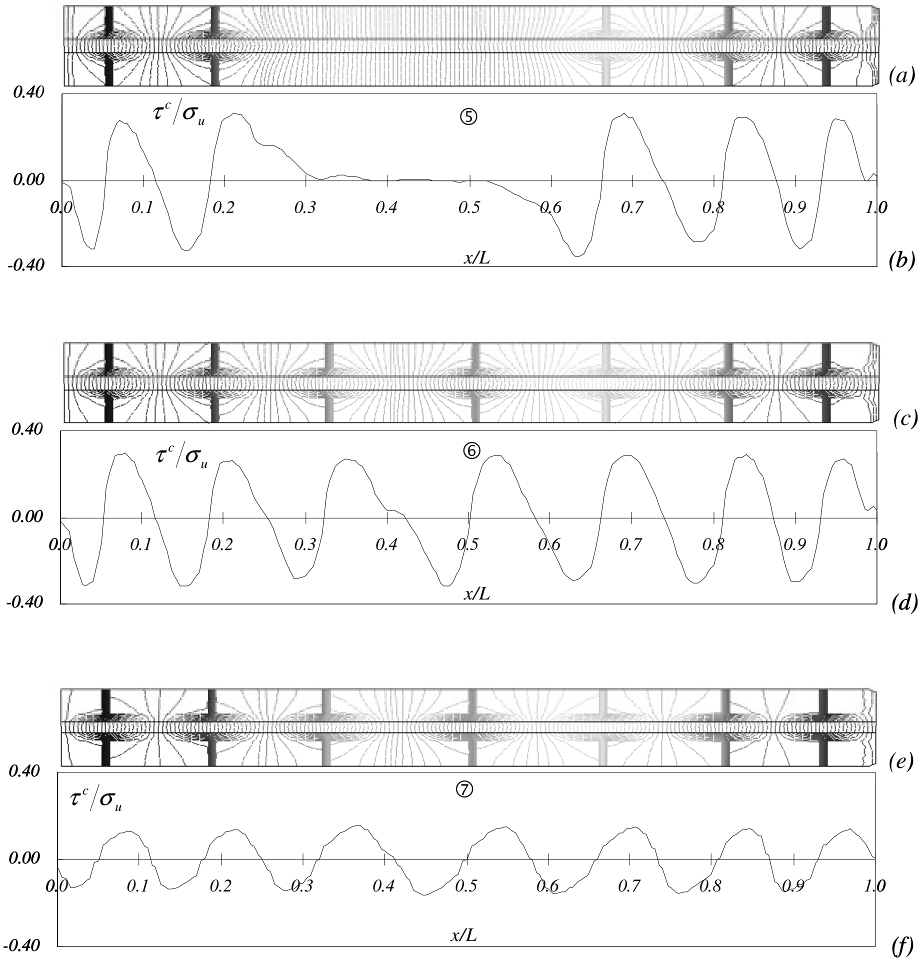

Figure 3.7. Numerical simulation of a tension test with reinforcement in center. Displacement contour lines and shear stress along the panel in the composite material zone (continuation): (a) and (b) for step 5, (c) and (d) for step 6, (e) and (f) for step 7.

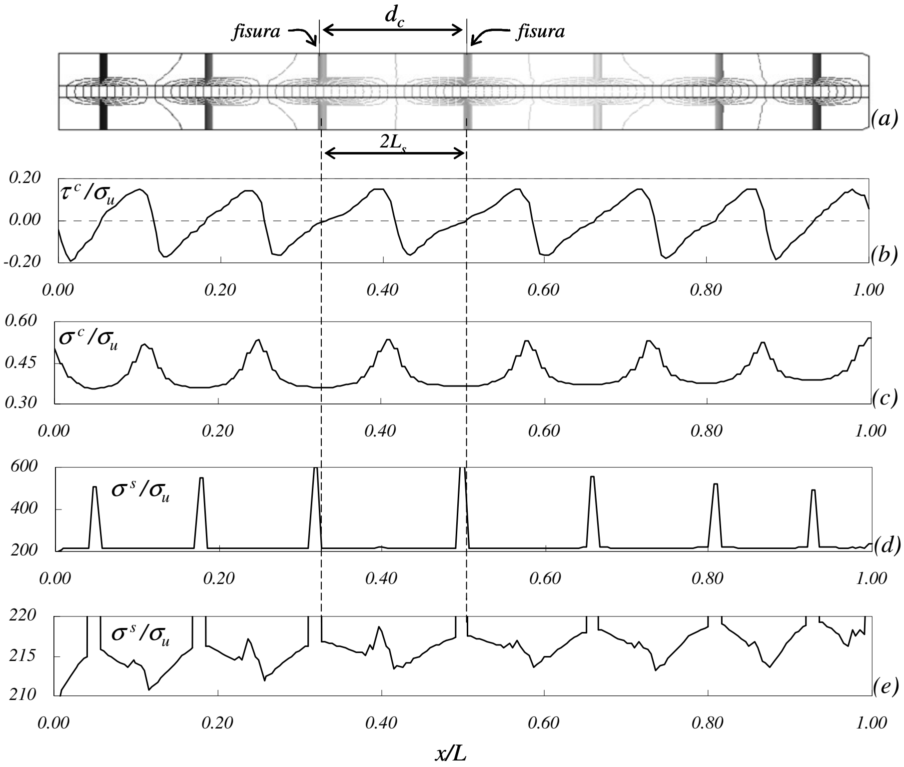

Figure 3.8. Numerical simulation of a tension test with reinforcement in center, for a load level in which d_c is equal to $2L_s$: (a) displacement contour lines, (b) shear concrete stress level, (c) axial concrete stress level, (d) axial steel stress level, (d) close up of axial steel stress level.

Almost constant crack spacing produces periodic results of the stress. The normal stress in the concrete σ^c is smaller in the nearby zones to each crack showing a smooth variation (Figure 3.8(c)). However, in the same zone the steel stress σ^s is bigger (Figure 3.8(d)), due to the strong increase of the concrete strain in the discontinuity over the strip of composite material.

To certain distance from a crack $0 < x \le L_s$, the concrete normal stress grows up to a maximum value, whereas the steel stress decrease down to a minimum value (Figure 3.8(e)). In a saturated crack condition as this is observed that the bonded zone between both materials disappears and consequently there is not a zone in which their stresses remain constant.

3.2.3. Comparison of results for meshes of different density

With the purpose of establishing the independence of the model with respect to the size of the element, the piece described in the previous section was simulated with a mesh of 4000 finite elements of 2.5mm of side that corresponds to the half size of the elements of the previous mesh (Figure 3.9).

The distribution of the cracks observed in the last load step, establishes an average spacing among them almost equal for both meshes, with a difference of the 3.8%, as shown in Figure 3.10(a) by means of the displacement contour lines.

Also, the relationship between the displacement imposed on the right end of the panel and summatory of forces in the same place divided by the area of the section (or also denominated average stress), is quite similar for the two meshes (Figure 3.10(b)).

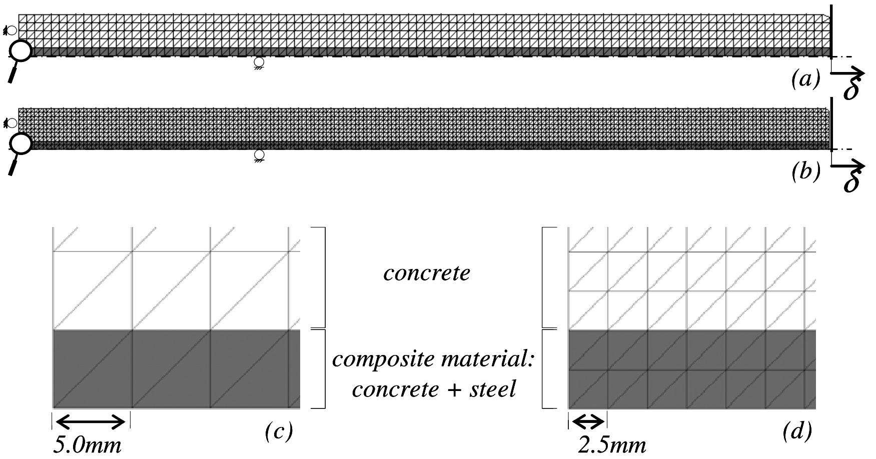

Figure 3.9. Numerical simulation of a tension test with reinforcement in center. General view and detail for meshes of different density: (a) and (c) mesh of 1000 elements, (b) and (d) mesh of 4000 elements.

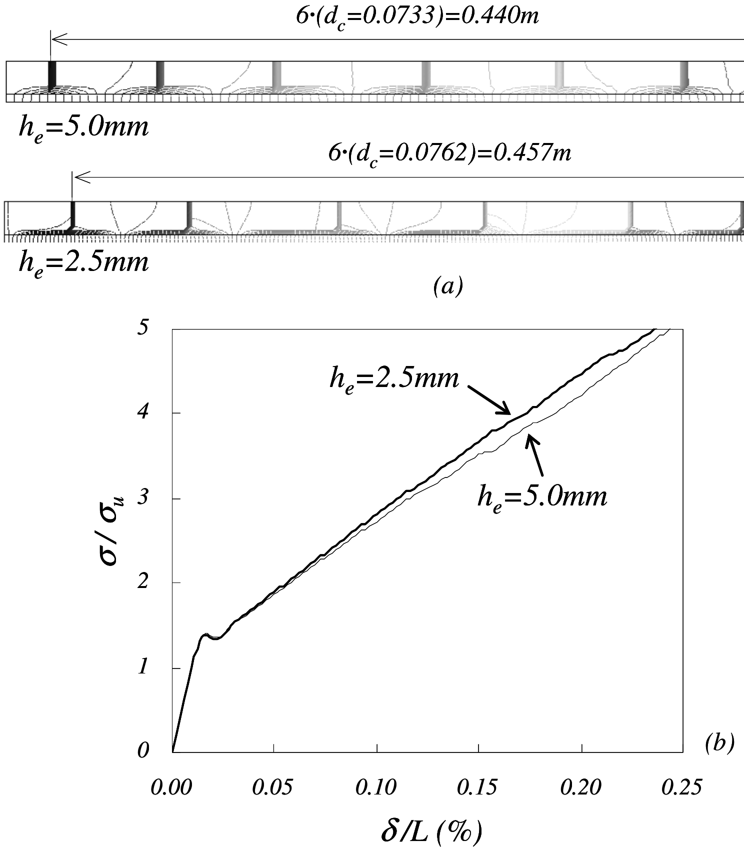

Figure 3.10. Numerical simulation of a tension test with reinforcement in center. Results with meshes of different density: (a) displacement contour lines and average crack spacing, (b) structural response.

3.2.4. Heterogeneous panel with elasto-plastic reinforcement in center

In this section, the results of a similar test to the earlier for loading states which produce steel plastic strain are presented.

Additionally to the mechanical characteristics shown in Table 3.1, a yielding stress in the steel $\sigma_y = 508$ MPa and a softening modulus $H^f = 0$ MPa (perfect plasticity) are assumed.

In Figure 3.11(a), the different stages of behavior of the panel are distinguished through the relationship between the imposed displacement and the equivalent stress in the free end. Subsequent to the elastic regime of both materials, the cracks in the concrete are developed in sequential form, as it was indicated in the previous test. From step 0 to step 1, the crack spacing remains constant (Figure 3.12). After step 1, the stiffness of the panel is lost because of the strain localization in the strip of composite material (Figure 3.11(b) and Figure 3.12).

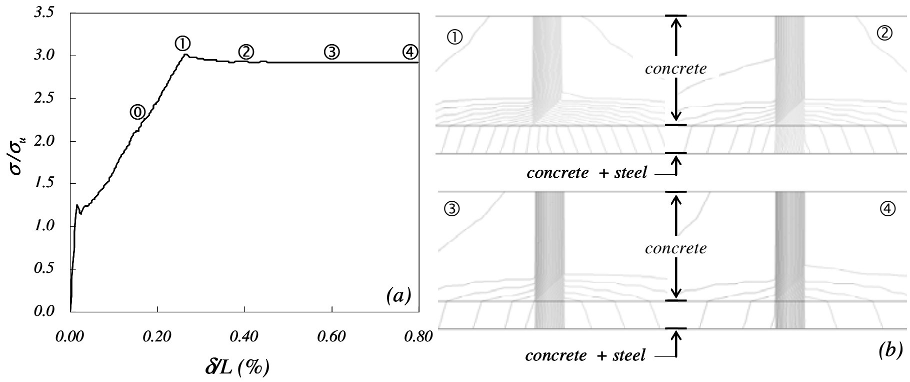

Figure 3.11. Numerical simulation of a tension test with reinforcement in center considering behavior elasto-plastic: (a) relationship (equivalent stress / concrete strength) versus (displacement in the end / panel length), (b) displacement contour lines at different steps in the zone F3 (Figure 3.12).

At step 2, the strain localization in the zone of composite material underneath each crack of the simple concrete is observed, maintaining approximately the same opening for the 7 consolidated cracks previously (Figure 3.13). At step 3 and in the zone of composite material, two of the cracks are unloaded and a greater opening of the other five cracks is produced. For the load level 4, the third crack from the left end (F3) shows a greater opening than the others and yet, the same five cracks of the previous step remain active. For greater load states this behavior is conserved due to the perfect plasticity regime of the steel.

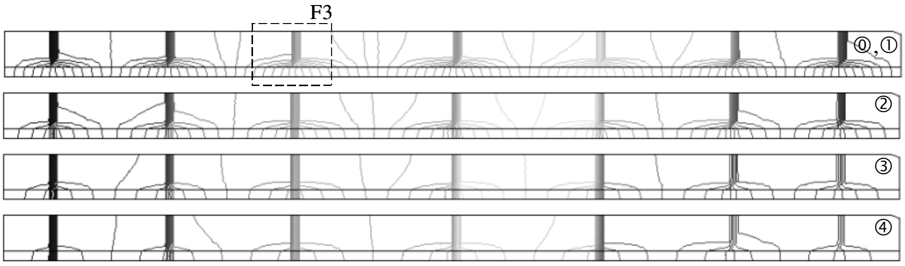

Figure 3.12. Numerical simulation of a tension test with reinforcement in center considering behavior elasto-plastic. Displacement contour lines at different load steps.

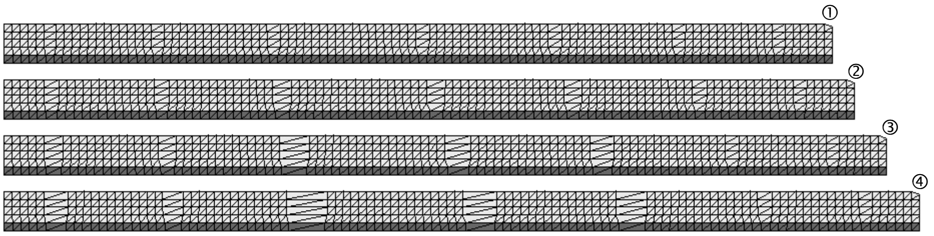

Figure 3.13. Numerical simulation of a tension test with reinforcement in center considering behavior elasto-plastic. Deformed shape of half panel at different load steps.

After obtaining the saturated crack spacing, new discontinuities are not formed, even in the plastic regime of fibers, in which case, some cracks have greater opening than others.

3.3. Numerical simulation of a heterogeneous reinforced concrete panel subjected to tension

The results of the numerical simulation with several meshes of a reinforced concrete panel subjected to tension tested by some authors (Ouyang & Shah 1994; Ouyang, Wollrab et al. 1997), are presented next. The member has 686 mm of length, 127 mm x 50.8 mm of rectangular cross section and a notch in center, as shown in Figure 3.14. The panel is reinforced with three steel bars of 9.5 mm in diameter, completely embedded in the concrete and distributed of homogeneous form in the cross section.

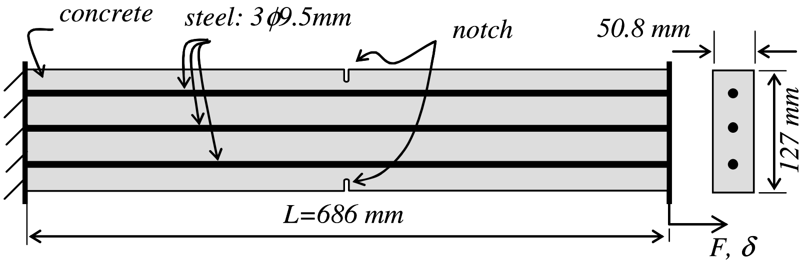

Figure 3.14. Numerical simulation of a tension panel. Descriptive sketch.

The mechanical properties of the component materials are as follows:

Concrete	
Young's modulus:	$E^m = 27.35$ GPa
Poisson's ratio:	$\nu^m = 0.2$
Fracture energy:	$G_f = $ 100N/m
Tensile strength:	$\sigma_u^m = $ 3.19mpa
Steel	
Young's modulus:	$E^{fr} = 191.6$ GPa
Yielding stress:	$\sigma_y^{fr} = 508.0$ MPa
Softening modulus:	$H^{fr} = 0$ GPa

Table 3.2. Mechanical properties of the concrete and the steel.

The phenomenon adherence between the matrix and fibers is characterized by means of the results obtained in a pull-out test of fiber of 0.5mm in diameter and 25.4mm in embedded length (Naaman, Namur et al. 1991). For this test, the maximum force P_{max}^i=0.061kN and the approximate slope of the force-displacement curve (P^i/δ^i) is between 8.01kN/mm (45000lb/pul) and 9.26kN/mm (52000lb/pul). According to the model of bond-slip effect described in Section 2.2.3, the value of the bond-slip modulus E^{ir} will be between 1111.GPa and 1283.GPa, and the stress of adherence loss will be equal to σ_{adh}^{ir}=311.1 MPa. Therefore, the tangent modulus in elastic regime of the slipping fiber model E^{dr} will be between $0.85E^{fr}$ and $0.87E^{fr}$ (Section 2.2.4). In the following section the results obtained for both adherence conditions are presented.

The dowel action can be neglected due to the axial character of the test where the mode I of fracture prevails.

3.3.1. Non-homogeneous mesh of finite elements of medium density

The mesh has linear triangular finite elements of two types as shown in Figure 3.15(a). The elements indicated in dark gray represent the composite material modeled with the proposed formulation, which is conformed by 84.34% of concrete and 15.67% of steel fibers. The elements in bright gray describe the simple concrete as a homogeneous material which obeys to an isotropic scalar damage model.

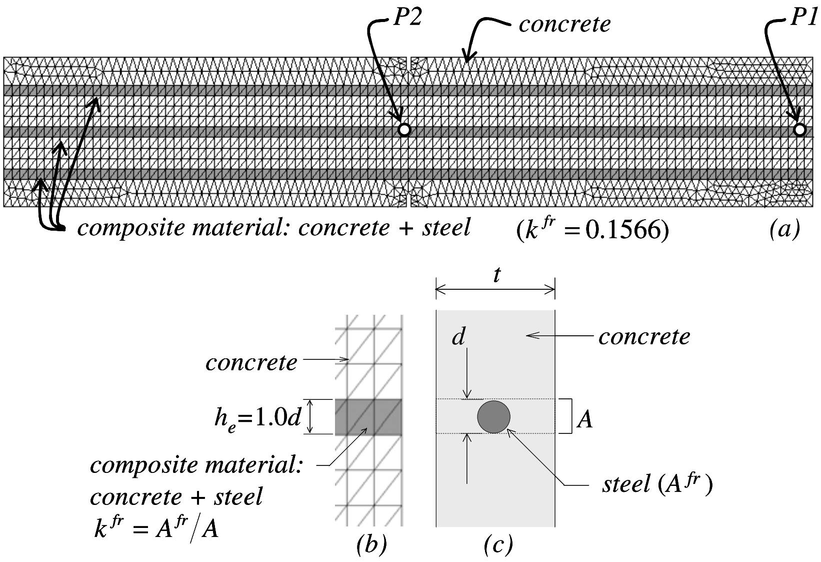

Figure 3.15. Numerical simulation of a tension panel. Non-homogeneous mesh of medium density: (a) finite elements mesh, (b) detail of a strip of finite elements of composite material, (b) detail of the cross section of a panel in the zone around a reinforcement bar.

With comparative aims this mesh has been denominated non-*homogeneous mesh of medium density*, in which, the height of the finite elements of composite material is equal to the diameter of the bar (Figure 3.15(b)-(c)), i.e. $h_e = 1.0d$.

Figure 3.16 shows displacement contour lines for different load levels indicated in the force *vs* displacement curve (Figure 3.17). Step 1 marks the beginning of the strain localization around the notch; however, after few increases of load, at step 2, new zones of localization appear along the panel. At step 3 several cracks appear in the upper and bottom zone of the panel, maintaining a characteristic spacing among them. Reaching this load step, the strain localization in the concrete between the bands of composite material is not perceived, which indicates a confinement effect given by the surrounding reinforcement. The loss of structural stiffness observed from step 4 is associated with the adherence loss between the steel bars and the concrete, modifying the cracks distribution in the panel. In fact, at step 4 new cracks appear where the concrete is surrounded by the composite material. In last step three cracks appear; one of them is located under the notch crossing completely the panel.

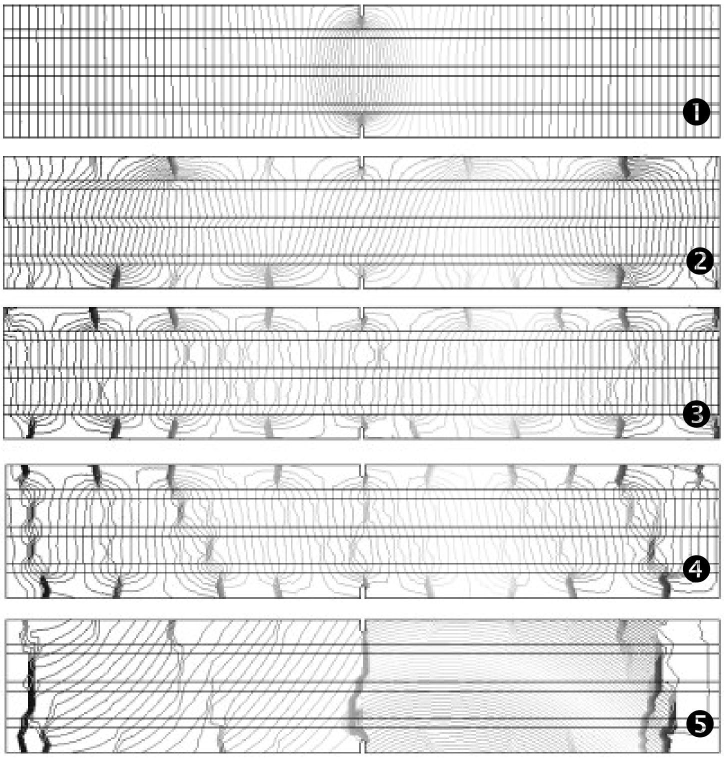

Figure 3.16. Numerical simulation of a tension panel. Displacement contour lines at different load steps.

The structural response obtained of the numerical analysis is near to the experimental results as shown in Figure 3.17. The gray region represents the experimental values and the two solid lines correspond to the numerical results for an elastic modulus of the slipping fiber model between 85% and 87% of Young's modulus of the steel.

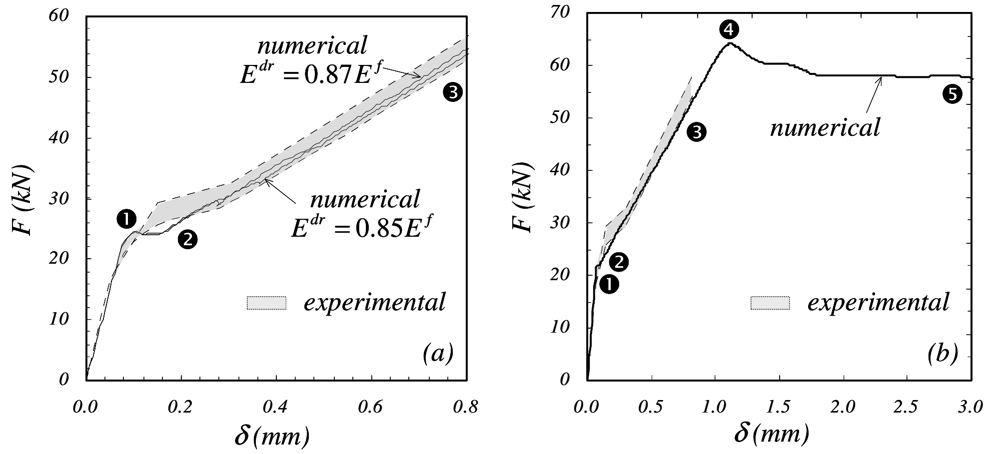

Figure 3.17. Numerical simulation of a tension panel. Relationship between force and displacement: (a) close-up, (b) whole curve.

The simple concrete presents a stage of stable damage where several cracks maintain constant spacing and opening, provided by the capacity of the reinforcement and the adherence in the interface. When such adherence is lost (or in some cases when the plastic regime of the steel begins), the structural capacity decays while the opening of a single crack prevails.

The evolution of matrix and fibers stress in the composite material zone is described by means of the stress-displacement curve displayed in Figure 3.18 (in the points *P1* and *P2* indicated in Figure 3.15). The point *P1* located in the right end of the panel does not present strain localization, however, the point *P2* located in the reduced cross section is part of one of the cracks formed at step 5 (Figure 3.16).

The matrix normal stress in x-direction (Figure 3.18(b)) is conserved almost constant from the beginning of the damage at step 1 to the maximum load at step 4 approximately, due to the elastic stiffness provided by the fibers that freezer the degradation of the matrix in the composite material. For greater values of the displacement δ, such stress is reduced of very smooth form in the point *P1* and of strong form in the point *P2*, until reaching zero value; this difference occurs by the strain localization presented in *P2* and the absence of her in *P1*.

In the fiber (Figure 3.18(a)), the axial stress increases up to the condition of total loss of adherence (or to the yielding condition in the case of perfect adherence), from which, the stress remains almost constant. The difference between the stresses in the points *P1* and *P2* after step 4, obeys to the variation of the stress state in the panel induced by the notch and the phenomenon of strain localization. This is reflected in the composite material stress shown in Figure 3.18(c).

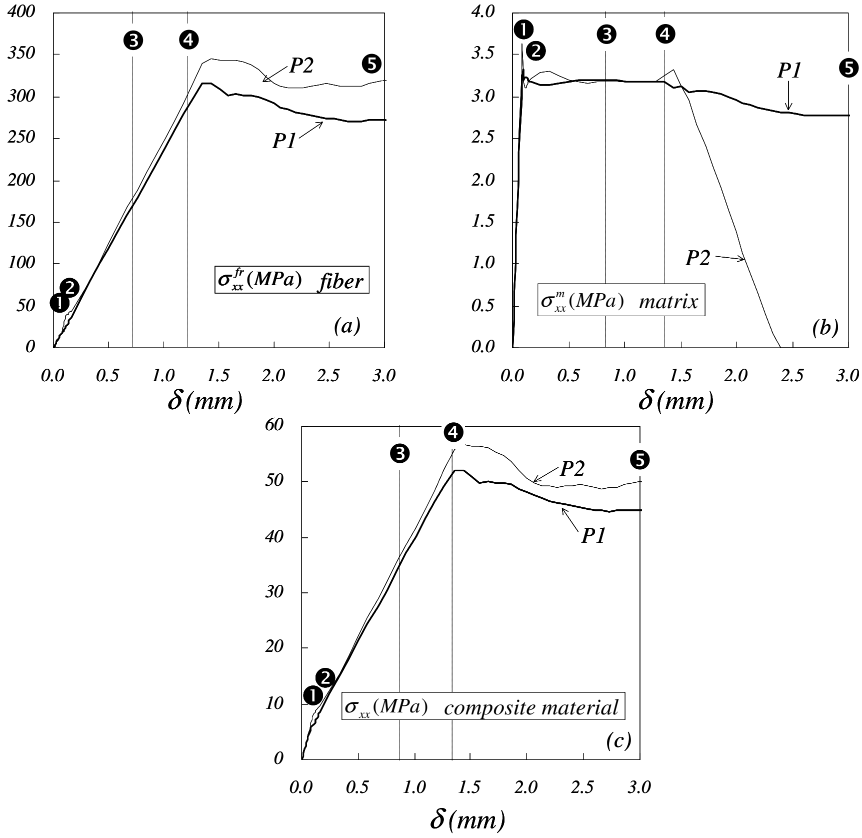

Figure 3.18. Numerical simulation of a tension panel. Evolution of the stress in the concrete matrix and steel fibers in the points *P1* and *P2* of the composite material zone: (a) fiber axial stress, (b) matrix normal stress in x-direction, (c) composite material normal stress in x-direction.

3.3.2. Comparison between non-homogeneous meshes of different density

The tension panel shown in Figure 3.14(a) is modeled with four structural meshes of linear triangular elements of average height h_e equal to 2.8d, 2.0d, 1.0d y 0.5d. The reinforced zones of the panel are represented by strips of finite elements where the volumetric participation of the steel depends on the height of the strip h_e, as showm in Figure 3.19.

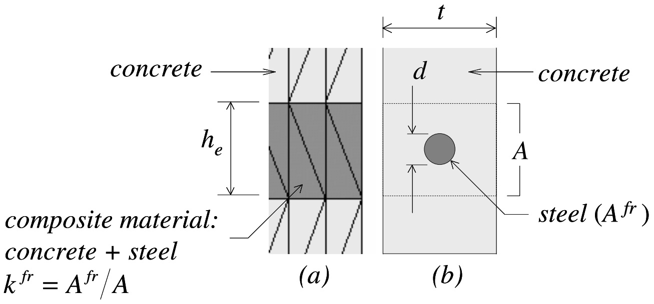

Figure 3.19. Numerical simulation of a tension panel: (a) detail of a strip of finite elements of composite material, (b) detail of the cross section of the panel in the surrounding zone to a reinforcement bar.

For different meshes, Figure 3.20 shows the central strip of finite elements of composite material and Table 3.3 indicates their general features.

mesh	elements	nodes	h_e/d	k^{fr}	$F_{\max}(kN)$
very coarse	1026	622	2.8	0.0542	77.2
coarse	1430	826	2.0	0.0783	75.0
medium	2872	1558	1.0	0.1566	72.6
fine	4746	2508	0.5	0.1566[3]	70.7

Table 3.3. Numerical simulation of a tension panel. Characteristics of the meshes

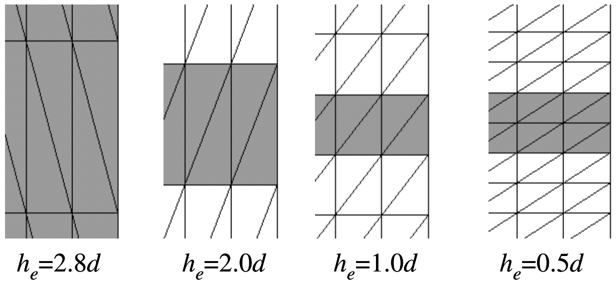

Figure 3.20. Numerical simulation of a tension panel. Detail of the central strip of finite elements of composite material for the different meshes.

In the very coarse mesh shown in Figure 3.21(a), the strip of finite elements of composite material includes all the bars of the panel, having almost homogeneous to the represented material (Figure 3.21(a)).

---

[3] The coefficient of volumetric participation is the same in the medium and fine mesh because the strip height of the composite material is common, although the fine mesh contains two rows of elements and the medium mesh contains only one.

The displacement contour lines for the meshes with h_e equal to 2.8d, 2.0d y 0.5d, shown in Figure 3.21(b), Figure 3.22(b) and Figure 3.23(b) respectively, allow distinguishing the two following stages:

- In the former, several cracks in the simple concrete successively appear until reaching a characteristic spacing among them. This stage finishes before reaching the maximum load of the test (at step 4 shown in Figure 3.24).
- In the latter, the strain localization appears in different points of the composite material until a single crack is formed through the cross section of the panel. This phase begins with a strong loss of structural stiffness subsequent to the maximum load (at step 5 shown in Figure 3.24). The same crack pattern is maintained when structural stiffness tends to zero.

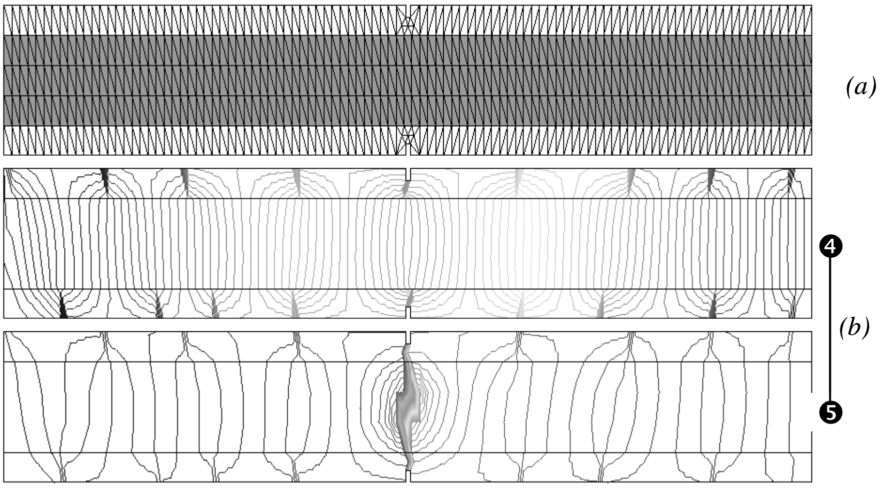

Figure 3.21. Numerical simulation of a tension panel. Modeling with finite elements of h_e=2.8d: (a)finite elements mesh, (b) displacement contour lines in step 4 and 5.

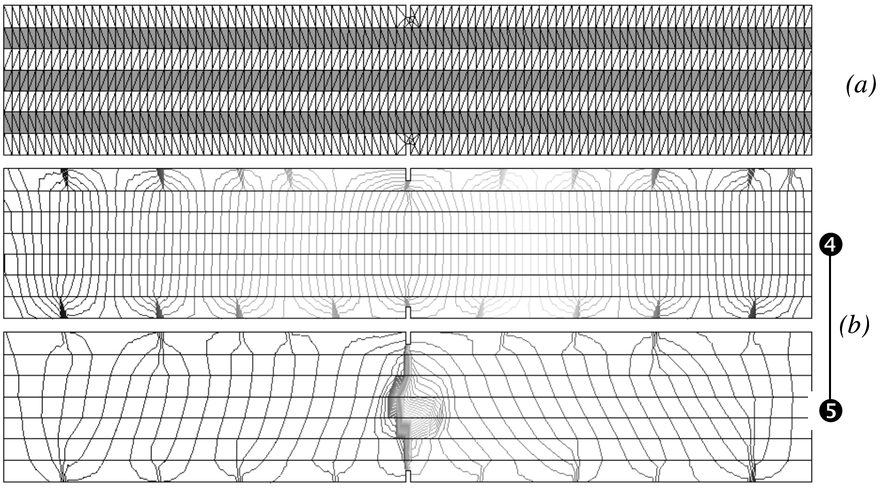

Figure 3.22. Numerical simulation of a tension panel. Modeling with finite elements of h_e=2.0d: (a)finite elements mesh, (b) displacement contour lines in step 4 and 5.

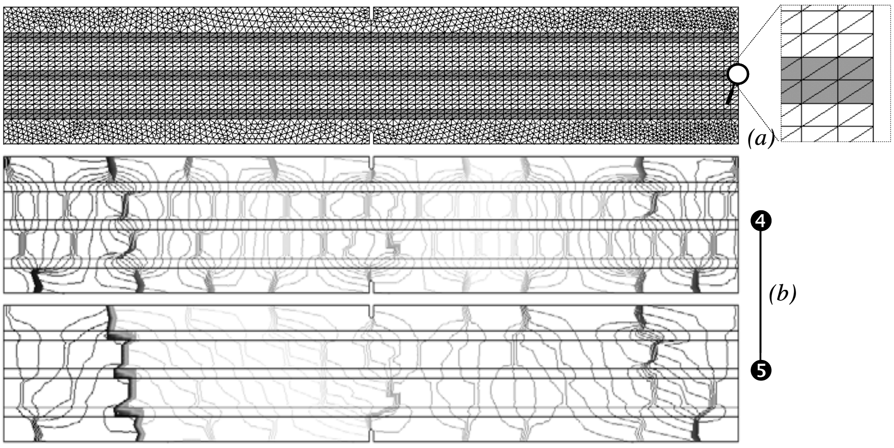

Figure 3.23. Numerical simulation of a tension panel. Modeling with finite elements of h_e=0.5d: (a)finite elements mesh, (b) displacement contour lines in step 4 and 5.

Figure 3.24 shows the response structural obtained of the numerical simulation of the panel with the four meshes previously described. In the coarse meshes, the oscillations of the force *vs* displacement curve (between steps 4 and 5), obey to the use of finite elements of greater size than the characteristic length of the composite material (Huespe, Oliver et al. 2006). Nevertheless, the solutions given by the meshes of h_e=2.8d, h_e=2.0d, converge to the curves of the finer meshes.

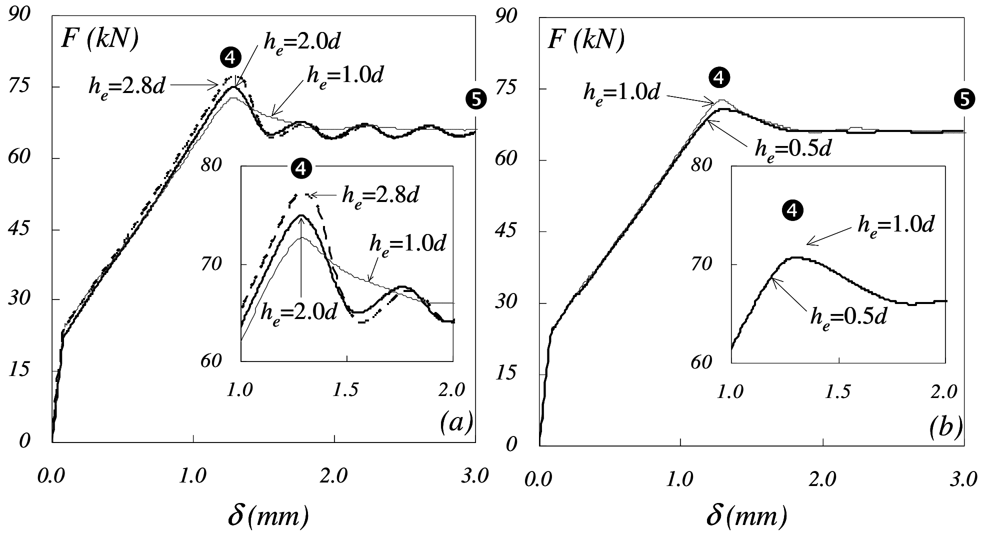

Figure 3.24. Numerical simulation of a tension panel. Comparison of the structural response for meshes of different density: (a) meshes with h_e=2.8d, h_e=2.0d and h_e=1.0d, (b) meshes with h_e=1.0d and h_e=0.5d.

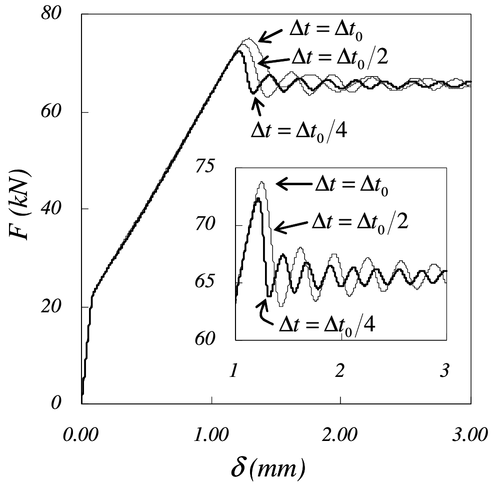

Figure 3.25. Numerical simulation of a tension panel with a mesh of h_e=2.0d. Comparison of the structural response for different sizes of the pseudo-time step.

For the mesh with average size of element h_e=2.0d, Figure 3.25 indicates the slight reduction of the amplitude of these oscillations according to the size of the pseudo-time step.

On the other hand, the maximum load undergoes variations smaller than 9%, according to the size element, as it is indicated in Table 3.3.

Finally, the comparison among meshes of different density shows the independence of the results with respect to average size of the finite element.

3.4. Lightly reinforced beams of three points

In this work a lightly reinforcement beam with two different steel ratios tested by some authors (Ruiz, Elices et al. 1998), was numerically modeled. The adherence level of the interface was characterized by a pull-out test presented in the earlier reference (Ruiz, Elices et al. 1998).

Two beams simply supported of 1200mm of length and 50mm x 300mm of cross section are loaded with a force *P* in mid-span as it is shown in Figure 3.26. The Beam-I is reinforced with four corrugated bars of 2.5mm of diameter that represents a 0.13% steel ratio (Figure 3.26(b)). However, the Beam-II has two bars of the same diameter and therefore, a 0.065% steel ratio. The features of the concrete and steel are presented in Table 3.4.

Concrete	
Young's modulus:	$E^m = 29.0$ GPa
Poisson's ratio:	$\nu^m = 0.2$
Compression strength:	$\sigma_u^m = 38.\ 0$ MPa
Fracture energy:	$G_f = 62.5$ N/m
Tensile strength:	$\sigma_u^m = 3.80$ MPa
Steel	
Young's modulus:	$E^{fr} = 162.0$ GPa
Softening modulus:	$H^{fr} = 0$ GPa
Yielding stress:	$\sigma_y^{fr} = 587.0$ MPa

Table 3.4. Numerical simulation of lightly reinforced beams of three points. Mechanical properties of the component materials.

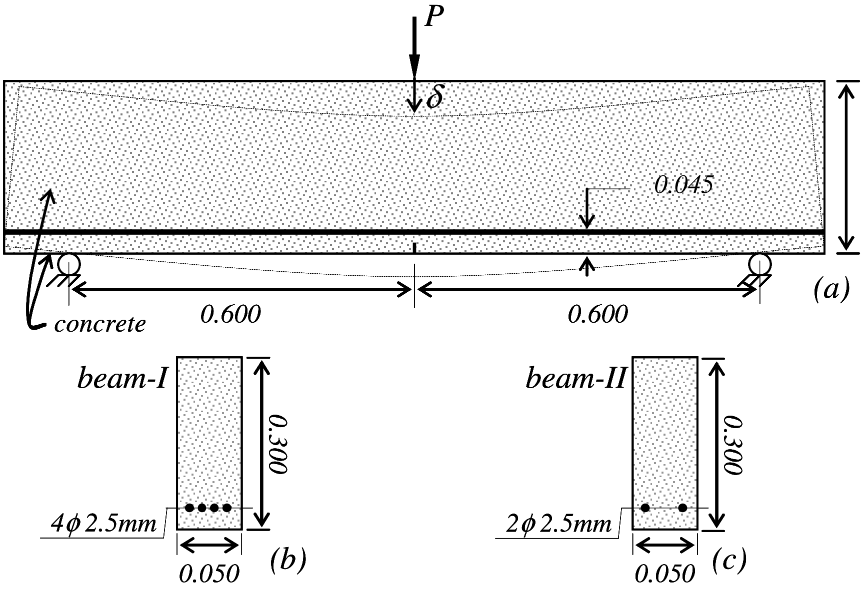

Figure 3.26. Numerical simulation of lightly reinforced beams of three points. Descriptive sketch: (a)geometry and loads on the beam, (b)cross section of Beam-I (0.13% of reinforcement ratio), (c)cross section of Beam-II (0.065% of reinforcement ratio).

The mechanical properties of the interface determine by the pull-out test (Ruiz, Elices et al. 1998), in which a corrugated bar is extracted from a concrete block. The bar embedded in the concrete has 2.5mm of diameter and 150mm of length. The experimental curve that relates to the force and the slip in the fiber, is approximately straight line with slope (P^i/δ^i) =20.0 kN/mm, until a maximum load P_{max}= 2.8kN. According to the bond-slip model described in the Section 2.2.3, the value of the bond-slip modulus E^{ir} will be equal to 611.1GPa and the stress of adherence loss will be σ^{ir}_{adh} =570.4mpa. The tangent modulus in elastic regime of the slipping fiber model will be E^{dr} = 128.1GPa.

In the numerical simulation, a damage model with degradation in tension and compression is used for represent the elements of simple concrete (Section 2.2.1), however, the formulation presented for composite materials is used in the zone of the reinforcement. The beam is discretized into linear triangular finite elements of simple material in bright gray and elements of composite material in a dark gray strip (Figure 3.27(a)).

With this formulation, elements of composite material greater than the real diameter of fibers can be used without loss of approach in the structural response of the problem. In this case the strip of finite elements of reinforced concrete is 4 times higher than the diameter of the reinforcement (Figure 3.27(b)-(d)).

Remark 3.3 *In spite of the symmetry of the problem, the complete beam was modeled avoiding that the boundary conditions in the symmetry axis are located on of the discontinuity path.*

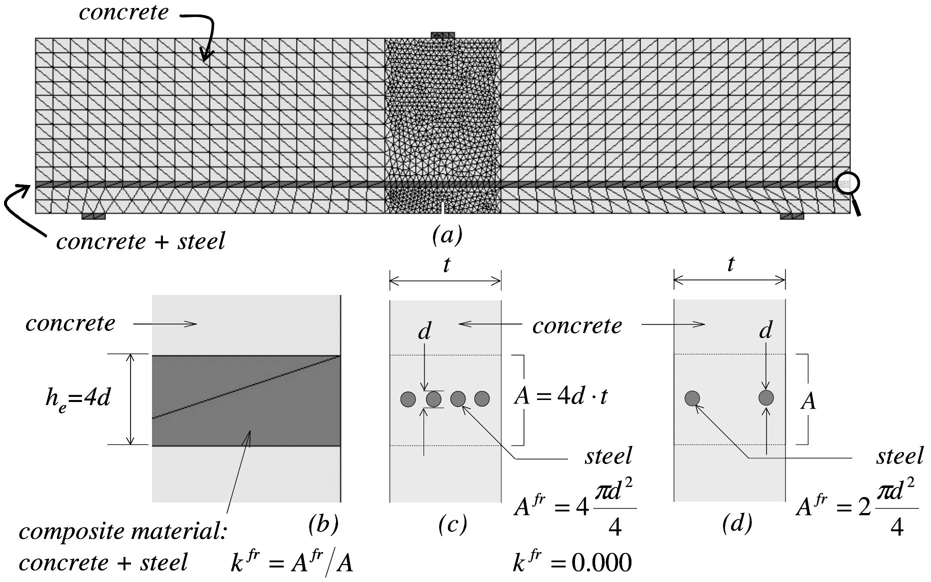

Figure 3.27. Numerical simulation of lightly reinforced beams of three points: (a) finite elements mesh, (b) detail of a finite element of composite material, (c) and (d) detail of the reinforced zone in the cross section of the Beam-I and Beam-II, respectively.

3.4.1. Beam-I (reinforcement ratio equal to 0.13%)

Four reinforcement bars of the Beam-I represent 0.13% of the cross section and also determining a volumetric participation factor $k^{fr} = 0.0393$ in each finite element of composite material (Figure 3.27(c)).

Figure 3.28(a) shows the structural response and the relationship between the load applied and mid-span displacement. The gray region delimits the experimental results and the solid line describes the numerical solution obtained.

The finite elements belonging to different crack pattern at the last load step are displayed in Figure 3.28(b). The value of –1 corresponds to the elements that are crossed by the primary crack and the other negative integer numbers of –2 to –20 indicate the elements associated with small secondary cracks that appear around the reinforced zone.

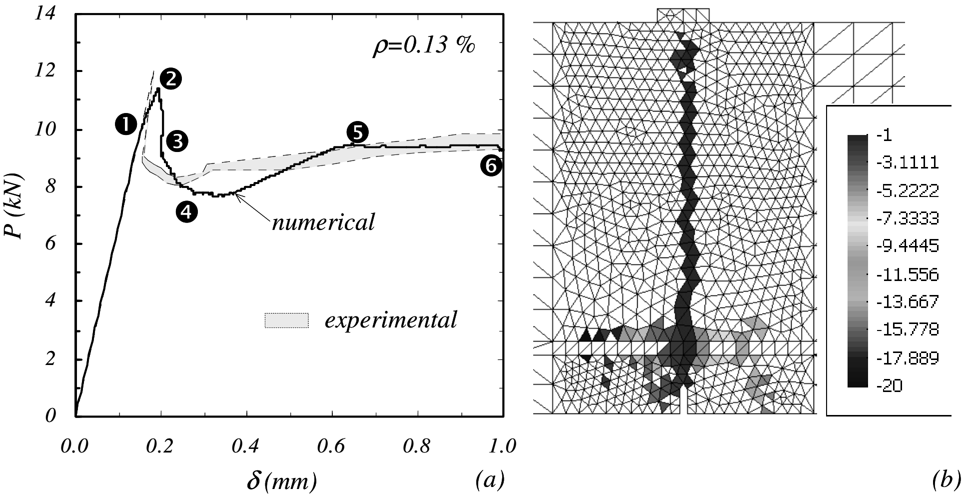

Figure 3.28. Numerical simulation of lightly reinforced beams of three points: (a) structural response, relationship between the load applied and the mid-span displacement, (b) Material bifurcation in the finite elements belonging to different crack pattern at the last load step (each negative integer between -1 and -20 indicates a crack path).

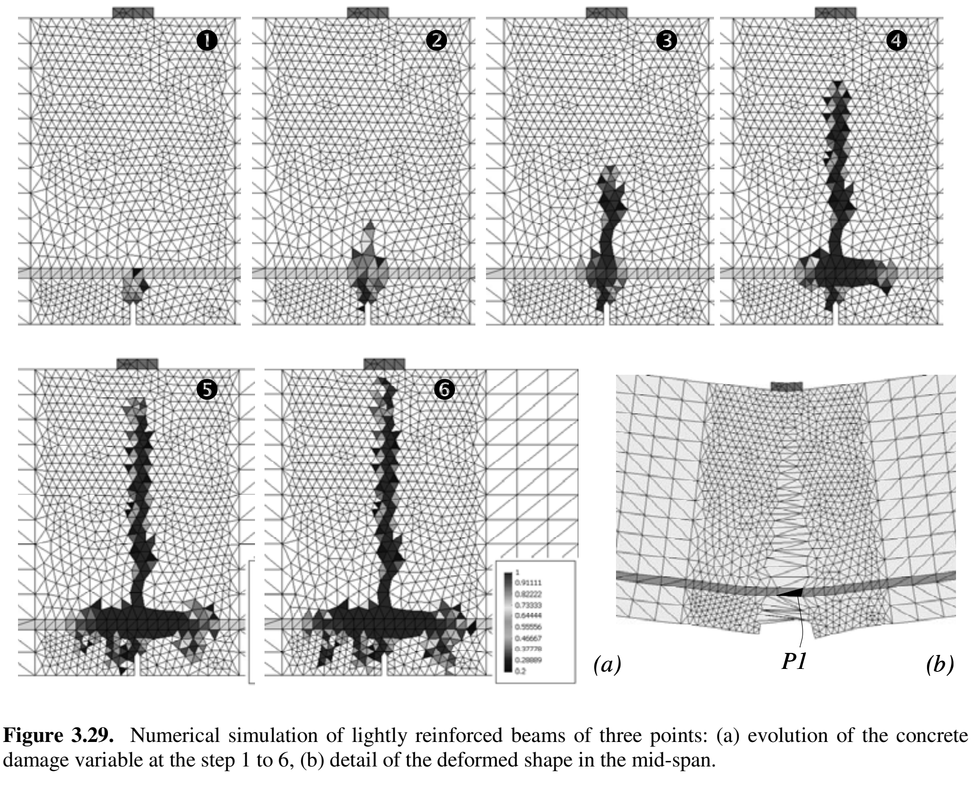

Figure 3.29. Numerical simulation of lightly reinforced beams of three points: (a) evolution of the concrete damage variable at the step 1 to 6, (b) detail of the deformed shape in the mid-span.

Next the evolution of the material failure of the beam is described at six load step according to the structural response shown in Figure 3.28(a), the damage variable of the concrete indicated in Figure 3.29(a) and the displacement contour lines drawn in Figure 3.31.

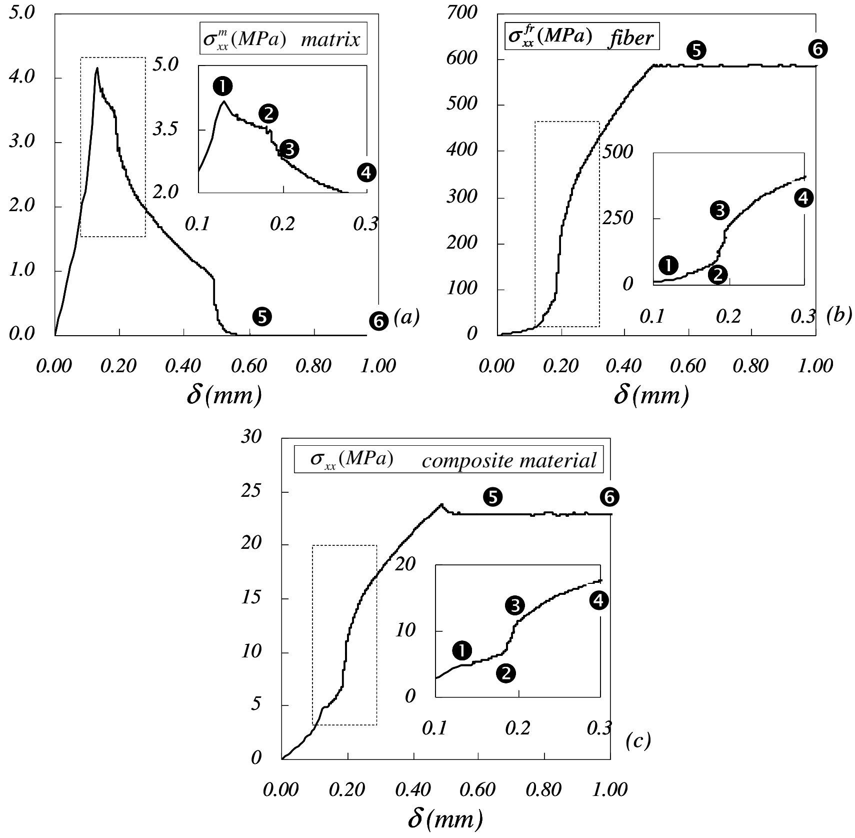

Figure 3.30. Numerical simulation of lightly reinforced beams of three points. Evolution of the stress in the concrete matrix and steel fibers in the *P1* point of the zone of composite material: (a) matrix normal stress in x-direction, (b) fiber axial stress, (c) composite material normal stress in x-direction.

Figure 3.30 illustrates the evolution of the normal stress in x-direction, on the element of composite material *P1* (Figure 3.29(b)), discriminating between the behaviors of the concrete matrix and the steel fibers.

From step 1 the strain localization begins on the notch to step 2, in which the crack is propagated to the inferior face of the composite material zone and the maximum load of the beam is reached. From this step, a negative slope in the force-displacement curve of the panel is observed as a product of the degradation of the matrix in the composite material elements being part of the crack (Figure 3.30(a)).

At step 3, the crack has already crossed the reinforcement; nevertheless, the strain localization in the homogeneous material over the strip of composite material is far smaller than below it. Two zones of maximum damage in the concrete are distinguished as well: the end of the crack and the neighborhood of the reinforcement bar.

At step 4, the strain localization and the highest levels of damage occuring in vertical direction to the notch define the primary crack path; whereas, the reinforced concrete elements where the damage variable is not equal to zero represent the secondary cracks. From this step the beam acquires a positive stiffness as a result of the total degradation of the simple concrete on the crack path (Figure 3.29(a)) and of the still elastic behavior of the reinforcement steel (Figure 3.30(b)).

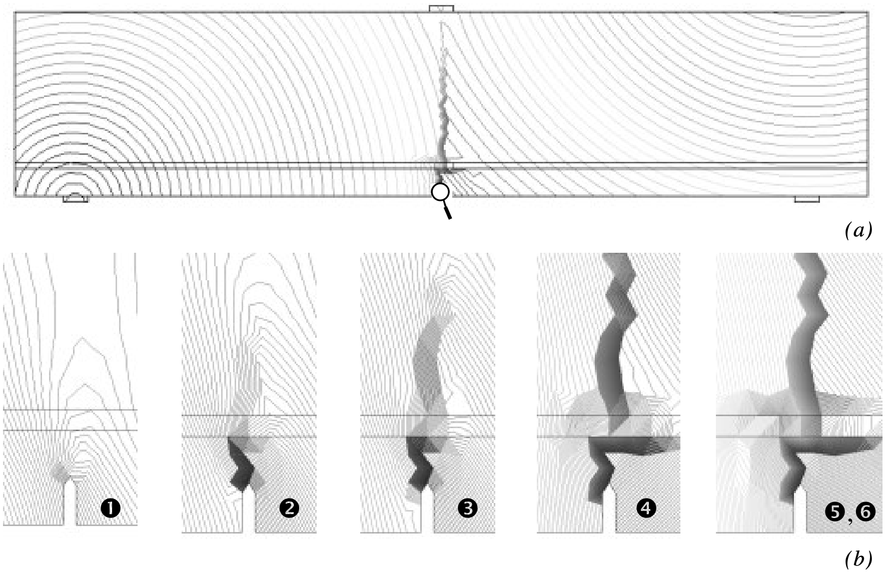

Figure 3.31. Numerical simulation of lightly reinforced beams of three points: (a) displacement contour lines in whole beam for the last load step, (b) detail of displacement contour lines for step 1 to 6 indicated in Figure 3.28(a).

In step 5, the stress of the slipping fiber model reaches a maximum value determined by the adherence conditions, producing a strong localization in the zone of composite material crossed by the primary crack (Figure 3.31(b)), as well as, the maximum levels of damage propagate on the strip of reinforced concrete to the sides of the primary crack. This condition is conserved up to step 6.

3.4.2. Beam II (reinforcement ratio equal to 0.065%)

In a second analysis, a beam with the same characteristics of the previous test with the exception of the reinforcement ratio was modeled. In this case, the beam has two bars of 2.5mm in diameter that represent a reinforcement ratio equal to 0.065% (Figure 3.26(b)) and a volumetric participation factor $k^{fr} = 0.0196$ (Figure 3.27(d)).

The structural response of the beam appears in Figure 3.32(a), where the gray region indicates the experimental result (Ruiz, Elices et al. 1998) and the solid line establishes the numerical solution.

At the last load step, a primary crack path ascending vertically from the reinforced zone is indicated with *-1* in Figure 3.32(b); the other crack paths around the reinforcement propagate very little in comparison with the previous test (reinforcement ratio equal to 0.13%).

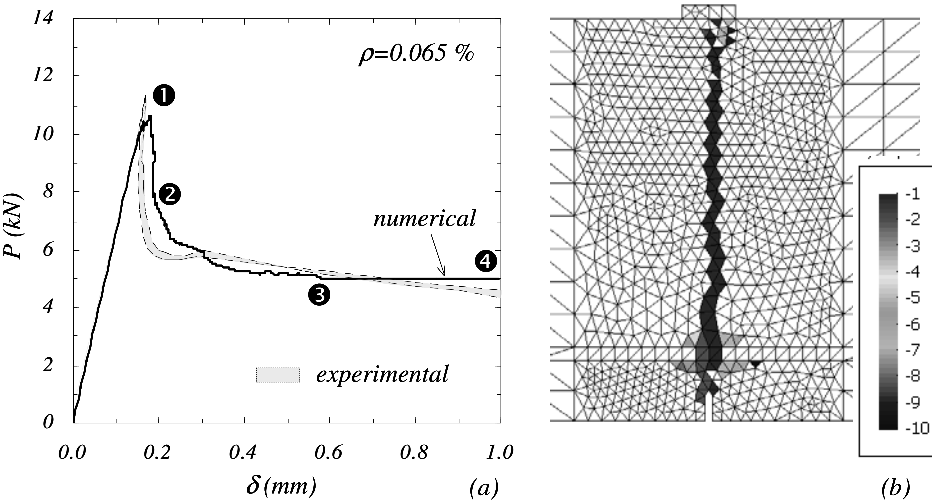

Figure 3.32. Numerical simulation of lightly reinforced beams of three points with reinforcement ratio equal to 0.065%: (a) structural response, relationship between the load applied and the mid-span displacement, (b) Material bifurcation in the finite elements belonging to different crack pattern at the last load step (each negative integer between -1 and -10 indicates a crack path).

The displacement contour lines in Figure 3.33 show how the primary crack crosses the reinforced zone without important strain localization appears to the sides of the discontinuity, unlike the observed thing in the earlier test (Figure 3.31(b)).

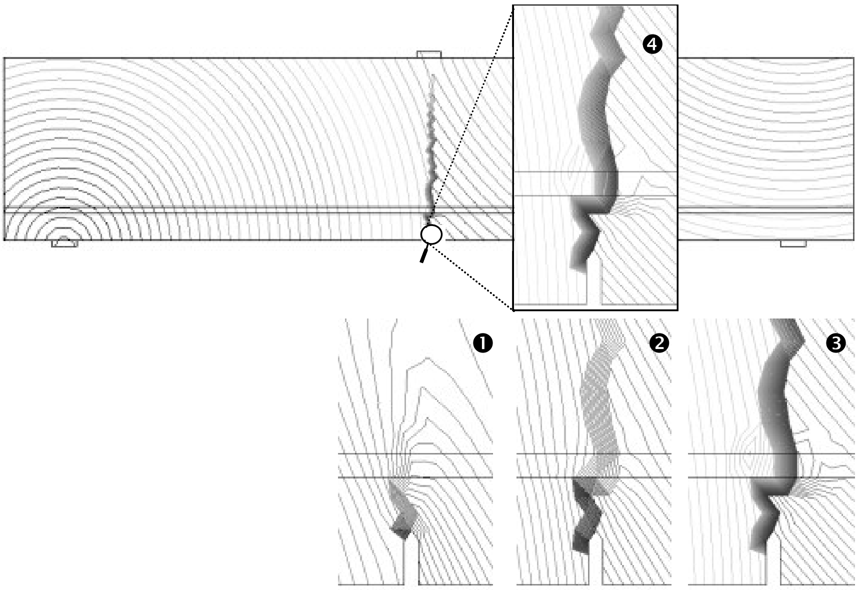

Figure 3.33. Numerical simulation of lightly reinforced beams of three points with reinforcement ratio equal to 0.065%. Displacement contour lines at the last load step in the whole beam and close-up view in the notched zone for step 1 to 4 indicated in Figure 3.32(a).

The force *vs* displacement curve and the primary crack path corresponds approximately with the experimental results in the beams with reinforcement ratio equal to 0.13% and 0.065%.

3.5. Strongly reinforced beams

A set of reinforced concrete beams similar to them tested by Leonhardt and Walther (Leonhardt 1965) is modeled next, as well as, the experimental crack pattern is qualitatively compared with the discontinuity lines resulting of the simulation.

A simply supported beam of span equal to 2.08m is subjected to two concentrated loads as it is indicated in Figure 3.34(a). The beam is reinforced longitudinally by two steel bars of 24mm of diameter located to a distance d_v=0.28m of her superior face. The mechanical properties of the concrete and the reinforcement steel are indicated in Table 3.5.

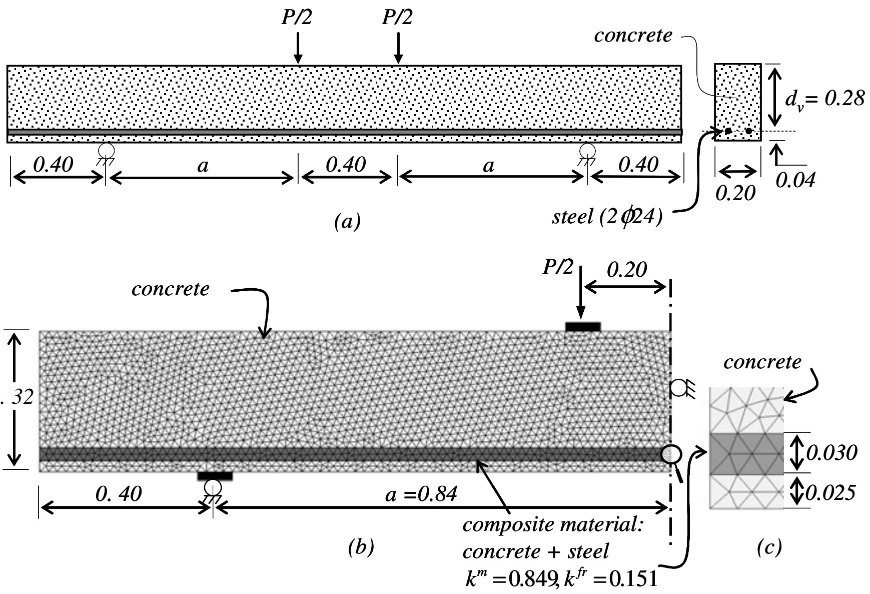

Figure 3.34. Numerical simulation of strongly reinforced beams: (a) descriptive sketch, (b) finite elements mesh of half beam, (c) close-up of the composite material zone.

Concrete	
Young's modulus:	$E^m = 20.0$ GPa
Poisson's ratio:	$\nu^m = 0.2$
Compressive strength:	$\sigma_u^m = 20.\,0$ MPa
Fracture energy:	$G_f = 60.0$ N/m
Tensile strength:	$\sigma_u^m = 2.00$ MPa
Steel	
Young's modulus:	$E^{fr} = 200.0$ GPa
Softening modulus:	$H^{fr} = 0$ GPa
Yielding stress:	$\sigma_y^{fr} = 456.0$ MPa
Poisson's ratio:	$\nu^{fr} = 0.2$

Table 3.5. Numerical simulation of strongly reinforced beams: Mechanical properties of the component materials.

The parameters of the bond-slip model has been determined through specific results of a pull-out test (Naaman, Namur et al. 1991), obtaining an elastic modulus E^{ir} =1111.GPa and a stress of adherence loss $\sigma^{ir}_{adh} = 311.1$mpa.

The numerical simulation includes the possible effects of the dowel action. This effect is characterized for an equivalent elastic modulus $G^{f\tau} = E^{fr}/2(1+\nu^{fr}) = 83.33$GPa, an equivalent yielding shear stress $\tau^{f}_{y} = \sigma^{fr}_{y}/\sqrt{3} = 263.3$mpa and a softening modulus equal to zero ($H^{f\tau} = 0$).

The finite elements mesh of the problem is in Figure 3.34(b), where the elements in bright gray indicate simple concrete which is represented with a damage model with degradation in tension and compression (Section 2.2.1), whereas the elements in dark gray correspond to a reinforced concrete treated as the composite material described by this formulation. Although the diameter of the bars is 24mm, the strip height of the composite material elements has been considered equal to 30mm (Figure 3.34(c)), where the volumetric participation factor of the corresponding steel is $k^{fr} = 0.151$.

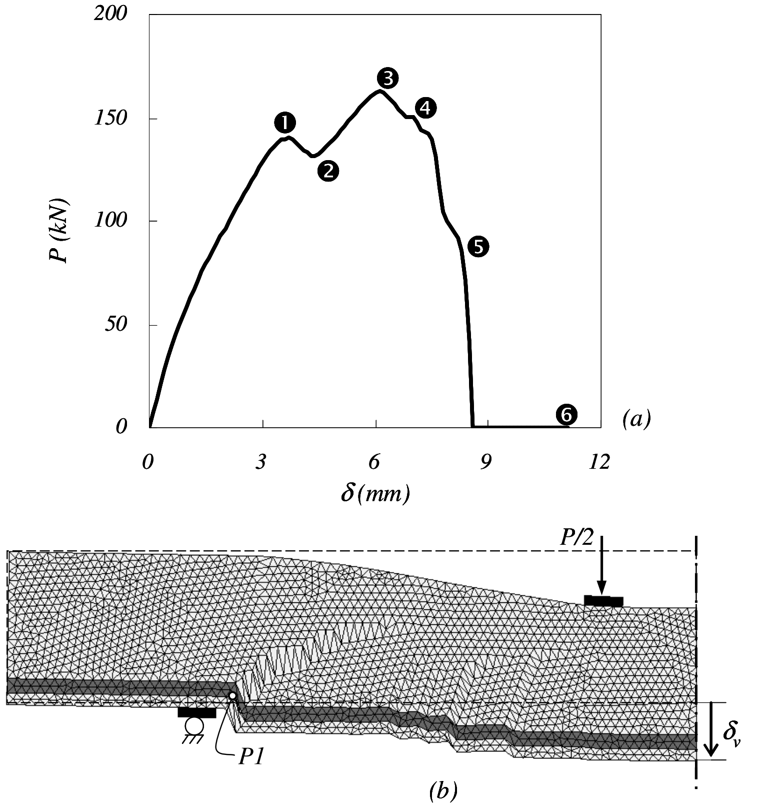

Figure 3.35. Numerical simulation of strongly reinforced beams: (a) relationship between the load applied and the mid-span vertical displacement, (b) deformed shape of the numerical model at step 4.

Remark 3.4 *In the strongly reinforced beams simulated here, the cracks propagate in symmetrical form with respect to mid-span and the boundary conditions in the symmetric axis are not located on a discontinuity path. According to the previously mentioned half of the beam can be modeled.*

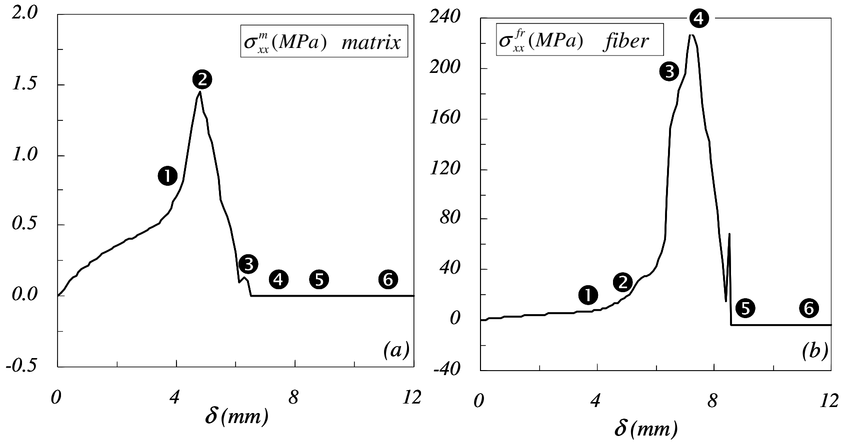

Figure 3.36. Numerical simulation of strongly reinforced beams. Evolution of the stress in the components of the composite material in *P1* (Figure 3.35(b)): (a) concrete normal stress in x-direction, (b) steel axial stress.

Figure 3.35(a) shows the relationship between the load applied P and the mid-span vertical displacement δ; for the steps there indicated, Figure 3.37 displays the displacement contour lines, whereas Figure 3.38 and Figure 3.39 present the elements in inelastic loading and with damage index equals to 1, respectively.

Figure 3.36 describes the stress evolution in the concrete and the steel in point *P1* of composite material (Figure 3.35(b)). Here it is observed that the concrete normal stress in x-direction increases up to step 2, from which the inelastic regime begins (Figure 3.38) and load is reduced down to reach the total degradation at step 4, 5 and 6. In steel fibers an elastic unloading appears from step 4, as a result of the total loss of stiffness of the beam after the formation of the diagonal crack shown in Figure 3.37. The small pick near to step 5 in Figure 3.36(b) is possibly produced to instabilities caused by the strain localization in the superior face of the beam.

With respect to the visualization of the results, as much the concentration of displacement contour lines (Figure 3.37), as the inelastic loading regime in the elements (Figure 3.38), are reversible processes; for example, a zone with localization and inelastic loading regime at step 5 is transformed into a zone with non-localization and unloading regime at step 6. That is, these results indicate the active cracks at every load step.

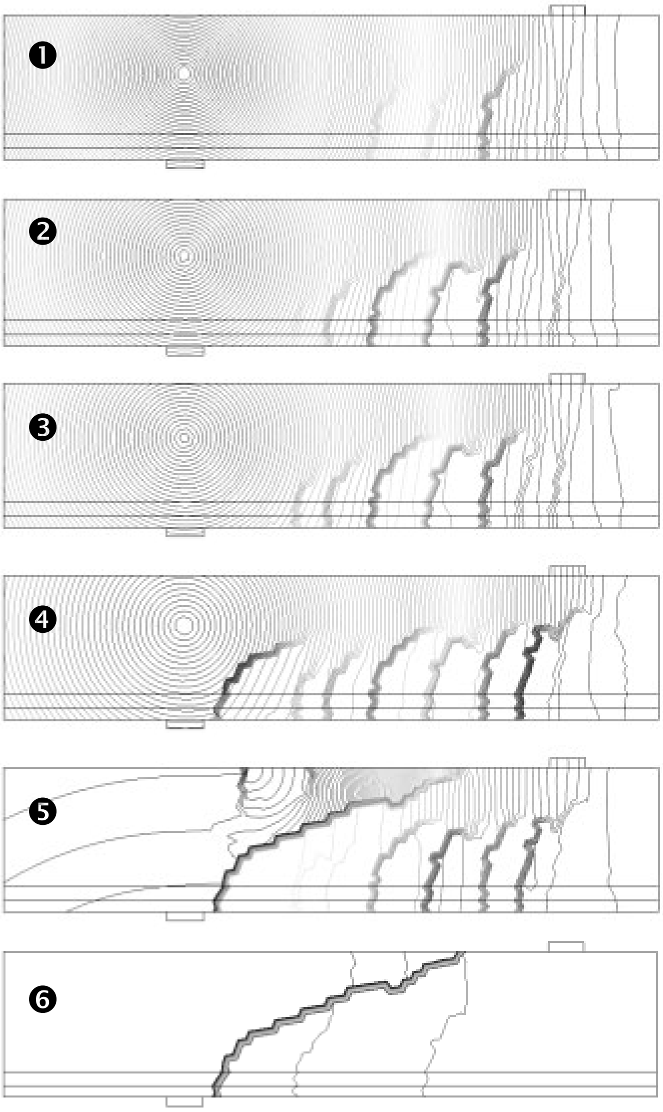

Figure 3.37. Numerical simulation of strongly reinforced beams. Displacement contour lines for steps 1 to 6.

The finite elements with damage index equals to 1 (Figure 3.39) provide an accumulated image of the crack pattern that can be compared with the photographers of the experiment at a specific step. Therefore in the last load step, the paths of active and inactive cracks during the load history are obtained.

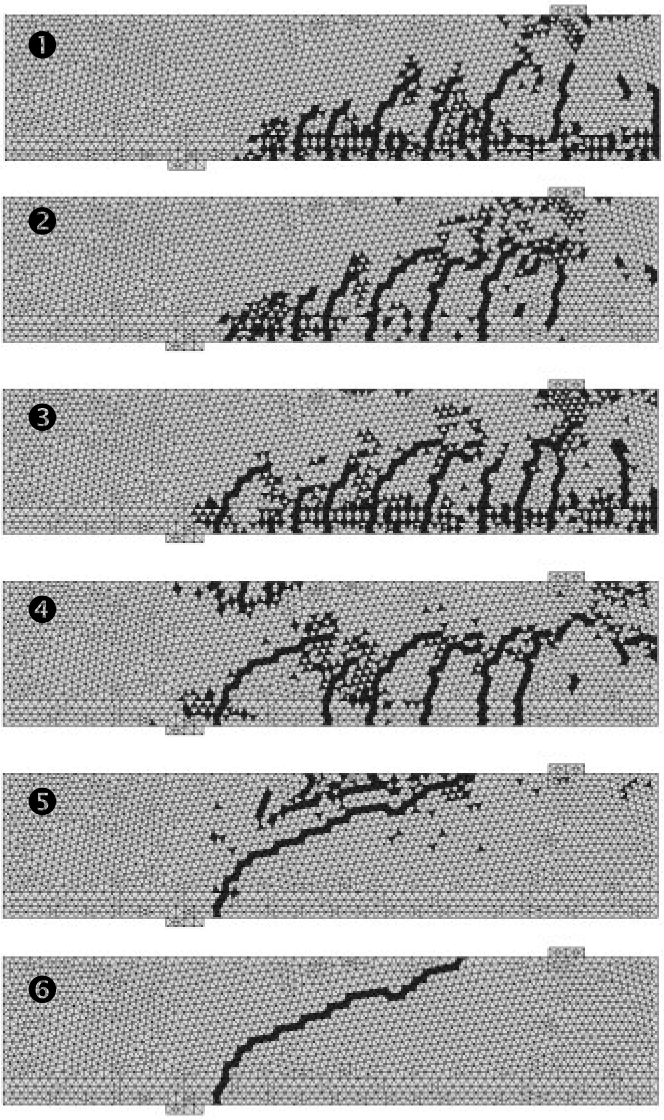

Figure 3.38. Numerical simulation of strongly reinforced beams. Finite elements in inelastic loading regime for steps 1 to 6.

At steps 1 and 2 appear the first cracks located between the applied load and the support, extending up to ¾ times the height of the beam. In load step 3, the number of cracks is increased and the maximum load of the structural response is reached. From this step the load decays while propagates a new crack more inclined than the others denominated *diagonal crack*, as shown at steps 4 and 5. Finally at step 6, when beam capacity is null, a single band in strain localization and inelastic loading is observed, which describes the path of the diagonal crack.

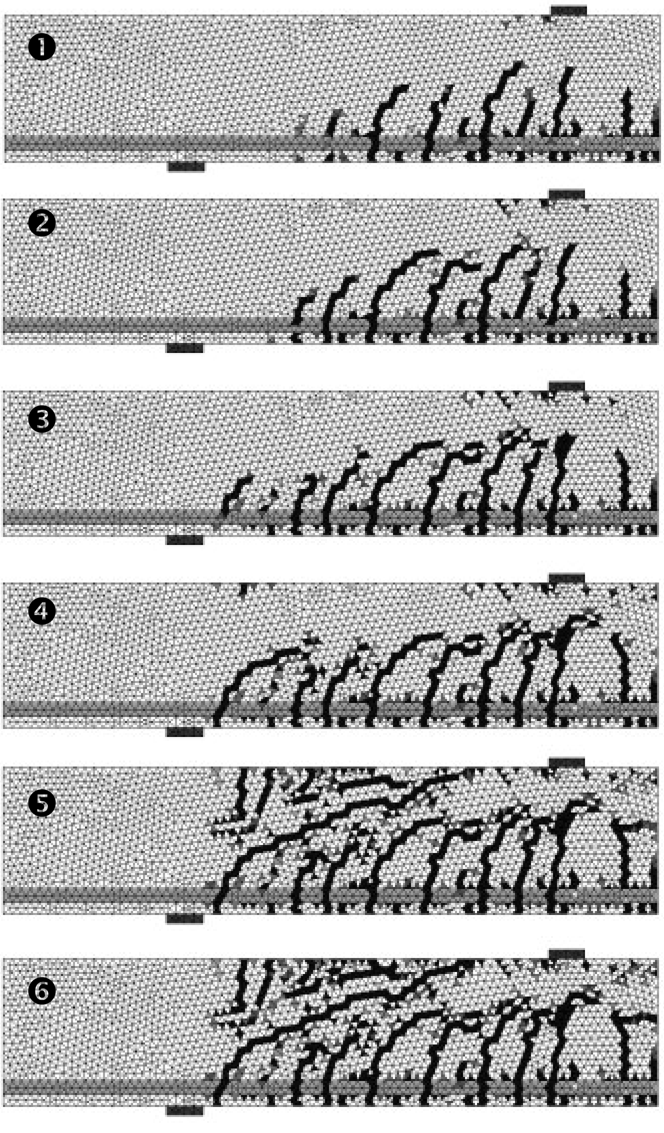

Figure 3.39. Numerical simulation of strongly reinforced beams. Finite elements with damage index equal to 1.0 for steps 1 to 6.

With the same characteristics previously described, three beams of equal height and different span were modeled, in which the factor a_v/d_v is equal to 1, 2 and 5, respectively. Next the numerical and experimental crack pattern is compared.

Figure 3.40 shows the concentration of displacement contour lines at load step of greater presence of active cracks and the real crack pattern of the beam after the maximum load.

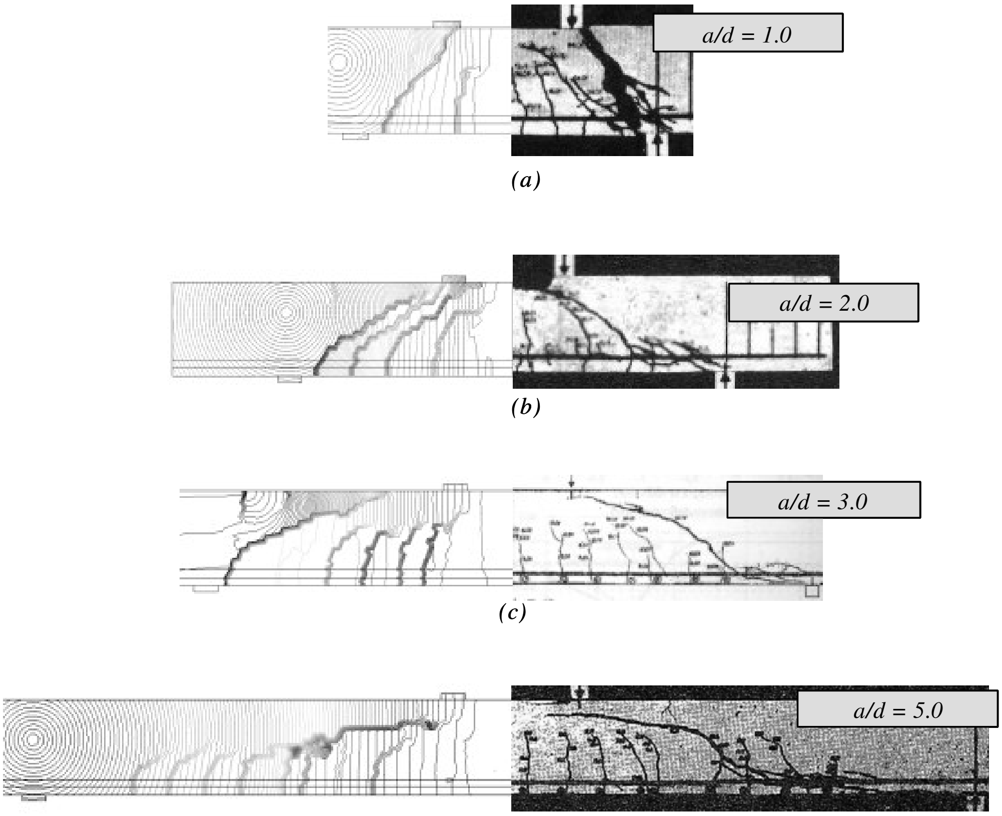

(a)

(b)

(c)

(d)

Figure 3.40. Numerical simulation of strongly reinforced beams. Comparison between the experimental and numerical crack pattern for beams of different span: (a) a_v/d_v=1.0, (b).a_v/d_v=2.0, (c) a_v/d_v=3.0, y (d) a_v/d_v=5.0.

Generally, the final cracking state corresponds qualitatively with the results taken from the experimental tests. The model captures as much the group of parallel cracks as the diagonal crack related to the total collapse of the beam.

> ***Remark 3.5*** *The modeling demonstrated that the amount of reinforcement steel of a beam determines the appearance and propagation of cracks and consequently modifies its structural capacity. In lightly reinforced beams, the maximum load happens shortly after the beginning of the damage in the concrete, presenting a primary crack in the mid-span. However, in strongly reinforced beams, the reinforcement steel increases the structural capacity and initially induces the appearance several perpendicular cracks to the axis of the bars. The general collapse appears with the formation of a diagonal crack associated with the normal and shear stress produced in the beam.*

3.6. Reinforced concrete panels subjected to shear

3.6.1. Panel with reinforcement in one-way subjected to pure shear

Next the results of the numerical simulation of a reinforced concrete panel subjected to pure shear are presented. The panel corresponds to PB18 test displayed in the reference (Bhide & Collins 1989).

The panel is 890mm square and 70mm thickness and is reinforced by 40 bars of 6mm diameter oriented in *x*, which they represent the 2.2% of the total volume of the panel (Figure 3.41(a)). A pure shear in the *xy*-plane is applied by means of a set of 5 anchorages or shear keys by each face adhered to the concrete and the steel.

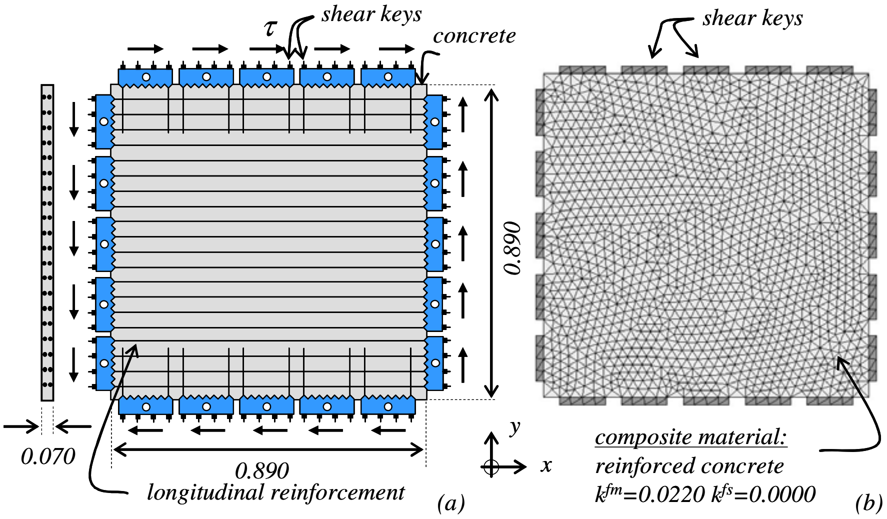

Figure 3.41. Panel with reinforcement in one-way subjected to pure shear: (a) descriptive sketch and (b) finite elements mesh.

In accordance with the distribution of the reinforcement bars inside the panel, it is valid to suppose that the reinforced concrete is a composite material conformed by steel fibers distributed uniformly in a concrete matrix. The mechanical properties of both component materials are presented in Table 3.6.

Concrete	
Young’s modulus:	E^m = 20.0 GPa
Poisson’s ratio:	ν^m = 0.2
Compressive strength:	σ_u^m = 20. 0 MPa
Fracture energy:	G_f = 100.0 N/m
Tensile strength:	σ_u^m = 2.00 MPa
Steel	
Young’s modulus:	E^{fr} = 200.0 GPa
Softening modulus:	H^{fr} = 0 GPa
Yielding stress:	σ_y^{fr} = 402.0 MPa
Poisson’s ratio:	ν^{fr} = 0.2

Table 3.6. Reinforced concrete panels subjected to shear. Mechanical properties of the component materials.

The numerical simulation assumes a high adherence between the concrete and the steel bars, as well as, an important effect of the dowel action, characterized by an equivalent elastic modulus $G^{f\tau} = E^{fr} / 2(1 + \nu^{fr})$ equal to 83.33GPa, an equivalent yielding shear stress $\tau_y^f = \sigma_y^{fr} / \sqrt{3} = 263.3$mpa and a softening modulus null $H^{f\tau} = 0$.

A mesh of 2736 linear triangular finite elements is used, in which the dark gray represents the shear keys and the bright gray represents the reinforced concrete (Figure 3.41(b)). a plane stress state and rigid shear keys is assumed in this problem. Also all the finite elements of the panel are considered composite material constituted by 97.8% of matrix (concrete) and 2.2% of fibers (steel) in x-direction.

The numerical model imposes displacement in each shear key; as indicated in Figure 3.42, which they on the whole generate a pure shear state on the panel.

The structural response shown in Figure 3.43 is defined by means of the relationship between the average shear strain ($\gamma = \delta / l$) and the applied shear stress in one of the faces of the panel, obtained as summatory of the reactions in each shear key F_i divided into the area of the face ($\tau = \sum F_i / (l \cdot t)$). In the graph, the experimental results are indicated with dots and the numerical ones with a solid line. The proposed solution shows to certain difference with the maximum load of the experimental response, nevertheless, the rest of the curve indicates a satisfactory approach; these differences can be caused by some boundary conditions unknown in the real problem and despised in the numerical model.

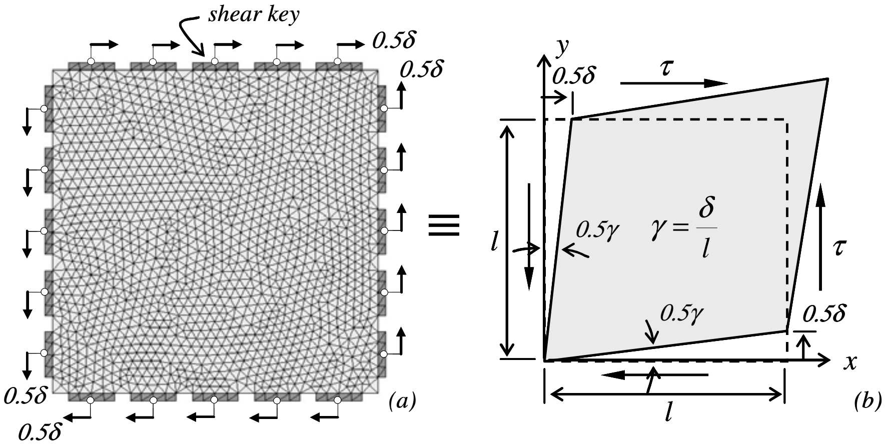

Figure 3.42. Panel with reinforcement in one-way subjected to pure shear: (a) boundary conditions in the numerical simulation and (b) stress and strain produced on the panel.

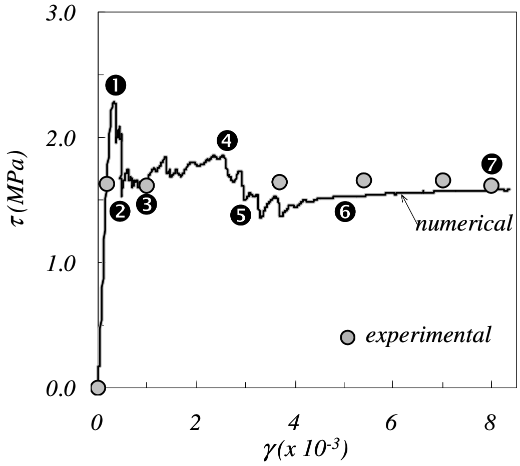

Figure 3.43. Panel with reinforcement in one-way subjected to pure shear. Average shear strain *versus* applied shear stress curve.

In Figure 3.44 the displacement contour lines represent the crack pattern at steps 1 to 7 indicated in Figure 3.43(a). If the material bifurcation appears the strain increases in a point with inelastic loading regime and diminishes in a neighboring point with unloading regime, maintaining the continuity of tractions. Therefore, the elements in inelastic loading regime surrounded by zones in unloading regime are an indicator of the cracking zone, as shown in Figure 3.45. The elements in dark gray are in inelastic loading regime and bright gray in unloading regime.

In Figure 3.46 appears a photography of the panel tested in the reference (Bhide & Collins 1989). This experimental result is compared with the elements in inelastic loading regime and the displacement contour lines obtained of the numerical simulation at step 3. In Figure 3.47 this comparison of results for step 7 is presented.

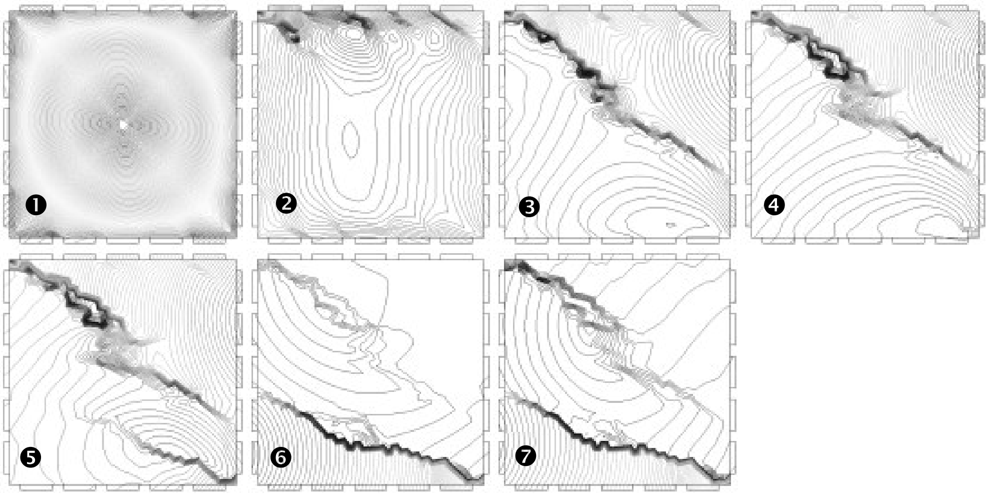

Figure 3.44. Panel with reinforcement in one-way subjected to pure shear. Displacement contour lines for steps 1 to 7.

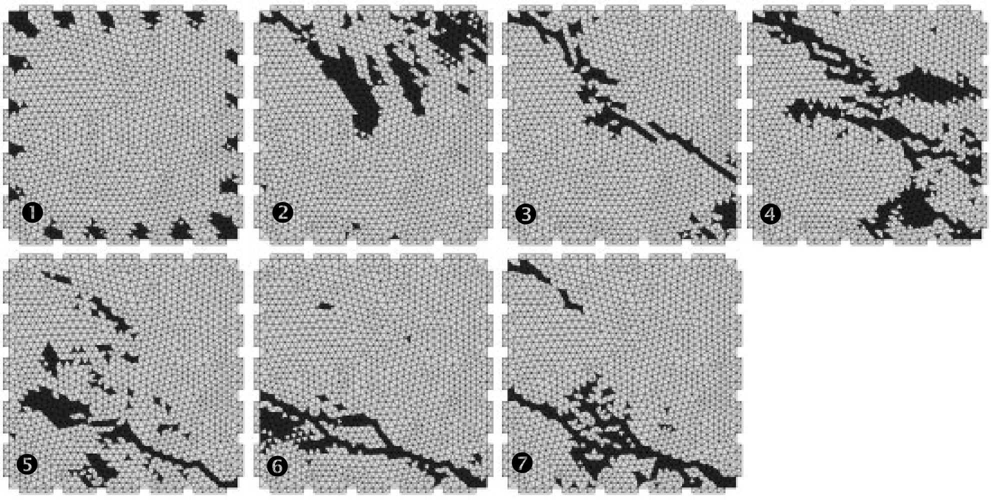

Figure 3.45. Panel with reinforcement in one-way subjected to pure shear. Elements in inelastic loading regime for steps 1 to 7.

Figure 3.48 shows to the experimental and numerical approximated values of the angle formed between the crack path and a horizontal line.

Up to step 1, the strain localization in the panel is not observed, although immediately afterwards decays the shear stress.

At step 2, small concentrations of the displacement contour lines appear in the upper face of the panel, while the rest of it presents an unloading regime. Shortly after, at step 3, two trajectories of localization appear: one starting from the top left end and the other beginning between two shear keys of the right face. According to experimental results observed in this step (Figure 3.46(a) y Figure 3.48), the first trajectory of strain localization is approximately the same as one of the cracks inclined 45° with respect to x (normal to the greater principal direction); nevertheless, the second trajectory has an incorrect direction with respect to the experimental result.

At step 4, the displacement contour lines begin to concentrate in the bottom right of the panel, while the finite elements belonging to previous cracks are in unloading regime.

At steps 5 and 6, obvious strain localization appears in the inferior part of the panel. This behavior is conserved up to step 7 coinciding with the experimental results (Figure 3.47).

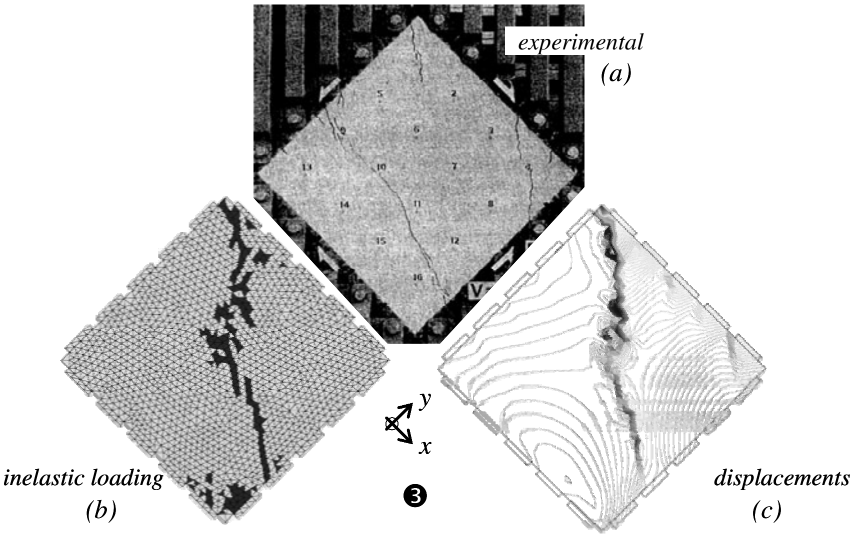

Figure 3.46. Panel with reinforcement in one-way subjected to pure shear. Comparison between the crack pattern at step 3: (a) experimental result (Bhide & Collins 1989), (b) elements in inelastic loading regime, (c) displacement contour lines.

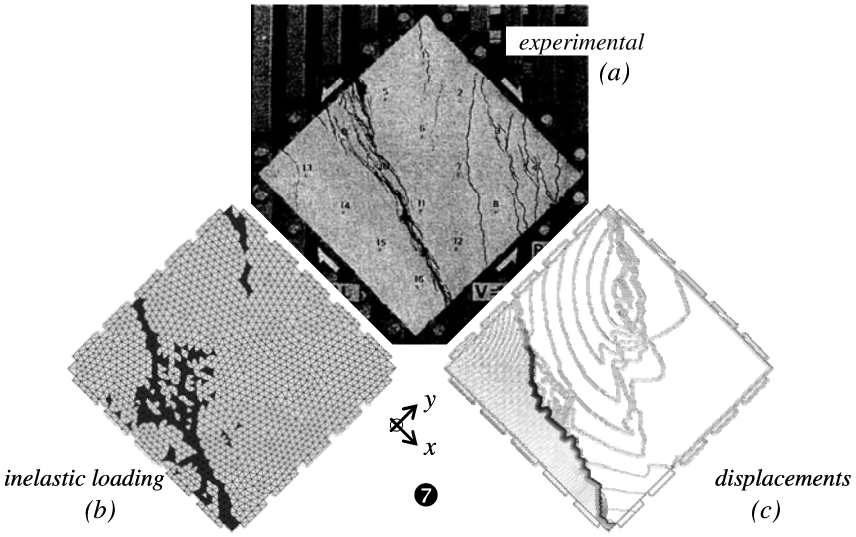

Figure 3.47. Panel with reinforcement in one-way subjected to pure shear. Comparison between the crack pattern at step 7: (a) experimental result (Bhide & Collins 1989), (b) elements in inelastic loading regime, (c) displacement contour lines.

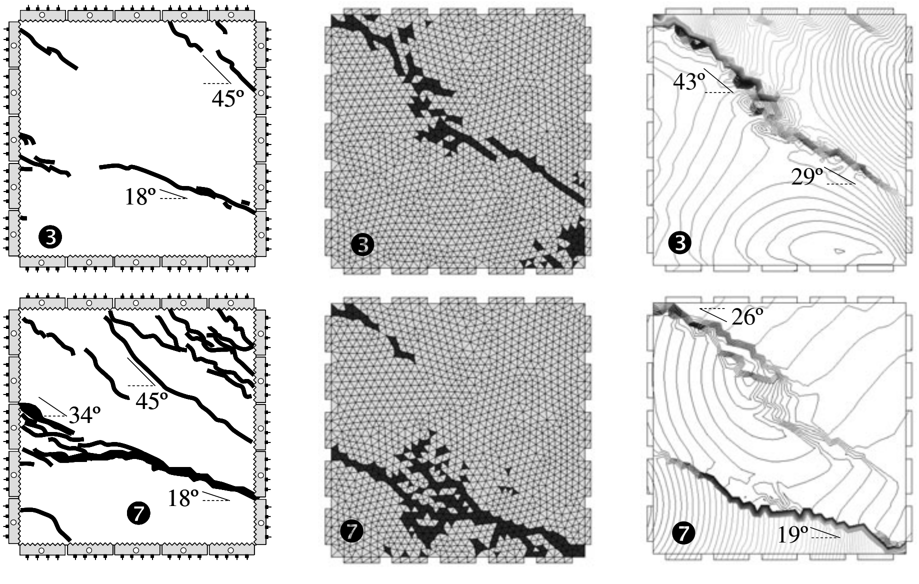

(a) (b) (c)

Figure 3.48. Panel with reinforcement in one-way subjected to pure shear. Comparison between the crack directions at steps 3 and 7: (a) reproduction of the experimental result (Bhide & Collins 1989), (b) elements in inelastic loading regime, (c) displacement contour lines.

By the homogeneous nature of the test, the place of initiation of the crack assumes random, therefore, in the simulation a parallel discontinuity to the experimental crack is considered correct in spite of its position in the panel, as observed at step 7.

3.6.2. Effect of the dowel action in panels subjected to pure shear

The shear capacity through the steel bars provides an important contribution to the response of reinforced concrete structures subjected to shear stress. This section displays the simulation results of the same panel neglecting the stiffness due to the dowel action.

If the panel subjected pure shear in the *xy*-plane and the dowel action is neglected, the axial capacity of the bars in *x*-direction does not generate any contribution to the shear capacity of the composite material, therefore, the crack pattern and the structural response are similar to the expected behavior in a simple concrete panel. Figure 3.49 compares the results including or not including the dowel action.

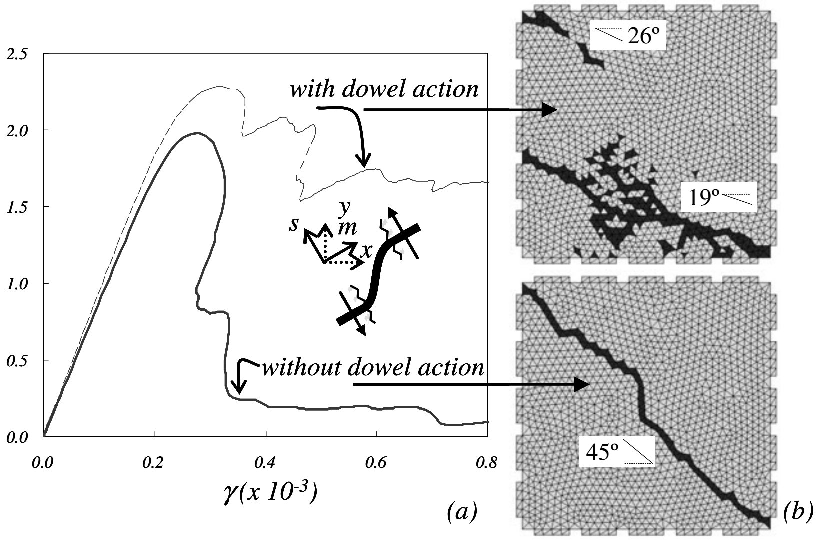

Figure 3.49. Panel with reinforcement in one-way subjected to pure shear. Comparison the results including or not the dowel action: (a) average shear strain *versus* applied shear stress curve, (b) elements in inelastic loading regime and displacement contour lines at last step.

3.6.3. Panel with reinforcement in two-way subjected to pure shear

This section shows the results of the numerical simulation of the a panel with reinforcement in two-way subjected to pure shear, tested in the reference (Collins, Vecchio et al. 1985).

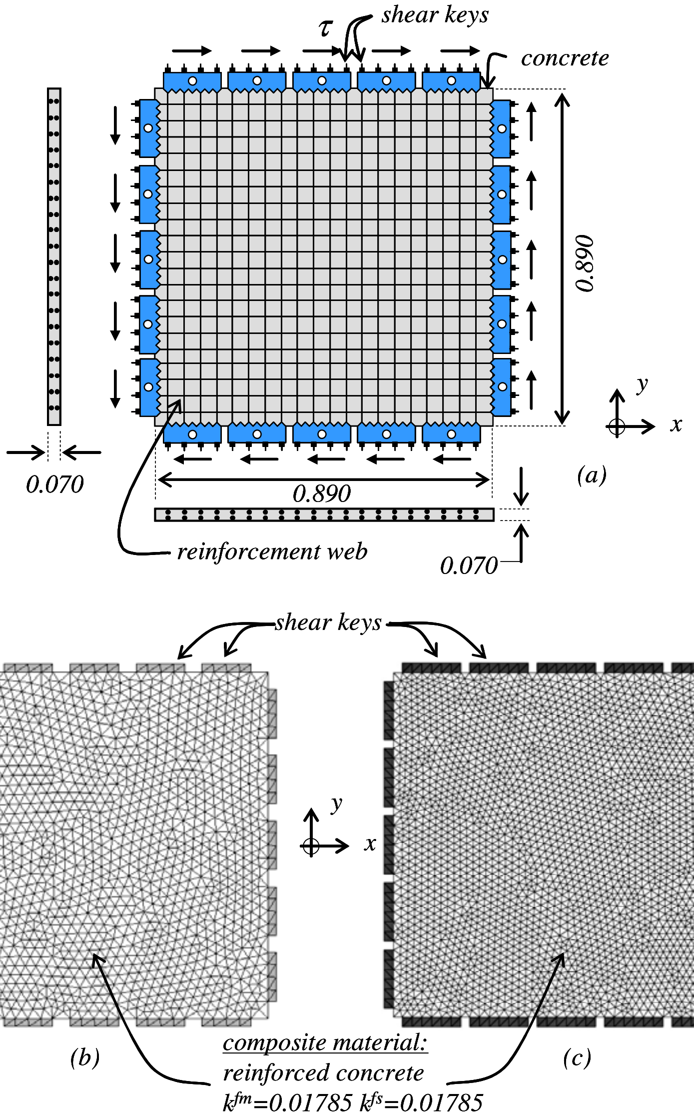

Figure 3.50. Panel with reinforcement in two-way subjected to pure shear: (a) descriptive sketch, (b)mesh with 2736 elements, (c) mesh with 5370 elements.

In this panel the reinforcement bars are oriented in x and y of uniform way, with volumetric participation factor equal to $k^{fr} = k^{fs} = 0.01785$. Table 3.6 displays the mechanical characteristics of the materials and Figure 3.50(a) shows a descriptive sketch of the problem.

Two meshes of finite elements have been used: the former with 2736 finite elements of 0.026m average size (Figure 3.50(b)) and the latter with 5370 elements of 0.019m average size (Figure 3.51(c)).

Figure 3.51 shows the relationship between the average shear strain and the applied shear stress for the two meshes. Figure 3.52 displays the finite elements in inelastic loading regime, the displacement contour lines, and the deformed panel at last load step, as well.

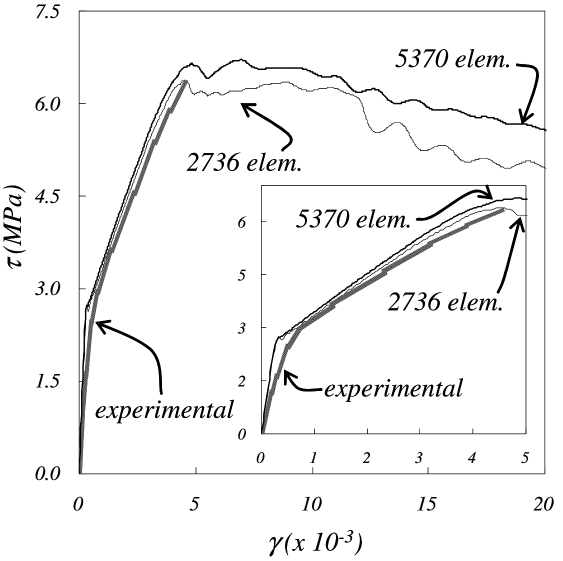

Figure 3.51. Panel with reinforcement in two-way subjected to pure shear. Relationship between the average shear strain and the applied shear stress for the two different meshes.

From the comparison of results between both meshes two things are concluded: the structural responses are similar and each crack path maintains the same direction and shape although appears in different places of the panel. For a uniform stress condition is considered that the crack position is random, therefore, the difference in the result is acceptable.

Next, the results obtained with the mesh of 2736 elements and its comparison with the experimental values is described. Figure 3.53 shows the relationship between the average shear strain and the shear stress applied to the panel, where the fine line corresponds to the numerical result and the coarse line to the experimental values.

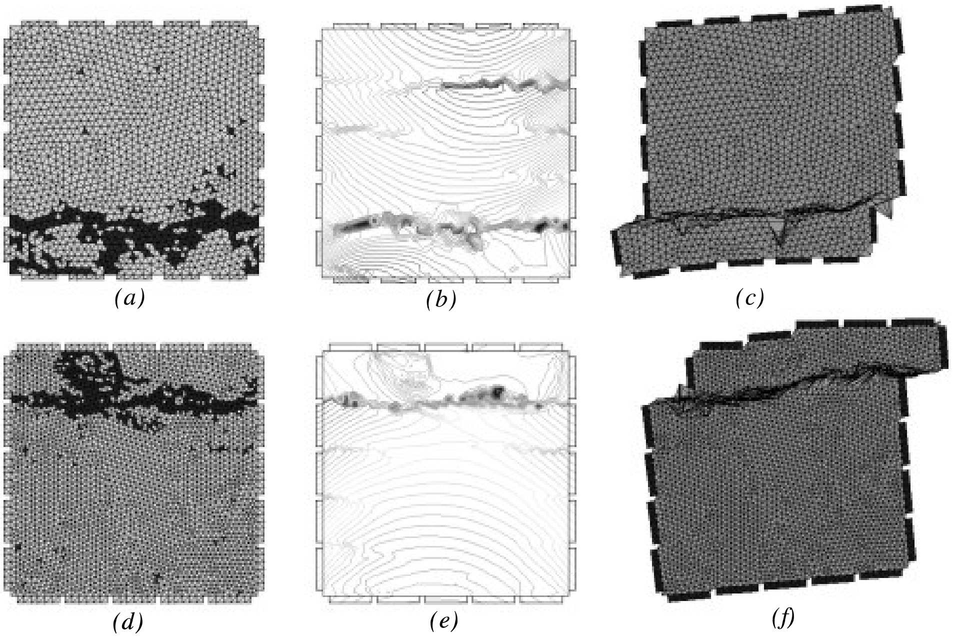

Figure 3.52. Panel with reinforcement in two-way subjected to pure shear. Elements in inelastic loading regime, displacement contour lines and deformed shapes for two different meshes at last step: (a), (b) and (c) in the mesh of 2736 elements, (d), (e) and (f) in the mesh of 5730 elements.

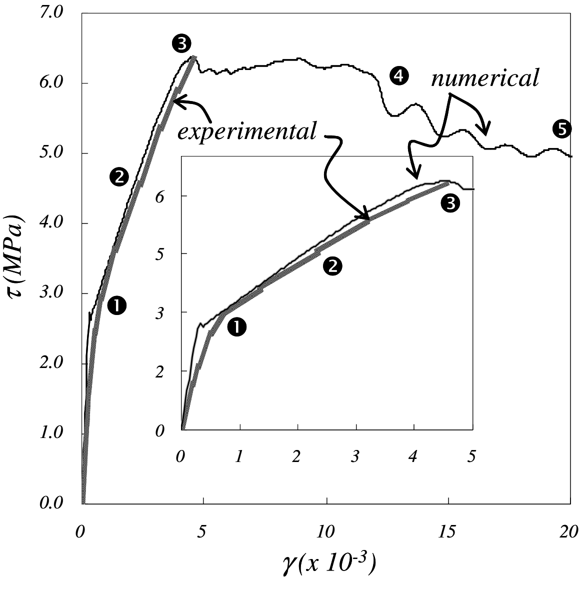

Figure 3.53. Panel with reinforcement in two-way subjected to pure shear. Relationship between average shear strain and applied shear stress for different load steps.

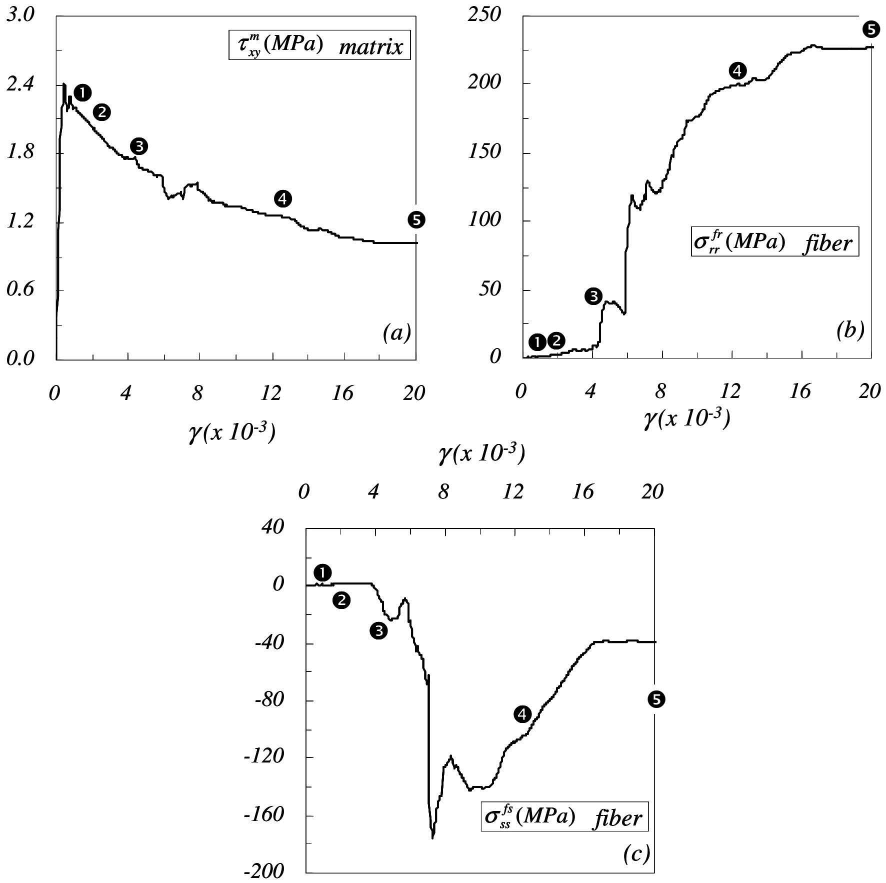

Figure 3.54. Panel with reinforcement in two-way subjected to pure shear. Evolution of the stress in the concrete and the steel on *P1*: (a) concrete shear stress, (b) steel stress in **r** direction, (c) steel stress in **s** direction.

Figure 3.54 displays the evolution of the stresses in the component materials on point *P1* located in center of the panel (Figure 3.50). The pure shear state (before step 1), in which the shear stress is supported essentially by the matrix, it disappears when the process of strain localization begins. From the beginning of the damage (step 1), the shear stress in the concrete matrix is reduced, whereas the fibers in **r** direction maintain an elastic behavior with an increasing axial tension. The compression stress in fibers oriented in **s** increases until a value of -155mpa between steps 3 and 4, and later decreases until a value of -40mpa approximately; this reflected a difference important in the contribution of each fiber package in the behavior of the composite material.

Figure 3.55 shows the elements in inelastic loading regime and the displacement contour lines for some load step.

During steps 1 and 2, an inelastic loading state in the whole panel without strain localization is observed, this means that in spite of the damage produced in the matrix, the displacement jump is not activated and therefore the determinant of the tangent localization tensor is positive. It is important to remember that in the calculation of this stress participates the stiffness of the matrix, fibers, and effects of interaction between both of them. At this stage of the experiment many cracks of little opening in the principal direction are distributed by the whole panel.

At step 3 the strain localization begins in three zones of the panel. In step 4 only two cracks are formed and at the final step a single discontinuity remains in x-direction in the inferior zone of the panel.

The experimental test indicates that the main crack is also parallel to x and appears in the superior part of the panel. Give the homogeneous state of the panel and the applied actions, it is considered that this crack can appear to any height of the panel.

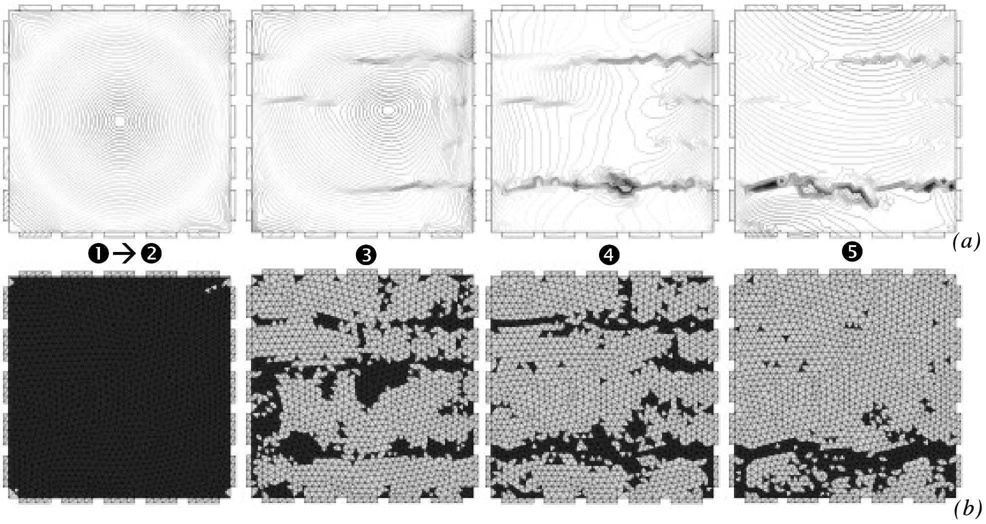

Figure 3.55. Panel with reinforcement in two-way subjected to pure shear. (a) displacement contour lines for steps 1 to 5, (b) elements in inelastic loading regime for steps 1 to 5.

The superposition of the zones of strain localization observed in the numerical model throughout the load process adjusts to the real distribution of the cracks in the final state.

Figure 3.56(a) and (d) shows the crack pattern at final step of the experimental test (Collins, Vecchio et al. 1985). The figures are rotated in such a way that it facilitates the comparison with the results of the numerical simulation, as well as, the elements in inelastic loading regime (Figure 3.56(b)) and the deformed shape (Figure 3.56(c)).

Remark 3.6. *Distributed cracking state: when many parallel cracks are distributed by the panel, in other words in a distributed cracking state, there is not an obvious process of strain localization in the study scale. In this case, the numerical simula-*

tion will show an inelastic loading regime on the whole panel and a constant spacing between displacement contour lines, as steps 1 and 2 indicate it in Figure 3.55.

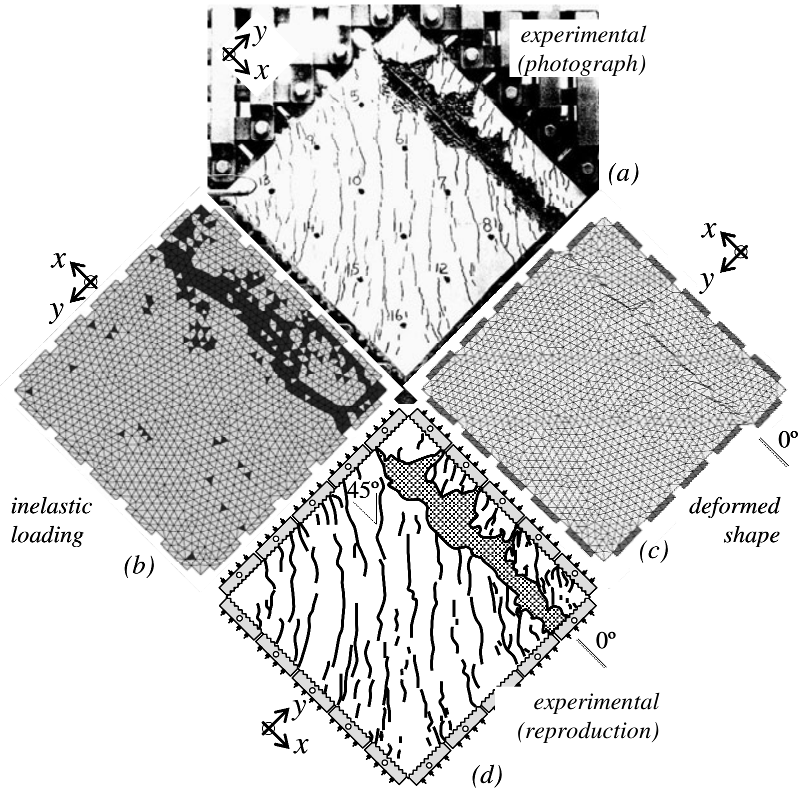

Figure 3.56. Panel with reinforcement in two-way subjected to pure shear for last load step: (a) photograph of the experimental result (Collins, Vecchio et al. 1985), (b) elements in inelastic loading regime, (c)deformed shape, (d) reproduction of the experimental result and cracking direction

3.6.4. Panel with reinforcement in one-way subjected to normal and tangent stress

The results of the numerical simulation of a reinforced concrete panel with bars in x-direction appear next. This panel is subjected to the combination of a normal stress in x-direction of magnitude 3.1τ and a shear stress τ in the xy-plane. This problem has been taken from the experimental tests of the reference (Bhide & Collins 1989).

The panel has the same geometry and mechanical properties presented in the test described in Section 3.6.1, only change the applied loads (Figure 3.57(a)). The finite elements mesh is the same that it has been used to model the first test (Figure 3.57(b)).

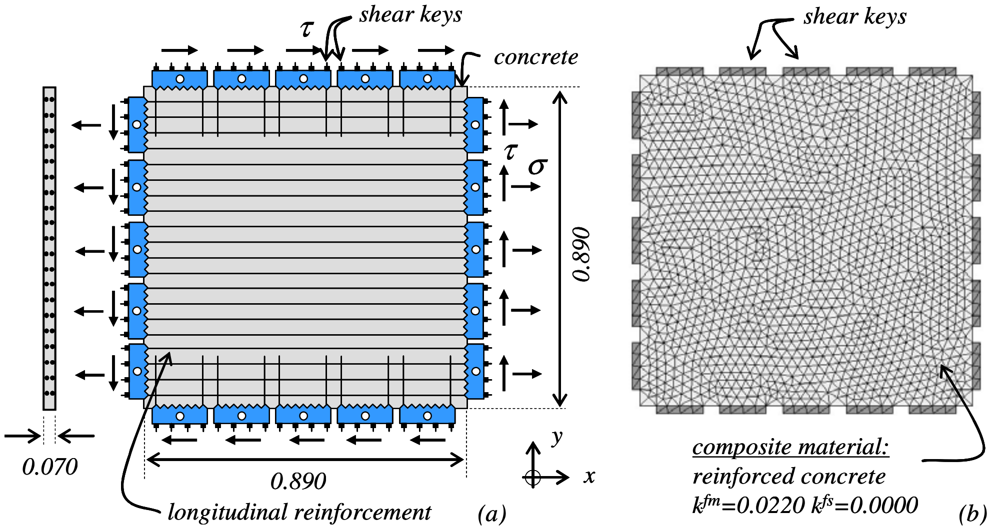

Figure 3.57. Panel with reinforcement in one-way subjected to normal and tangent stress: (a) descriptive sketch, (b) finite elements mesh.

The structural response defines by means of the relationship between the average shear strain and the applied tangent stress τ as shown in Figure 3.58. The dots indicate the experimental result and the solid line displays the numerical modeling. A good correlation between the numerical and experimental results is observed except in the last load steps, possibly due to differences among the actions of the shear keys on the panel.

At step 1, experimental test shows manifold cracks oriented to 71° with respect to x, smeared in the whole panel (Figure 3.59(a)). This direction of the distributed cracking is equal to the principal direction in the strain field. The presence of a fiber set in x-direction induces an orthotropic behavior of the composite material and consequently the principal directions of stress and the strain are not exactly the same (Figure 3.58(c) and (d)).

The numerical simulation describes a distributed cracking state when the elements of the panel are in an inelastic loading regime without strain localization, as shown in Figure 3.59(b) and (c).

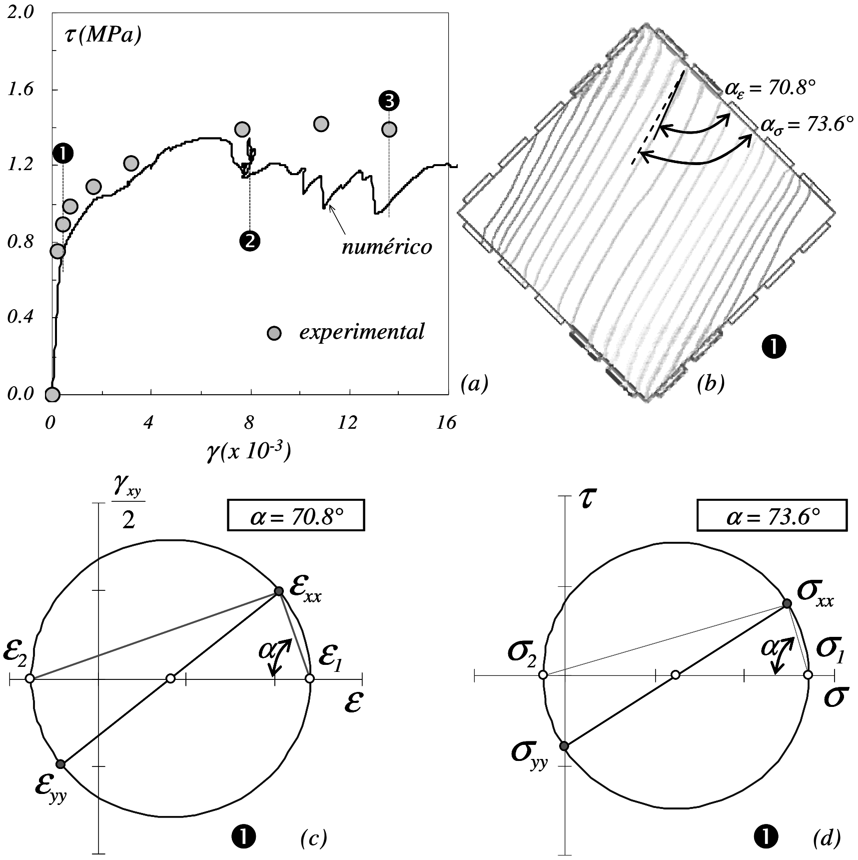

Figure 3.58. Panel with reinforcement in one-way subjected to normal and tangent stress: (a) relationship between average shear strain and applied shear stress for different load steps, (b) localization angle on the panel at step 1, (c) Mohr's circle in strain for step 1, (d) Mohr's circle in stress for step 1.

At step 2, the strain localization begins (Figure 3.58(a)), accompanied by a small instability in the structural response (Figure 3.60). From now on, a single crack is formed while the structural curve descends slightly of oscillating way.

At step 3 the structural response of the numerical simulation moves away a little from the experimental test (Figure 3.58(a)); however, the discontinuity trajectory defined through the displacement contour lines in Figure 3.61(c) is similar to the main crack observed in Figure 3.61(a), with a difference of 2° between both crack directions.

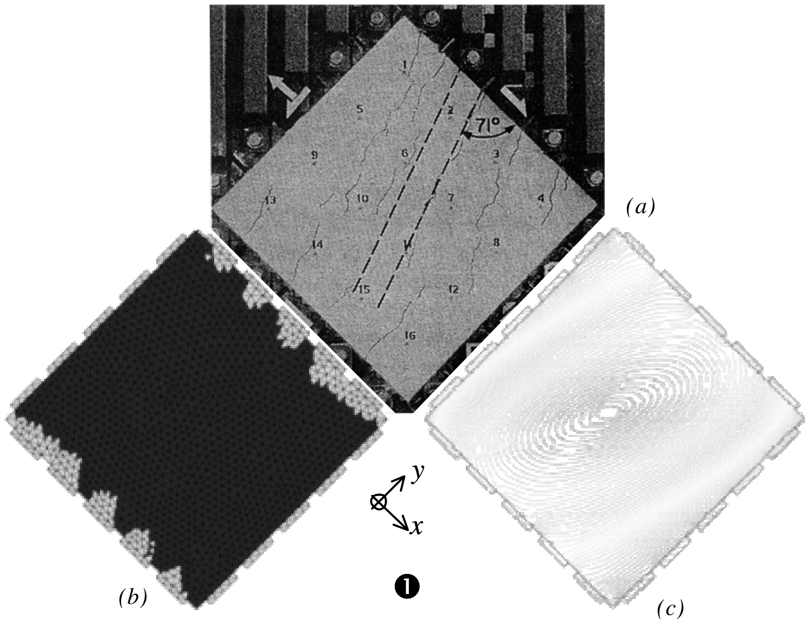

Figure 3.59. Panel with reinforcement in one-way subjected to normal and tangent stress. Load step 1: (a)crack pattern taken from reference (Bhide & Collins 1989), (b) elements in inelastic loading regime, (c) displacement contour lines.

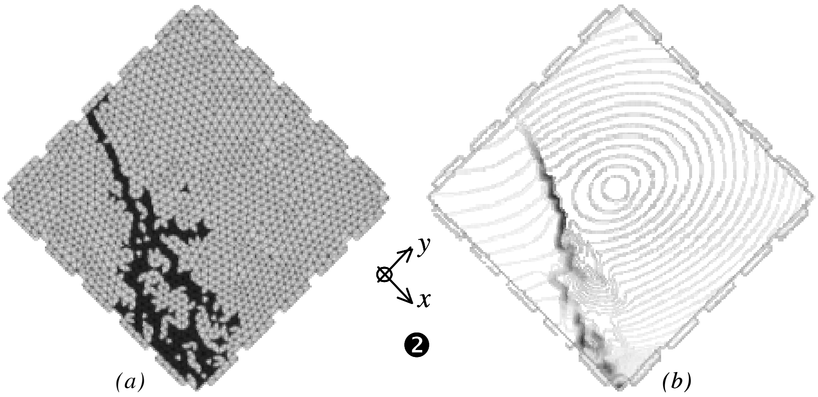

Figure 3.60. Panel with reinforcement in one-way subjected to normal and tangent stress. Load step 2: (a)elements in inelastic loading regime, (b) displacement contour lines.

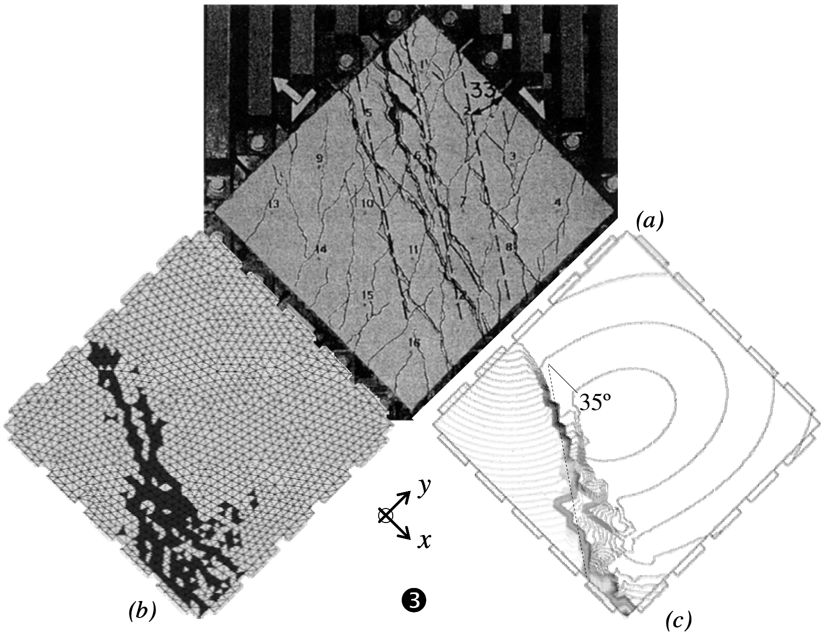

Figure 3.61. Panel with reinforcement in one-way subjected to normal and tangent stress. Load step 3: (a)crack pattern taken from reference (Bhide & Collins 1989), (b) elements in inelastic loading regime, (c) displacement contour lines.

3.7. Summary

In this section, the most important about the numerical simulation of reinforced concrete members that has been presented in this chapter is summarized.

- The general considerations of the problem assume plane stress, infinitesimal strain and non-linear constitutive models of the component materials and the effects of interaction among them. The modeling is made from linear triangular elements with embedded discontinuities, which represent the behavior of the reinforced concrete treated as a composite material or in some cases, the simple concrete treated as a homogeneous material.

- The process of fracture in the reinforced concrete presents some characteristics according to the kind of test. In the pieces submitted to tension, it is easily observed the spacing between cracks (Figure 3.8 y Figure 3.16) and the contribution of the reinforcement to the stiffness and stability of the composite material (Figure 3.17). In the shear panels (Figure 3.41(a)), a mixed mode or mode II of fracture prevails, in which, the shear capacity of the bars in the faces of the crack or dowel influences in the structural response (Figure 3.49).

- The propagation of several macro-cracks with different directions can be observed in strongly reinforced beams subjected to bending (Figure 3.37), however, in lightly reinforced beams a single crack in the central cross section appears (Figure 3.31).

- In comparison with the simple concrete treated as a homogeneous material, the presence of the reinforcement in the composite material delays the process of strain localization and produces a stable distributed cracking state.

- During the failure process of the tension panel reinforced in center being described in Section 3.2, the spacing between cracks is reduced, while the bond-slip zone between of them increases progressively as indicated in Figure 3.5(b). Both distances are equal and approximately constant from the step of load 5 to step 7, as indicated by the contour lines of displacement (Figure 3.7). This means that after the total loss of adherence between both materials, the transference of stress is zero and new discontinuities in the concrete do not appear. Therefore a constant spacing between the existing cracks denominated *saturated crack spacing* is observed. Until this moment the same opening of each crack is conserved, nevertheless, if the fibers reach the yielding stress and begin a stage of perfect plasticity or softening, some cracks take greater opening than others, as shown in Figure 3.13.

- In the Section 3.3, the simulation of the reinforced concrete panel tested to tension by Ouyang and others (Ouyang & Shah 1994; Ouyang, Wollrab et al. 1997) is described (Figure 3.14). In this example, the simple concrete shows a stable damage stage, between the steps 1 and 4 (Figure 3.16 and Figure 3.17), where several cracks maintain a spacing and constant opening given by the capacity of the reinforcement and the adherence in the interface. From step 4 such adherence is lost and consequently the structural capacity decays while it prevails the opening of a single crack that completely crosses the transversal section of the panel, as shown in Figure 3.16 at step 5.

- The amount of reinforcement determines the distribution of the cracks in the beams. For low ratio or non-existence of steel, a single crack in mode I of fracture at half beam is observed as a result of the high tension by bending. However, in strongly reinforced beams, the pick load increases and the bars induce the propagation of several symmetrical cracks from the center to the supports. The numerical simulation presented in Sections 3.4 and 3.5 describes both behaviors.

- The simulation of lightly reinforced beams (Ruiz, Elices et al. 1998) presented in Section 3.4 (Figure 3.26), shows the development of a main crack (Figure 3.31) at mid-span like the localization of displacement contour lines. The damage in the concrete around the reinforcement and to both sides of the main crack represents the formation of secondary cracks (Figure 3.29).

- During the process of fracture of strongly reinforced beams (Figure 3.34(a)), approximately parallel cracks appear in a sequential way. Nevertheless, the general collapse of the structure is determined by the development of a diagonal crack propagating between the support and the applied load (Figure 3.37). Three beams with different ratios length/height were simulated (Figure 3.40), obtaining crack patterns comparable to those presented by experimental tests (Leonhardt 1965).

- The panels conformed by numerous bars distributed uniformly can be represented as solids of a unique composite material, in which; the amount of reinforcement in each direction is given by the respective volumetric participation. Some numerical examples of shear panels (Collins, Vecchio et al. 1985; Bhide & Collins 1989) are presented in Section 3.6.

- When the dowel action is neglected in a panel subjected to pure shear (Figure 3.49), the axial capacity of the bars in x-direction does not generate any contribution to the shear capacity of the composite material. Therefore in this case, the crack pattern and the structural response obtained in a reinforced concrete panel and in a simple concrete panel are similar.

- In the shear tests two different cracking states are observed (Figure 3.50(a)). From load steps 1 (Figure 3.53) to 3 (Figure 3.53), the panel exhibit a *distributed cracking state*. This is represented as the increase of the damage in the matrix stabilized by the behavior of the steel and without strain localization of the composite material. However, in the *localized cracking state* observed after step 3, some macro-cracks of greater opening appear which they are represented in the simulation by strain localization bands.

- In general, the numerical model reaches satisfactory results of the simulation of experimental tests and also preserves the objectivity of the finite elements mesh.

Chapter 4
Conclusions, contributions and future developments

A formulation describing the fracture process of reinforced concrete represented as a composite material by means of the *continuum strong discontinuity approach* (CSDA) and the *mixing theory*, has been developed, implemented and validated in this work. Next the most important aspects are summarized.

- *Formulation.* By means of the *mixing theory* (Truesdell & Toupin 1960), a constitutive model of composite material constituted by one or two groups of long fibers (steel bars) embedded in a matrix of concrete was developed. Likewise, each component is characterized by an especial constitutive model, being the concrete described by a damage model with degradation in tension and compression (Oliver, Cervera et al. 1990). A uniaxial plasticity model (Simó & Hughes 1998) was used for the steel. As well as, the bond-slip effect and dowel action (Park & Paulay 1975) are included and represented by additional models. On the other hand, the initiation and propagation of cracks understood as a strain localization process was described by means of CSDA (Oliver 1996b; Oliver 1996a; Oliver 2000; Oliver, Huespe et al. 2003; Oliver & Huespe 2004a; Huespe, Oliver et al. 2006; Oliver, Huespe et al. 2006). A discontinuous bifurcation analysis of composite material is proposed to establish the bifurcation time and direction of the crack.

- *Implementation.* The formulation has been implemented in a two-dimensional analysis program by using the finite element method (FEM), where material nonlinearity and infinitesimal strains are assumed. Special finite elements with embedded discontinuities were used, allowing the condensation at elemental level of the degrees of freedom related to the displacement jump. The use of an *implicit-*

explicit integration scheme (IMPLEX) for the constitutive equation (Oliver, Huespe et al. 2004a; Oliver, Huespe et al. 2006) ensures a positive defined stiffness matrix of the problem and increases the robustness and stability of the solution. On the other hand, a match of discontinuity paths among elements is achieved through a tracking strategy of discontinuity paths (Samaniego 2002; Oliver & Huespe 2004a).

- *Validation.* Reinforced concrete members submitted to tension, bending and shear were simulated. The numerical results, mainly the structural response and cracks pattern, were compared with experimental test of other authors. With the purpose of establishing the evolution of the crack spacing and the bond-slip length, a piece of great length reinforced in center with a steel bar and submitted to tension was modeled. Likewise, tests carried out by Ouyang and Shah (1994), in which a concrete panel under tension is reinforced by three steel bars were modeled. Next, two lightly reinforced beams with different ratio of steel reported by references (Ruiz, Elices et al. 1998) and four strongly reinforced beams with diverse relations between length and height presented by Leonhardt (1965), were simulated. Finally, three panels subjected to shear with uniformly distributed steel bars in one or two directions presented by Collins and Vecchio (Collins, Vecchio et al. 1985) were modeled. Each problem was discretized with linear triangular finite elements describing the behavior of the reinforced concrete treated as a composite material or in some cases, the simple concrete treated as a homogeneous material. During the fracture process, the structural response and crack pattern were represented in the numerical model by means of the load-displacement curve and the concentration of contour lines of displacement respectively.

4.1. Conclusions

The conclusions derived from the formulation, implementation and application of the model presented in this work are as follows:

4.1.1. General Conclusions

- A numerical model based on the *continuum strong discontinuity approach* (CSDA) and the *mixing theory* can simulate the structural response and cracks pattern during the fracture process, in reinforced concrete members under different states of static loads.

- The correlation obtained between numerical results by using the propose formulation and real results reported by some references (Leonhardt 1965; Collins, Vecchio et al. 1985; Ouyang & Shah 1994; Ruiz, Elices et al. 1998), was quantitative and qualitatively satisfactory.

- The presence of reinforcement besides of increasing the stiffness and the strength of the composite material modifies the instability material condition and the cracks propagation. These changes are perceived in the discontinuous bifurcation analysis of each material reinforced concrete point, which depends on the concrete and steel properties, as well as, on the amount and direction of the reinforcement bars.

- The model can represents two cracking states in the reinforced concrete. Initially, in a stable distributed cracking state, several cracks maintain spacing and constant opening, provided by the capacity of the reinforcement and the adherence in the concrete-steel interface. Next, in localized cracking state, one or few cracks prevail while the structural capacity decays.

- Part of the practical application of model appears in the evaluation of preexisting reinforced concrete structures as walls and beams, where it is necessary to simulate the fracture process from the formation of cracks to the global collapse. It is important to keep in the mind that in the analysis scale each material point consists of a steel fraction and another of concrete, supposing a uniform distribution of the reinforcement and neglecting consequently the constructive details such as hooks, overlap, ties, etc.

4.1.2. Conclusions derived from the formulation and implementation of the model

- The formulation of a constitutive model that directly describes the strain and stress fields in a point of composite material as the reinforced concrete offers two important advantages. The former facilitates the implementation in the finite elements method, since many of the ingredients of the conventional numerical procedure are kept. The latter analyses the problem in a structural or macroscopic scale that avoids the high computational cost because of mesh for each component material and its effects of interaction.

- The *continuum strong discontinuity approach* can be applied to materials reinforced with long fibers with facility, considering a common strain field such as it is established by *mixing theory*.

- The presented formulation preserves the context of the continuous mechanics, although each material point shows a discontinuous character due to the development of cracks and the mechanical differences between concrete and steel.

- The *slipping fiber model* incorporates the difference between the strain of matrix and fiber as resulting from the adherence loss between both materials, without affecting the basic hypotheses of the *mixing theory*. The parameters necessary to describe this model are obtained from some pull-out tests of bars embedded in a concrete block.

- The *dowel action* is defined as the shear capacity of the reinforcement bars crossing a crack. In the formulation is introduced a one-dimensional shear model in the steel for simulating this behavior. This effect is characterized by the mechanical properties of the material and the geometric properties of the cross section of the bars.

4.1.3. Conclusions derived from numerical modeling

- By means of the numerical simulation a good approach of the real structural response of the tests of tension panels (Ouyang & Shah 1994) and lightly reinforced beams (Ruiz, Elices et al. 1998) was obtained. In the same way, the concentration of the displacement contour lines of the numerical analysis, matches with the pattern of the cracks in the strongly reinforced beams (Leonhardt 1965). The numerical results of shear panels (Collins, Vecchio et al. 1985; Bhide & Collins 1989) were satisfactory, as much in the structural response as in the propagation of the cracks.

- During the fracture process to tension of a panel reinforced in the center, the amount of cracks and the slipping zone increases progressively. However, after the total debonding between both materials, the loss of stress transference prevents the development of new discontinuities in the concrete, maintaining a constant distance between the existing cracks; this stage denominates *saturated crack condition*. Until this moment the same opening in each of the cracks is conserved, but when the fibers reach the yielding stress some cracks will have more opening than others.

- In the simulation of a panel under tension load (Ouyang & Shah 1994; Ouyang, Wollrab et al. 1997), the capacity of reinforcement and the interface adherence produce in the concrete a stable damage stage, where several cracks maintain a constant spacing and opening. When the adherence is lost, the structural capacity decreases while the opening of a single crack crossing the member prevails.

- The amount of reinforcement of the beams determines the maximum load and the distribution of the cracks. For low steel ratio or for simple concrete, in half of the beam appears a single crack in mode I of fracture as a result of the high tension by bending. However, for strongly reinforced beams the propagation of several symmetrical cracks from the center to the supports is induced by the steel bars.

- The numerical result of lightly reinforced beams (Ruiz, Elices et al. 1998), can represent the main crack as the concentration of the displacement contour lines and the secondary cracks as the evolution of the damage varible in the concrete around the reinforcement.

- During the fracture process of strongly reinforced beams (Leonhardt 1965), approximately parallel cracks appear in a sequential way. However, the general collapse of the structure is determined by the development of a diagonal crack, which is propagated between the support and the applied load.

- The reinforced concrete members with bars distributed uniformly can be represented as solids of a unique composite material, in which, the amount of reinforcement in each direction is determined by the respective volumetric participation. In the numerical modeling of the shear panels (Collins, Vecchio et al. 1985; Bhide & Collins 1989), two cracking stages were observed. In the *stable distributed cracking stage* appear many parallel cracks distributed by the entire panel, nevertheless, the numerical simulation does not show a specific process of localization, in spite of the inelastic regime present in the panel. Such situation can be understood as the development of multiple cracks stabilized by the presence of the reinforcement steel. In return, the *localized cracking stage* shows the development of some macro-cracks of greater opening, represented in the simulation by the bands of localization of the strain.

- The shear capacity of the steel bars provides an important contribution structural response of reinforced concrete panel submitted to shear. When the *dowel action* is despised in a panel subjected to pure shear in plane *xy*, the axial capacity of the bars in *x*-direction does not generate any contribution to the capacity to shear of the composite material; therefore, the crack pattern and the structural response show a behavior similar to the expected in a simple concrete panel.

4.2. Main contributions of the work

The main contributions given by this work are indicated next.

- The formulation of a constitutive model of composite material conformed by matrix and two long fiber packages able to represent the development and propagation of cracks.

- The extension of the *continuum strong discontinuity approach* to composite materials that maintain a common enhanced kinematics between their components.

- The discontinuous bifurcation analysis that establishes the bifurcation time and the direction of the discontinuity surface in a point of composite material, based on the properties of the matrix and fibers.

- The implementation of the model for static two-dimensional problems using a *kinematically consistent symmetrical finite elements* with *embedded discontinuities* linear triangular.

- The application of the contributions before mentioned to the reinforced concrete, considering the shear capacity of the bars between the faces of a crack and the adherence loss between concrete and steel.

4.3. Future work

This work tries to provide a departure point for new developments and applications related to the numerical simulation of the material failure on composite materials. The future lines of this work are as follows:

- The application to materials reinforced with long fibers different to the reinforced concrete; this requires appropriate constitutive models for the matrix, the fibers and the effects of slipping between both of them.

- The two-dimensional simulation of materials reinforced with fibers oriented in three or more different directions, adding to the presented formulation new component materials defined by one-dimensional constitutive models.

- The extension of the formulation to three-dimensional problems where the material is reinforced with three or more fiber packages oriented in the space. As well as the respective implementation in solid finite elements, for example, elements linear tetrahedrons.

- The addition of new analytical and numerical models of interaction fiber-matrix to the formulation. For example, formulations in a smaller scale on a unitary cell by means of homogenization methods.

- The elaboration of a model that allows the modeling of process of fracture in plates and reinforced concrete shells.

- The development of a model describing the behavior of materials reinforced with short fibers considering the character random of its direction.

- A formulation considering strain finite with the purpose of representing the ductile behavior of the composite material given by fibers in advanced states of strain.

- The insertion into the model of other effects as the local buckling of fibers and the reorientation of the same by great displacements.

- The application of the model in the numerical simulation of reinforced concrete structures of great size, under static load or mainly dynamic load.

Appendix A.
Damage and plasticity models

A.1. Scalar damage constitutive model

A.1.1. Mechanical representation of damage (Lemaitre 1992)

From the physical point of view, the amounts defined in a material point represent average values on certain characteristic volume. This volume must be small enough to avoid the incorrect smoothing of high gradients, but large enough to represent conveniently an average of the mechanical processes of the micro-structure.

In an isotropic damage model the directional characteristics of the virgin material are conserved during the degradation process. It is the case of the scalar damage models, where a scalar internal variable affects equally to all the components of the material constitutive tensor.

The damage represents the micro-cracking level of material in a defined volume. The size of this volume must be small enough to allow describing the phenomenon as an average value of the strain in his interior. In a representative volume, the damage variable in a specific direction $\mathbf{n}_d$ is expressed as the relation between the area of the projection of the crack on a plane normal to $\mathbf{n}_d$ and the area of that same plane.

Given a volume differential in a solid material point M and a normal plane of $\mathbf{n}_d$ which cuts it, the surface dS will be the intersection between that plane and the differential volume dV. The surface dS_d will be the projection of all the micro-cracks on the surface dS as is indicated in Figure A.1.

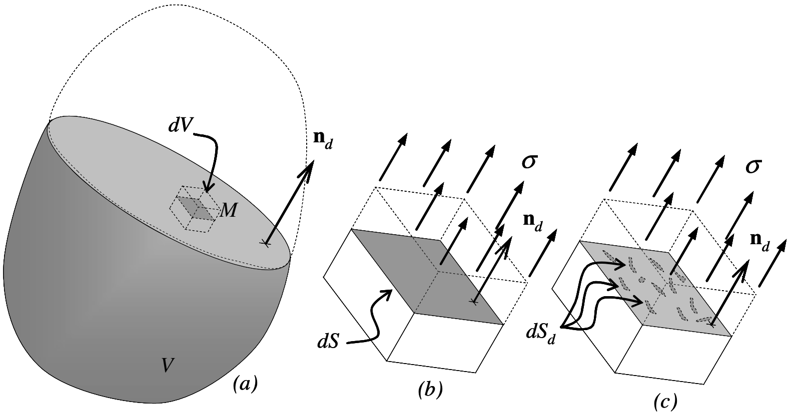

Figure A.1. Description of the damage: (a) solid, (b) non-damaged differential volume, (c) damaged differential volume.

The damage variable in material point $M(\mathbf{x},t)$ in location $\mathbf{x}$, at a time t and the direction $\mathbf{n}_d$ is defined as:

$$d_n(\mathbf{x},t,\mathbf{n}_d)=\frac{dS_d}{dS} \quad , \quad 0\le d_n\le 1 \tag{A.1}$$

where $d_n=0$ indicates that there is no damage in the material; however, when $d_n=1$, the material completely is damaged (Kachanov 1986). The internal forces on the surface *dS* disappear in the formation zones of the micro-cracks reducing the stress normal surface to the effective area $(dS - dS_d)$.

The applied tension σ normal to the plane $\mathbf{n}_d$ in the differential volume *dV* is equal to axial force *dF* per unit area of the cross section *dS*. Likewise, the effective stress $\bar{\sigma}$ normal to the plane $\mathbf{n}_d$ is defined as force *dF* per unit of effective area $(dS - dS_d)$, of the form:

$$\sigma=\frac{dF}{dS} \quad , \quad \bar{\sigma}=\frac{dF}{dS-dS_d} \tag{A.2}$$

The effective stress can be written in terms of the applied stress and the damage variable, thus:

$$\bar{\sigma}=\frac{\sigma}{1-d_n} \tag{A.3}$$

Assuming that the degradation of a material point $M(\mathbf{x},t)$ at a time t is the same in any direction as establishes an isotropic model, the damage variable will be:

$$d_n(\mathbf{x},t,\mathbf{n}_d)=d(\mathbf{x},t) \quad \forall\, \mathbf{n}_d \tag{A.4}$$

In a three-dimensional space considering a scalar damage variable, the tension of the effective stress tensor $\bar{\boldsymbol{\sigma}}$ is equal to:

$$\bar{\boldsymbol{\sigma}} = \left(\frac{1}{1-d_n} \right) \boldsymbol{\sigma} \tag{A.5}$$

where $\boldsymbol{\sigma}$ corresponds to the applied stress tensor.

In an anisotropic damage model where the directional character of the material degradation is considered, the damage is described by means of a vector, a second-order tensor or even a fourth-order tensor. The most general way to define the effective stress tensor is indicated in the following equation, where $\mathbb{M}$ is the fourth-order damage tensor.

$$\bar{\boldsymbol{\sigma}} = \mathbb{M}^{-1} : \boldsymbol{\sigma} \tag{A.6}$$

The isotropic damage model is the special case in which the tensor $\mathbb{M}$ is isotropic. Likewise, the scalar damage model is, particularly, an isotropic model in which $\mathbb{M} = (1-d_n)\mathbb{I}$ (where $\mathbb{I}$ is the fourth-order identity tensor).

A.1.2. Constitutive equation of the damage model

Strain equivalence principle defined by Lemaitre and Chaboche (Lemaitre 1992) establishes that the strain associated to a damaged state under the action of the applied stress is equivalent to the strain associated to a non-damaged state under the action of the effective stress. Therefore, the one-dimensional law of the material behavior can be written as,

$$\left. \begin{array}{r} d_n = 0 \\ \varepsilon = \dfrac{\sigma}{E} \rightarrow \sigma = E\varepsilon \end{array} \right\} \text{ (non-damage material)} \tag{A.7}$$

$$\left. \begin{array}{r} 0 < d_n < 1 \\ \varepsilon = \dfrac{\bar{\sigma}}{E} = \dfrac{\sigma}{(1-d_n)E} \\ \bar{\sigma} = E\varepsilon,\ \sigma = (1-d_n)E\varepsilon \end{array} \right\} \text{ (damage material)} \tag{A.8}$$

On the other hand, Helmholtz's free energy density per unit volume in a scalar degradation process is given by the following expression (Simó & Ju 1987):

$$\begin{aligned} \Psi(\boldsymbol{\varepsilon}, d) &= (1-d_n)\Psi_e(\boldsymbol{\varepsilon}) \\ \Psi_e(\boldsymbol{\varepsilon}) &= \frac{1}{2}\boldsymbol{\varepsilon} : \mathbb{C} : \boldsymbol{\varepsilon} \end{aligned} \tag{A.9}$$

where $\psi_e(\boldsymbol{\varepsilon})$ is elastic free energy density per unit volume and $\mathbb{C}$ is two-dimensional elastic constitutive tensor expressed as:

$$\mathbb{C} = \frac{E}{1-\nu^2}\left[\nu(\mathbf{1} \otimes \mathbf{1}) + (1-\nu)\mathbb{I}\right] \text{ (plane stress)} \tag{A.10}$$

$$\mathbb{C} = \frac{E}{(1+\nu)(1-2\nu)}\left[\nu\,(\mathbf{1}\otimes\mathbf{1}) + (1-2\nu)\,\mathbb{I}\right] \quad \text{(plane strain)} \tag{A.11}$$

In the earlier equations E and ν are Young's modulus and Poisson's ratio of the material. Likewise, **1** and $\mathbb{I}$ indicate the identity tensors of second-order and fourth-order, respectively.

The energy dissipation per unit volume in mechanical problems with infinitesimal strain is equal to:

$$\Xi = \boldsymbol{\sigma} : \dot{\boldsymbol{\varepsilon}} - \dot{\Psi} \geq 0 \tag{A.12}$$

where $\boldsymbol{\sigma}$ y $\boldsymbol{\varepsilon}$ correspond to the stress and strain tensor.

Since $\dot{\Psi}(\boldsymbol{\varepsilon}, d_n) = (\partial_{\varepsilon}\Psi) : \dot{\boldsymbol{\varepsilon}} + (\partial_{d^m}\Psi)\,\dot{d}_n$ and $(\partial_{d^m}\Psi) = -\Psi_e$, the earlier equation can be written as:

$$\Xi = \left[\boldsymbol{\sigma} - (\partial_{\varepsilon}\Psi)\right] : \dot{\boldsymbol{\varepsilon}} + \Psi_e \dot{d} \geq 0 \tag{A.13}$$

By applying Coleman's method (Maugin 1992) to the inequality expressed in the earlier equation, the constitutive equation of the model and the energy dissipation per unit volume are obtained of the form:

$$\boldsymbol{\sigma} = \partial_{\varepsilon}\Psi = (1-d_n)\mathbb{C} : \boldsymbol{\varepsilon} \tag{A.14}$$

$$\Xi = \Psi_e \dot{d}_n \geq 0 \rightarrow \dot{d}_n \geq 0 \tag{A.15}$$

The following expression of the effective stress is extracted from Equation (A.14).

$$\bar{\boldsymbol{\sigma}} = \mathbb{C} : \boldsymbol{\varepsilon} \tag{A.16}$$

A.1.3. Ingredients of the damage model

The essential ingredients of the scalar damage model (Simó & Ju 1987) are summarized in Table A.1.

Here the damage variable d_n is indicated in terms of the stress-like internal variable q and strain-like internal variable r, Helmholtz's free energy density per unit volume $\psi(\boldsymbol{\varepsilon}, r)$, the relationship between stress $\boldsymbol{\sigma}$ and strain $\boldsymbol{\varepsilon}$, the evolution law of the internal variable and the softening, the damage function $f(\boldsymbol{\varepsilon}, r)$ and loading-unloading conditions of the model.

$d_n = 1 - \frac{q}{r}$	(damage variable)	(A.17)
$\psi(\boldsymbol{\varepsilon}, r) = \frac{q}{r}\left(\frac{1}{2}\boldsymbol{\varepsilon} : \mathbb{C} : \boldsymbol{\varepsilon}\right)$	(free energy)	(A.18)
$\boldsymbol{\sigma} = \frac{\partial \psi(\boldsymbol{\varepsilon}, r)}{\partial \boldsymbol{\varepsilon}} = \frac{q}{r}\mathbb{C} : \boldsymbol{\varepsilon} = \frac{q}{r}\bar{\boldsymbol{\sigma}}$	(constitutive equation)	(A.19)
$\dot{r} = \lambda, \quad r_{t=0} = \frac{\sigma_u}{\sqrt{E}}$	(evolution law)	(A.20)
$\left.\begin{array}{l} \dot{q} = H(r)\,\dot{r} \quad , \quad H = \frac{dq}{dr} \leq 0 \\ 0 \leq q \leq r_{t=0} \quad , \quad q_{t=0} = r_{t=0} \end{array}\right\}$	(softening law)	(A.21)
$f(\boldsymbol{\varepsilon}, r) = \tau_\varepsilon - r$	(damage criteria)	(A.22)
$\left.\begin{array}{l} f \leq 0, \quad \lambda \geq 0, \quad \lambda f = 0 \\ \lambda \dot{f} = 0 \;\; (f = 0) \end{array}\right\}$	(loading-unloading and persistency conditions)	(A.23)

Table A.1. Ingredients of an isotropic scalar damage model.

In earlier equations, σ_u is the tensile strength of the material, H is the softening parameter, λ is the damage multiplier and τ_ε is the strain norm.

From the evolution law of r given in Equation (A.20) and of the loading and unloading conditions in Equation (A.23), the increasing character of the strain-like internal variable is obtained. Therefore r can be integrated of closed form as (Figure A.2):

$$r(t) = \max_{t' \in [0,t]}\left(r_{t'}, \tau_\varepsilon(t')\right) \tag{A.24}$$

The norm τ_ε is a scalar function which indicates the strain state and determines the elastic domain of the model. Simó and Ju (Simó & Ju 1987) propose a strain norm, applicable to materials with the same strength to tension and compression $\left(\sigma_{u(c)} = \sigma_u\right)$, thus:

$$\tau_\varepsilon = \sqrt{\bar{\boldsymbol{\sigma}} : (\mathbb{C})^{-1} : \bar{\boldsymbol{\sigma}}} \tag{A.25}$$

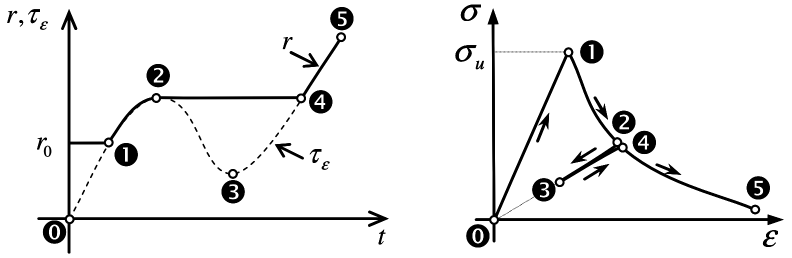

(a) *(b)*

Figure A.2. Scalar damage model: (a) evolution of the internal variable and the strain norm, (b) uniaxial stress *vs* strain curve.

A.1.4. Damage model with degradation in tension and compression

A modification to the earlier scheme considers the degradation of a material with different strength to tension and compression. The model developed by Oliver and collaborators (Oliver, Cervera et al. 1990) represents the degradation of a material whose compressive strength $\sigma_{u(c)}$ is n_σ times the tensile strength σ_u, i.e. $n_\sigma = \sigma_{u(c)} / \sigma_u$. The elements of this model appear in Table A.1. In addition, the strain norm is defined as:

$$\tau_\varepsilon = \phi \sqrt{\bar{\boldsymbol{\sigma}} : (\mathbb{C})^{-1} : \bar{\boldsymbol{\sigma}}} \tag{A.26}$$

where,

$$\phi = \frac{\sum_{i=1}^{3} \langle \bar{\sigma}_i \rangle}{\sum_{i=1}^{3} |\bar{\sigma}_i|} \left(1 - \frac{1}{n_\sigma} \right) + \frac{1}{n_\sigma} \tag{A.27}$$

and $|\bar{\sigma}_i|$ is the absolute value of the stress $\bar{\sigma}_i$.

$$\langle \bar{\sigma}_i \rangle = \frac{1}{2} \left(\bar{\sigma}_i + |\bar{\sigma}_i| \right) \tag{A.28}$$

Also, $\bar{\sigma}_1, \bar{\sigma}_2, \bar{\sigma}_3$ correspond to effective stresses in principal directions 1,2 and 3 respectively.

For a two-dimensional tensional state where $(\bar{\sigma}_1 < 0, \bar{\sigma}_2 < 0)$, the elastic domain is n_σ times greater than the elastic domain defined when $(\bar{\sigma}_1 > 0, \bar{\sigma}_2 > 0)$ as observed in Figure A.3(a). If $\bar{\sigma}_1$ is positive and $\bar{\sigma}_2$ is negative or vice versa, a approximate transition defined by the factor ϕ takes place (Equation (A.27)).

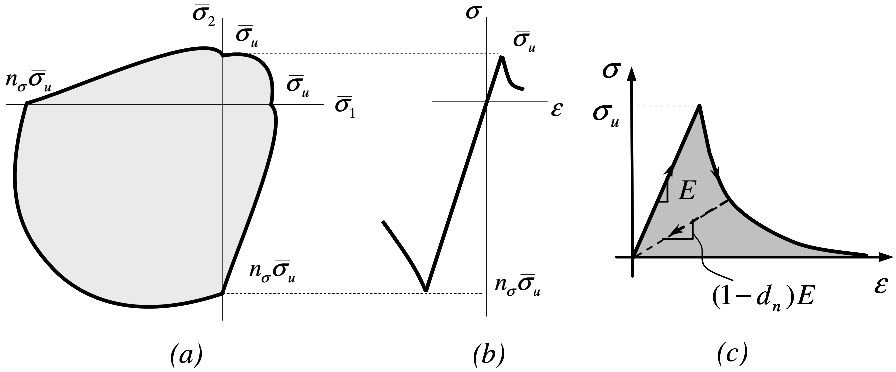

Figure A.3. Damage model with degradation in tension and compression: (a) Damage surface, (b) uniaxial stress *vs* strain curve.

Remark A.1 *Unlike the plasticity models, in the used damage model is not necessary that the elastic domain is convex in order to conserve uniqueness of the solution; therefore, the non-convex damage surface shown in Figure A.3(a) is permissible for this constitutive model.*

The strain norm rate is obtained by differentiation of Equation (A.26) on the time, thus:

$$\dot{\tau}_\varepsilon = \left(\frac{\tau_\varepsilon}{\phi} \mathbb{C} : (\partial_{\bar{\boldsymbol{\sigma}}} \phi) + \frac{\phi^2}{\tau_\varepsilon} \bar{\boldsymbol{\sigma}} \right) : \dot{\boldsymbol{\varepsilon}} \tag{A.29}$$

Likewise, the stress rate computed from Equation (A.19) and the softening law (Equation (A.21)), is equal to:

$$\dot{\boldsymbol{\sigma}} = \frac{q}{r} \mathbb{C} : \dot{\boldsymbol{\varepsilon}} + \frac{Hr - q}{r^2} \dot{r}\, \bar{\boldsymbol{\sigma}} \tag{A.30}$$

Therefore, in elastic or unloading regime ($\lambda = \dot{r} = 0$), the stress rate is equal to $\dot{\boldsymbol{\sigma}} = (q/r)\mathbb{C} : \dot{\boldsymbol{\varepsilon}}$. In return, in inelastic loading regime ($\lambda = \dot{r} > 0$) must be fulfilled that $\lambda \dot{f} = 0$ for $f = \tau_\varepsilon - r = 0$; consequently, the internal variable is equal to the strain norm ($r = \tau_\varepsilon$) indicated in Equation (A.26) and internal variable rate $\dot{r} = \dot{\tau}_\varepsilon$ expressed in Equation (A.29). Replacing the values of r and $\dot{r}$ into Equation (A.30),

$$\dot{\boldsymbol{\sigma}} = \frac{q}{r} \mathbb{C} : \dot{\boldsymbol{\varepsilon}} + \frac{Hr - q}{r^2} \left(\frac{r}{\phi} \left(\bar{\boldsymbol{\sigma}} \otimes \left(\mathbb{C} : \partial_{\bar{\boldsymbol{\sigma}}} \phi \right) \right) + \frac{\phi^2}{r} \left(\bar{\boldsymbol{\sigma}} \otimes \bar{\boldsymbol{\sigma}} \right) \right) : \dot{\boldsymbol{\varepsilon}} \tag{A.31}$$

The tangent constitutive equation of the model is defined as:

$$\dot{\boldsymbol{\sigma}} = \mathbb{C}_{tg} : \dot{\boldsymbol{\varepsilon}} \tag{A.32}$$

in which, the tangent constitutive tensor $\mathbb{C}_{tg}$ in elastic or unloading regime is equal to:

$$\mathbb{C}_{tg} = \frac{q}{r}\mathbb{C} \tag{A.33}$$

and in inelastic loading regime corresponds to:

$$\mathbb{C}_{tg} = \frac{q}{r}\mathbb{C} - \left(\frac{q-Hr}{r^3}\right)\cdot\left[\frac{r^2}{\phi}\left(\bar{\boldsymbol{\sigma}}\otimes\mathbf{A}\right)+\phi^2\left(\bar{\boldsymbol{\sigma}}\otimes\bar{\boldsymbol{\sigma}}\right)\right] \tag{A.34}$$

where,

$$\mathbf{A} = \mathbb{C} : \partial_{\bar{\boldsymbol{\sigma}}}\phi \tag{A.35}$$

$$\partial_{\bar{\boldsymbol{\sigma}}}\phi = \frac{\left(1-\dfrac{1}{n_\sigma}\right)}{\left(\sum_{i=1}^{3}\left|\bar{\sigma}_i\right|\right)^2}\cdot\left[\sum_{i=1}^{3}\left|\bar{\sigma}_i\right|\cdot\sum_{i=1}^{3}\frac{\partial\left\langle\bar{\sigma}_i\right\rangle}{\partial\bar{\boldsymbol{\sigma}}}-\sum_{i=1}^{3}\left\langle\bar{\sigma}_i\right\rangle\cdot\sum_{i=1}^{3}\frac{\partial\left|\bar{\sigma}_i\right|}{\partial\bar{\boldsymbol{\sigma}}}\right] \tag{A.36}$$

When both effective principal stresses are positive the parameter ϕ is equal to 1 and its derivative with respect to the effective stress $\partial_{\bar{\boldsymbol{\sigma}}}\phi$ is equal to a null tensor. In this case the tangent constituent operator recovers the form obtained for an isotropic damage model of symmetrical elastic domain to tension and compression, whose strain norm is indicated in the Equation (A.25). For negative effective principal stresses $\phi = 1/n_\sigma$ and $\partial_{\bar{\boldsymbol{\sigma}}}\phi = \mathbf{0}$; therefore, the tangent constitutive tensor is equal to the corresponding tensor of the damage model with symmetrical elastic domain limited by a stress $n_\sigma\sigma_u$. In other cases where the sign of the effective principal stresses is different, the derivative $\partial_{\bar{\boldsymbol{\sigma}}}\phi \neq \mathbf{0}$ and the parameter ϕ is calculated as it is indicated in Equation (A.27). In two-dimensional problems the parameter ϕ is obtained by replacing the principal stress expressions,

$$\begin{aligned} \bar{\sigma}_1 &= \left(\frac{\bar{\sigma}_{xx}+\bar{\sigma}_{yy}}{2}\right)+\bar{\sigma}_r \quad , \quad \bar{\sigma}_2 = \left(\frac{\bar{\sigma}_{xx}+\bar{\sigma}_{yy}}{2}\right)-\bar{\sigma}_r \\ \bar{\sigma}_r &= \sqrt{\left(\frac{\bar{\sigma}_{xx}-\bar{\sigma}_{yy}}{2}\right)^2+\left(\bar{\tau}_{xy}\right)^2} \end{aligned} \tag{A.37}$$

into Equation (A.27), yielding:

$$\phi = \left(1-\frac{1}{n_\sigma}\right)\cdot\left[\frac{1}{2}+\left(\frac{\bar{\sigma}_{xx}+\bar{\sigma}_{yy}}{4\bar{\sigma}_r}\right)\right]+\frac{1}{n_\sigma} \tag{A.38}$$

The derivatives of ϕ with respect to the effective stresses tension $\partial_{\bar{\boldsymbol{\sigma}}}\phi$ are the result of replacing Equation (A.37) into Equation (A.36), as follows:

$$
\begin{aligned}
\partial_{\bar{\boldsymbol{\sigma}}}\phi &= \begin{bmatrix} \partial\phi/\partial\bar{\sigma}_{xx} & \partial\phi/\partial\bar{\sigma}_{xy} \\ \partial\phi/\partial\bar{\sigma}_{xy} & \partial\phi/\partial\bar{\sigma}_{yy} \end{bmatrix} \\
\partial\phi/\partial\bar{\sigma}_{xx} &= \left(1-\frac{1}{n}\right)\cdot\frac{1}{4\bar{\sigma}_r}\cdot\left[1-\left(\frac{\bar{\sigma}_{xx}-\bar{\sigma}_{yy}}{2\bar{\sigma}_r}\right)\left(\frac{\bar{\sigma}_{xx}+\bar{\sigma}_{yy}}{2\bar{\sigma}_r}\right)\right] \\
\partial\phi/\partial\bar{\sigma}_{yy} &= \left(1-\frac{1}{n}\right)\cdot\frac{1}{4\bar{\sigma}_r}\cdot\left[1+\left(\frac{\bar{\sigma}_{xx}-\bar{\sigma}_{yy}}{2\bar{\sigma}_r}\right)\left(\frac{\bar{\sigma}_{xx}+\bar{\sigma}_{yy}}{2\bar{\sigma}_r}\right)\right] \\
\partial\phi/\partial\bar{\sigma}_{xy} &= -\left(1-\frac{1}{n}\right)\cdot\frac{\bar{\sigma}_{xy}}{4(\bar{\sigma}_r)^2}\cdot\left(\frac{\bar{\sigma}_{xx}+\bar{\sigma}_{yy}}{\bar{\sigma}_r}\right)
\end{aligned}
\qquad \text{(A.39)}
$$

When the effective stresses have different signs, the tensor **A** depends on the elastic constitutive operator as shown in Equation (A.35). Therefore, in plane stress condition,

$$
\mathbf{A} = \frac{E}{1-\nu^2}\left[\nu\, tr(\partial_{\bar{\boldsymbol{\sigma}}}\phi)\mathbf{1} + (1-\nu)\partial_{\bar{\boldsymbol{\sigma}}}\phi\right] \qquad \text{(A.40)}
$$

and plane strain condition,

$$
\mathbf{A} = \frac{E}{(1+\nu)(1-2\nu)}\left[\nu\, tr(\partial_{\bar{\boldsymbol{\sigma}}}\phi)\mathbf{1} + (1-2\nu)\partial_{\bar{\boldsymbol{\sigma}}}\phi\right] \qquad \text{(A.41)}
$$

In summary, for all tensional state, the tensor **A** and the derivative of ϕ with respect to the effective stress $\partial_{\bar{\boldsymbol{\sigma}}}\phi$ correspond to:

$$
\begin{aligned}
&for \quad (\bar{\sigma}_1 > 0 \wedge \bar{\sigma}_2 > 0): \quad \phi = 1 \quad , \quad \partial_{\bar{\boldsymbol{\sigma}}}\phi = \mathbf{0} \quad \rightarrow \quad \mathbf{A} = \mathbf{0} \\
&for \quad (\bar{\sigma}_1 < 0 \wedge \bar{\sigma}_2 < 0): \quad \phi = 1/n_\sigma \, , \quad \partial_{\bar{\boldsymbol{\sigma}}}\phi = \mathbf{0} \quad \rightarrow \quad \mathbf{A} = \mathbf{0} \\
&for \quad (\bar{\sigma}_1 > 0 \wedge \bar{\sigma}_2 < 0) \quad \vee \quad (\bar{\sigma}_1 < 0 \wedge \bar{\sigma}_2 > 0) \quad en \quad 2D: \\
&\qquad \phi \rightarrow \text{(A.38)}\, , \ \partial_{\bar{\boldsymbol{\sigma}}}\phi \neq \mathbf{0} \rightarrow \text{(A.39)}\, , \ \mathbf{A} \neq \mathbf{0} \rightarrow \text{(A.40) o (A.41)}.
\end{aligned}
\qquad \text{(A.42)}
$$

In Equation (A.34), it is observed that the tangent constitutive tensor loses its symmetry when $\mathbf{A} \neq \mathbf{0}$. As the earlier equation indicates it, this occurs for a tensional state in which the effective principal stresses are of opposite sign.

A.2. One-dimensional plasticity constitutive model

In this section, the one-dimensional plasticity isotropic constitutive model with hardening or softening strain is presented (Simó & Hughes 1998).

The ingredients of the mathematical model are indicated in Table A.2, such as the constitutive equation, the flow rule, the evolution law of the internal variable, the plasticity criterion, the softening rule and the loading and unloading conditions of the model.

$\sigma = E(\varepsilon - \varepsilon_p)$	(constitutive equation)	(A.43)
$\dot{\varepsilon}_p = \lambda \operatorname{sign}(\sigma)$	(flow rule)	(A.44)
$\dot{\alpha} = \lambda$	(evolution law)	(A.45)
$f(\sigma, \alpha) = \lvert\sigma\rvert - (q + \sigma_y)$	(plasticity criterion)	(A.46)
$\dot{q} = H\dot{\alpha}$	(softening rule)	(A.47)
$\left.\begin{array}{r} f \le 0\,;\ \lambda \ge 0\,;\ \lambda f = 0 \\ \lambda \dot{f} = 0\ (f = 0) \end{array}\right\}$	(loading-unloading and persistency conditions)	(A.48)

Table A.2. Ingredients of a one-dimensional plasticity model.

In the earlier equations, E and σ_y correspond to Young's modulus and yielding stress of the material. ε_p is the plastic strain, λ is the plastic multiplier, $f(\sigma, \alpha)$ is the yielding function, $H < 0$ is the softening parameter, and α and q are strain-like and stress-like internal variable, respectively.

The tangent constitutive equation of the model is written as:

$$\dot{\sigma} = E_{tg} \dot{\varepsilon} \tag{A.49}$$

where the tangent constitutive operator is equal to:

$$E_{tg} = \begin{cases} E & si \quad \lambda = 0 \\ \dfrac{EH}{E + H} & si \quad \lambda > 0 \end{cases} \tag{A.50}$$

Figure A.4 shows the relationship between stress and strain for the one-dimensional plasticity model with softening strain.

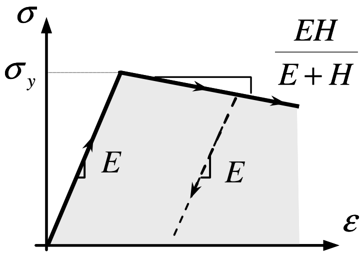

Figure A.4. One-dimensional plasticity model with softening strain.

Appendix B.
Mixing theory for composite materials

The *mixing theory* or *rule of mixtures* (Truesdell & Toupin 1960) allows representing the behavior of a composite material from the constitutive law and of the volume of each component, considering that all point of composite material consists of several components. In this theory, the component materials maintain a common strain among them simultaneously, that contribute to the composite material stress according to their volumetric participation.

Next, the basic hypotheses of mixing theory are indicated and the ingredients of the constitutive model of the composite material are described, such as, the free energy, the stress tensor and the tangent constitutive tensor (Oller, Oñate et al. 1996; Car 2000; Luccioni & Lopez 2002; Oller 2003).

B.1. Basic hypotheses

The description of a point of composite material in the context of continuum mechanics presented by mixing theory is based on the following hypotheses (Truesdell & Toupin 1960):

- In each infinitesimal volume of composite material, all the participated component materials.

- Each component contributes to the behavior of the composite material in proportion to its volumetric participation.

- The volume occupied by each component is less than the total volume of the composite material.

- All the component materials have the same strain (compatibility equation).

In accord with the two first hypotheses, there is a homogenous distribution of all the components in each point of the composite material, which is determined by volumetric participation factor:

$$k^c = \frac{dV^c}{d\bar{V}} \tag{B.1}$$

where $d\bar{V}$ and dV^c correspond to the infinitesimal volume of the composite material and of the component *c*, respectively. Likewise, the volumetric participation factor of the components of a composite material must guarantee the conservation of the mass by means of the following condition:

$$\sum_{c=1}^{cn} k^c = 1 \tag{B.2}$$

The last hypothesis establishes that the strain compatibility equation is of the form:

$$\boldsymbol{\varepsilon} = \boldsymbol{\varepsilon}^{(1)} = \boldsymbol{\varepsilon}^{(2)} = \ldots = \boldsymbol{\varepsilon}^{c} = \ldots = \boldsymbol{\varepsilon}^{cn} \tag{B.3}$$

where $\boldsymbol{\varepsilon}$, $\boldsymbol{\varepsilon}^c$ and $\boldsymbol{\varepsilon}^{cn}$ correspond to the strains in the composite material, in the component *c* and in the component *cn*, respectively.

B.2. Free energy of the composite material

The free energy of a composite material is given by the sum of the free energies of each of the component materials, weighted according to its volumetric participation in the composite material, thus (Truesdell & Toupin 1960):

$$\Psi(\boldsymbol{\varepsilon},\boldsymbol{\alpha}) = \sum_{c=1}^{cn} k^c \Psi^c(\boldsymbol{\varepsilon}^c,\boldsymbol{\alpha}^c) \tag{B.4}$$

where $\Psi(\boldsymbol{\varepsilon},\boldsymbol{\alpha})$ is the free energy per unit volume of composite material in terms of the strain tensor $\boldsymbol{\varepsilon}$ and the internal variables vector $\boldsymbol{\alpha}$. Similarly, $\Psi^c(\boldsymbol{\varepsilon}^c,\boldsymbol{\alpha}^c)$ corresponds to the free energy per unit volume of the component *c*, in terms of the strain tensor $\boldsymbol{\varepsilon}^c$ and the internal variables vector $\boldsymbol{\alpha}^c$.

The energy dissipation per unit volume in the composite material can be expressed of the form:

$$\Xi = \boldsymbol{\sigma} : \dot{\boldsymbol{\varepsilon}} - \dot{\Psi} \geq 0 \tag{B.5}$$

where $\boldsymbol{\sigma}$ is the stress tensor.

Since $\dot{\Psi}(\boldsymbol{\varepsilon}, \boldsymbol{\alpha}) = (\partial_{\varepsilon}\Psi) : \dot{\boldsymbol{\varepsilon}} + (\partial_{\alpha}\Psi) \cdot \dot{\boldsymbol{\alpha}}$, Equation (B.5) can be written as:

$$\Xi = \left[\boldsymbol{\sigma} - (\partial_{\varepsilon}\Psi)\right] : \dot{\boldsymbol{\varepsilon}} - (\partial_{\alpha}\Psi) \cdot \dot{\boldsymbol{\alpha}} \geq 0 \tag{B.6}$$

Applying Coleman's method to earlier inequality (Lubliner 1990), the stress tensor of the composite material is equal to:

$$\boldsymbol{\sigma} = (\partial_{\varepsilon}\Psi) = \sum_{c=1}^{cn} k^{c} (\partial_{\varepsilon}\Psi^{c}) = \sum_{c=1}^{cn} k^{c} \boldsymbol{\sigma}^{c} \tag{B.7}$$

where $\boldsymbol{\sigma}^{c}$ is the stress tensor of the component *c*.

B.3. Tangent constitutive equation of the composite material

The compatibility of the strain field between the components given by *classical mixing theory* facilitates the formulation of a constitutive model for the composite material.

A tangent constitutive equation of the composite material can be written of the form:

$$\dot{\boldsymbol{\sigma}} = \mathbb{C}_{tg} : \dot{\boldsymbol{\varepsilon}} \tag{B.8}$$

where $\mathbb{C}_{tg}$ is the tangent constitutive tensor of the composite material.

The stress rate of the composite material $\dot{\boldsymbol{\sigma}}$ can be obtained by differentiating Equation (B.7) with respect to time, thus:

$$\dot{\boldsymbol{\sigma}} = \sum_{c=1}^{cn} k^{c} \dot{\boldsymbol{\sigma}}^{c} \tag{B.9}$$

where $\dot{\boldsymbol{\sigma}}^{c}$ corresponds to the stress rate of the component *c*.

The compatibility condition or Equation (B.3) can be expressed in terms of the strain rates of the form:

$$\dot{\boldsymbol{\varepsilon}} = \dot{\boldsymbol{\varepsilon}}^{(1)} = \dot{\boldsymbol{\varepsilon}}^{(2)} = \ldots = \dot{\boldsymbol{\varepsilon}}^{c} = \ldots = \dot{\boldsymbol{\varepsilon}}^{cn} \tag{B.10}$$

where, $\dot{\boldsymbol{\varepsilon}}$, $\dot{\boldsymbol{\varepsilon}}^{c}$ and $\dot{\boldsymbol{\varepsilon}}^{cn}$ represent the strain rate of the composite material, of the component *c* and of the component *cn*, respectively.

The behavior of each component is described by means of a particular law, in such a way that, the tangent constitutive equation of component *c* can be expressed as:

$$\dot{\boldsymbol{\sigma}}^c = \mathbb{C}_{tg}^c : \dot{\boldsymbol{\varepsilon}}^c \qquad \text{(B.11)}$$

where $\dot{\boldsymbol{\varepsilon}}^c$ and $\mathbb{C}_{tg}^c$ correspond to the strain rate and the tangent constitutive operator of the component *c*. According to Equation (B.10), the strain rate of the component *c* is equal to strain rate of the composite material, i.e. $\dot{\boldsymbol{\varepsilon}}^c = \dot{\boldsymbol{\varepsilon}}$.

If Equations (B.8) and (B.11) are replaced into Equation (B.9),

$$\mathbb{C}_{tg} : \dot{\boldsymbol{\varepsilon}} = \sum_{c=1}^{cn} k^c \mathbb{C}_{tg}^c : \dot{\boldsymbol{\varepsilon}}^c \qquad \text{(B.12)}$$

Given Equation (B.10) of compatibility of the strain rates, the tangent constitutive tensor of the composite material is equal to:

$$\mathbb{C}_{tg} = \sum_{c=1}^{cn} k^c \mathbb{C}_{tg}^c \qquad \text{(B.13)}$$

Appendix C.

Continuum strong discontinuity approach

In this appendix, the basic ingredients of *continuum strong discontinuity approach* (CSDA) is summarized (Oliver 1996; Oliver 2000; Oliver, Huespe et al. 2002; Oliver, Huespe et al. 2003; Oliver & Huespe 2004a).

The main features of this approach are the following:

- It uses conventional non-linear continuous constitutive equations (stress *vs* strain), equipped with softening strain.

- It considers *strong discontinuity kinematics*. In other words, the discontinuity is induced by the appearance of a jump in the displacement field and consequently unbounded values of the strain field arise in the context of continuum mechanics.

- By means of a mathematical reasoning, called *strong discontinuity analysis*, the approach preserves the compatibility between the constitutive equations in the continuum medium and the strong discontinuity kinematics.

The previous thing demonstrates that each continuous constitutive model induces, in a consistent way, a discrete model (traction - jump). This provides a link between continuum mechanics and the non-linear fracture mechanics (cohesive).

C.1. Strong discontinuity kinematics

C.1.1. One-dimensional description

During the axial extension of a bar of length l and area of the cross section A, a discontinuity strong or jump in the displacement field takes place on a surface S (Figure C.1(c)).

In the notation, Ω / S indicates the set of material points of the domain Ω that they are not part of the surface S. Likewise, Ω^+ and Ω^- indicate the sub-domains of Ω / S around of S. The discontinuous field of the displacement rate can be written as:

$$u(x,t) = \bar{u}(x,t) + \mathcal{H}_S(x) \cdot [\![u]\!](t) \tag{C.1}$$

where $\bar{u}(x,t)$ and $[\![u]\!](t)$ are smooth functions and $\mathcal{H}_S(x)$ is Heaviside's function on S defined as $\mathcal{H}_S(x) = 0$ for $x < x_s$ and $\mathcal{H}_S(x) = 1$ for $x \geq x_s$.

The strains field compatible with the displacements indicated in the Equation (C.1) is equal to:

$$\begin{gathered} \varepsilon(x,t) = \partial_x u(x,t) = \bar{\varepsilon}(x,t) + \delta_S(x)[\![u]\!](t) \text{ , where} \\ \bar{\varepsilon}(x,t) = \partial_x \bar{u}(x,t) + \mathcal{H}_S(x) \cdot \partial_x [\![u]\!](t) \end{gathered} \tag{C.2}$$

and $\delta_S(x)$ is Dirac's delta function on S.

The jump displacement field $[\![u]\!](t)$ is defined as:

$$[\![u]\!](t) = u\big|_{x_s^+} - u\big|_{x_s^-} \tag{C.3}$$

Differentiating the earlier expressions, the strong discontinuity kinematics is obtained as:

$$\begin{cases} \dot{u}(x,t) = \dot{\bar{u}}(x,t) + \mathcal{H}_S(x) \cdot [\![\dot{u}]\!](t) \quad ; \quad [\![\dot{u}]\!](t) = \dot{u}\big|_{x_s^+} - \dot{u}\big|_{x_s^-} \\ \dot{\varepsilon}(x,t) = \dot{\bar{\varepsilon}}(x,t) + \delta_S(x)[\![\dot{u}]\!](t) \end{cases} \tag{C.4}$$

where $\dot{\bar{\varepsilon}}(x,t)$ and $\delta_S(x)[\![\dot{u}]\!](t)$ correspond to the regular part (bounded) and the singular part (unbounded) of the rate strain, respectively (Figure C.1).

Dirac's delta function $\delta_S(x)$ is treated of approximate form as a regularized function $\delta_S^k(x)$, when the discontinuity surface S is replaced by a discontinuity band Ω_k with width $k \cong 0$, as indicated in Figure C.1(d). Therefore, Dirac's delta regularized function can be expressed of the form:

$$\delta_S^k(x) = \lim_{k \to 0} \frac{1}{k} \mu_S(x) \quad ; \quad \mu_S(x) = \begin{cases} 1 & \forall x \in \Omega_k \\ 0 & \forall x \notin \Omega_k \end{cases} \tag{C.5}$$

where $\mu_S(x)$ is a collocation function in Ω_k.

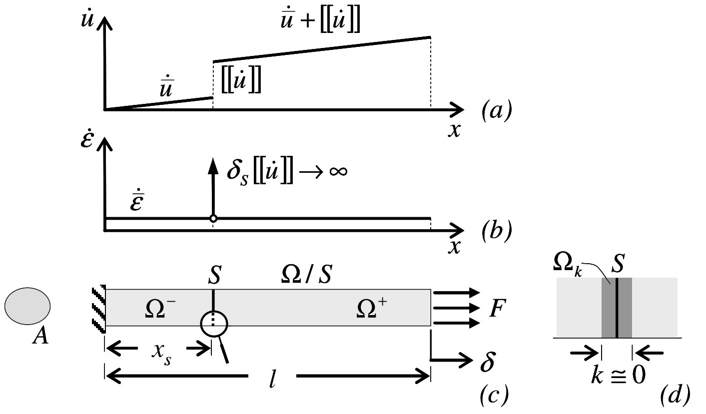

Figure C.1. One-dimensional kinematics of the strong discontinuity: (a) displacement rate, (b) strain rate, (c) discontinuity in the bar and (d) details of the discontinuity zone.

C.1.2. Two-dimensional or three-dimensional description

Next, the kinematics description indicated in the earlier section is extended to the two-dimensional or three-dimensional space.

Let Ω be a body exhibiting a strong discontinuity on surface S of normal $\mathbf{n}$, which splits the body in the domains Ω^+ and Ω^- as shown in Figure C.2(a). The strong discontinuity kinematics indicated in Equation (C.4) can be extended to (Oliver, Cervera et al. 1999):

$$\begin{cases} \dot{\mathbf{u}}(\mathbf{x},t)=\dot{\bar{\mathbf{u}}}(\mathbf{x},t)+\mathcal{H}_S(\mathbf{x})\cdot[\![\dot{\mathbf{u}}]\!](\mathbf{x},t) \quad ; \quad [\![\dot{\mathbf{u}}]\!](\mathbf{x},t)=\dot{\mathbf{u}}\big|_{\mathbf{x}\in S^+}-\dot{\mathbf{u}}\big|_{\mathbf{x}\in S^-} \\ \dot{\boldsymbol{\varepsilon}}(\mathbf{x},t)=\nabla^s\dot{\mathbf{u}}(\mathbf{x},t)=\dot{\bar{\boldsymbol{\varepsilon}}}(\mathbf{x},t)+\delta_s\,(\mathbf{n}\otimes[\![\dot{\mathbf{u}}]\!])^s \end{cases} \tag{C.6}$$

where Heaviside's function is equal to:

$$\mathcal{H}_S(\mathbf{x})=\begin{cases} 0 & \forall\mathbf{x}\in\Omega^- \\ 1 & \forall\mathbf{x}\in\Omega^+ \end{cases} \tag{C.7}$$

and δ_s is Dirac's delta function obtained by the gradient (in a generalized sense) of $\mathcal{H}_S$, which corresponds to $\nabla\mathcal{H}_S=\delta_s\mathbf{n}$.

According to Equation (C.6) the difference between the strain rate inside and outside the discontinuity surface S is equal to:

$$[\![\dot{\boldsymbol{\varepsilon}}]\!]=\dot{\boldsymbol{\varepsilon}}\big|_{\mathbf{x}\in S^+}-\dot{\boldsymbol{\varepsilon}}\big|_{\mathbf{x}\in S^-}=\delta_s(\mathbf{n}\otimes[\![\dot{\mathbf{u}}]\!])^s \tag{C.8}$$

Figure C.2(c) describes the rates of displacement and strain in the discontinuity surface.

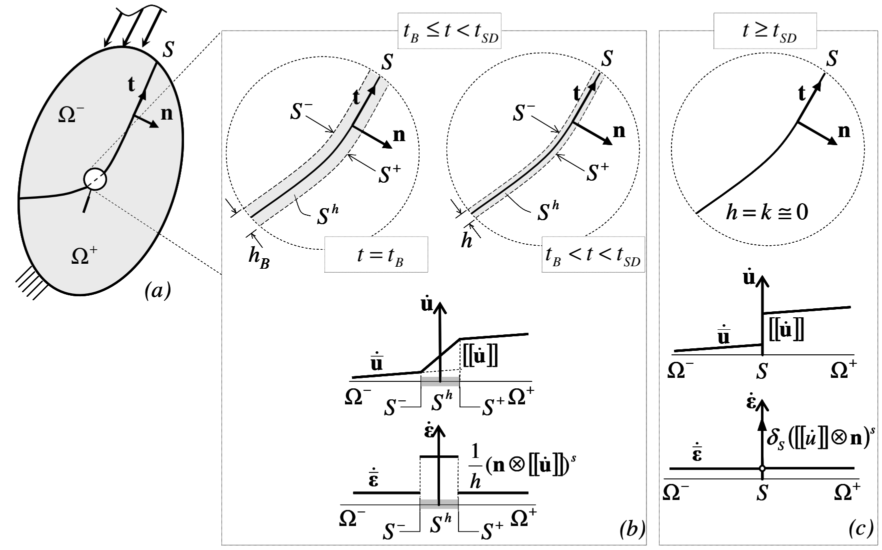

Figure C.2. Discontinuity evolution of the: (a) solid exhibiting a discontinuity, (b) weak discontinuity kinematics, (c) strong discontinuity kinematics.

In the following mathematical analysis, it is advisable to consider a regularized version of the kinematics given in Equation (C.6), defining a discontinuity band S^h with width h which contains the surface S (Figure C.2(b)). Dirac's delta function is calculated by means of a regularized function of the form:

$$\delta_S^h(\mathbf{x}) = \lim_{h\to 0}\frac{1}{h}\mu_S^h(\mathbf{x}) \quad ; \quad \mu_S^h(\mathbf{x}) = \begin{cases} 1 & \forall \mathbf{x}\in S^h \\ 0 & \forall \mathbf{x}\in \Omega / S^h \end{cases} \tag{C.9}$$

where $\mu_S^h(\mathbf{x})$ is a collocation function on S^h and Ω / S^h[1]. Likewise, regularized strain rate can be written as:

$$\dot{\boldsymbol\varepsilon}(\mathbf{x},t) = \nabla^s \dot{\mathbf{u}}(\mathbf{x},t) = \dot{\bar{\boldsymbol\varepsilon}}(\mathbf{x},t) + \delta_s^h(\mathbf{n}\otimes[[\dot{\mathbf{u}}]])^s \tag{C.10}$$

for which, the singular part $\delta_s^h(\mathbf{n}\otimes[[\dot{\mathbf{u}}]])^s$ is unbounded when $h \to 0$. This kinematics establishes the concept of strong discontinuity.

In general, the bandwidth is different from zero of such form that the strain field remains bounded in terms of an apparent jump $[[\dot{\mathbf{u}}]](\mathbf{x},t) = \dot{\mathbf{u}}|_{\mathbf{x}\in S^+} - \dot{\mathbf{u}}|_{\mathbf{x}\in S^-}$, which corresponds to the difference between the displacements to both sides of the band, such situation defines to the weak discontinuity.

Therefore, the strain rate of the weak and strong discontinuity can be presented as:

---

[1] Notation *A*/*B* indicates the set of all the material points of *A* that do not belong to *B*.

$$\dot{\boldsymbol{\varepsilon}}(\mathbf{x},t) = \nabla^s \dot{\mathbf{u}}(\mathbf{x},t) = \dot{\bar{\boldsymbol{\varepsilon}}}(\mathbf{x},t) + \frac{1}{h}\mu_S(\mathbf{n} \otimes [[\dot{\mathbf{u}}]])^s \quad ; \quad \mu_S(\mathbf{x}) = \begin{cases} 1 & \forall \mathbf{x} \in S \\ 0 & \forall \mathbf{x} \in \Omega / S \end{cases}$$
$$\begin{cases} \text{weak discontinuity} & \rightarrow (h \neq 0) \\ \text{strong discontinuity} & \rightarrow (h \rightarrow 0) \end{cases} \tag{C.11}$$

In this framework, the formation process of a strong discontinuity in a material point of the body can be modeled as a weak discontinuity that degenerates in a strong discontinuity during the strain localization (Figure C.2). At the material bifurcation time t_B where $[[\dot{\mathbf{u}}]] \neq \mathbf{0}$, the strains in S and in Ω / S are different according to the kinematics indicated in Equation (C.11), showing a bandwidth of the strain localization h_B which indicates the onset of the weak discontinuity (Figure C.2(b)). At the following load steps the bandwidth decreases according to a material evolution law until reaching a null value (due to computational purposes, k can be as small as the precision of the machine allows it), in a pseudo-time t_{SD} which indicates the onset of the strong discontinuity.

At a level of the solid, the evolution of the discontinuity in the material points can be observed as follows (Figure C.3):

- Material points defined in the continuous zone Y-B, which have reached the behavior non-linear (damage, plasticity, etc), but they do not fulfill the bifurcation criterion yet.

- Material points defined in the zone B-SD, which fulfill the bifurcation criterion and experience a kinematics of weak discontinuity, producing a jump in the displacement and a bandwidth different to zero.

- Material points defined in the zone SD-S, which have reached the regime of strong discontinuity, i.e. $h = k \cong 0$.

The fracture process zone considered commonly in fracture mechanics non-linear (Bazant & Oh 1983; Bazant & Planas 1998), corresponds to zone Y-CL in which exists a cohesive action in the crack. However, the total loss of cohesion between the faces of a crack appears in zone CL-S.

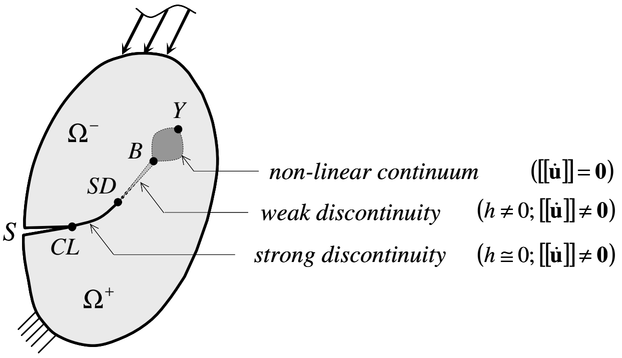

Figure C.3. Fracture process zone for the strong discontinuities approach.

C.2. Boundary value problem in a strong discontinuity

The equations indicated in Table C.1 describe the boundary value problem (BVP) of a body Ω that experiences a strong discontinuity in a surface S of normal $\mathbf{n}$ (Figure C.2(a)).

Equations (C.12) to (C.15) are the classic conditions of a continuum medium with continuous displacement, where $\mathbf{b}$ is the body forces vector, $\mathbf{t}^*$ is the prescribed tractions vector, Γ_u is the contour prescribed displacements and $\mathbf{v}_t$ is the normal vector to the contour of prescribed tractions Γ_σ.

The equation (C.16) is a specific additional expression for the strong discontinuity problem, in which the continuity of the tractions field through the discontinuity surface S is established.

$\nabla \cdot \dot{\boldsymbol{\sigma}} + \dot{\mathbf{b}} = \mathbf{0}$	(internal equilibrium in $\Omega \backslash S$)	(C.12)
$\dot{\boldsymbol{\sigma}} \cdot \mathbf{v}_t = \dot{\mathbf{t}}^*$	(external equilibrium on Γ_σ)	(C.13)
$\dot{\mathbf{u}} = \dot{\mathbf{u}}^*$	(prescribed displacements on Γ_u)	(C.14)
$\dot{\boldsymbol{\sigma}}_{\Omega^-/S} \cdot \mathbf{n} - \dot{\boldsymbol{\sigma}}_{\Omega^+/S} \cdot \mathbf{n} = 0$	(outer traction continuity on S)	(C.15)
$\dot{\boldsymbol{\sigma}}_S \cdot \mathbf{n} - \dot{\boldsymbol{\sigma}}_{\Omega^+/S} \cdot \mathbf{n} = 0$	(inner traction continuity on S)	(C.16)

Table C.1. Equilibrium equations and continuity conditions in a body with strong discontinuity.

It is essential to obtain bounded values of the stress in S, in order that to the inner traction continuity expressed in the Equation (C.16) can be fulfilled. By this reason, the continuum strong discontinuity approach allows computing a bounded stress field with the same constitutive model used in the continuum medium, as much in the discontinuity surface *S*, as outside it, in spite of the unbounded character of the strains in *S*.

C.3. Material bifurcation analysis

In a material point of a solid Ω, a stress uniform rate $\dot{\boldsymbol{\sigma}}(\mathbf{x},t)$ induces a strain rate $\dot{\boldsymbol{\varepsilon}}(\mathbf{x},t)$ and a displacement rate $\dot{\mathbf{u}}(\mathbf{x},t)$. This analysis seeks the existence condition of a discontinuity surface *S* (with normal **n**), of the strain rate, as indicated in Figure C.2(a) (Rice 1976; Rice & Rudnicki 1980).

The tangent constitutive equation of the material is:

$$\dot{\boldsymbol{\sigma}} = \mathbb{C}_{tg} : \dot{\boldsymbol{\varepsilon}} \tag{C.17}$$

where $\mathbb{C}_{tg}$ corresponds to the tangent constitutive tensor.

In the context of continuum mechanics, the tractions vector is continuous through surface *S*, i.e.,

$$[\![\dot{\boldsymbol{\sigma}} \cdot \mathbf{n}]\!] = \dot{\boldsymbol{\sigma}}_{\Omega^-/S} \cdot \mathbf{n} - \dot{\boldsymbol{\sigma}}_{\Omega^+/S} \cdot \mathbf{n} = 0 \tag{C.18}$$

Replacing Equation (C.17) into Equation (C.18) is obtained:

$$[\![\dot{\boldsymbol{\sigma}} \cdot \mathbf{n}]\!] = [\![\dot{\boldsymbol{\sigma}}]\!] \cdot \mathbf{n} = [\![\mathbb{C}_{tg} : \dot{\boldsymbol{\varepsilon}}]\!] \cdot \mathbf{n} \tag{C.19}$$

Maxwell's compatibility equation is used to describe the general form of the discontinuity of a second-order gradient tensor. Therefore the jump in the strain rate can be written as:

$$[\![\dot{\boldsymbol{\varepsilon}}]\!] = \dot{\boldsymbol{\varepsilon}}\big|_{\mathbf{x}\in S^+} - \dot{\boldsymbol{\varepsilon}}\big|_{\mathbf{x}\in S^-} = (\mathbf{n} \otimes \mathbf{g})^s \tag{C.20}$$

where **g** is the displacement jump vector. For $\mathbf{g} = 0$ there is not discontinuity, whereas $\mathbf{g} \neq 0$ is a sufficient condition in order that the discontinuity exist.

Considering continuity in the tangent constitutive tensor through surface *S*, i.e., $\mathbb{C}_{tg} = \mathbb{C}_{tg(\Omega^+)} = \mathbb{C}_{tg(\Omega^-)}$, is obtained:

$$[\![\mathbb{C}_{tg} : \dot{\boldsymbol{\varepsilon}}]\!] \cdot \mathbf{n} = \mathbb{C}_{tg} : [\![\dot{\boldsymbol{\varepsilon}}]\!] \cdot \mathbf{n} = \mathbb{C}_{tg} : (\mathbf{n} \otimes \mathbf{g})^s \cdot \mathbf{n} \tag{C.21}$$

Since $\mathbb{C}_{tg}$ has minor symmetry,

$$\mathbb{C}_{tg} : (\mathbf{n} \otimes \mathbf{g})^s \cdot \mathbf{n} = (\mathbf{n} \cdot \mathbb{C}_{tg} \cdot \mathbf{n}) \cdot \mathbf{g} \tag{C.22}$$

Therefore, the discontinuity in the strain rate exists when:

$$(\mathbf{n} \cdot \mathbb{C}_{tg} \cdot \mathbf{n}) \cdot \mathbf{g} = \mathbf{0} \quad \wedge \quad \mathbf{g} \neq \mathbf{0} \tag{C.23}$$

and consequently $(\mathbf{n} \cdot \mathbb{C}_{tg} \cdot \mathbf{n})$ represented of matrix form is singular and **g** is an eigenvector of this matrix.

The second-order tensor indicated in the earlier equation is called *localization tensor* $\mathbf{Q}_{tg}(t,\mathbf{n}) = (\mathbf{n}\cdot\mathbb{C}_{tg}\cdot\mathbf{n})$.

The classic bifurcation criterion presented by Hill (1962) establishes that the singularity of the localization tensor $\mathbf{Q}_{tg}(t,\mathbf{n})$ is a sufficient condition for the presence of the discontinuity, i.e.,

$$\det\left[\mathbf{Q}_{tg}(t_B,\mathbf{n})\right] = \det\left[\mathbf{n}\cdot\mathbb{C}_{tg}\cdot\mathbf{n}\right] = 0 \quad para \quad t = t_B \tag{C.24}$$

where t_B and $\mathbf{n}$ correspond to the bifurcation time and the direction of localization band, respectively.

In an isotropic damage model, the curve[2] $\det(\mathbf{Q}_{tg})/\det(\mathbf{Q})$ *versus* θ_n shown in Figure C.4 indicates two equal minimum values that they define two possible angles of bifurcation. These angles measured between the principal direction 1 and vector **n** are of equal magnitude and opposite sense, as it shows the analytical solution given by some authors (Runesson, Ottosen et al. 1991; Rizzi, Carol et al. 1995) for the two-dimensional space and by other authors (Chaves 2003; Oliver & Huespe 2004b) for the three-dimensional space.

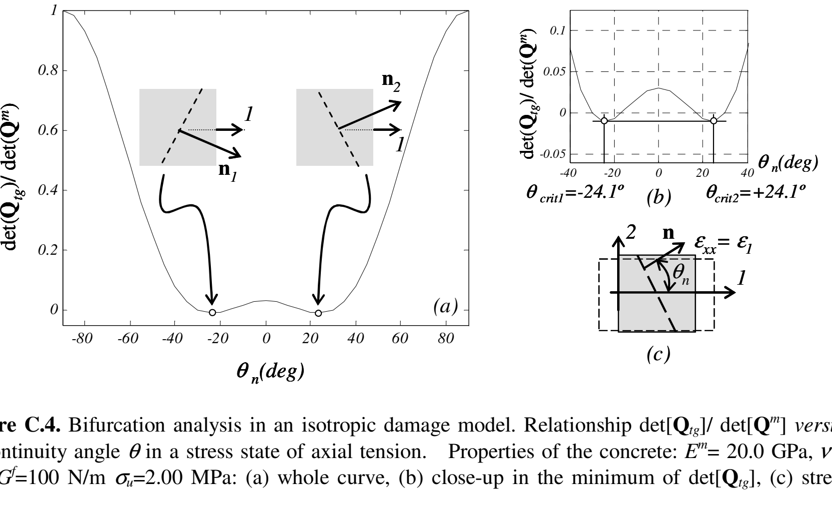

Figure C.4. Bifurcation analysis in an isotropic damage model. Relationship det[$\mathbf{Q}_{tg}$]/ det[$\mathbf{Q}^m$] *versus* discontinuity angle θ in a stress state of axial tension. Properties of the concrete: E^m= 20.0 GPa, ν = 0.2, G^f=100 N/m σ_u=2.00 MPa: (a) whole curve, (b) close-up in the minimum of det[$\mathbf{Q}_{tg}$], (c) stress state.

C.4. Strong discontinuity analysis for continuous damage models

Next, the strong discontinuities approach is applied to the isotropic scale damage model indicated in Appendix A.1 (Oliver 2000; Samaniego 2002).

---

[2] The elastic localization tensor or acoustic tensor is defined as $\mathbf{Q} = \mathbf{n}\cdot\mathbb{C}\cdot\mathbf{n}$.

For a material point belonging to the discontinuity surface *S* and at a time $t > t_{SD}$, the strain rate is equal to:

$$\dot{\boldsymbol{\varepsilon}}_S = \dot{\bar{\boldsymbol{\varepsilon}}}_S + \delta_S (\mathbf{n} \otimes [\![\dot{\mathbf{u}}]\!]_S)^s \tag{C.25}$$

Defining Dirac's delta regularized function δ_s^h as:

$$\delta_S^h = \frac{1}{h}\mu_S(\mathbf{x}) \quad , \quad \mu_S(\mathbf{x}) = \begin{cases} 1 & \mathbf{x} \in S^h \\ 0 & \mathbf{x} \in \Omega / S^h \end{cases} \tag{C.26}$$

such that $\lim_{h \to 0} \delta_s^h = \delta_s$. The kinematics indicated in Equation (C.25) can be written of the form:

$$\dot{\boldsymbol{\varepsilon}}_S^h = \dot{\bar{\boldsymbol{\varepsilon}}}_S + \frac{1}{h}\mu_S (\mathbf{n} \otimes [\![\dot{\mathbf{u}}]\!]_S)^s \tag{C.27}$$

where $\mu_S(\mathbf{x})$ corresponds to the collocation function and S^h is the discontinuity band that contains *S*, whose width is the regularization parameter *h*.

The strain field in strong discontinuity regime is obtained by integrating the earlier equation at the pseudo-time, thus:

$$\begin{aligned} \boldsymbol{\varepsilon}_S\Big|_{t \geq t_{SD}} &= \int_0^t \dot{\bar{\boldsymbol{\varepsilon}}}_S \, dt + \mu_S \int_0^{t_{SD}} \frac{1}{h} (\mathbf{n} \otimes [\![\dot{\mathbf{u}}]\!]_S)^s \, dt + \mu_S \int_{t_{SD}}^t \frac{1}{h} (\mathbf{n} \otimes [\![\dot{\mathbf{u}}]\!]_S)^s \, dt \\ &= \bar{\boldsymbol{\varepsilon}}_S + \mu_S \frac{1}{h} (\mathbf{n} \otimes \Delta[\![\mathbf{u}]\!]_S)^s \end{aligned} \tag{C.28}$$

where $\Delta[\![\mathbf{u}]\!]_S = [\![\mathbf{u}]\!]_S(t) - [\![\mathbf{u}]\!]_S(t_{SD})$.

The tractions vector $\mathbf{t}_S = \boldsymbol{\sigma}_S \cdot \mathbf{n}$ for $t \geq t_{SD}$ is computed from the constitutive equation $\boldsymbol{\sigma}_S = (q_S / r_S)\mathbb{C} : \boldsymbol{\varepsilon}_S$ and Equation (C.28), as follows:

$$\begin{aligned} \mathbf{t}_S &= \lim_{h \to 0} \frac{q_S}{r_S} \mathbf{n} \cdot \mathbb{C} : \left[\bar{\boldsymbol{\varepsilon}}_S + \frac{1}{h} (\mathbf{n} \otimes \Delta[\![\mathbf{u}]\!]_S)^s \right] \\ &= \lim_{h \to 0} \frac{q_S}{h r_S} \mathbf{n} \cdot \mathbb{C} : \left[h \bar{\boldsymbol{\varepsilon}}_S + (\mathbf{n} \otimes \Delta[\![\mathbf{u}]\!]_S)^s \right] \\ &= \left(\lim_{h \to 0} \frac{1}{h r_S} \right) q_S (\mathbf{n} \cdot \mathbb{C} \cdot \mathbf{n}) \cdot \Delta[\![\mathbf{u}]\!]_S \\ &= \left(\lim_{h \to 0} \frac{1}{h r_S} \right) \underbrace{q_S \mathbf{Q} \cdot \Delta[\![\mathbf{u}]\!]_S}_{\text{b}\textit{ounded} \text{ y } \neq 0} \end{aligned} \tag{C.29}$$

If $\mathbf{Q} = \mathbf{n} \cdot \mathbb{C} \cdot \mathbf{n}$ is a positive definite tensor and $[\![\mathbf{u}]\!]_S \neq 0$ for $t > t_{SD}$ is fulfilled that $q_S \mathbf{Q} \cdot \Delta[\![\mathbf{u}]\!]_S$ is bounded and different to zero. Therefore, the traction vector remains bounded when $\lim_{h \to 0} (1/h r_S)$ is bounded. This is possible defining a discrete internal variable $\bar{\alpha}$ in terms of r_S, thus:

$$\frac{1}{\dot{\bar{\alpha}}} = \delta_S \frac{1}{\dot{r}_S} \quad ; \quad \dot{r}_S = \delta_S \dot{\bar{\alpha}} \tag{C.30}$$

using again Dirac's delta function $\delta_s = \lim_{h \to 0} \delta_s^h$.

The internal variable r_S is obtained by integrating the earlier equation at the pseudo-time, as follows:

$$\begin{aligned} r_S(t) &= \int_0^{t_{SD}} \dot{r}_S \, dt = r_S(t_{SD}) + \delta_S \int_{t_{SD}}^{t} \dot{\bar{\alpha}} \, dt \\ r_S(t) &= r_S(t_{SD}) + \delta_S \Delta\bar{\alpha} \end{aligned} \tag{C.31}$$

where $\Delta\bar{\alpha} = \bar{\alpha}(t) - \bar{\alpha}(t_{SD})$. The unbounded character of r_S and of its rate $\dot{r}_S$

Replacing Equation (C.30) into softening law $\dot{q}_S = H \dot{r}_S$, it is obtained:

$$\dot{q}_S = \bar{H} \dot{\bar{\alpha}} \tag{C.32}$$

where $\bar{H}$ is defined as discrete softening parameter of the form:

$$\bar{H} = \delta_S H \quad ; \quad \frac{1}{H} = \delta_S \frac{1}{\bar{H}} \tag{C.33}$$

The stress-like internal variable can be expressed from Equation (C.32) of incremental way, thus:

$$q_s(t) = q_s(t_{SD}) + \bar{H} \Delta\bar{\alpha} \tag{C.34}$$

The following discrete constitutive equation is obtained by replacing the internal variable r_S of Equation (C.31) into Equation (C.29) when $\lim_{h \to 0}(h r_S) = \Delta\bar{\alpha}$.

$$\mathbf{t}_S = \frac{q_S}{\Delta\bar{\alpha}} \mathbf{Q} \cdot \Delta[\![\mathbf{u}]\!]_S \tag{C.35}$$

On the other hand, the energy per unit area consumed in the formation of the discontinuity surface S in strong discontinuity regime is equal to:

$$G_{SD} = \int_{t_{SD}}^{t_\infty} \mathbf{t}_S \cdot [\![\dot{\mathbf{u}}]\!]_S \, dt \tag{C.36}$$

considering that G_{SD} is equal to the fracture energy per unit area of the material G_f.

Using the damage criteria given by Equations (A.22) and (A.26), it is possible to obtain the following relationship:

$$\mathbf{t}_S \cdot [\![\dot{\mathbf{u}}]\!]_S = q_S \dot{\bar{\alpha}} \tag{C.37}$$

Replacing the earlier expression into Equation (C.36) and integrating the result, the fracture energy per unit area to tension and compression are obtained as:

$$G_f = -\frac{(\sigma_u)^2}{2E\overline{H}} \quad \text{(tension)} \tag{C.38}$$

$$G_f^{(c)} = n_\sigma^2 G_f \quad \text{(compression)} \tag{C.39}$$

C.5. Strong discontinuity analysis for one-dimensional plasticity models

In this section the application of the strong discontinuities approach to one-dimensional plasticity constitutive models is summarized (Simó, Oliver et al. 1993; Manzoli 1998; Oliver, Cervera et al. 1999).

For a material point belonging to the discontinuity surface S at time $t > t_{SD}$, the strain rate is defined as $\dot{\varepsilon}_S = \left(\dot{\sigma}_S / E\right) + \dot{\varepsilon}_S^p$ according to plasticity model or of the form $\dot{\varepsilon}_S = \dot{\bar{\varepsilon}}_S + \delta_S [\![\dot{u}]\!]_S$ according to strong discontinuity kinematics. From the earlier expressions it is obtained:

$$\dot{\varepsilon}_S = \left(\dot{\sigma}_S / E\right) + \dot{\varepsilon}_S^p = \dot{\bar{\varepsilon}}_S + \delta_S [\![\dot{u}]\!]_S \tag{C.40}$$

Replacing the flow rule $\dot{\varepsilon}_S^p = \lambda \operatorname{sign}(\sigma_S)$ into earlier equation,

$$\underbrace{\left(\dot{\sigma}_S / E\right)}_{\text{regular}} + \lambda \operatorname{sign}(\sigma_S) = \underbrace{\dot{\bar{\varepsilon}}_S}_{\text{regular}} + \underbrace{\delta_S [\![\dot{u}]\!]_S}_{\text{singular}} \tag{C.41}$$

Since the strain rate $\dot{\bar{\varepsilon}}_S$ and stress rate $\dot{\sigma}_S$ are regular values, the problem maintains its p physical meaning when:

$$\lambda \operatorname{sign}(\sigma_S) = \delta_S [\![\dot{u}]\!]_S \tag{C.42}$$

The singular character of the continuous plastic multiplier is observed, therefore, a discrete plastic multiplier $\bar{\lambda}$ is defined as:

$$\lambda = \delta_S \bar{\lambda} \tag{C.43}$$

and consequently,

$$\bar{\lambda} = [\![\dot{u}]\!]_S \operatorname{sign}(\sigma_S) \tag{C.44}$$

In accord with evolution law in continuum, it is established that

$$\dot{\alpha} = \delta_S \dot{\bar{\alpha}}_S \tag{C.45}$$

where $\bar{\alpha}$ is discrete internal variable.

At the time $t > t_{SD}$ the internal variable is equal to:

$$\begin{aligned} \alpha_S(t) &= \int_0^{t_{SD}} \dot{\alpha}_S \, dt = \alpha_S(t_{SD}) + \delta_S \int_{t_{SD}}^{t} \dot{\bar{\alpha}} \, dt \\ \alpha_S(t) &= \alpha_S(t_{SD}) + \delta_S \Delta\bar{\alpha} \end{aligned} \tag{C.46}$$

where $\Delta\bar{\alpha} = \bar{\alpha}(t) - \bar{\alpha}(t_{SD})$.

Replacing Equation (C.45) into softening law $\dot{q}_S^f = H^f \dot{\alpha}_S^f$, it is obtained:

$$\dot{q}_S = \bar{H}\dot{\bar{\alpha}} \tag{C.47}$$

where $\bar{H}$ is discrete softening parameter defined as:

$$\bar{H} = \delta_S H \quad ; \quad \frac{1}{H} = \delta_S \frac{1}{\bar{H}} \tag{C.48}$$

The stress-like internal variable can be expressed from Equation (C.32) of the incremental way, as follows:

$$q_s(t) = q_s(t_{SD}) + \bar{H}\Delta\bar{\alpha} \tag{C.49}$$

Differentiating yielding function $f(\sigma, \alpha)$ at the time (Equation (A.46)) and applying the plasticity criteria, the stress rate on discontinuity surface is obtained as:

$$\dot{\sigma}_S = \dot{q}_S \operatorname{sign}(\sigma_S) \tag{C.50}$$

Replacing Equations (C.44) and (C.47) into earlier expression,

$$[\![\dot{u}]\!]_S = \frac{1}{\bar{H}} \dot{\sigma}_S \tag{C.51}$$

The fracture energy per unit area in one-dimensional plasticity models can be evaluated as:

$$G_f = \int_{t_{SD}}^{t_\infty} \sigma_S \cdot [\![\dot{\mathbf{u}}]\!]_S \, dt \tag{C.52}$$

Replacing Equation (C.51) into the earlier equation and integrating at the time,

$$G_f = -\frac{(\sigma_y)^2}{2\bar{H}} \tag{C.53}$$

Appendix D.
Tracking of discontinuity paths

The material bifurcation analysis provides the information necessary to establish the appearance and direction of a discontinuity in a material point based on the stress state and on the internal variables of the constitutive model that governs it. However, in the numerical implementation, the geometric location of the discontinuity inside a finite element is not defined. Therefore, it is necessary an algorithm that establishes the location of the discontinuity in each element in order that it conserves the continuity of the discontinuity line in the solid.

Next, some tracking strategy of discontinuity paths in the context of finite elements method (Samaniego 2002; Oliver & Huespe 2004a) are described.

D.1. Overview

The discontinuity surface S splits a body Ω into the domain Ω^+ and Ω^- according to the positive direction of normal vector $\mathbf{n}$, as shown in Figure D.1(a). This body can be meshed with linear triangular finite elements, whose domain Ω_e is divided by the domain Ω_e^+ and Ω_e^-, by means of a discontinuity line of location unknown inside the element (Figure D.1(b)).

If node i is located in the domain Ω^+ of the body and it belongs to the elements crossed by the same discontinuity line e and e', this node must be part of the domains Ω_e^+ and $\Omega_{e'}^+$. A continuous trajectory of the discontinuity line through the elements assures is condition, as shown in Figure D.1(c).

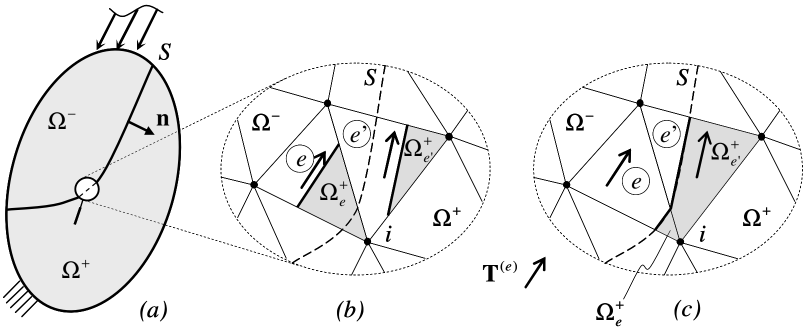

Figure D.1. Tracking of discontinuity paths: (a) discontinuity line in the body, (b) random location of the discontinuity line inside two finite elements, (c) alignment between the discontinuity paths of two finite elements.

D.2. Local strategy

In the local strategy, the alignment is explicitly made between an element and its neighbouring element which is also part of the same discontinuity. Next, this procedure is indicated:

- Initially, the location of the discontinuity is fixed in an arbitrary form inside the first element fulfilling the bifurcation criterion, obtaining an output point of the discontinuity in this element or an input point in the neighbouring element.

- For the following neighbouring element, the discontinuity line is traced from its direction and its input point in the element (given by the earlier element).

When a single path is considered, this algorithm is simple and robust; however, when the number of possible discontinuities increases, the local strategy loses robustness.

In reinforced concrete structures, commonly several crack paths appear, therefore, a global strategy of tracking of discontinuities is more appropriate.

D.3. Global strategy

D.3.1. Basic considerations

In the global strategy (Samaniego 2002; Oliver & Huespe 2004a; Oliver, Huespe et al. 2004a), all the possible discontinuity lines S_i as members of the contours family of a scalar field $\theta(\mathbf{x})$ coinciding with the envelopes of the vector field $\mathbf{T}(\mathbf{x},t)$, which is orthogonal to **n** and defines the propagation direction of the discontinuity in the solid (Figure D.2(a)) Therefore:

$$S_i = \{\mathbf{x} \in \Omega \,;\, \theta(\mathbf{x}) = \theta_{S(i)}\} \tag{D.1}$$

where $\theta_{S(i)}$ is a constant acting as labels of the possible discontinuity line S_i.

The tracking algorithm of a line S_i at elemental level and at a time *t* is the following:

- The label $\theta_{S(i)}$ is fixed as an arbitrary value of θ inside the root element, for example, the average between the values of θ in the nodes, i.e., $\theta_{S(i)} = (1/3)(\theta_1 + \theta_2 + \theta_3)$

- Given the value of the envelopes of $\mathbf{T}(\mathbf{x},t)$ in the three nodes of the element $\theta_1, \theta_2, \theta_3$ and the label $\theta_{S(i)}$, the location of the possible discontinuity line calculates by linear interpolation in the sides of the element, as shown in Figure D.2(b).

In order to determine a root element at a time *t*, it must be verified that this element has not been crossed by the discontinuity line of another root element; this requires the concept of active discontinuity line. A possible discontinuity line S_i is active when it crosses at least one element fulfilling the bifurcation criterion. Therefore, when the bifurcation in an element occurs, two situations can appear:

- If the element is crossed by an active line S_i, its location inside the element calculated by linear interpolation of θ in the sides of the element, as it were previously indicated.

- Otherwise, the element is taken as root element and the possible discontinuity line passing through its centroid becomes activated.

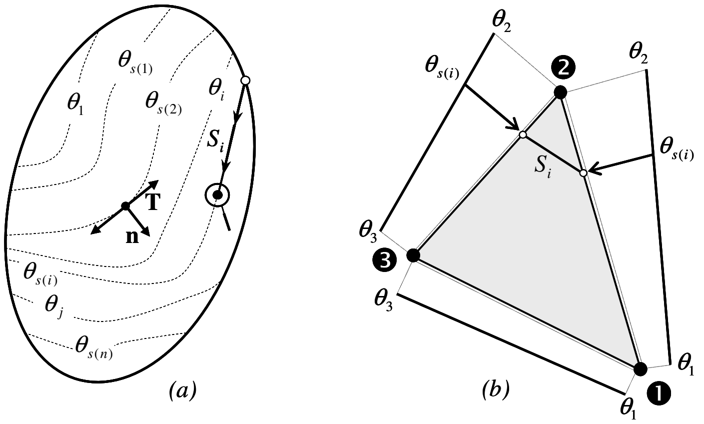

Figure D.2. Global strategy of tracking of discontinuity lines: (a) envelopes of the propagation direction of the discontinuity in the solid, (b) location of a possible discontinuity line inside a finite element.

D.3.2. Envelopes of the propagation vector field

Next, it is described a procedure to calculate the envelopes of the vector field $\mathbf{T}(\mathbf{x},t)$ which defines the propagation direction of the possible discontinuities, in a two-dimensional space Ω (Samaniego 2002; Oliver & Huespe 2004a; Oliver, Huespe et al. 2004a).

Let $\theta(\mathbf{x})$ be the envelop of the vector $\mathbf{T}(\mathbf{x},t)$, it is established that:

$$\partial_{\mathbf{T}}\theta = \mathbf{T}\cdot\nabla\theta = \nabla\theta\cdot\mathbf{T} = 0 \tag{D.2}$$

where $\partial_{\mathbf{T}}\theta$ corresponds to directional derivate of θ with respect to **T**.

D.3.2.1. Analogy with the heat conduction problem

The envelope curves of the propagation direction can be calculated as the temperatures obtained in a heat conduction problem.

Multiplying by **T** the Equation (D.2) is obtained:

$$\mathbf{T}\partial_{\mathbf{T}}\theta = (\mathbf{T}\otimes\mathbf{T})\cdot\nabla\theta = 0 \tag{D.3}$$

In addition, it is defined to the heat conduction-like tensor:

$$\mathbf{K}_T = (\mathbf{T}\otimes\mathbf{T}) \tag{D.4}$$

in such a way that:

$$\mathbf{q}_T = -\mathbf{K}_T \cdot \nabla\theta \tag{D.5}$$

This problem can be considered analogous to a heat conduction problem without internal heat sources and null heat flow input $(\mathbf{q}_T \cdot \mathbf{v}_t = 0 \quad \text{on} \quad \Gamma_q)$, expressed as a boundary value problem of the form:

Find the scalar field $\theta(\mathbf{x})$ such that:

$$\begin{cases} \nabla \cdot \mathbf{q}_T = 0 & \text{en} \quad \Omega \\ \mathbf{q}_T = -\mathbf{K}_T \cdot \nabla\theta = -\mathbf{T} \cdot \partial_{\mathbf{T}}\theta & \text{en} \quad \Omega \\ \mathbf{q}_T \cdot \mathbf{v}_t = (\mathbf{T} \cdot \mathbf{v}_t)\partial_{\mathbf{T}}\theta & \text{en} \quad \Gamma_q \\ \theta = \theta^* & \text{en} \quad \Gamma_\theta \end{cases} \tag{D.6}$$

Therefore, θ corresponds to the temperature-like field, $\mathbf{q}_T$ is the heat flow-like vector and $\mathbf{K}_T$ is the thermal conductivity-like anisotropic tensor that varies from point to point and whose represented matrix is:

$$[\mathbf{K}_T] = [(\mathbf{T} \otimes \mathbf{T})] = \begin{bmatrix} T_x^2 & T_x T_y \\ T_x T_y & T_y^2 \end{bmatrix} \tag{D.7}$$

Notice that $\mathbf{K}_T(\mathbf{T}) = \mathbf{K}_T(-\mathbf{T})$. Consequently, the solution of the problem is affected by the direction of vector **T**, but it is independent of its sense.

D.3.3. Implementation in the method of the finite elements

The weak and discrete form of the continuous problem indicated in Equation (D.6) and applied to a mesh of *e* finite elements and *n* nodes representing the domain Ω, can be expressed as:

Find:

$$\theta(\mathbf{x}) = \sum_{i=1}^{n} N_i \theta_i = [\mathbf{N}]^T [\boldsymbol{\theta}]$$
$$\begin{cases} [\mathbf{N}] = [N_1, \ldots, N_n]^T \\ [\boldsymbol{\theta}] = [\theta_1, \ldots, \theta_n]^T \end{cases} \tag{D.8}$$

such that:

$$\begin{aligned} &[\mathbf{D}_T][\theta] = [0] \\ &\theta_i\big|_{\Gamma_\theta} = \theta^* \\ &[\mathbf{D}_T] = \int_\Omega [\nabla\mathbf{N}]^T [\mathbf{K}_T][\nabla\mathbf{N}] d\Omega \end{aligned} \tag{D.9}$$

where N_i are the standard shape functions and $[\mathbf{D}_T]$ is the stiffness matrix.

Equation (D.9) defines an analogous problem to heat conduction problem, which has been solved in the onset of each load step of the original mechanical problem. This analysis provides the location of the discontinuity paths inside each finite element according to the algorithm presented in Section D.3.

Appendix E.
Implicit-explicit integration scheme

In this appendix the *implicit-explicit integration scheme* (IMPLEX) for constitutive models proposed by Oliver and collaborators (Oliver, Huespe et al. 2004b; Oliver, Huespe et al. 2006), is described. Also, it is shown its application to a damage model with degradation in tension and compression (Oliver, Cervera et al. 1990) and one-dimensional plasticity models (Simó & Hughes 1998).

The implicit-explicit integration scheme of the constitutive model is a stable algorithm numerically able to represent, of robust form, the unstable response due to the material softening.

E.1. Integration scheme for a damage model with degradation in tension and compression

E.1.1. Implicit integration scheme: consistent algorithmic operator

The implicit integration of the equations describing the damage model indicated in Table A.1, allows obtaining, at the time t_{n+1}, the stress tensor $\boldsymbol{\sigma}_{n+1}$ and strain-like internal variable r_{n+1} and stress-like internal variable q_{n+1}, in terms of the current strain tensor $\boldsymbol{\varepsilon}_{n+1}$, thus:

Given $\boldsymbol{\varepsilon}_{n+1}$, determinate:

$$\bar{\boldsymbol{\sigma}}_{n+1} = \mathbb{C} : \boldsymbol{\varepsilon}_{n+1} \quad \text{(effective stress tensor)} \tag{E.1}$$

$$\tau_{\varepsilon}(\boldsymbol{\varepsilon}_{n+1}) = \phi_{n+1}\sqrt{\bar{\boldsymbol{\sigma}}_{n+1} : (\mathbb{C})^{-1} : \bar{\boldsymbol{\sigma}}_{n+1}} \quad \text{(strain norm)} \tag{E.2}$$

$$\phi_{n+1} = \frac{\sum_{i=1}^{3}\langle\bar{\sigma}_i\rangle_{n+1}}{\sum_{i=1}^{3}|\bar{\sigma}_i|_{n+1}}\left(1-\frac{1}{n_\sigma}\right)+\frac{1}{n_\sigma} \quad \text{(factor associated to degradation in tension and compression)} \tag{E.3}$$

$$r_{n+1} = r(\boldsymbol{\varepsilon}_{n+1}) = \max_{t\in[0,t_{n+1}]}\left(r_t\,,\tau_{\varepsilon}(\boldsymbol{\varepsilon}_{n+1})\right) \quad \text{(strain-like internal variable)} \tag{E.4}$$

$$q_{n+1} = q(\boldsymbol{\varepsilon}_{n+1}) = q_n + H_n(r_{n+1}-r_n) \quad \text{(stress-like internal variable)} \tag{E.5}$$

$$\boldsymbol{\sigma}_{n+1} = \boldsymbol{\sigma}(\boldsymbol{\varepsilon}_{n+1}) = \frac{q_{n+1}}{r_{n+1}}\mathbb{C} : \boldsymbol{\varepsilon}_{n+1} \quad \text{(stress tensor)} \tag{E.6}$$

Table E.1. Implicit integration of the damage model with degradation in tension and compression.

The consistent algorithmic operator $\mathbb{C}_{n+1}^{(con)}$ defines as:

$$\mathbb{C}_{n+1}^{(con)} = \frac{\partial\boldsymbol{\sigma}_{n+1}}{\partial\boldsymbol{\varepsilon}_{n+1}} \tag{E.7}$$

Therefore, if Equation (E.6) is derived with respect to the strain tensor $\boldsymbol{\varepsilon}_{n+1}$, the following operator $\mathbb{C}_{n+1}^{(con)}$ is obtained for elastic and unloading regime,

$$\mathbb{C}_{n+1}^{(con)} = \frac{q_{n+1}}{r_{n+1}}\mathbb{C}_{n+1} \tag{E.8}$$

and for inelastic loading regime,

$$\mathbb{C}_{n+1}^{(con)} = \frac{q_{n+1}}{r_{n+1}}\mathbb{C}_{n+1} - \frac{q_{n+1}-H_n r_{n+1}}{r_{n+1}^3}\left[\frac{r_{n+1}^2}{\phi_{n+1}}\left(\bar{\boldsymbol{\sigma}}_{n+1}\otimes\mathbf{A}_{n+1}\right)+\phi_{n+1}^2\left(\bar{\boldsymbol{\sigma}}_{n+1}\otimes\bar{\boldsymbol{\sigma}}_{n+1}\right)\right] \tag{E.9}$$

For two-dimensional problems, the scalar $\phi_{n+1} = \phi(\bar{\boldsymbol{\sigma}}_{n+1})$ and the tensor $\mathbf{A}_{n+1} = \mathbf{A}(\bar{\boldsymbol{\sigma}}_{n+1})$ are defined by Equations (A.35) to (A.41).

The second term of Equation (E.9) shows the defined negative character of the consistent algorithmic operator.

E.1.2. Implicit-explicit integration scheme: effective algorithmic operator

Next, the *implicit-explicit* procedure in each step of pseudo-time t_{n+1} is described.

With an *implicit* scheme the implicit variables of the problem $r_{n+1}(\boldsymbol{\varepsilon}_{n+1}), q_{n+1}(\boldsymbol{\varepsilon}_{n+1}), \boldsymbol{\sigma}_{n+1}(\boldsymbol{\varepsilon}_{n+1})$ are obtained in terms of the current strain $\boldsymbol{\varepsilon}_{n+1}$, as indicated in Equations (E.4) to (E.6).

At the same time t_{n+1}, the internal variable is extrapolated of *linear explicit* form in terms of the *implicit* internal variables r_n and r_{n-1}, calculated at the times t_n and t_{n-1} (Figure E.1(a)), thus:

$$\begin{aligned} \tilde{r}_{n+1} &= r_n + \dot{r}_n \Delta t_{n+1} = r_n + \frac{\Delta r_n}{\Delta t_n} \Delta t_{n+1} \\ \Delta r_n &= r_n - r_{n-1} \; ; \; \Delta t_n = t_n - t_{n-1} \; ; \; \Delta t_{n+1} = t_{n+1} - t_n \end{aligned} \tag{E.10}$$

According to the earlier equation, $\tilde{r}_{n+1}$ corresponds to a prediction of the internal variable for *n+1*, which can be calculated at the end of step *n*, taking advantage of its independence in relation to the current strain $\boldsymbol{\varepsilon}_{n+1}$.

The error produced by the extrapolation can be controlled by reducing the size of the load step or increasing the order of the extrapolation function.

The stress-like *explicit* internal variable $\tilde{q}_{n+1}$ and the *explicit* stress tensor $\tilde{\boldsymbol{\sigma}}_{n+1}$ at the time t_{n+1} correspond to:

$$\tilde{q}_{n+1} = q_n + H_n(\tilde{r}_{n+1} - r_n) \quad ; \quad \tilde{q}_{n+1} \geq 0 \tag{E.11}$$

$$\tilde{\boldsymbol{\sigma}}_{n+1} = \frac{\tilde{q}_{n+1}}{\tilde{r}_{n+1}} \mathbb{C} : \boldsymbol{\varepsilon}_{n+1} \tag{E.12}$$

In the earlier equation, it is observed that as much $\tilde{q}_{n+1}$ as $\tilde{r}_{n+1}$ are independent of the current strain $\boldsymbol{\varepsilon}_{n+1}$, of such form that the explicit stress $\tilde{\boldsymbol{\sigma}}_{n+1}$ depends linearly on $\boldsymbol{\varepsilon}_{n+1}$.

On the other hand, the *effective algorithmic operator* $\mathbb{C}_{n+1}^{(efe)}$ is defined as:

$$\mathbb{C}_{n+1}^{(efe)} = \frac{\partial \tilde{\boldsymbol{\sigma}}_{n+1}}{\partial \boldsymbol{\varepsilon}_{n+1}} \tag{E.13}$$

According to the earlier expression, differentiating Equation (E.12) in terms of current strain $\boldsymbol{\varepsilon}_{n+1}$, a tensor $\mathbb{C}_{n+1}^{(efe)}$ constant with respect to the implicit variables at t_{n+1} is obtained as:

$$\mathbb{C}_{n+1}^{(efe)} = \frac{\tilde{q}_{n+1}}{\tilde{r}_{n+1}} \mathbb{C} \tag{E.14}$$

Given the positive character of $\tilde{r}_{n+1}, \tilde{q}_{n+1}$ and $\mathbb{C}$, it can be concluded that the *effective algorithmic operator* is defined positive for any time t_{n+1} (Figure E.1 (b)).

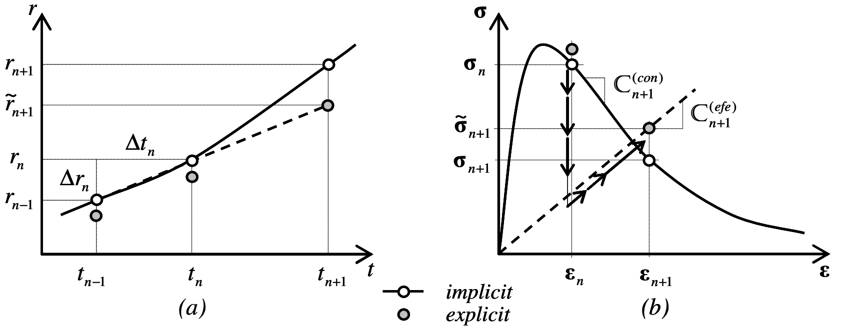

Figure E.1. Implicit-explicit integration scheme for damage models: (a) extrapolation of the strain-like internal variable, (b) prediction-correction phases of the stress.

E.2. Integration scheme for one-dimensional plasticity models

E.2.1. Implicit integration scheme: consistent algorithmic operator

The implicit integration of the equations describing one-dimensional plasticity models is the result of the application of a time discretization scheme type *Euler-backward standard* on these equations. As it is indicated in Table A.2, for a time t_{n+1}, the stress σ_{n+1}, the strain-like internal variable α_{n+1} and stress-like internal variable q_{n+1} are obtained in terms of the strain ε_{n+1}.

Given $\boldsymbol{\varepsilon}_{n+1}$, determinate:

$$\left.\begin{array}{l}\dot{\alpha}=\lambda\geq 0 \quad ; \quad \alpha\big|_{t=0}=0 \\ \Delta\alpha_{n+1}=\alpha(\varepsilon_{n+1})-\alpha(\varepsilon_n)=\alpha_{n+1}-\alpha_n\end{array}\right\} \quad \text{(strain-like internal variable)} \tag{E.15}$$

$$q_{n+1}=q(\boldsymbol{\varepsilon}_{n+1})=q_n+H_n\Delta\alpha_{n+1} \quad \text{(stress-like internal variable)} \tag{E.16}$$

$$\sigma_{n+1}=\sigma_n+E(\varepsilon_{n+1}-\varepsilon_n)-E\Delta\alpha_{n+1}\mathrm{sign}(\sigma_{n+1}) \quad \text{(stress)} \tag{E.17}$$

Table E.2. Implicit integration of one-dimensional plasticity models

The *consistent algorithmic operator* for the one-dimensional plasticity model $E^{(con)}_{n+1}$ is defined as:

$$E_{n+1}^{(con)} = \frac{\partial \sigma_{n+1}}{\partial \varepsilon_{n+1}} \tag{E.18}$$

Replacing Equation (E.17) into the earlier expression, the operator $E_{n+1}^{(con)}$ is obtained for elastic and unloading regime, thus:

$$E_{n+1}^{(con)} = E \tag{E.19}$$

and inelastic loading regime,

$$E_{n+1}^{(con)} = \frac{EH}{E+H} \tag{E.20}$$

where E is Young's modulus. Since the softening modulus $H \leq 0$, the consistent algorithmic operator in inelastic loading regime is defined negative.

E.2.2. Implicit-explicit integration scheme: effective algorithmic operator

By means of a procedure similar to the presented for damage models, the *implicit-explicit* integration scheme is applied to one-dimensional plasticity models.

At a time t_{n+1}, the variables $\alpha_{n+1}(\varepsilon_{n+1}), q_{n+1}(\varepsilon_{n+1}), \sigma_{n+1}(\varepsilon_{n+1})$ are obtained in *implicit* form, from of Equations (E.15) to (E.17). From the *explicit* linear extrapolation of the internal variable in terms of the *implicit* variables α_n and α_{n-1}, it is obtained:

$$\tilde{\alpha}_{n+1} = \alpha_n + \dot{\alpha}_n \Delta t_{n+1} = \alpha_n + \frac{\Delta \alpha_n}{\Delta t_n} \Delta t_{n+1} \tag{E.21}$$

where $\Delta\alpha_n = \alpha_n - \alpha_{n-1}$; $\Delta t_n = t_n - t_{n-1}$; $\Delta t_{n+1} = t_{n+1} - t_n$.

The explicit stress-like internal variable $\tilde{q}_{n+1}$ and the explicit stress tensor $\tilde{\boldsymbol{\sigma}}_{n+1}$ at the time t_{n+1} correspond to:

$$\tilde{q}_{n+1} = q_n + H_n(\tilde{\alpha}_{n+1} - \alpha_n) \quad ; \quad 0 \leq \tilde{q}_{n+1} \leq \sigma_y \tag{E.22}$$

$$\begin{aligned} \tilde{\sigma}_{n+1} &= \sigma_n + E\ (\varepsilon_{n+1} - \varepsilon_n) - E\ \Delta\tilde{\alpha}_{n+1} \operatorname{sign}(\tilde{\sigma}_{n+1}) \\ \tilde{\sigma}_{n+1} &= \sigma_n + E\ (\varepsilon_{n+1} - \varepsilon_n) - E\ \Delta\tilde{\alpha}_{n+1} \frac{\tilde{\sigma}_{n+1}}{\left|\tilde{\sigma}_{n+1}\right|} \end{aligned} \tag{E.23}$$

where $\Delta\tilde{\alpha}_{n+1} = \tilde{\alpha}_{n+1} - \alpha_n$.

In inelastic loading regime, the yielding function in terms of the explicit variables can be written of the form:

$$f(\tilde{\sigma}_{n+1}, \tilde{q}_{n+1}) = \left|\tilde{\sigma}_{n+1}\right| - (\sigma_y + \tilde{q}_{n+1}) = 0 \rightarrow \left|\tilde{\sigma}_{n+1}\right| = (\sigma_y + \tilde{q}_{n+1}) \tag{E.24}$$

Replacing Equation (E.24) into Equation (E.23), $\tilde{\sigma}_{n+1}$ is equal to:

$$\tilde{\sigma}_{n+1} = \frac{\sigma_n + E(\varepsilon_{n+1} - \varepsilon_n)}{1 + \dfrac{\Delta\tilde{\alpha}_{n+1}E}{(\sigma_y + \tilde{q}_{n+1})}} \tag{E.25}$$

The *effective algorithmic operator* $E_{n+1}^{(efe)}$ for one-dimensional plasticity models is defined as:

$$E_{n+1}^{(efe)} = \frac{\partial\tilde{\sigma}_{n+1}}{\partial\varepsilon_{n+1}} \tag{E.26}$$

Differentiating Equation (E.25) as indicated in earlier equation, it is obtained that,

$$E_{n+1}^{(efe)} = \frac{E}{1 + \dfrac{\Delta\tilde{\alpha}_{n+1}E}{(\sigma_y + \tilde{q}_{n+1})}} \tag{E.27}$$

where $E_{n+1}^{(efe)}$ is constant with respect to implicit variables at the time t_{n+1} and it is greater than zero due to positive character of $\Delta\tilde{\alpha}_{n+1}$, $\tilde{q}_{n+1}$, σ_y and E.

Figure E.2 describes the extrapolation of internal variables and the prediction of the stress in the implicit-explicit integration scheme, specifically applied to one-dimensional plasticity constitutive models.

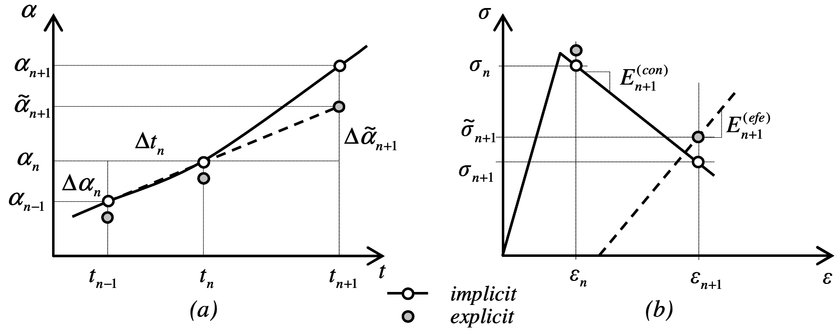

Figure E.2. Implicit-explicit interpolation scheme for one-dimensional plasticity models: (a) extrapolation of the strain-like internal variable, (b) prediction-correction phases of the stress.

Appendix F.
Notation

F.1. Two-dimensional Voigt notation

In the implementation of the constitutive models in the finite elements method, Voigt notation is frequently used, which allows writing the second-order symmetrical tensor as column vectors and the fourth-order stresses as square matrices.

A second-order tensor representing the stress field in two-dimensional problems can be characterized by a vector column of the form:

$$\underbrace{\boldsymbol{\sigma} = \begin{bmatrix} \sigma_{xx} & \tau_{xy} \\ \tau_{xy} & \sigma_{yy} \end{bmatrix}}_{tensor} \rightarrow \underbrace{\{\boldsymbol{\sigma}\} = \begin{Bmatrix} \sigma_{xx} \\ \sigma_{yy} \\ \tau_{xy} \end{Bmatrix}}_{Voigt} \tag{F.1}$$

Likewise, the strain tensor can be represented by a column vector; however, the shear strain must be multiplied by two, in order that the strain energy calculated in tensorial form and in matrix form be equals.

$$\underbrace{\boldsymbol{\varepsilon} = \begin{bmatrix} \varepsilon_{xx} & \varepsilon_{xy} \\ \varepsilon_{xy} & \varepsilon_{yy} \end{bmatrix}}_{tensor} \rightarrow \underbrace{\{\boldsymbol{\varepsilon}\} = \begin{Bmatrix} \varepsilon_{xx} \\ \varepsilon_{yy} \\ 2\varepsilon_{xy} \end{Bmatrix}}_{Voigt} \tag{F.2}$$

The constitutive operator is a fourth-order tensor relating to the strain and stress tensors, of the form:

$$\boldsymbol{\sigma} = \mathbb{C} : \boldsymbol{\varepsilon} \tag{F.3}$$

Such a constitutive relation can be written in Voigt notation as:

$$\{\boldsymbol{\sigma}\} = [\mathbb{C}]\{\boldsymbol{\varepsilon}\} \tag{F.4}$$

i.e.,

$$\begin{Bmatrix} \sigma_{xx} \\ \sigma_{yy} \\ \tau_{xy} \end{Bmatrix} = \begin{bmatrix} C_{xxxx} & C_{xxyy} & C_{xxxy} \\ C_{yyxx} & C_{yyyy} & C_{yyxy} \\ C_{xyxx} & C_{xyyy} & C_{xyxy} \end{bmatrix} \begin{Bmatrix} \varepsilon_{xx} \\ \varepsilon_{yy} \\ 2\varepsilon_{xy} \end{Bmatrix} \tag{F.5}$$

Consequently, a constitutive operator represented by a square matrix is obtained as:

$$[\mathbb{C}] = \begin{bmatrix} C_{xxxx} & C_{xxyy} & C_{xxxy} \\ C_{yyxx} & C_{yyyy} & C_{yyxy} \\ C_{xyxx} & C_{xyyy} & C_{xyxy} \end{bmatrix} \tag{F.6}$$

F.2. Special functions

In the following table the functions used in the formulation are indicated.

$\langle \wp \rangle = \begin{cases} \wp & si\ \wp > 0 \\ 0 & si\ \wp \le 0 \end{cases}$ o $\langle \wp \rangle = \frac{1}{2}\left(\wp + \lvert \wp \rvert\right)$	(Mac-Auley's parenthesis)	(F.7)
$\dot{\wp} = \frac{\partial \wp}{\partial t}$	(material derivative)	(F.8)
$[\![\wp(\mathbf{x})]\!] = \wp(\mathbf{x})\rvert_{\mathbf{x} \in S^+} - \wp(\mathbf{x})\rvert_{\mathbf{x} \in S^-}$	(jump function)	(F.9)
$\mathcal{H}_S(x) = \begin{cases} 0 & si\ x < x_s \\ 1 & si\ x \ge x_s \end{cases}$	(Heaviside's function)	(F.10)
$\delta_S(x) = \begin{cases} 0 & si\ (x < x_s) \vee (x > x_s) \\ \infty & si\ x = x_s \end{cases}$	(Dirac's delta function)	(F.11)

Table F.1. Special functions

References

Barenblatt, G. (1962). "The mathematical theory of equilibrium of cracks in brittle fracture." *Advances in Applied Mechanics* **7**: 55-129.

Bazant, Z. (1976). "Instability, ductility and size effect in strain-softening concrete." *Journal of Engeeniering Mechanics. ASCE* **102**: 331-344.

Bazant, Z. & Cedolin, L. (1980). "Fracture mechanics of reinforced concrete." *Journal of Engeeniering Mechanics. ASCE* **106**: 1287 - 1306.

Bazant, Z. & Cedolin, L. (1983). "Finite element modelling of crack band propagation." *Journal of Structural Engineering. ASCE* **109**: 69-92.

Bazant, Z. & Oh, B. (1983). "Crack band theory for fracture of concrete." *Materials and Structures* **16**(93): 155-177.

Bazant, Z. & Planas, J. (1998). *Fracture and size effect in concrete and other quasibrittle materials*, CRC Press.

Beeby, A. & Narayanan, R. (1995). *Desingners' Handbook to Eurocode 2. Part 1.1: Design or concrete structures*. London, Thomas Telford.

Belytschko, T., Fish, J. & Engelmann, B. (1988). "A finite element with embedded localization zones." *Computer Methods in Applied Mechanics and Engineering* **70**: 59-89.

Belytschko, T., Moes, N., Usui, S. & Parimik, C. (2001). "Arbitrary discontinuities in finite elements." *International Journal for Numerical Methods in Engineering* **50**: 993-1013.

Belletti, B., Bernardi, P., Cerioni, R. & Iori, I. (2003). *On the behaviour of R/C beams without shear reinforcement*. Computational modelling of concrete structures, *N. Bicanic, R. d. Borst et al (eds)*, Austria, Balkema Publisher.

Belletti, B., Cerioni, R. & Iori, I. (2001). "Physical approach for reinforced-concrete (PARC) membrane elements." *Journal of Structural Engineering. ASCE* **127**(12): 1412-1426.

Bhide, S. & Collins, P. (1989). "Influence of axial tension on the shear capacity of reinforced concrete members." *ACI Structural Journal* **86**(5): 570 -581.

Blanco, S. (2007). *Contribuciones al análisis del fallo material en tres dimensiones usando la aproximación de discontinuidades fuertes*. Tesis Doctoral, Universidad Politécnica de Cataluña, Barcelona.

Böhm, H. (2000). *A Short Introduction to Basis Aspects of Continuum Micromechanics*. Vienna, Institute of Lightweight Design and Structural Biomechanics. Vienna University of Technology.

Buckle, I. & Jackson, A. (1981). A filamented beam element for the non-linear analysis of reinforced concrete shells with edge beams. New Zealand, University of Auckland.

Car, E. (2000). *Modelo constitutivo continuo para el estudio del comportamiento mecánico de los materiales compuestos*. Tesis Doctoral, Universidad Politécnica de Cataluña, Barcelona.

Carol, I., López, C. & Roa, O. (2001). "Micromechanical analysis of quasi-brittle materials using fracture-based interface elements." *International Journal for Numerical Methods in Engineering* **52**(1-2): 193-215.

Carol, I. & Prat, P. (1997). "Normal/Shear Cracking Model: Application to Discrete Crack Analysis." *Journal Engineering Mechanics ASCE* **123**(8): 765-773

Carol, I., Prat, P. C. & Bazant, Z. P. (1992). "New explicit microplane model for concrete: Theoretical aspects and numerical implementation." *International Journal of Solids and Structures* **29**(9): 1173-1191.

Carpinteri, A., Ferro, G. & Ventura, G. (2003). "Size effects on flexural response of reinforced concrete elements with a nonlinear matrix." *Engineering Fracture Mechanics* **70**(7-8): 995-1013.

CEB-FIB (1990). "Model code 1990." *Bulletin d'Information.*

CEB-FIB (2000). "Bond of reinforcement in concrete." *F. B. 10*, *State-of-art report.*

Cervenka, V. (1985). "Constitutive model for cracked reinforced concrete." *ACI Journal* **82**: 877-882.

Cervera, M., Agelet, C. & Chiumenti, M. (2001). COMET. Contact Mechanical and Thermal analysis. Multi purpose coupled nonlinear program for steady and transient conditions. Barcelona.

Collins, M., Vecchio, F. & Mehlhorn, G. (1985). "An International competition to predict the response of reinforced concrete panels." *Canadian Journal of Civil Engineering* **12**: 624-644.

Cox, J. & Hermann, L. (1998). "Development of a plasticity bond model for steel reinforcement." *Mechanics of cohesive-frictional materials* **3**: 155 -180.

Cox, J. & Herrmann, L. (1999). "Validation of a plasticity bond model for steel reinforcement." *Mechanics of cohesive-frictional materials* **4**: 361 - 389.

Crisfield, M. & Wills, J. (1989). "Analysis of RC panels using different concrete models." *Journal of Engeeniering Mechanics. ASCE* **115**(3): 578-597.

Chaboche, J., Girard, R. & Schaff, A. (1997). "Numerical analysis of composite systems by using interphase/interface models." *Computational Mechanics* **20**: 3 - 11.

Chaves, E. (2003). *A three dimensional setting for strong discontinuities modelling en failure mechanics*. Doctoral Thesis, Technical University of Catalonia, Barcelona.

Chen, G. & Baker, G. (2003). "Influence of bond slip on crack spacing in numerical modeling of reinforced concrete." *Journal of Structural Engineering ASCE* **129**(11): 1514-1521.

Chong, K., Gilbert, I. & Foster, S. (2004). "Modelling time-dependent cracking in reinforced concrete using bong-slip interface elements." *Computers and Concrete* **1**(2): 151-168.

de Borst, R. (2001). "Some recent issues in computational failure mechanics." *International Journal for Numerical Methods in Engineering* **52**: 63-95.

Dugdale, D. (1960). "Yielding of steel sheets containing slits." *Journal for Mechanics of Phisics and Solids* **8**: 100-108.

Dvorak, G. & Bahei-el-Din, Y. (1982). "Plasticity analysis of fibrous composites." *Journal of Applied Mechanics* **49**: 327-335.

Dvorking, E., Cuitino, A. & Gioia, G. (1990). "Finite elements with displacement embedded localization lines insensitive to mesh size and distortions." *International Journal for Numerical Methods in Engineering* **30**: 541-564.

Eligehausen, R., Popov, E. & Bertero, V. (1983). "Local bond stress-slip relations of deformed bar under generalized excitations." *Report UCB/EERC-83.*

Feenstra, P. & de Borst, R. (1995). "Constitutive model for reinforced concrete." *Journal of Engineering Mechanics – ASCE* **121**(5): 587-595.

Gambarova, P., Rosati, G. & Zasso, B. (1989). "Steel-to-concrete bond after concrete spliting: test results." *Materials and Structures* **127**(22): 35 - 47.

Goto, Y. & Otsuka, K. (1979). "Experimental studies on cracks formed in concrete around deformed tension bars." *The technology report of the Tohoku University* **44**(1): 49 - 83.

Gupta, A. & Akbar, H. (1984). "Cracking in reinforced concrete analysis." *Journal of Structural Engineering* **110**(8): 1735-1746.

Hill, R. (1962). "Acceleration waves in solid." *Journal for Mechanics of Phisics and Solids* **10**: 1 -16.

Hill, R. (1963). "Elastic properties of reinforced solids: some theorical principies." *Journal of Mechanics and Physical of Solid* **11**: 357-372.

Hill, R. (1967). "The essencial structure of constitutive laws for metal composites and polycristals." *Journal of Mechanics and Physical of Solid* **15**: 79-95.

Hillerborg, A. (1985). "The teoretical basic of a method to determine the fracture energy gf of concrete." *Materials and Structures* **18**(106): 291-296.

Hillerborg, A., Modeer, M. & Petersson, P. E. (1976). "Ananlysis of crack formation and crack growth in concrete by means of fracture mechanics and finite elements." *Cement and concrete research* **6**(6): 773-782.

Huespe, A. E., Oliver, J., Pulido, M. D. G., Blanco, S. & Linero, D. L. (2006). "On the fracture models determined by the continuum-strong discontinuity approach." *International Journal of Fracture* **137**: 211-229.

Hughes, T. J. R. (2000). *The finite element method.* New York, Dover.

Hutchinson, J. & Jensen, H. (1990). "Models of fiber debonding and pullout in brittle composites with friction." *Mechanics of Materials* **9**(2): 139-163.

Ingraffea, A., Gerstle, W., Gergely, P. & Saouma, V. (1984). "Fracture mechanics of bond in reinforcement concrete." *Journal of Structural Engineering. ASCE* **110**(4): 871 - 890.

Jirasek, M. (2000). "Comparative study on finite elements with embedded discontinuities." *Computer Methods in Applied Mechanics and Engineering* **188**(1-3): 307-330.

Kachanov, L. M. (1986). *Introduction to continuum damage mechanics*, Martinus Nijhoff Publishers.

Kollegger, J. & Mehlhorn, G. (1990). "Material model for the analysis of reinforced concrete surface structures." *Computational Mechanics* **6**: 341-357.

Kwak, H. & Filippou, F. (1997). "Nonlinear FE analysis of R/C structures under monotonic loads." *Computer and Structures* **65**(1): 1-16.

Larsson, R., Runnesson, K. & Ottosen, N. (1993). "Discontinuities displacement approximation for capturing plastic localization." *International Journal for Numerical Methods in Engineering* **36**(2087-2105).

Lemaitre, J. (1992). *A course on damage mechanics*, Springer-Verlag.

Leonhardt, F. (1965). "Reducing the shear reinforcement in reinforced concrete and slabs." *Magazine of concrete research* **17**(53): 187 - 198.

Liao, K. & Reifsnider, L. (2000). "A tensile strength model for unidirectional fiber-reinforced brittle matriz composite." *International Journal of Fracture* **106**: 95 - 115.

Lin, S. (1997). "Use of filamented beam elements for bored pile analysis." *Journal of Structural Engineering ASCE* **123**(9): 1236-1244.

Linero, D. L., Oliver, J., Huespe, A. E. & Pulido, M. D. G. (2005). *Formulación de Discontinuidades Fuertes en la Fractura de Materiales Compuestos Conformados por Fibras Orientadas en una Dirección*. Congreso de Métodos Numéricos en Ingeniería, *SEMNI (ed)* Granada (España).

Linero, D. L., Oliver, J., Huespe, A. E. & Pulido, M. D. G. (2006). *Cracking Modeling in reinforced concrete via the strong discontinuity approach*. EURO-C 2006 Computational Modelling of Concrete Structures, *N. Bicanic, R. d. Borst et al (eds)*, Tyrol (Austria), Balkema Publishers.

Lubliner, J. (1990). *Plasticity theory*. New York, MacMillan.

Luccioni, B. & Lopez, D. (2002). Modelo para materiales compuestos con deslizamiento de fibras. *Análisis y cálculo de estructuras de materiales compuestos*. S. Oller. Barcelona, CIMNE.

Luccioni, B., Lopez, D. & Danesi, R. (2005). "Bond-slip in reinforced concrete elements." *Journal of Structural Engineering ASCE* **131**(11): 1690-1698.

Malvar, J. (1992). "Bond of reinforcement under controlled confinement." *ACI Material Journal* **89**(6): 593 - 601.

Manzoli, O. (1998). *Un modelo analítico y numérico para la simulación de discontinuidades fuertes en mecánica de sólidos*. Tesis Doctotal, Universidad Politécnica de Cataluña, Barcelona.

Marí, A. (2000). "Numerical simulation of th segmental constrution of three dimensional concrete frames." *Engineering Structures* **22**: 585-596.

Maugin, G. A. (1992). *The termodinamics of plasticity and fracture*, Cambridge University Press.

Naaman, A., Namur, G., Alwan, J. & Najm, H. (1991). "Fiber pullout and bond slip II. Experimental validation." *Journal of Structural Engineering ASCE* **117**(9): 2791-2800.

Ogasawara, T., Ishikawa, T., Ito, H., Watanabe, N. & Davies, I. (2001). "Multiple cracking and tensile behavior for an orthogonal 3-D woven Si-Ti-C-O fiber/Si-Ti-C-O matrix composite." *Journal American Ceramic Society* **84**(7): 1565-1574.

Okabe, T., Komotori, J., Shimizu, M. & Takeda, N. (1999). "Mechanical behavior of SiC fiber reinforced brittle-matrix composites." *Journal of Materials Science* **34**: 3405-3412.

Oliver, J. (1989). "A consistent characteristic length for smeared cracking models." *International Journal for Numerical Methods in Engineering* **28**: 461-474.

Oliver, J. (1996a). "Modelling strong discontinuities in solid mechanics via strain softening constitutive equations. Part I: Fundamentals." *International Journal for Numerical Methods in Engineering* **39**: 3575-3600.

Oliver, J. (1996b). "Modelling strong discontinuities in solid mechanics via strain softening constitutive equations. Part II: Numerical Simulation." *International Journal for Numerical Methods in Engineering* **39**: 3601-3623.

Oliver, J. (2000). "On the discrete constitutive models induced by strong discontinuity kinematics and continuum constitutive equa-tions." *International Journal of Solid and Structures* **37**: 7207-7229.

Oliver, J., Cervera, M. & Manzoli, O. (1999). "Strong discontinuities and continuum plasticity models: the strong discontinuities approach." *International Journal of Plasticity* **15**(3): 319-351.

Oliver, J., Cervera, M., Oller, S. & Lubliner, J. (1990). *Isotropic damage models and smeared crack analysis of concrete*. SCI-C Computer Aided Analysis and Design of Concrete Structures, *N. B. e. al. (ed).*

Oliver, J. & Huespe, A. (2004a). "Continuum approach to material failure in strong discontinuity settings." *Computer Methods in Applied Mechanics and Engineering* **193**: 3195 - 3220.

Oliver, J. & Huespe, A. (2004b). "Theoretical and computational issues in modelling material failure in strong discontinuity scenarios." *Computer Methods in Applied Mechanics and Engineering* **193**: 2987-3014.

Oliver, J., Huespe, A. & Samaniego, E. (2003). "A study on finite elements for capturing strong discontinuities." *International Journal for Numerical Methods in Engineering* **56**: 2135-2161.

Oliver, J., Huespe, A., Samaniego, E. & Chaves, E. (2004a). "Continuum approach to the numerical simulation of material failure in concrete." *International Journal for Numerical and Analytical Methods in Geomechanics* **28**: 609-632.

Oliver, J., Huespe, A. E., Blanco, S. & Linero, D. L. (2006). "Stability and robustness issues in numerical modeling of material failure in the strong discontinuity approach." *Computer Methods in Applied Mechanics and Engineering* **(article in press)**.

Oliver, J., Huespe, A. E. & Linero, D. L. (2005a). *Strong Discontinuity Approach to Fracture of Composite Materials*. 11th International Conference on Fracture, Turin (Italia).

Oliver, J., Huespe, A. E., Linero, D. L. & Pulido, M. D. G. (2005b). *Fractura de Materiales Compuestos en Elementos Sometidos a Tracción Uniforme Mediante la Formulación de Discontinuidades Fuertes*. XXII Encuentro del Grupo Español de la Fractura, Almagro (España).

Oliver, J., Huespe, A. E., Pulido, M. D. G. & Blanco, S. (2004b). *Recent advances in computational modelling of material failure*. 4th European Congress on Computational Methods in Applied Sciences and Engineering (ECCOMAS 2004), University of Jyväskylä. Jyväskylä - (Finland).

Oliver, J., Huespe, A. E., Pulido, M. D. G., Blanco, S. & Linero, D. L. (2004c). *New developments in Computational Material Failure Mechanics*. Sixth World Congress on Computational Mechanics (WCCM VI), Beijing, (P.R. of China), Tshinghua University Press.

Oliver, J., Huespe, A. E., Pulido, M. D. G., Blanco, S. & Linero, D. L. (2005c). *Recent developments on the numerical modelling of cracking of plane and reinforced concrete with the Continuum Strong Discontinuity Approach (CSDA).* EUROMECH Colloquium 460 on Numerical Modelling of Concrete Cracking, University of Innsbruck (Austria).

Oliver, J., Huespe, A. E., Pulido, M. D. G. & Chaves, E. (2002). "From continuum mechanics to fracture mechanics: the strong discontinuity approach." *Engineering Fracture Mechanics* **69**(2): 113-136.

Oliver, X. & Agelet, C. (2002). *Mecánica de medios continuos para ingenieros*. Barcelona, UPC.

Oller, S. (2003). *Simulación numérica del comportamiento mecánico de los materiales compuestos*. Barcelona, CIMNE.

Oller, S., Oñate, E., Miquel, J. & Botello, S. (1996). "A plastic damage constitutive model for composite materials." *International Journal of Solid and Structures* **33**(17): 2501 - 2518.

Ortiz, M. (1987). "An analytical study of the localized failure modes of concrete." *Mechanics of cohesive-frictional materials* **6**: 159-174.

Ortiz, M., Leroy, Y. & Needleman, A. (1987). "A finite element method for localized failure analysis." *Computer Methods in Applied Mechanics and Engineering* **61**: 189-214.

Ortiz, M. & Quigley, J. (1991). "Adaptive mesh refinement in strain localization problems." *Computer Methods in Applied Mechanics and Engineering* **90**: 781-804.

Ouyang, C. & Shah, P. (1994). "Fracture energy approach for predicting cracking of reinforced concrete tensile members." *ACI Structural Journal* **91**(1): 69-78.

Ouyang, C., Wollrab, E., Kulkarni, S. & Shah, P. (1997). "Prediction of cracking response of reinforced concrete tensile members." *Journal of Structural Engineering. ASCE* **123**(1): 70 - 78.

Park, R. & Paulay, T. (1975). *Reinfored Concrete Structures*.

Pietruszczak, S. & Winnicki, A. (2003). "Constitutive model for concrete with embedded sets of reinforcement." *Journal of Engineering Mechanics – ASCE* **129**(7): 725-738.

Pietruszczak, S. & Xu, G. (1995). "Brittle response of concrete as a localization problem." *International Journal of Solid and Structures* **32**: 1517-1533.

Pijaudier Cabot, G. & Bazant, Z. (1987). "Nonlocal damage theory." *Journal Engineering Mechanics ASCE* **113**: 1512-1533.

Pulido, M. D. G. (2004). *Contribuciones a la simulación numérica del fallo material en grandes deformaciones*. Tesis Doctotal, Universidad Politécnica de Cataluña, Barcelona.

Rashid, Y. (1968). "Analysis or prestressed concrete presure vessels." *Nuclear Engineering and Design* **7**: 773-782.

Reinhardt, H., Blauwendrad, J. & Vos, E. (1984). "Prediction of bond between steel and concrete by numerical analysis." *Materials and Structures* **17**(100).

Rice, J. R. (1976). The Localization of Plastic Deformation. *Theoretical and Applied Mechanics*. K. W.T., North-Holland Publ. Co.**:** 207-220.

Rice, J. R. & Rudnicki, J. W. (1980). "A note on some feature of the theory of localization of deformation." *International Journal of Solid and Structures* **16**: 597-605.

Rizzi, E., Carol, I. & William, K. (1995). "Localization analysis of elastic degradation with aplication to scalar damage." *Journal of Engineering Mechanics – ASCE* **121**(4): 541 - 554.

Ruiz, G. (2001). "Propagation of a cohesive crack crossing a reinforcement layer." *International Journal of Fracture* **111**: 265-282.

Ruiz, G., Carmona, J. & Cendón, D. (2005). "Propation of a cohesive crack through adherent reinforcement layers." *Computer Methods in Applied Mechanics and Engineering* **(article in press)**.

Ruiz, G., Elices, M. & Planas, J. (1998). "Experimental study of fracture of lightly reinforced concrete beams." *Materials and Structures* **31**: 683-691.

Ruiz, G. & Planas, J. (1994). "Propagación de una fisura cohesiva en vigas de hormigón debilmente armadas: modelo de la longitud efectiva de anclaje." *Anales de la Mecánica de Fractura* **11**: 506-513.

Runesson, K., Ottosen, N. & Peric, D. (1991). "Discontinuous bifurcations of elastic-plastic solutions at plane stress and plane strain " *International Journal of Plasticity* **7**: 99 - 121.

Samaniego, E. (2002). *Contributions to the continuum modelling of strong discontinuities in two-dimensional solids*. Doctoral Thesis, Technical University of Catalonia, Barcelona.

Sanchez-Palencia, E. & Zaoui, A. (1987). *Homogenization techniques for composite media*, Springer Verlag.

Sancho, J. M., Planas, J., Cendón, D., Reyes, E. & Gálvez, J. (2004). *Análisis de la fractura del hormigón mediante elementos finitos con fisura cohesiva embebida: Fundamentos*. Métodos Computacionais em Engenharia, *C. Soares, A. Batista et al (eds)*, Lisboa, APMTAC - SEMNI.

Sancho, J. M., Planas, J., Cendón, D., Reyes, E. & Gálvez, J. (2005). *On the need of enforcement of crack path continuity in the simulation of concrete fracture using embedded crack elements*. EUROMECH Colloquium 460 on Numerical Modelling of Concrete Cracking, Austria.

Sancho, J. M., Planas, J., Cendón, D., Reyes, E. & Gálvez, J. (2006). "An embedded crack model for finite element analysis of concrete fracture." *Engineering Fracture Mechanics* **(accepted for publication)**.

Simó, J. & Hughes, T. H. R. (1998). *Computational Inelasticity*. New York, Springer-Verlag.

Simó, J. & Ju, J. (1987). "Strain and stress based continuum damage models. I. Formulation." *International Journal of Solid and Structures* **23**: 821-840.

Simó, J., Oliver, J. & Armero, F. (1993). "An analysis of strong discontinuities induced by strain-softening in rate-independent inelastic solid." *Computational Mechanics* **12**: 277 - 296.

Simó, J. & Rifai, S. (1990). "A class of mixed assumed strain methods and the method of incompatible modes." *International Journal for Numerical Methods in Engineering* **29**: 1595-1638.

Soh, C., Chiew, S. & Dong, Y. (1999). "Damage model for concrete-steel interface." *Journal of Structural Engineering ASCE* **125**(8): 979-983.

Timoshenko, S. P. & Young, D. H. (1965). *Theory of Structures*, Mcgraw-Hill College.

Truesdell, C. & Toupin, R. (1960). *The classical field theories*. Berlín.

Vasiliev, V. & Morozov, E. (2001). *Mechanics and Analysis of Composite Materials*. Oxford, Elsevier.

Vecchio, F. (2000). "Disturbed stress field model for reinforced concrete: formulation." *Journal of Structural Engineering. ASCE* **126**(6): 1070-1077.

Vecchio, F. (2001). "Disturbed stress field model for reinforced concrete: implementation." *Journal of Structural Engineering ASCE* **127**(1): 12-20.

Vecchio, F. & Collins, M. (1986). "The modified compression-field theory for reinforced concrete elements subjected to shear." *ACI Journal* **83**(2): 219-231.

Vecchio, F., Lai, D., Shim, W. & Ng, J. (2001). "Disturbed stress field model for reinforced concrete: validation." *Journal of Structural Engineering. ASCE* **127**(4): 350 - 358.

Yu, R. & Ruiz, G. (2004). "Static multi-crack modeling in concrete solved by a modified DR method." *Computer and Concrete* **1**(4): 1-17.

Yu, R. & Ruiz, G. (2005). *Static multi-cracking modeling of LRC beams*. VII International Conference on Computational Plasticity, *E. Oñate & D. Owen (eds)*, Barcelona, CIMNE.